frontiers | Research Topics

Forward and inverse solvers in multi-modal electric and magnetic brain imaging: theory, implementation, and application

Edited by
Sampsa Pursiainen, Takfarinas Medani, Johannes Vorwerk,
Richard Leahy and Maria-Carla Piastra

Published in
Frontiers in Human Neuroscience

ISSN 1664-8714
ISBN 978-2-8325-6492-9
DOI 10.3389/978-2-8325-6492-9

Generative AI statement
Any alternative text (Alt text) provided alongside figures in the articles in this ebook has been generated by Frontiers with the support of artificial intelligence and reasonable efforts have been made to ensure accuracy, including review by the authors wherever possible. If you identify any issues, please contact us.

About Frontiers

Frontiers is more than just an open access publisher of scholarly articles: it is a pioneering approach to the world of academia, radically improving the way scholarly research is managed. The grand vision of Frontiers is a world where all people have an equal opportunity to seek, share and generate knowledge. Frontiers provides immediate and permanent online open access to all its publications, but this alone is not enough to realize our grand goals.

Frontiers journal series

The Frontiers journal series is a multi-tier and interdisciplinary set of open-access, online journals, promising a paradigm shift from the current review, selection and dissemination processes in academic publishing. All Frontiers journals are driven by researchers for researchers; therefore, they constitute a service to the scholarly community. At the same time, the *Frontiers journal series* operates on a revolutionary invention, the tiered publishing system, initially addressing specific communities of scholars, and gradually climbing up to broader public understanding, thus serving the interests of the lay society, too.

Dedication to quality

Each Frontiers article is a landmark of the highest quality, thanks to genuinely collaborative interactions between authors and review editors, who include some of the world's best academicians. Research must be certified by peers before entering a stream of knowledge that may eventually reach the public - and shape society; therefore, Frontiers only applies the most rigorous and unbiased reviews. Frontiers revolutionizes research publishing by freely delivering the most outstanding research, evaluated with no bias from both the academic and social point of view. By applying the most advanced information technologies, Frontiers is catapulting scholarly publishing into a new generation.

What are Frontiers Research Topics?

Frontiers Research Topics are very popular trademarks of the *Frontiers journals series*: they are collections of at least ten articles, all centered on a particular subject. With their unique mix of varied contributions from Original Research to Review Articles, Frontiers Research Topics unify the most influential researchers, the latest key findings and historical advances in a hot research area.

Find out more on how to host your own Frontiers Research Topic or contribute to one as an author by contacting the Frontiers editorial office: frontiersin.org/about/contact

Forward and inverse solvers in multi-modal electric and magnetic brain imaging: theory, implementation, and application

Topic editors
Sampsa Pursiainen — Tampere University, Finland
Takfarinas Medani — University of Southern California, United States
Johannes Vorwerk — University of Innsbruck, Austria
Richard Leahy — University of Southern California, United States
Maria-Carla Piastra — University of Twente, Netherlands

Citation
Pursiainen, S., Medani, T., Vorwerk, J., Leahy, R., Piastra, M.-C., eds. (2025). *Forward and inverse solvers in multi-modal electric and magnetic brain imaging: theory, implementation, and application*. Lausanne: Frontiers Media SA.
doi: 10.3389/978-2-8325-6492-9

Table of contents

04 Editorial: Forward and inverse solvers in multi-modal electric and magnetic brain imaging: theory, implementation, and application
Takfarinas Medani, Sampsa Pursiainen, Maria-Carla Piastra, Johannes Vorwerk and Richard M. Leahy

07 CutFEM forward modeling for EEG source analysis
Tim Erdbrügger, Andreas Westhoff, Malte Höltershinken, Jan-Ole Radecke, Yvonne Buschermöhle, Alena Buyx, Fabrice Wallois, Sampsa Pursiainen, Joachim Gross, Rebekka Lencer, Christian Engwer and Carsten Wolters

19 An F-ratio-based method for estimating the number of active sources in MEG
Amita Giri, John C. Mosher, Amir Adler and Dimitrios Pantazis

32 Optimized high-definition tDCS in patients with skull defects and skull plates
Alexander Guillen, Dennis Q. Truong, Abhishek Datta and Yu Huang

39 Visualizing interferential stimulation of human brains
Yu Huang

46 How to assess the accuracy of volume conduction models? A validation study with stereotactic EEG data
Maria Carla Piastra, Robert Oostenveld, Simon Homölle, Biao Han, Qi Chen and Thom Oostendorp

57 Lattice layout and optimizer effect analysis for generating optimal transcranial electrical stimulation (tES) montages through the metaheuristic L1L1 method
Fernando Galaz Prieto, Maryam Samavaki and Sampsa Pursiainen

70 Global sensitivity of EEG source analysis to tissue conductivity uncertainties
Johannes Vorwerk, Carsten H. Wolters and Daniel Baumgarten

85 The SESAMEEG package: a probabilistic tool for source localization and uncertainty quantification in M/EEG
Gianvittorio Luria, Alessandro Viani, Annalisa Pascarella, Harald Bornfleth, Sara Sommariva and Alberto Sorrentino

97 Structured noise champagne: an empirical Bayesian algorithm for electromagnetic brain imaging with structured noise
Sanjay Ghosh, Chang Cai, Ali Hashemi, Yijing Gao, Stefan Haufe, Kensuke Sekihara, Ashish Raj and Srikantan S. Nagarajan

frontiers | Frontiers in Human Neuroscience

TYPE Editorial
PUBLISHED 10 June 2025
DOI 10.3389/fnhum.2025.1629489

Check for updates

OPEN ACCESS

EDITED AND REVIEWED BY
Gernot R. Müller-Putz,
Graz University of Technology, Austria

*CORRESPONDENCE
Takfarinas Medani
✉ MEDANI@USC.EDU

RECEIVED 15 May 2025
ACCEPTED 21 May 2025
PUBLISHED 10 June 2025

CITATION
Medani T, Pursiainen S, Piastra M-C, Vorwerk J and Leahy RM (2025) Editorial: Forward and inverse solvers in multi-modal electric and magnetic brain imaging: theory, implementation, and application.
Front. Hum. Neurosci. 19:1629489.
doi: 10.3389/fnhum.2025.1629489

Editorial: Forward and inverse solvers in multi-modal electric and magnetic brain imaging: theory, implementation, and application

Takfarinas Medani[1]*, Sampsa Pursiainen[2], Maria-Carla Piastra[3], Johannes Vorwerk[4,5] and Richard M. Leahy[1]

[1]Ming Hsieh Department of Electrical and Computer Engineering, University of Southern California, Los Angeles, CA, United States, [2]Mathematics, Computing Sciences, Tampere University, Tampere, Finland, [3]Clinical Neurophysiology, Technical Medical Centre, Faculty of Science and Technology, University of Twente, Enschede, Netherlands, [4]Biomedical Engineering Group, Department of Mechatronics, University of Innsbruck, Innsbruck, Austria, [5]Institute of Measurement and Sensor Technology, UMIT TIROL - Private University for Health Sciences and Health Technology, Hall in Tirol, Austria

KEYWORDS

EEG/MEG, sEEG/ECoG, forward and inverse analyses, modeling, simulation, sensitivity analysis

Editorial on the Research Topic
Forward and inverse solvers in multi-modal electric and magnetic brain imaging: theory, implementation, and application

Understanding the complexities of brain function and structure remains one of the most challenging and exciting frontiers in neuroscience (Sporns, 2013). Advances in multi-modal brain imaging, integrating electrophysiological and magnetophysiological techniques such as non-invasive electroencephalography (EEG), invasive electroencephalography (iEEG), including both stereo-electroencephalography (sEEG), electrocorticography (ECoG), and magnetoencephalography (MEG), have provided unprecedented insights into neural dynamics (Hämäläinen et al., 1993; Gross et al., 2001; Baillet et al., 2001). A central challenge in this domain is solving the forward and inverse problems, which enable the estimation of the brain activity underlying measured signals (Baillet et al., 2001; Wolters et al., 2004; Mosher et al., 1999; Wolters et al., 2006; Piastra et al., 2021; Brette and Destexhe, 2012; Pursiainen et al., 2011).

This Research Topic aimed to bring together cutting-edge research on the theoretical foundations, computational methodologies, and practical applications of forward and inverse solvers in multi-modal electric and magnetic brain imaging. The contributions within this Research Topic span fundamental methodological advances, novel algorithmic frameworks, and state-of-the-art applications that push the boundaries of neuroimaging.

Theoretical and computational advances

One of the significant challenges in EEG/MEG source analysis is accounting for the uncertainties in tissue conductivity. Vorwerk et al. investigated the global sensitivity of EEG source analysis to tissue conductivity uncertainties, emphasizing the importance of accurate head volume conductor models in forward problem solutions (Vorwerk et al., 2014, 2019; Lucka et al., 2012). Their findings highlight how variations in tissue conductivity can significantly impact source localization accuracy, concluding that an accurate parametrization of the head volume conductor model is as important as an accurate representation of the geometry (Wolters et al., 2006; Vorwerk et al., 2014, 2019). Piastra et al. conducted a validation study using stereotactic sEEG data to assess the accuracy of head volume conductor models. Their work underscores the necessity of precise modeling in achieving reliable source localization in combination with empirical validations. Erdbrügger et al. introduced the CutFEM forward modeling approach for EEG source analysis (Miinalainen et al., 2019; Vorwerk et al., 2017; Medani et al., 2015; Dubarry et al., 2023). This method offers enhanced flexibility in handling complex geometries and tissue interfaces in head volume conductor models, contributing to more accurate forward solutions in EEG studies.

Algorithmic innovations and implementations

Advancements in algorithmic frameworks are crucial for improving source localization techniques. Luria et al. presented the SESAMEEG package, a probabilistic tool for source localization and uncertainty quantification in MEG/EEG analysis (Wipf and Nagarajan, 2009; Aydin et al., 2015; Mosher and Leahy, 1998). This package facilitates more robust and interpretable source estimates by incorporating probabilistic modeling. Ghosh et al. developed the Structured Noise Champagne algorithm, an empirical Bayesian approach for electromagnetic brain imaging that accounts for structured noise. This method enhances the reliability of source reconstructions in the presence of complex noise structures (Baillet et al., 2001; Mosher et al., 1999). Giri et al. proposed an F-ratio-based method for estimating the number of active sources in MEG data. Their approach aids in determining the optimal model complexity, balancing the trade-off between model fit and overfitting (Adler et al., 2022).

Applications and future directions

The practical impact of these methodological advancements has been demonstrated in numerous studies. Guillen et al. explored optimized high-definition transcranial direct current stimulation (tDCS) in patients with skull defects and implants, demonstrating the clinical relevance of accurate modeling in neuromodulation therapies (Carla Piastra et al., 2021; Rampersad et al., 2014; Armonaite et al., 2025; Pursiainen et al., 2018). Huang visualized interferential stimulation of human brains, providing insights into the spatial distribution of electric fields during stimulation protocols (Huang et al., 2018; Saturnino et al., 2019). This work contributes to the optimization of stimulation parameters for therapeutic interventions. Furthermore, Prieto et al. analyzed the effects of lattice layout and optimizer selection on generating optimal transcranial electrical stimulation (tES) montages using the metaheuristic L1L1 method. Their findings inform the design of more effective stimulation configurations.

Collectively, these contributions underscore the importance of integrating theoretical, computational, and practical perspectives in advancing EEG/MEG source analysis as well as tES modeling. Future research directions may include the development of standardized pipelines (Vorwerk et al., 2014; Rampersad et al., 2014; Erdbrügger et al., 2024; Medani et al., 2023; He et al., 2020), the incorporation of machine learning techniques for model selection and parameter estimation, and the expansion of open-source tools to facilitate broader accessibility and reproducibility in the field (He et al., 2020; Vorwerk et al., 2018; Oostenveld et al., 2011; Tadel et al., 2011, 2019; Gramfort et al., 2013; Delorme and Makeig, 2004; Schrader et al., 2021; Cui et al., 2024).

We extend our sincere gratitude to all authors for their high-quality contributions and to the reviewers for their thoughtful feedback. We hope this Research Topic serves as a valuable resource for both newcomers and experienced researchers aiming to advance the state of the art in neuroelectromagnetic modeling.

Author contributions

TM: Writing – original draft, Writing – review & editing. SP: Writing – review & editing. M-CP: Writing – review & editing. JV: Writing – review & editing. RL: Writing – review & editing.

Conflict of interest

The authors declare that the research was conducted in the absence of any commercial or financial relationships that could be construed as a potential conflict of interest.

Publisher's note

References

Adler, A., Wax, M., and Pantazis, D. (2022). "Brain source localization by alternating projection," in *IEEE 19th International Symposium on Biomedical Imaging (ISBI)* (Kolkata: IEEE), 1–5.

Armonaite, K., Assenza, G., Bertoli, M., Conti, L., Croce, P., Iorio, D., et al. (2025). R, et al. Local neurodynamics and tDCS effects: a guide for symptom mitigation interventions. *Brain Stimul.* 18:288. doi: 10.1016/j.brs.2024.12.223

Aydin, Ü., Vorwerk, J., Dümpelmann, M., Küpper, P., Kugel, H., Heers, M., et al. (2015). Combined EEG/MEG can outperform single modality EEG or MEG source reconstruction in presurgical epilepsy diagnosis. *PLoS ONE.* 10:e0118753. doi: 10.1371/journal.pone.0118753

Baillet, S., Mosher, J. C., and Leahy, R. M. (2001). Electromagnetic brain mapping. *IEEE Signal Process. Mag.* 18, 14–30. doi: 10.1109/79.962275

Brette, R., and Destexhe, A. (eds.). (2012). *Handbook of Neural Activity Measurement.* Cambridge: Cambridge University Press, 479. doi: 10.1017/CBO9780511979958

Carla Piastra, M., van der Cruijsen, J., Piai, V., Jeukens, F. E. M., Manoochehri, M., Schouten, A. C., et al. (2021). ASH: an Automatic pipeline to generate realistic and individualized chronic Stroke volume conduction Head models. *J. Neural Eng.* 18:044001. doi: 10.1088/1741-2552/abf00b

Cui, W., Jeong, W., Thölke, P., Medani, T., Jerbi, K., Joshi, A. A., et al. (2024). "Neuro-GPT: towards a foundation model for EEG," in *2024 IEEE International Symposium on Biomedical Imaging (ISBI); May 27–30, Athens, Greece.* p. 1–5. doi: 10.1109/ISBI56570.2024.10635453

Delorme, A., and Makeig, S. (2004). EEGLAB: an open source toolbox for analysis of single-trial EEG dynamics including independent component analysis. *J. Neurosci. Methods.* 134, 9–21. doi: 10.1016/j.jneumeth.2003.10.009

Dubarry, A.- S., Mosher, J. C., Dalal, S. S., and Bénar, C. G. (2023). *What are the Promises, and Challenges of Simultaneous MEG and Intracranial Recordings? Studies in Neuroscience, Psychology and Behavioral Economics.* Cham: Springer International Publishing, 199–216. doi: 10.1007/978-3-031-20910-9_13

Erdbrügger, T., Antonakakis, M., Aydin, Ü., Westhoff, A., Höltershinken, M., Vorwerk, J., et al. (2024). *The University of Münster DUNEuro-Based Pipeline to Create Personalized Head Models with Calibrated Skull Conductivity for EEG/MEG Source Analysis and Optimized Multi-Channel tES.* Genève: Zenodo.

Gramfort, A., Luessi, M., Larson, E., Engemann, D. A., Strohmeier, D., Brodbeck, C., et al. (2013). MEG and EEG data analysis with MNE-Python. *Front. Neurosci.* 7:267. doi: 10.3389/fnins.2013.00267

Gross, J., Kujala, J., Hamalainen, M., Timmermann, L., Schnitzler, A., Salmelin, R., et al. (2001). Dynamic imaging of coherent sources: Studying neural interactions in the human brain. *Proc. Natl. Acad. Sci. USA.* 98, 694–699. doi: 10.1073/pnas.98.2.694

Hämäläinen, M., Hari, R., Ilmoniemi, R. J., Knuutila, J., and Lounasmaa, O. V. (1993). Magnetoencephalography—theory, instrumentation, and applications to noninvasive studies of the working human brain. *Rev. Mod. Phys.* 65, 413–497. doi: 10.1103/RevModPhys.65.413

He, Q., Rezaei, A., and Pursiainen, S. (2020). Zeffiro user interface for electromagnetic brain imaging: a GPU accelerated FEM tool for forward and inverse computations in Matlab. *Neuroinformatics* 18, 237–250. doi: 10.1007/s12021-019-09436-9

Huang, Y., Datta, A., Bikson, M., and Parra, L. C. (2018). *ROAST: An Open-Source, Fully-Automated, Realistic Volumetric-Approach-Based Simulator For TES.* Available online at: https://ieeexplore.ieee.org/abstract/document/8513086 (accessed May 12, 2025).

Lucka, F., Pursiainen, S., Burger, M., and Wolters, C. H. (2012). Hierarchical Bayesian inference for the EEG inverse problem using realistic FE head models: depth localization and source separation for focal primary currents. *Neuroimage* 61, 1364–1382. doi: 10.1016/j.neuroimage.2012.04.017

Medani, T., Garcia-Prieto, J., Tadel, F., Antonakakis, M., Erdbrügger, T., Höltershinken, M., et al. (2023). Brainstorm-DUNEuro: an integrated and user-friendly Finite Element Method for modeling electromagnetic brain activity. *Neuroimage* 267:119851. doi: 10.1016/j.neuroimage.2022.119851

Medani, T., Lautru, D., Schwartz, D., Ren, Z., and Sou, G. F. E. M. (2015). method for the EEG forward problem and improvement based on modification of the Saint Venant's method. *Prog. Electromagnet. Res.* 153, 11–22. doi: 10.2528/PIER15050102

Miinalainen, T., Rezaei, A., Us, D., Nüßing, A., Engwer, C., Wolters, C. H., et al. (2019). A realistic, accurate and fast source modeling approach for the EEG forward problem. *Neuroimage* 184, 56–67. doi: 10.1016/j.neuroimage.2018.08.054

Mosher, J. C., and Leahy, R. M. (1998). Recursive MUSIC: a framework for EEG and MEG source localization. *IEEE Trans. Biomed. Eng.* 45, 1342–1354. doi: 10.1109/10.725331

Mosher, J. C., Leahy, R. M., and Lewis, P. S. E. E. G. (1999). and MEG: forward solutions for inverse methods. *IEEE Trans. Biomed. Eng.* 46, 245–259. doi: 10.1109/10.748978

Oostenveld, R., Fries, P., Maris, E., and Schoffelen, J.-., M. (2011). FieldTrip: Open source software for advanced analysis of MEG, EEG, and invasive electrophysiological data. *Comput. Intell. Neurosci.* 2011:156869. doi: 10.1155/2011/156869

Piastra, M. C., Nüßing, A., Vorwerk, J., Clerc, M., Engwer, C., Wolters, C. H. A., et al. (2021). comprehensive study on electroencephalography and magnetoencephalography sensitivity to cortical and subcortical sources. *Hum. Brain Mapp.* 42, 978–992. doi: 10.1002/hbm.25272

Pursiainen, S., Agsten, B., Wagner, S., and Wolters, C. H. (2018). Advanced boundary electrode modeling for tES and parallel tES/EEG. *IEEE Trans. Neural Syst. Rehabil. Eng.* 26, 37–44. doi: 10.1109/TNSRE.2017.2748930

Pursiainen, S., Sorrentino, A., Campi, C., and Piana, M. (2011). Forward simulation and inverse dipole localization with the lowest order Raviart—Thomas elements for electroencephalography. *Inverse Probl.* 27:045003. doi: 10.1088/0266-5611/27/4/045003

Rampersad, S. M., Janssen, A. M., Lucka, F., Aydin, Ü., Lanfer, B., Lew, S., et al. (2014). Simulating transcranial direct current stimulation with a detailed anisotropic human head model. *IEEE Trans. Neural Syst. Rehabil. Eng.* 22, 441–452. doi: 10.1109/TNSRE.2014.2308997

Saturnino, G. B., Puonti, O., Nielsen, J. D., Antonenko, D., Madsen, K. H., Thielscher, A., et al. (2019). "SimNIBS 2.1: A comprehensive pipeline for individualized electric field modelling for transcranial brain stimulation," in *Brain and Human Body Modeling* (Cham: Springer International Publishing), 3–25.

Schrader, S., Westhoff, A., Piastra, M. C., Miinalainen, T., Pursiainen, S., Vorwerk, J., et al. (2021). DUNEuro-A software toolbox for forward modeling in bioelectromagnetism. *PLoS ONE.* 16:e0252431. doi: 10.1371/journal.pone.0252431

Sporns, O. (2013). Structure and function of complex brain networks. *Dialogues Clin. Neurosci.* 15, 247–262. doi: 10.31887/DCNS.2013.15.3/osporns

Tadel, F., Baillet, S., Mosher, J. C., Pantazis, D., and Leahy, R. M. (2011). Brainstorm: a user-friendly application for MEG/EEG analysis. *Comput. Intell. Neurosci.* 2011:879716. doi: 10.1155/2011/879716

Tadel, F., Bock, E., Niso, G., Mosher, J. C., Cousineau, M., Pantazis, D., et al. (2019). MEG/EEG group analysis with brainstorm. *Front. Neurosci.* 13:76. doi: 10.3389/fnins.2019.00076

Vorwerk, J., Aydin, Ü., Wolters, C. H., and Butson, C. R. (2019). Influence of head tissue conductivity uncertainties on EEG dipole reconstruction. *Front. Neurosci.* 13:531. doi: 10.3389/fnins.2019.00531

Vorwerk, J., Cho, J.-., H., Rampp, S., Hamer, H., Knösche, T. R., et al. (2014). guideline for head volume conductor modeling in EEG and MEG. *Neuroimage.* 100, 590–607. doi: 10.1016/j.neuroimage.2014.06.040

Vorwerk, J., Engwer, C., Pursiainen, S., and Wolters, C. H. A. (2017). mixed finite element method to solve the EEG forward problem. *IEEE Trans. Med. Imaging.* 36, 930–941. doi: 10.1109/TMI.2016.2624634

Vorwerk, J., Oostenveld, R., Piastra, M. C., Magyari, L., and Wolters, C. H. (2018). The FieldTrip-SimBio pipeline for EEG forward solutions. *Biomed. Eng. Online* 17:37. doi: 10.1186/s12938-018-0463-y

Wipf, D., and Nagarajan, S. A. (2009). unified Bayesian framework for MEG/EEG source imaging. *Neuroimage.* 44, 947–966. doi: 10.1016/j.neuroimage.2008.02.059

Wolters, C. H., Anwander, A., Tricoche, X., Weinstein, D., Koch, M. A., MacLeod, R. S. (2006). Influence of tissue conductivity anisotropy on EEG/MEG field and return current computation in a realistic head model: a simulation and visualization study using high-resolution finite element modeling. *Neuroimage* 30, 813–826. doi: 10.1016/j.neuroimage.2005.10.014

Wolters, C. H., Grasedyck, L., and Hackbusch, W. (2004). Efficient computation of lead field bases and influence matrix for the FEM-based EEG and MEG inverse problem. *Inverse Probl.* 20:1099. doi: 10.1088/0266-5611/20/4/007

frontiers | Frontiers in Human Neuroscience

TYPE Original Research
PUBLISHED 22 August 2023
DOI 10.3389/fnhum.2023.1216758

OPEN ACCESS

EDITED BY
Stefan Haufe,
Technische Universität Berlin, Germany

REVIEWED BY
German Castellanos-Dominguez,
National University of Colombia,
Manizales, Colombia
Ji Chen,
University of Houston, United States
Luis Gomez,
Purdue University, United States

*CORRESPONDENCE
Tim Erdbrügger
✉ tim.erdbruegger@uni-muenster.de

RECEIVED 04 May 2023
ACCEPTED 10 July 2023
PUBLISHED 22 August 2023

CITATION
Erdbrügger T, Westhoff A, Höltershinken M, Radecke J-O, Buschermöhle Y, Buyx A, Wallois F, Pursiainen S, Gross J, Lencer R, Engwer C and Wolters C (2023) CutFEM forward modeling for EEG source analysis. *Front. Hum. Neurosci.* 17:1216758. doi: 10.3389/fnhum.2023.1216758

CutFEM forward modeling for EEG source analysis

Tim Erdbrügger[1,2]*, Andreas Westhoff[1], Malte Höltershinken[1,2], Jan-Ole Radecke[3,4], Yvonne Buschermöhle[1,5], Alena Buyx[6], Fabrice Wallois[7], Sampsa Pursiainen[8], Joachim Gross[1,5], Rebekka Lencer[3,4,5,9], Christian Engwer[2] and Carsten Wolters[1,5]

[1]Institute for Biomagnetism and Biosignalanalysis, University of Münster, Münster, Germany, [2]Institute for Analysis and Numerics, University of Münster, Münster, Germany, [3]Department of Psychiatry and Psychotherapy, University of Lübeck, Lübeck, Germany, [4]Center of Brain, Behaviour and Metabolism, University of Lübeck, Lübeck, Germany, [5]Otto Creutzfeldt Center for Cognitive and Behavioral Neuroscience, University of Münster, Münster, Germany, [6]Institute of History and Ethics in Medicine, Technical University of Munich, Munich, Germany, [7]Institut National de la Santé et de la Recherche Médicale, University of Picardie Jules Verne, Amiens, France, [8]Computing Sciences Unit, Faculty of Information Technology and Communication Sciences, Tampere University, Tampere, Finland, [9]Institute for Translational Psychiatry, University of Münster, Münster, Germany

Introduction: Source analysis of Electroencephalography (EEG) data requires the computation of the scalp potential induced by current sources in the brain. This so-called EEG forward problem is based on an accurate estimation of the volume conduction effects in the human head, represented by a partial differential equation which can be solved using the finite element method (FEM). FEM offers flexibility when modeling anisotropic tissue conductivities but requires a volumetric discretization, a mesh, of the head domain. Structured hexahedral meshes are easy to create in an automatic fashion, while tetrahedral meshes are better suited to model curved geometries. Tetrahedral meshes, thus, offer better accuracy but are more difficult to create.

Methods: We introduce CutFEM for EEG forward simulations to integrate the strengths of hexahedra and tetrahedra. It belongs to the family of unfitted finite element methods, decoupling mesh and geometry representation. Following a description of the method, we will employ CutFEM in both controlled spherical scenarios and the reconstruction of somatosensory-evoked potentials.

Results: CutFEM outperforms competing FEM approaches with regard to numerical accuracy, memory consumption, and computational speed while being able to mesh arbitrarily touching compartments.

Discussion: CutFEM balances numerical accuracy, computational efficiency, and a smooth approximation of complex geometries that has previously not been available in FEM-based EEG forward modeling.

KEYWORDS

EEG forward problem, realistic head modeling, volume conductor modeling, unfitted FEM, level set, finite element method

1. Introduction

Electroencephalography (EEG) is a widely used tool for the assessment of neural activity in the human brain (Brette and Destexhe, 2012). To estimate the area of the brain responsible for the measured data, one has to simulate the electric potential as induced by hypothetical current sources in the brain, i.e., the EEG forward problem has to be solved. While quasi-analytical solutions to the differential equation underlying the forward problem exist, these are only available in simplified geometries such as the multi-layer sphere model

(De Munck and Peters, 1993). One, thus, requires numerical methods to incorporate accurate representations of the head's shape and volume conduction properties. Popular approaches are the boundary element method (BEM) (Mosher et al., 1999; Gramfort et al., 2011; Makarov et al., 2020), finite difference method (FDM) (Song et al., 2015; Cuartas Morales et al., 2019), and the finite element method (FEM) (Zhang et al., 2004; Vallaghé and Papadopoulo, 2010; Medani et al., 2015; Acar et al., 2016; Azizollahi et al., 2018). Here, we will focus on the FEM due to its flexibility in modeling complex geometries with inhomogeneous and anisotropic compartments (Schimpf et al., 2002; Van Uitert et al., 2004; Wolters et al., 2007; Bangera et al., 2010; Nüßing et al., 2016; Beltrachini, 2018; He et al., 2020; Vermaas et al., 2020). Efficient solvers and the transfer matrix approach (Wolters et al., 2004; Lew et al., 2009) allow significantly reduced computational costs.

When employing FEM, one usually chooses between either a hexahedral or tetrahedral discretization of the head. Both choices come with their own strengths and limitations. The mesh creation requires a classification of the MRI into tissue types. This segmentation data often come in the form of binary maps with voxels of approximately 1mm resolution, allowing for quick and simple hexahedral mesh generation. However, as head tissue surfaces are smooth, approximating them with regular hexahedra is bound to be inaccurate. While the methods for geometry adaptation exist (Wolters et al., 2007), the resulting meshes still have an (reduced) angular pattern. Furthermore, when applying a standard continuous Galerkin FE scheme, areas with very thin compartments may suffer from leakage effects where current can bypass the insulating effects of the skull (Sonntag et al., 2013). To alleviate this, flux-based methods, such as the discontinuous Galerkin method, offer a robust alternative (Engwer et al., 2017). These, however, severely increase the number of degrees of freedom (DOF) and thus necessary for computational effort.

Surface-based tetrahedral FEM approaches, on the other hand, are able to accurately model the curvature of smooth tissue surfaces. Creating high quality tetrahedra, e.g., ones fulfilling a delaunay criterion, requires tissue surface representations in the form of triangulations first. These triangulations have to be free of self-intersections and are often nested, usually leading to modeling inaccuracies such as neglecting skull holes or an artificial separation of gray matter and skull. Therefore, we will not discuss surface-based tetrahedral FEM approaches throughout this study.

In the study by Rice et al. (2013), the impact of prone vs. supine subject positioning on EEG amplitudes was investigated. In the small group study, average differences of up to 80% were found. These were accompanied by differences in MRI-based CSF-thickness estimation of up to 30% underlining the importance of correctly modeling CSF-thickness and areas of contact between the skull and brain surfaces.

Recently, an unfitted discontinuous Galerkin method (UDG) (Bastian and Engwer, 2009) was introduced to solve the EEG forward problem (Nüßing et al., 2016). Rather than working with mesh elements that are tailored to the geometry, it uses a background mesh which is cut by level set functions, each representing a tissue surface. It was shown to outperform the accuracy of a discontinuous Galerkin approach on a hexahedral mesh while not being limited by the assumptions necessary to create tetrahedral meshes.

Extending the ideas of the UDG method, this study introduces a multi-compartment formulation of the CutFEM (Burman et al., 2015) for EEG source analysis. Compared with UDG, it operates on a simpler trial function space and adds a ghost penalty based on the study by Burman (2010). The ghost penalty couples small mesh elements to their neighbors to improve the conditioning of the method.

This study is structured as follows. After introducing the theory behind CutFEM, three successively more realistic scenarios are tested. These scenarios include a multi-layer sphere model, followed by realistic brain tissues embedded in spherical skull and scalp compartments. Finally, a fully realistic five-compartment head model is used for source analysis of the P20/N20 component of measured somatosensory evoked potentials (SEP). Comparison results from different FEM and meshing approaches will be considered throughout the scenarios.

2. Methods

2.1. A cut finite element method

Deviating from classical, fitted FEM-approaches, where the mesh cells resolve tissue boundaries, CutFEM uses a level set-based representation of domain surfaces. Let $\Omega = \bigcup_i \Omega_i$ be the head domain divided into m disjunct open subdomains, e.g., the gray matter, white matter, CSF, skull, and skin. The level set function for compartment i is then defined as follows:

$$\Phi_i(x) \begin{cases} < 0, \text{ if } x \in \Omega_i \\ = 0, \text{ if } x \in \partial\Omega_i \\ > 0, \text{ else} \end{cases}$$

and $\mathcal{L}_i = \{x \in \Omega : \Phi_i(x) = 0\}$ denotes its (zero) level set. We proceed by defining a background domain $\hat{\Omega} \subset \mathbb{R}^3$ covering the head domain Ω. This background is, then tesselated, yielding a regular hexahedral mesh $\mathcal{T}(\hat{\Omega})$, the fundamental or background mesh. Taking on the level set representation, submeshes $\mathcal{T}_h^i \subset \mathcal{T}_h(\hat{\Omega})$ are created from the background mesh, containing all cells that have at least partial support within the respective subdomain Ω_i. This results in an overlap of submeshes at compartment interfaces. For each submesh, we define a conforming $\mathbb{Q}_1$ space V_h^i. Thus, up to this point, each submesh is treated the way a conforming Galerkin method would treat the entire mesh.

The difference, then, lies in restricting the trial and test functions to their respective compartment, effectively cutting them off at the boundary and giving rise to the name CutFEM. A fundamental mesh cell intersected by a level set $\mathcal{L}_i$ is called a cut cell. Their respective fundamental cells are contained in multiple compartments and thus have more DOF. On the other hand, compared with classical conforming discretizations, a coarser mesh resolution can be chosen, as the mesh does not have to follow small geometric features. As the trial functions are only continuous on their respective compartment and cut off at the boundary, using them to approximate the electric potential requires internal coupling conditions at the tissue interfaces. We define the internal skeleton as the union of all subdomain interfaces.

$$\Gamma = \bigcup \left\{ \bar{\Omega}_i \cap \bar{\Omega}_j : i \neq j,\ \mu_{d-1}(\bar{\Omega}_i \cap \bar{\Omega}_j) > 0 \right\}. \tag{1}$$

μ_{d-1} is the d-1 dimensional measure in d-dimensional space. For two sets, E, F sharing both a common interface (an element of Γ) and a possibly discontinuous function u operating on them we can define a scalar- or vector-valued jump operator as $[\![u]\!] := u|_E \cdot n_E + u|_F \cdot n_F$ with n_E, n_F the outer unit normal of the respective set. Additionally, a (skew-)weighted average can be stated as follows:

$$\{u\} = \omega_E u|_E + \omega_F u|_F \tag{2}$$

$$\{u\}^* = \omega_F u|_E + \omega_E u|_F. \tag{3}$$

with $\omega_E = \frac{\delta_E}{\delta_E + \delta_F}$, $\delta_E = n_E^t \sigma_E n_E$. Here, σ_E refers to the symmetric 3×3, positive definite electric conductivity tensor on E. Notably, $[\![uv]\!] = [\![u]\!]\{v\}^* + \{u\}[\![v]\!]$. The purpose of these definitions will become clear when deriving the weak formulation for our forward model.

Typically, the EEG forward problem for the electric potential u induced by a neural source term f is derived from the quasi-static formulation of Maxwell's equations (Brette and Destexhe, 2012).

$$\nabla \cdot \sigma \nabla u = f, \quad \text{in} \bigcup_i \Omega_i \tag{4}$$

$$\langle \sigma \nabla u, n \rangle = 0, \quad \text{on } \partial \bar{\Omega} \tag{5}$$

And in addition we require continuity of the electric potential and the electric current

$$[\![u]\!] = 0, \quad \text{on } \Gamma \tag{6}$$

$$[\![\sigma \nabla u]\!] = 0, \quad \text{on } \Gamma. \tag{7}$$

As trial and test space, we employ V_h as direct sum of all V_h^i.

The weak formulation can be obtained by multiplying with a test function, integrating and applying subdomain-wise integration by parts. This yields:

$$\sum_i \left(\int_{\Omega_i} \sigma \nabla u_h^i \nabla v_h^i dx \right) - \int_\Gamma \{\sigma \nabla u_h\} [\![v_h]\!] dS = - \sum_i \left(\int_{\Omega_i} f v_h^i dx \right),$$

where the jump formula for a product of two functions as well as (7) were used. u_h^i is the restriction of $u_h \in V$ to V_i. A symmetry term $\pm \int_\Gamma \{\sigma \nabla v_h\} [\![u_h]\!] dS$ is added to end up with either a symmetric or non-symmetric bilinearform.

To incorporate (6), a Nitsche penalty term (Nitsche, 1971) is added that weakly couples the domains. Asymptotically, it enforces continuity of the electric potential over tissue boundaries and ensures the coercivity necessary for the methods' convergence (Burman et al., 2015):

$$P_\gamma(u, v) = \gamma \nu_k \int_\Gamma \frac{\hat{\sigma}}{\hat{h}} [\![u_h]\!] [\![v_h]\!] dS. \tag{8}$$

Here, ν_k, $\hat{h}$, and $\hat{\sigma}$ are scaling parameters based on the ratio of cut cell area on each interfaces' side, dimension, degree of trial functions used, and conductivity. See Di Pietro and Ern (2011) for a further discussion. γ is a free parameter to be discussed later.

A challenge is the shape of the cut-cells. Distorted or sliver-like snippets with very small volumes lead to very small entries in the stiffness matrix, deteriorating the conditioning of the forward problem. To alleviate this, a ghost penalty (Burman, 2010) term is used, which takes place on the interfaces of all the fundamental mesh cells cut by a level set. Let

$$\hat{\Gamma} = \cup \left\{ \partial E_i : E_i \in \mathcal{T}_h, E_i \cap \Gamma \neq \emptyset \right\}. \tag{9}$$

Note the difference between Γ and $\hat{\Gamma}$. Γ operates on compartment interfaces, $\hat{\Gamma}$ on faces of the fundamental mesh. The ghost penalty is then defined as follows:

$$a^G(u_h, v_h) = \gamma_G \int_{\hat{\Gamma}} \hat{h} [\![\sigma \nabla u_h]\!] [\![\nabla v_h]\!] dS, \tag{10}$$

where γ_G is again a free parameter, usually a couple orders of magnitude smaller than γ. Penalizing the jump in the gradient ensures that trial functions which are only active on small snippets cannot deviate too strongly from the solution in neighboring cells. When using higher order trial functions, higher order derivatives are no longer zero and have to be penalized as well. Notably, by adding a ghost penalty, the method is no longer fully consistent with the original problem. However, due to the size of γ_G, the effect on the overall result is negligible. The weak CutFEM EEG-forward problem can now be stated as finding the electric potential $u_h \in V_h$ such that

$$a(u_h, v_h) + a_{n/s}^N(u_h, v_h) + a^G(u_h, v_h) = l(v_h) \ \forall v_h \in V_h, \tag{11}$$

with

$$a(u_h, v_h) = \sum_i \int_{\Omega_i} \sigma \nabla u_h^i \nabla v_h^i dx,$$

$$l(v_h) = - \sum_i \int_{\Omega_i} f v_h^i dx$$

and

$$a_{n/s}^N(u_h, v_h) := - \int_\Gamma \{\sigma \nabla u_h\} [\![v_h]\!] \pm \int_\Gamma \{\sigma \nabla v_h\} [\![u_h]\!] dS + \gamma \nu_k \int_\Gamma \frac{\hat{\sigma}}{\hat{h}} [\![u_h]\!] [\![v_h]\!] dS.$$

In the following, we will refer to these two variants as NWIPG/SWIPG, short for the non-symmetric/symmetric weighted interior penalty Galerkin method.

In the study by Oden et al. (1998) and Guzmán and Rivière (2009), it was shown that the non-symmetric DG-methods may result in a sub-optimal convergence rate in the L2-norm (full convergence in H1), a result that also extends to CutFEM (Burman and Hansbo, 2012). However, while SWIPG is coercive only if γ is chosen sufficiently large (Burman and Hansbo, 2012), NWIPG does not have such a limitation. Therefore, we will employ the NWIPG method throughout this study due to its stability with regard to the selection of γ.

2.1.1. Integration over the cut domains

Fundamental cells that are cut by level sets, the cut cells; can be integrated over by employing a topology preserving marching cubes algorithm (TPMC) (Engwer and Nüßing, 2017). The initial cell is divided into a set of snippets, each completely contained within one subdomain. These snippets are of a simple geometry and therefore easy to integrate over. Thus, integrals over the fundamental cell or subdomain boundaries are replaced by integrals over the snippets or their boundaries. The trial functions are effectively cut off at the compartment boundaries.

See Figure 1 for an overview of the reconstruction steps. Notably, the trial functions are coupled to their respective submesh, not to the TPMC reconstruction of the domain. The latter only determines the area over which the functions are integrated.

Starting on the fundamental mesh, the algorithm is applied once per level set. Each following iteration is applied on the cut cells of the previous iteration, i.e., first the fundamental mesh is cut, then the resulting snippets are cut. This ensures the correct handling of mesh cells that are cut by multiple level sets.

2.1.2. Source model and transfer matrix

Following the principle of St. Venant, the source term f will be approximated by a set of monopoles. Where fitted FEM use mesh vertices as monopole locations, this is not feasible for CutFEM as fundamental cells may have vertices not belonging to the source compartment. Only gray matter cut cells are used, and the locations are based on a Gauss-Legendre quadrature rule. For more information on the Venant source model, see Buchner et al. (1997) and Medani et al. (2015).

For an accurate source analysis, it is necessary to compute the EEG-forward solution for a large number, i.e., tens of thousands, of possible sources. However, the electric potential induced by a source is only of interest at a set of predetermined points, namely, the electrodes at the scalp. However, rather than solving (11) for each source individually, a transfer matrix approach (Gençer and Acar, 2004; Wolters et al., 2004) is employed, significantly reducing the amount of computation time needed.

2.2. Numerical validation

2.2.1. Head models

For numerical evaluations, three progressively more realistic scenarios were created, two sphere models, one of which contains realistic brain tissues, and a five compartment model created from anatomical data. For each model, we will compare CutFEM and a geometry-adapted hexahedral CG-FEM approach (*Hex*) with a

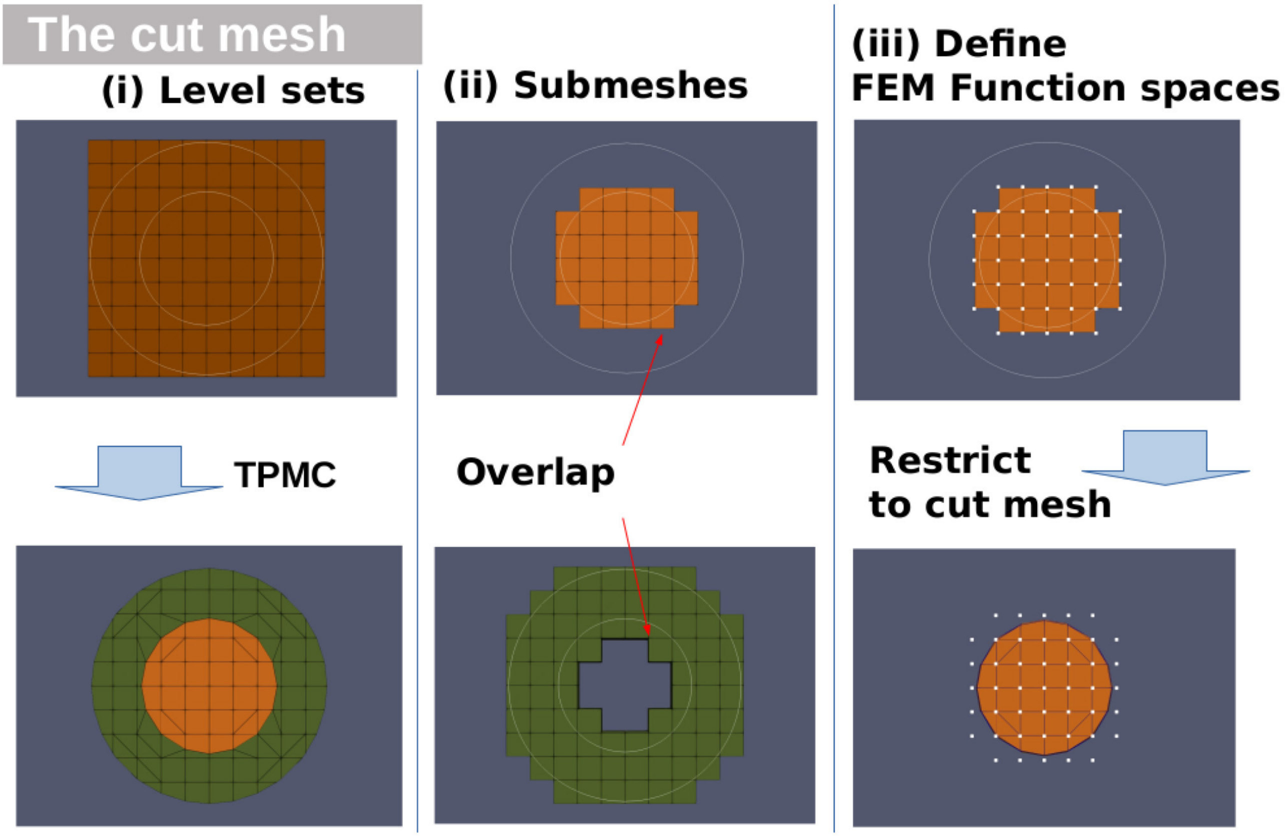

FIGURE 1
Level sets over fundamental mesh and TPMC reconstruction. **Left**: Fundamental mesh with two spherical level sets, topology preserving marching cubes reconstruction. **Center**: Overlapping submeshes for the two compartments enclosed by the level sets. **Right**: Trial function space for the inner compartment with white dots representing degrees of freedom, cut area that the DOF are restricted to.

TABLE 1 Radii, center, and conductivities for the shifted sphere model.

	Radius [mm]	Center [mm]	σ [S/m]
Scalp	92	(127 127 127)	0.43
Skull	86	(127 127 127)	0.01
CSF	80	(127 127 127)	0.33
Brain	78	(129 127 127)	0.33

node shift for the geometry-adaptation of 0.33 (Wolters et al., 2007). In the first model, the UDG approach of Nüßing et al. (2016) will also be added to the comparisons. To balance computational load, *Hex* will use 1 mm meshes, whereas for CutFEM and UDG, we use a 2 mm background mesh. Additionally, in the sphere model, the convergence rate for CutFEM will be investigated by comparing models with 16, 8, 4, and 2 mm resolution. The realistic 5-compartment model will feature an additional tetrahedral head model.

2.2.1.1. Shifted spheres

The first scenario contains the four spherical compartments, such as the brain, CSF, skull, and scalp. The brain sphere will be shifted to one side, simulating a situation where the subject lies down and the brain sinks to the back of the skull. Conductivities were chosen according to study by McCann et al. (2019), with the exception that the CSF and brain use the same conductivity. In terms of volume conduction, the model is thus indistinguishable from a 3-layer concentric sphere model, and analytical solutions (De Munck and Peters, 1993) can be used as benchmark. These would not be available if a realistic CSF conductivity was used. Conductivity values and radii of the compartments are shown in Table 1. Notably, the spherical geometries used here cannot properly represent the shape of the human head. They are commonly used as an initial validation in a simplified scenario where exact reference solutions are available (Wolters et al., 2004; Medani et al., 2015). Thus, they are merely the first of three numerical validation steps in this study.

TPMC was applied twice, once on the fundamental mesh and once on the resulting cut cells. Notably, this additional refinement step does not change the number of trial functions of the model. In total, 200 evenly spaced electrodes were placed on the surface of the outer layer, and a total of 13,000 Evaluation points were distributed evenly throughout the inner sphere. Lead fields for both radial and tangential source directions were computed at each point. For CutFEM, a combination of $\gamma = 16$ and $\gamma_G = 0.1$ has shown promising results. For UDG, no ghost penalty was implemented and $\gamma = 4$ was chosen, following Nüßing et al. (2016).

2.2.1.2. Spheres containing realistic brain

In the previous section, the level set functions could be computed analytically up to an arbitrary accuracy. In a realistic scenario where the segmentation quality is limited by the MRI resolution as well as partial volume effects and MRI artifacts, this is not the case. An easy way to pass level sets to CutFEM is by using tissue probability map (TPM), a typical intermediate result (Ashburner et al., 2014) from segmentation which provides for each voxel the probability that it is located in a certain compartment.

To examine the performance of CutFEM when used together with TPM's, another sphere model is employed, this time containing realistic gray and white matter compartments obtained from MRI scans of a human brain. The subject was a healthy 24-year-old male from whom T1- and T2-weighted MRI scans were acquired using a 3 Tesla MRI Scanner (MagnetomTrio, Siemens, Munich, Germany) with a 32-channel head coil. For the T1, a fast gradient-echo pulse sequence (TFE) using water selective excitation to avoid fat shift (TR/TE/FW = 2300/3.51 ms/8°, inversion pre-pulse with TI = 1.1 s, cubic voxels of 1 mm edge length) was used. For the T2, a turbo spin echo pulse sequence (TR/TE/FA = 3200/408 ms/90°, cubic voxels, 1 mm edge length) was used. TPM's were extracted from both T1- and T2-MRI using SPM12 (Ashburner et al., 2014) as integrated into fieldtrip (Oostenveld et al., 2011). For each voxel, the average of both TPM's was computed, and a threshold probability of 0.4 was set as zero-line.

The inner skull surface was defined as the minimal sphere containing the entire segmented brain with CSF filling the gaps. The spherical skull and scalp were chosen to have a thickness of 6 mm. The same conductivities as before were used with CSF, and gray and white matter being identical, and again 200 sensors were placed on the scalp surface.

2.2.1.3. Realistic 5 compartment head model

As an extension of the previous model, realistic 5-compartment head models were created using the same anatomical data, replacing the spherical skin, skull, and CSF by realistic segmentations. Again, level sets were created from probability maps. To obtain smooth skull and scalp surfaces in the TPM case, binary maps of the skull and skin were created following the procedure in the study by Antonakakis et al. (2020). The level sets of the skull/skin were then calculated as an average of the binary map and the T1/T2 TPM again with a threshold of 0.4. Following the study by Antonakakis et al. (2020), the level sets were cut off below the neck to reduce computational load while maintaining a realistic current flow below the skull. Again, lead fields from a hexahedral mesh were created for comparison as well as a 5-compartment tetrahedral model with surfaces created using SIMNIBS' headreco pipeline (Saturnino et al., 2019). SIMNIBS provides an automated segmentation and meshing pipeline taking both T1 and T2 MRI into account, similar to the model using TPM. Level sets were created from the surfaces, and another CutFEM model was created from these, yielding four lead fields: TPM-CutFEM and *Hex*, which are based on the tissue probability maps as well as Tri-CutFEM and*Tet*, which are based on the headreco surface triangulations. DOF, number of cut cells/mesh elements and the resulting number of snippets are shown in Table 2. Now, we have lead fields based on two different segmentation routines. TPM is closer to the original MRI while surface triangulations yield smoother surfaces at the cost of demanding nested compartments. The question which of the two segmentation routines is preferable is beyond the $n = 1$ study performed in this paper. Thus, neither method can be used as a reference solution. It is rather our goal to test CutFEM in both scenarios and showcase differences compared with the respective alternative, a standard first order tetrahedral or hexahedral FEM.

TABLE 2 Number of degrees of freedom/snippets/cut cells for CutFEM and number of degrees of freedom/elements for hexahedral/tetrahedral mesh.

	DOF	Cut cells/ elements	Snippets
TPM-CutFEM	917,463	716,994	7,950,120
TRI-CutFEM	1,159,831	911,567	7,647,088
Hex	3,909,303	3,475,138	-
Tet	1,135,379	6,475,318	-

2.2.2. Forward and inverse comparisons

For the two spherical scenarios, analytical forward solutions were calculated as a reference. For the realistic cases, somatosensory evoked potentials were recorded, and a dipole scan was performed as described in detail in Section 2.2.2.2.

The two latter scenarios including realistic gray/white matter use a regular 2 mm source grid created using Simbio https://www.mrt.uni-jena.de/simbio/. It was ensured that the sources are located inside the gray matter compartment for both approaches (*Hex* + CutFEM). The resulting source space contains 58.542 different dipole locations with no orientation constraint being applied.

2.2.2.1. Error measures

Two different metrics were employed to quantify the observed errors, the relative difference measure (RDM) and the magnitude error (MAG) (Wolters et al., 2007).

The RDM measures the difference in potential distribution at the scalp electrodes.

$$RDM(\%)(u^{ana}, u^{num}) = 50 * ||\frac{u^{ana}}{||u^{ana}||_2} - \frac{u^{num}}{||u^{num}||_2}||_2. \quad (12)$$

It ranges from 0 to 100, the optimal value being 0. MAG determines the differences in signal strength at the electrodes.

$$MAG(u^{ana}, u^{num}) = 100 * (\frac{||u^{num}||_2}{||u^{ana}||_2} - 1). \quad (13)$$

Measured in percent, its optimal value is 0. It is unbounded from above and bound by -100 from below. $u^{ana}, u^{num} \in \mathbb{R}^s$ contain the analytical and numerical potential at the s different sensor locations.

CutFEM is implemented into the DUNEuro toolbox https://www.medizin.uni-muenster.de/duneuro (Schrader et al., 2021), where the FEM calculations were performed. Analytical EEG solutions were calculated using the fieldtrip toolbox (Oostenveld et al., 2011). An example data set including somatosensory data was uploaded to Zenodo https://zenodo.org/record/3888381#.Yf0tT_so9H4.

For a comparison of runtime and memory usage, the forward calculation is split into five steps. The time necessary to create a driver, i.e., the time DUNEuro needs to setup the volume conductor, the times needed to assemble the stiffness matrix and AMG solver, the transfer matrix solving process using Dune-ISTL (Bastian et al., 2021), and the calculation of the final lead field matrix. All computations are performed on a bluechip workstation with an AMD Ryzen Threadripper 3960X and 128 GB RAM. A total of 16 threads are used to calculate the 200 transfer matrix/lead field columns in parallel. In the current implementation, CutFEM is limited to six compartments but that is an arbitrary restriction which can be increased at will.

2.2.2.2. Somatosensory data and dipole scan

To investigate CutFEM's influence on source reconstruction, an electric stimulation of the median nerve was performed on the same subject the anatomical data was acquired from. The subject gave written informed consent before the experiment and had no history of neurological or psychiatric disorders. The institution's ethical review board (Ethik Kommission der Ärztekammer Westfalen-Lippe und der WWU) approved all experimental procedures on 2 February 2018 (Ref. No. 2014-156-f-S). The stimuli were monophasic square-wave pulses of 0.5ms width in random intervals between 350 and 450ms. The stimulus strength was adjusted such that the right thumb moved clearly. EEG data were measured using an 80 channel cap (EASYCAP GmbH, Herrsching, Germany, 74 channel EEG plus additional 6 channels EOG to detect eye artifacts). EEG positions were digitized using a Polhemus device (FASTRAK, Polhemus Incorporated, Colchester, Vermont, U.S.A.). In total, 2,200 stimuli were digitally filtered between 20 and 250 Hz (50 Hz notch) and averaged to improve signal-to-noise ratio. A single dipole scan was conducted over the whole source space using the data at the peak and the CutFEM lead field.

The P20/N20 component typically exerts a high signal-to-noise ratio and a strongly dipolar topography, making it an ideal candidate for a dipole scan approach as motivated for example by Buchner et al. (1994).

3. Results

3.1. Shifted sphere model

The first investigated model is the shifted sphere scenario, where the brain sphere was moved within the CSF-sphere until there was exactly one contact point between the skull and brain (see 2.2.1.1). In Figure 2, the convergence speed for both radial and tangential source directions can be seen. Fundamental meshes with a resolution of 16, 8, 4, and 2 mm were created yielding finite element spaces with 4600/21401/111,192 and 552,985 DOF, respectively. Mean RDM decreases from 10.54 to 3.47 to 0.63 to 0.18 while the mean of the absolute value of the MAG decreases from 17.63 to 3.37 to 0.80 to 0.33. A 2 mm resolution, thus, already yields excellent numerical results.

When comparing number of DOF and RAM usage, it is clear that CutFEM is by far the most memory efficient approach, using approximately one-fifth of the number of trial functions and approximately one-tenth of the amount of RAM as UDG (Table 3). *Hex* also uses significantly more resources than CutFEM.

Regarding computation time, as UDG has to solve a significantly larger system, each iteration step in the solution phase takes longer than for CutFEM. As most time is spent on solving the system, CutFEM is overall approximately 16 min or 34% faster than UDG. The same cannot be said for comparisons to the standard *Hex* approach. While each iteration of the solver required less time than for *Hex*, it required an average of 92 iterations compared with 14 for *Hex*. The unfitted approaches spend less time calculating

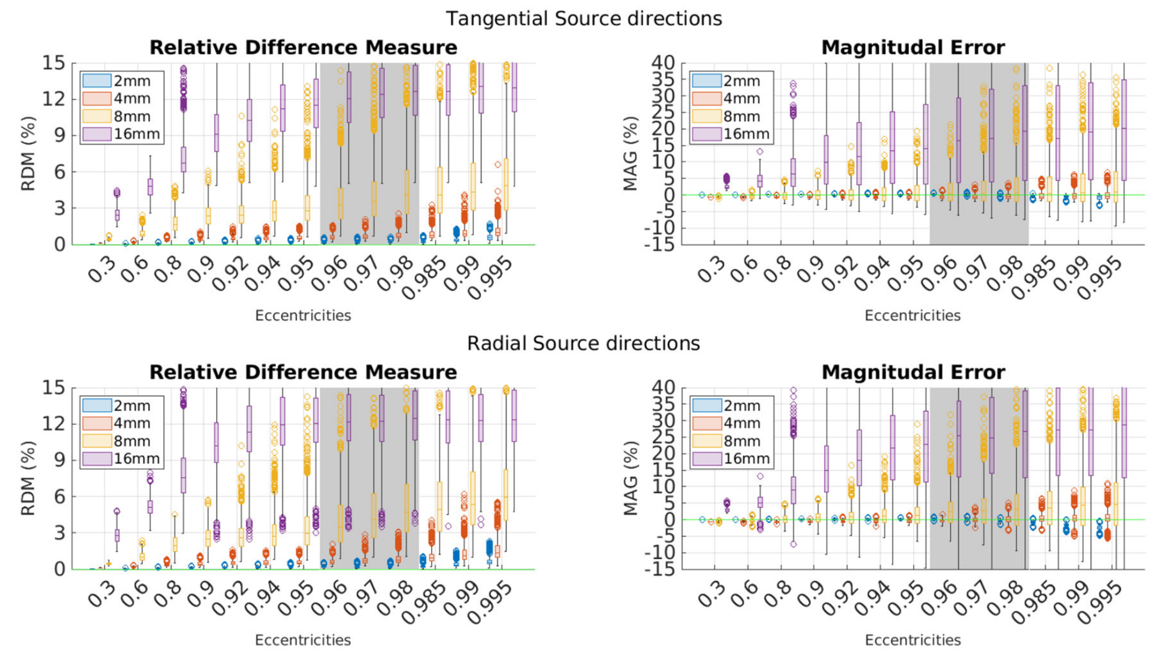

FIGURE 2
EEG forward modeling errors for different fundamental mesh resolutions in a shifted sphere scenario. **Top**: Errors for tangential source directions. **Bottom**: Errors for radial source directions. Errors are in percent and grouped by eccentricities. The green line marks optimal error values. The gray area indicates the physiologically most realistic eccentricities.

TABLE 3 Computation times, RAM/degree of freedom usage in the shifted sphere model.

	CutFEM	UDG	*Hex*
Number DOF	552 985	3 601 824	3 341 280
Max. RAM used	6.91 GB	64.77 GB	40.2 GB
Driver setup	44 s	45 s	52 s
Matrix assembly	319 s	161 s	25 s
Solver setup	353 s	235 s	45 s
Solving	1,111 s	2,367 s	1,550 s
Lead field	22 s	20 s	125 s
Total time	1,849 s	2,828 s	1,797 s

the final lead field as the time needed to locate each dipole within the 2 mm background mesh is lower than the 1 mm hexahedral mesh. In total, the hexahedral CG was only faster than CutFEM by a negligible 3% or 52 s.

Error comparisons between CutFEM, UDG, and *Hex* are shown in Figure 3. CutFEM outperforms *Hex* in all eccentricity categories and for both radial and tangential source directions. As the pyramidal cells that give rise to the EEG potential are located in layer 5 of the gray matter (Murakami and Okada, 2006), eccentricities corresponding to 1–2 mm distance to the skull are the physiologically most relevant. For eccentricities between 0.96 and 0.98 and both source directions, CutFEM has average RDM/MAG values of 0.18 and −0.06%, comparable to UDGs 0.17 and −0.2% and significantly lower than *Hex*'s 0.94 and 1.57%.

The most pronounced differences are at low eccentricities or when looking at magnitudes. CutFEM performance is similar for both radial and tangential source directions, and UDG shows similar or slightly better results at low eccentricities. However, except for radial RDM's, UDG deteriorates faster at high eccentricities above 0.98. As both operate on the same cut mesh, the larger variance in the UDG results can most likely be explained by CutFEM's use of the ghost penalty stabilization. The overall largest absolute error values for CutFEM are 3.08 % RDM and 8.21 % MAG, underlining its performance with regard to outliers. Due to the similar numerical accuracy of CutFEM and UDG, we will only compare CutFEM and *Hex* in the following scenarios.

3.2. Sphere containing realistic brain

The results in the previous section were achieved using analytically computed level sets. Deviating from this, we will now use a semi-realistic case where realistic brain compartments are contained within spheres. Again, several different penalty parameters were tried, showing that a combination of $\gamma = 40$ and a ghost penalty of $\gamma_g = 0.5$ yield good results for CutFEM.

The results are presented in Figure 4. Notably, eccentricity is stated with respect to the distance to the skull. As source points are only inside the gray matter, the number of source points at high eccentricities is much lower. The eccentricity groups 0.98, 0.985, 0.99, and 0.995 were thus combined into one group containing 136 points.

Much like before, CutFEM remains well below 1.5 and 2% RDM and MAG, respectively, whereas *Hex* has higher median values for

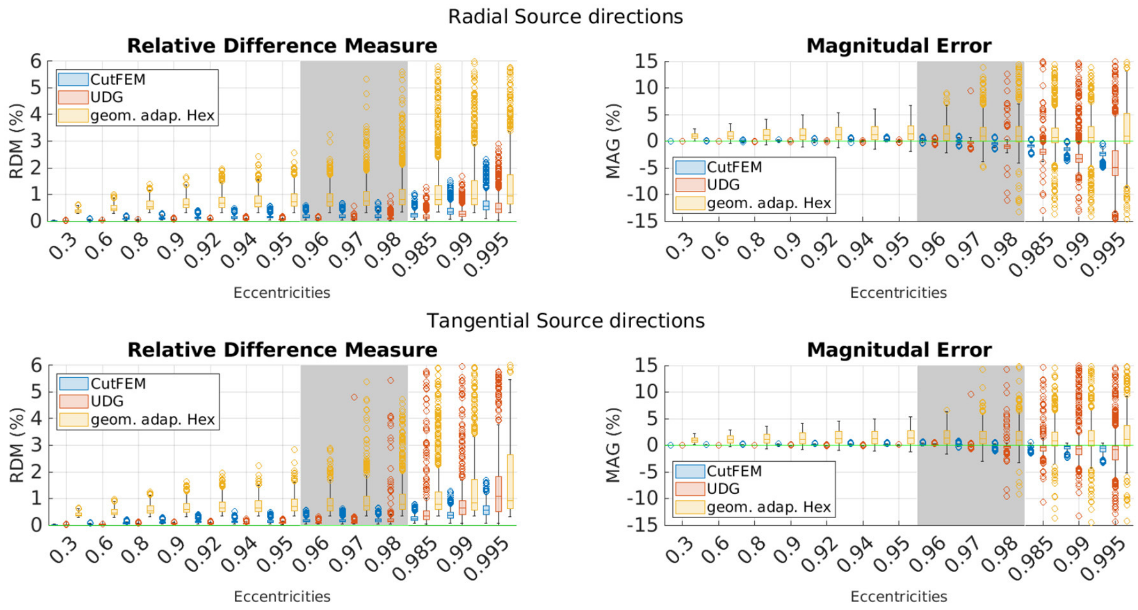

FIGURE 3
EEG forward modeling errors for *Hex* and unfitted FEM approaches in a shifted sphere scenario. **Top**: Errors for tangential source directions. **Bottom**: Errors for radial source directions. Errors are in percent and grouped by eccentricities. The green line marks optimal error values. The gray area indicates the physiologically most realistic eccentricities.

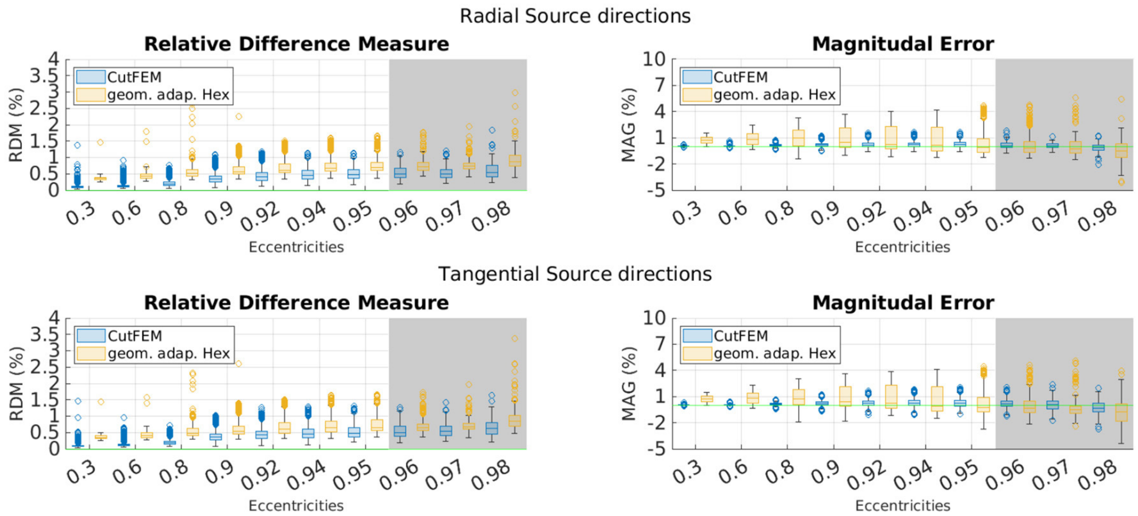

FIGURE 4
Overview of different EEG-errors for five layer continuous Galerkin- and CutFEM approaches using realistic brain compartments contained in spherical skull and scalp shells. **Top**: Errors for tangential source directions. **Bottom**: Errors for radial source directions. Errors are in percent and grouped by eccentricities. The green line marks optimal error values. The gray area indicates the physiologically most realistic eccentricities.

nearly all eccentricities and more outliers going up to more than 1.5% RDM and 4% MAG. CutFEM is again more stable with regard to outliers and especially when looking at magnitudes, differences between the two methods are in the several percent range.

Overall, it can be stated that CutFEM is about as fast as and more accurate than *Hex* and about as accurate as and faster than UDG.

3.3. Realistic 5-compartment head model

For the final part of this study, two lead fields, one from CutFEM, one from hexahedral CG, were created using realistic 5-compartment head models including the gray and white matter, CSF, skull and scalp tissues. Somatosensory evoked potentials were acquired from a medianus stimulation of the right hand.

3.3.1. Lead field differences

Before looking at inverse reconstructions, we will investigate the differences between the forward results. As the same source space and electrodes were used for both models, we can again compute MAG and RDM values. In the absence of an analytical solution, these measurements cannot capture errors but rather differences between the methods without making a clear statement which is more accurate.

For visualization purposes, for each gray matter centerpoint of the *Hex* mesh, the closest source point is identified, RDM and MAG are computed for each spatial direction and averages over the directions are calculated. The results are shown in Figure 5. Looking first at the differences between the *Hex* and TPM-CutFEM model, we see that in both measures, the highest differences can be observed in inferior areas near the foramen magnum and optic channels or in superior areas. Overall, the difference in potential distribution was 9.40 ± 4.15% and the difference in magnitude was 18.94 ± 12.03%. Interestingly, with a correlation coefficient of only 0.22, high RDM values do not necessarily coincide with high MAG values.

When comparing *Tet* to Tri-CutFEM we see that the differences are significantly smaller. With RDMs of 4.59 ± 3.54% and MAGs of 8.74 ± 8.30%, they average less than half the differences between the TPM-based models. Additionally, the differences between Tri-CutFEM and TPM-CutFEM are 4.52± 2.86% (RDM)/0.03 ± 14.50%(MAG) lower than when comparing *Tet* and *Hex*. This is to be expected as the CutFEM lead fields only differ in the way the surfaces are provided while the differences between hexahedral and tetrahedral FEM also encompass geometry adaptation, multi-linear vs. linear FE-spaces and local differences in mesh resolution.

3.3.2. Reconstruction of somatosensory stimulation

Finally, all four lead fields were used to perform a source reconstruction of the P20 component of an electric wrist stimulation. Dipole scans were conducted over the entire source space, the results of which are shown in Figure 6. In total, 93.03 and 92.15% of the data could be explained the TPM-CutFEM and the *Hex* lead field, respectively, resulting in dipole strengths of 5.8 and 7.56 nAm. These are slightly weaker than the Tri-CutFEM and *Tet* dipoles at 8.1 and 8.7 nAm, respectively. From the literature (Buchner et al., 1994), one expects the P20 component to be located in Brodmann Area 3b, located in the anterior wall of the postcentral gyrus (and oriented toward the motor cortex). This is in line with the TPM-CutFEM reconstruction while the other three lead fields yield reconstructed dipoles that located on the posterior wall. Overall, the CutFEM-based reconstructions are located slightly more medial and frontal than their counterparts. While this is only a single subject study, it shows that the choice of the FEM method can significantly change the localization result of a dipole scan.

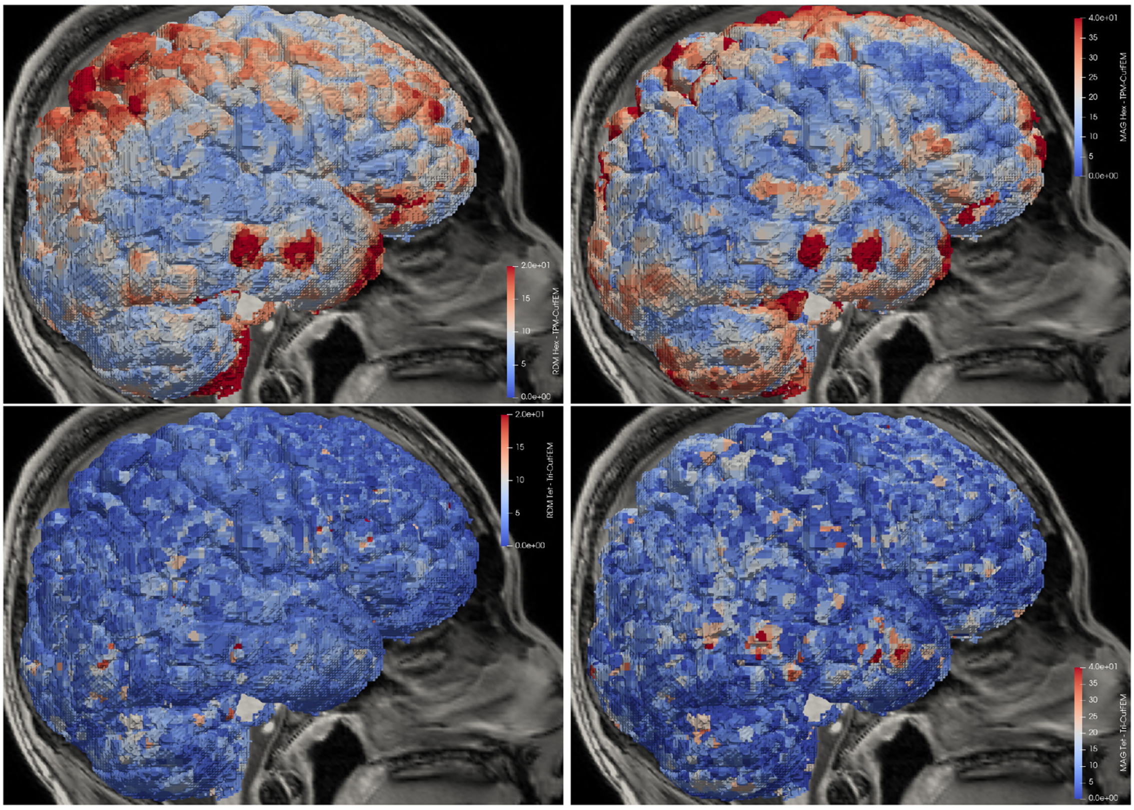

FIGURE 5
Lead field differences in distribution and magnitude. **Top**: TPM-CutFEM vs. *Hex*, **Bottom**: Tri-CutFEM vs. *Tet*. Differences are interpolated onto the gray matter.

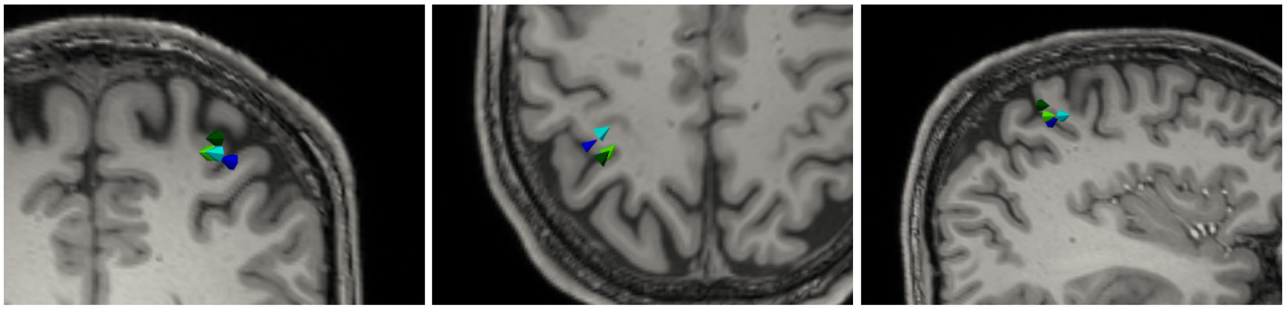

FIGURE 6
Dipole reconstruction results of P20 component of the medianus stimulation based on four different lead fields: *Tet* (dark green), *Hex* (dark blue), Tri-CutFEM (light blue), and TPM-CutFEM (light green). **Left** to **right**: Axial, Coronal, and Sagittal view.

4. Discussion

The purpose of this study is to introduce CutFEM, an unfitted FEM for applications in EEG forward modeling. After discussing the mathematical theory behind CutFEM and implementational aspects, three progressively more realistic scenarios are introduced, ranging from a multi-layer sphere model to the reconstruction of somatosensory evoked potentials.

At similar computation times, CutFEM shows preferable results when compared with a geometry-adapted hexahedral CG-FEM (Wolters et al., 2007) in both a shifted sphere scenario and a sphere model with realistic brain tissues. While CutFEM requires significantly less DOF, both methods require similar computation times due to the different number of solver iterations. Thus, a thorough investigation of different iterative solver techniques such as multigrid methods and possibly a modification of the ghost penalty will be a part of future studies.

Compared with UDG (Bastian and Engwer, 2009), it is shown that CutFEM combined with a ghost penalty leads to a decrease in outlier values at high eccentricities as well as a significant reduction in memory consumption and computation time.

Using a realistic five-compartment head model based on either tissue probability maps or surface triangulations, we found larger differences compared with standard hexahedral or tetrahedral first order FEM when using TPM. Of all four computed lead fields, only CutFEM in conjunction with tissue probability maps correctly localizes the somatosensory P20 in the expected Brodmann area 3b. Especially in applications such as presurgical epilepsy diagnosis, such accurate reconstructions might contribute significantly to the correct localization of the irritative zone (Neugebauer et al., 2022). The employed somatosensory experiment featured clear peaks and a high signal-to-noise ratio, making it an ideal candidate for an initial study. Further investigations and a larger study size are necessary to determine CutFEM's contribution to accurate source reconstructions when used with noisier data and/or more advanced inverse methods.

In the study by Vallaghé and Papadopoulo (2010), a trilinear immersed FEM approach was introduced that like CutFEM employs level sets as tissue surfaces. Rather than using a Nitsche-based coupling, continuity of the electric potential is enforced by modifying the trial function space. Compared with CutFEM, no free parameters such as γ and γ_G are introduced but the absence of overlapping submeshes means that there is no increased resolution in areas with complex geometries.

In the study by Windhoff et al. (2013); Nielsen et al. (2018), the process of building a tetrahedral mesh from segmentation data is investigated. Surface triangulations that are free of topological defects, self-intersections, or degenerate angles have to be created before volumetric meshing. The authors show that it is possible to create such high quality surfaces and subsequent tetrahedral meshes for realistic head models; however, they may come at the cost of modeling inaccuracies such as the separation of the gray matter and skull by a thin layer of CSF.

A main advantage of CutFEM is its flexibility with regard to the anatomical input data. Level sets can be created from a variety of sources, such as tissue probability maps, binary images, or surface triangulations. This simplifies the question of how to create a mesh from segmentation data. However, CutFEM does not answer the question which of these sources should be used in future. Numerically, one can expect the smoother level sets created from surface triangulations to produce fewer distorted cut cells than those created from TPM. As shown in the results though, CutFEM is stable with regard to tissue probability maps. Future investigations will show whether staying close to the raw MRI data by using tissue probability maps is preferable over having nested, smooth surfaces as required for tetrahedral models. The $n = 1$ study we performed here cannot conclusively answer this question. From an anatomical perspective, CutFEM now offers the possibility to accurately model supine subject positioning where the brain touches the skull. Quantifying the impact, this has on EEG source estimation will also be a part of future investigations.

5. Conclusion

CutFEM performed well both when the underlying head model was created using analytical level sets or realistic segmentation results. Application to an inverse reconstruction of a somatosensory evoked potential yielded findings that are in line with the literature. The level sets underlying CutFEM impose few restrictions on the compartments, thus allowing for more simplified segmentation routines when compared with other FEM approaches using surface triangulations.

Data availability statement

The data analyzed in this study is subject to the following licenses/restrictions: the software in which the new methodology was implemented can be found under https://www.medizin.uni-muenster.de/duneuro, an example data set can be found under https://zenodo.org/record/3888381#.Yf0tT_so9H4. The dataset used in the realistic head model section is from a different subject than the one uploaded to Zenodo but otherwise identical. Requests to access these dataset should be directed to tim.erdbruegger@uni-muenster.de.

Ethics statement

The studies involving human participants were reviewed and approved by Ethik Kommission der Ärztekammer Westfalen-Lippe und der WWU (Ref. No. 2014-156-f-S). The patients/participants provided their written informed consent to participate in this study.

Author contributions

CE, AW, and CW: conceptualization. CE, TE, AW, and CW: methodology. CE, TE, and AW: software. TE: investigation and writing—original draft. YB, CE, TE, JG, MH, RL, J-OR, and CW: writing—reviewing and editing. CE and CW: supervision. AB, JG, RL, SP, FW, and CW: funding acquisition. All authors contributed to the article and approved the submitted version.

Funding

This study was supported by ERA PerMed as project ERAPERMED2020-227 PerEpi (Bundesministerium für Gesundheit, project ZMI1-2521FSB006; Academy of Finland, project 344712; Bundesministerium für Bildung und Forschung, project FKZ 01KU2101; French National Research Agency, project RPV21010EEA) and by the Deutsche Forschungsgemeinschaft (DFG), projects WO1425/10-1, GR2024/8-1, LE1122/7-1. CE was supported by the Deutsche Forschungsgemeinschaft (DFG, German Research Foundation) under Germany's Excellence Strategy EXC 2044-390685587, Mathematics Münster: Dynamics-Geometry-Structure. TE, MH, CW, and SP were additionally supported by the DAAD/AoF researcher mobility project (DAAD project 57663920, AoF decision 354976) and SP by the AoF Centre of Excellence (CoE) in Inverse Modelling and Imaging 2018-2025 (AoF decision 353089). We acknowledge support from the Open Access Publication Fund of the University of Muenster.

Conflict of interest

The authors declare that the research was conducted in the absence of any commercial or financial relationships that could be construed as a potential conflict of interest.

Publisher's note

References

Acar, Z. A., Acar, C. E., and Makeig, S. (2016). Simultaneous head tissue conductivity and EEG source location estimation. *Neuroimage* 124, 168–180. doi: 10.1016/j.neuroimage.2015.08.032

Antonakakis, M., Schrader, S., Aydin, U., Khan, A., Gross, J., Zervakis, M., et al. (2020). Inter-subject variability of skull conductivity and thickness in calibrated realistic head models. *Neuroimage* 223, 117353. doi: 10.1016/j.neuroimage.2020.117353

Ashburner, J., Barnes, G., Chen, C. C., Daunizeau, J., Flandin, G., Friston, K., et al. (2014). *SPM12 Manual.* Wellcome Trust Centre for Neuroimaging, London.

Azizollahi, H., Darbas, M., Diallo, M. M., El Badia, A., and Lohrengel, S. (2018). EEG in neonates: Forward modeling and sensitivity analysis with respect to variations of the conductivity. *Math. Biosci. Eng.* 15, 905–932. doi: 10.3934/mbe.2018041

Bangera, N. B., Schomer, D. L., Dehghani, N., Ulbert, I., Cash, S., Papavasiliou, S., et al. (2010). Experimental validation of the influence of white matter anisotropy on the intracranial EEG forward solution. *J. Comput. Neurosci.* 29, 371–387. doi: 10.1007/s10827-009-0205-z

Bastian, P., Blatt, M., Dedner, A., Dreier, N. A., Engwer, C., Fritze, R., et al. (2021). The Dune framework: basic concepts and recent developments. *Comput. Math. Appl.* 81, 75–112. doi: 10.1016/j.camwa.2020.06.007

Bastian, P., and Engwer, C. (2009). An unfitted finite element method using discontinuous Galerkin. *Int. J. Num. Methods Eng.* 79, 1557–1576. doi: 10.1002/nme.2631

Beltrachini, L. (2018). Sensitivity of the projected subtraction approach to mesh degeneracies and its impact on the forward problem in EEG. *IEEE Trans. Biomed. Eng.* 66, 273–282. doi: 10.1109/TBME.2018.2828336

Brette, R., and Destexhe, A. (2012). *Handbook of Neural Activity Measurement.* Cambridge University Press.

Buchner, H., Fuchs, M., Wischmann, H. A., Dössel, O., Ludwig, I., Knepper, A., et al. (1994). Source analysis of median nerve and finger stimulated somatosensory evoked potentials: multichannel simultaneous recording of electric and magnetic fields combined with 3D-MR tomography. *Brain Topogr.* 6, 299–310. doi: 10.1007/BF01211175

Buchner, H., Knoll, G., Fuchs, M., Rienacker, A., Beckmann, R., Wagner, M., et al. (1997). Inverse localization of electric dipole current sources in finite element models of the human head. *Electroencephalogr. Clin. Neurophysiol.* 102, 267–278.

Burman, E. (2010). Ghost penalty. *Comptes Rendus Mathematique* 348, 1217–1220. doi: 10.1016/j.crma.2010.10.006

Burman, E., Claus, S., Hansbo, P., Larson, M. G., and Massing, A. (2015). CutFEM: discretizing geometry and partial differential equations. *Int. J. Num. Methods Eng.* 104, 472–501. doi: 10.1002/nme.4823

Burman, E., and Hansbo, P. (2012). Fictitious domain finite element methods using cut elements: II. A stabilized Nitsche method. *Appl. Num. Math.* 62, 328–341. doi: 10.1016/j.apnum.2011.01.008

Cuartas Morales, E., Acosta-Medina, C. D., Castellanos-Dominguez, G., and Mantini, D. (2019). A finite-difference solution for the EEG forward problem in inhomogeneous anisotropic media. *Brain Topogr.* 32, 229–239. doi: 10.1007/s10548-018-0683-2

De Munck, J., and Peters, M. J. (1993). A fast method to compute the potential in the multisphere model. *IEEE Trans. Biomed. Eng.* 40, 1166–1174.

Di Pietro, D., and Ern, A. (2011). *Mathematical Aspects of Discontinuous Galerkin Methods, Vol. 69.* Springer Science & Business Media.

Engwer, C., and Nüßing, A. (2017). Geometric reconstruction of implicitly defined surfaces and domains with topological guarantees. *ACM Trans. Math. Softw.* 44, 1–20. doi: 10.1145/3104989

Engwer, C., Vorwerk, J., Ludewig, J., and Wolters, C. H. (2017). A discontinuous Galerkin method to solve the EEG forward problem using the subtraction approach. *SIAM J. Sci. Comput.* 39, B138–B164. doi: 10.1137/15M1048392

Gençer, N. G., and Acar, C. E. (2004). Sensitivity of EEG and MEG measurements to tissue conductivity. *Phys. Med. Biol.* 49, 701. doi: 10.1088/0031-9155/49/5/004

Gramfort, A., Papadopoulo, T., Olivi, E., and Clerc, M. (2011). Forward field computation with OpenMEEG. *Comput. Intell. Neurosci.* 2011, 923703. doi: 10.1155/2011/923703

Guzmán, J., and Rivière, B. (2009). Sub-optimal convergence of non-symmetric discontinuous Galerkin methods for odd polynomial approximations. *J. Sci. Comput.* 40, 273–280. doi: 10.1007/s10915-008-9255-z

He, Q., Rezaei, A., and Pursiainen, S. (2020). Zeffiro user interface for electromagnetic brain imaging: a GPU accelerated fem tool for forward and inverse computations in Matlab. *Neuroinformatics* 18, 237–250. doi: 10.1007/s12021-019-09436-9

Lew, S., Wolters, C., Dierkes, T., Röer, C., and MacLeod, R. (2009). Accuracy and run-time comparison for different potential approaches and iterative solvers in finite element method based EEG source analysis. *Appl. Num. Math.* 59, 1970–1988. doi: 10.1016/j.apnum.2009.02.006

Makarov, S. N., Hämäläinen, M., Okada, Y., Noetscher, G. M., Ahveninen, J., and Nummenmaa, A. (2020). Boundary element fast multipole method for enhanced modeling of neurophysiological recordings. *IEEE Trans. Biomed. Eng.* 68, 308–318. doi: 10.1109/TBME.2020.2999271

McCann, H., Pisano, G., and Beltrachini, L. (2019). Variation in reported human head tissue electrical conductivity values. *Brain Topogr.* 32, 825–858. doi: 10.1007/s10548-019-00710-2

Medani, T., Lautru, D., Schwartz, D., Ren, Z., and Sou, G. (2015). FEM method for the EEG forward problem and improvement based on modification of the Saint Venant's method. *Prog. Electromagnet. Res.* 153, 11–22. doi: 10.2528/PIER15050102

Mosher, J. C., Leahy, R. M., and Lewis, P. S. (1999). EEG and MEG: forward solutions for inverse methods. *IEEE Trans. Biomed. Eng.* 46, 245–259. doi: 10.1109/10.748978

Murakami, S., and Okada, Y. (2006). Contributions of principal neocortical neurons to magnetoencephalography and electroencephalography signals. *J. Physiol.* 575, 925–936. doi: 10.1113/jphysiol.2006.105379

Neugebauer, F., Antonakakis, M., Unnwongse, K., Parpaley, Y., Wellmer, J., Rampp, S., et al. (2022). Validating EEG, MEG and combined MEG and EEG beamforming for an estimation of the epileptogenic zone in focal cortical dysplasia. *Brain Sci.* 12, 114. doi: 10.3390/brainsci12010114

Nielsen, J. D., Madsen, K. H., Puonti, O., Siebner, H. R., Bauer, C., Madsen, C. G., et al. (2018). Automatic skull segmentation from MR images for realistic volume conductor models of the head: assessment of the state-of-the-art. *Neuroimage* 174, 587–598. doi: 10.1016/j.neuroimage.2018.03.001

Nitsche, J. (1971). "Über ein Variationsprinzip zur Lösung von Dirichlet-Problemen bei Verwendung von Teilräumen, die keinen Randbedingungen unterworfen sind," in *Abhandlungen aus dem mathematischen Seminar der Universität Hamburg, Vol. 36* (Berlin/Heidelberg: Springer-Verlag).

Nüßing, A., Wolters, C. H., Brinck, H., and Engwer, C. (2016). The unfitted discontinuous Galerkin method for solving the EEG forward problem. *IEEE Trans. Biomed. Eng.* 63, 2564–2575. doi: 10.1109/TBME.2016.2590740

Oden, J. T., Babuŝka, I., and Baumann, C. E. (1998). A discontinuoushpfinite element method for diffusion problems. *J. Comput. Phys.* 146, 491–519.

Oostenveld, R., Fries, P., Maris, E., and Schoffelen, J.-M. (2011). FieldTrip: open source software for advanced analysis of MEG, EEG, and invasive electrophysiological data. *Comput. Intell. Neurosci.* 2011, 156869. doi: 10.1155/2011/156869

Rice, J. K., Rorden, C., Little, J. S., and Parra, L. C. (2013). Subject position affects EEG magnitudes. *Neuroimage* 64, 476–484. doi: 10.1016/j.neuroimage.2012.09.041

Saturnino, G. B., Puonti, O., Nielsen, J. D., Antonenko, D., Madsen, K. H., Thielscher, A., et al. (2019). "SimNIBS 2.1: A comprehensive pipeline for individualized electric field modelling for transcranial brain stimulation," in *Brain and Human Body Modeling: Computational Human Modeling at EMBC 2018,* eds S. Makarov, M. Horner, and G. Noetscher (Springer International Publishing), 3–25.

Schimpf, P. H., Ramon, C., and Haueisen, J. (2002). Dipole models for the EEG and MEG. *IEEE Trans. Biomed. Eng.* 49, 409–418. doi: 10.1109/10.995679

Schrader, S. et al. (2021). DUNEuro–A software toolbox for forward modeling in bioelectromagnetism. *PLoS ONE* 16, e0252431. doi: 10.1371/journal.pone.0252431

Song, J., Davey, C., Poulsen, C., Luu, P., Turovets, S., Anderson, E., et al. (2015). EEG source localization: Sensor density and head surface coverage. *J. Neurosci. Methods* 256, 9–21. doi: 10.1016/j.jneumeth.2015.08.015

Sonntag, H., Vorwerk, J., Wolters, C. H., Grasedyck, L., Haueisen, J., and Maeß, B. (2013). "Leakage effect in hexagonal FEM meshes of the EEG forward problem," in *International Conference on Basic and Clinical Multimodal Imaging (BaCI)*, Vol. 102.

Vallaghé, S., and Papadopoulo, T. (2010). A trilinear immersed finite element method for solving the EEG forward problem. *SIAM J. Sci. Comp.* 32, 2379–94. doi: 10.1137/09075038X

Van Uitert, R., Johnson, C., and Zhukov, L. (2004). Influence of head tissue conductivity in forward and inverse magnetoencephalographic simulations using realistic head models. *IEEE Trans. Biomed. Eng.* 51, 2129–2137. doi: 10.1109/TBME.2004.836490

Vermaas, M., Piastra, M. C., Oostendorp, T. F., Ramsey, N. F., and Tiesinga, P. H. (2020). FEMfuns: a volume conduction modeling pipeline that includes resistive, capacitive or dispersive tissue and electrodes. *Neuroinformatics* 18, 569–580. doi: 10.1007/s12021-020-09458-8

Windhoff, M., Opitz, A., and Thielscher, A. (2013). *Electric Field Calculations in Brain Stimulation Based on Finite Elements: An Optimized Processing Pipeline for the Generation and Usage of Accurate Individual Head Models.* Technical report, Wiley Online Library.

Wolters, C., Grasedyck, L., and Hackbusch, W. (2004). Efficient Computation of lead field bases and influence matrix for the FEM-based EEG and MEG inverse problem. *Inverse Prob.* 20, 1099–1116. doi: 10.1088/0266-5611/20/4/007

Wolters, C. H., Anwander, A., Berti, G., and Hartmann, U. (2007). Geometry-adapted hexahedral meshes improve accuracy of finite-element-method-based EEG source analysis. *IEEE Trans. Biomed. Eng.* 54, 1446–1453. doi: 10.1109/TBME.2007.890736

Zhang, Y., Zhu, S., and He, B. (2004). A second-order finite element algorithm for solving the three-dimensional EEG forward problem. *Phys. Med. Biol.* 49, 2975. doi: 10.1088/0031-9155/49/13/014

Frontiers in Human Neuroscience

TYPE Original Research
PUBLISHED 14 September 2023
DOI 10.3389/fnhum.2023.1235192

EDITED BY
Takfarinas Medani,
University of Southern California, United States

REVIEWED BY
Sampsa Pursiainen,
Tampere University, Finland
Umit Aydin,
University of Reading, United Kingdom

*CORRESPONDENCE
Amita Giri
✉ amita3gb@mit.edu

RECEIVED 05 June 2023
ACCEPTED 22 August 2023
PUBLISHED 14 September 2023

CITATION
Giri A, Mosher JC, Adler A and Pantazis D (2023) An F-ratio-based method for estimating the number of active sources in MEG.
Front. Hum. Neurosci. 17:1235192.
doi: 10.3389/fnhum.2023.1235192

An F-ratio-based method for estimating the number of active sources in MEG

Amita Giri[1]*, John C. Mosher[2], Amir Adler[1,3] and Dimitrios Pantazis[1]

[1]McGovern Institute for Brain Research, Massachusetts Institute of Technology, Cambridge, MA, United States, [2]Department of Neurology, McGovern Medical School, Texas Institute for Restorative Neurotechnologies, UTHealth, Houston, TX, United States, [3]Department of Electrical Engineering, Braude College of Engineering, Karmiel, Israel

Introduction: Magnetoencephalography (MEG) is a powerful technique for studying the human brain function. However, accurately estimating the number of sources that contribute to the MEG recordings remains a challenging problem due to the low signal-to-noise ratio (SNR), the presence of correlated sources, inaccuracies in head modeling, and variations in individual anatomy.

Methods: To address these issues, our study introduces a robust method for accurately estimating the number of active sources in the brain based on the F-ratio statistical approach, which allows for a comparison between a full model with a higher number of sources and a reduced model with fewer sources. Using this approach, we developed a formal statistical procedure that sequentially increases the number of sources in the multiple dipole localization problem until all sources are found.

Results: Our results revealed that the selection of thresholds plays a critical role in determining the method's overall performance, and appropriate thresholds needed to be adjusted for the number of sources and SNR levels, while they remained largely invariant to different inter-source correlations, translational modeling inaccuracies, and different cortical anatomies. By identifying optimal thresholds and validating our F-ratio-based method in simulated, real phantom, and human MEG data, we demonstrated the superiority of our F-ratio-based method over existing state-of-the-art statistical approaches, such as the Akaike Information Criterion (AIC) and Minimum Description Length (MDL).

Discussion: Overall, when tuned for optimal selection of thresholds, our method offers researchers a precise tool to estimate the true number of active brain sources and accurately model brain function.

KEYWORDS

F-ratio, source localization, Alternating Projection (AP), source enumeration, MEG, AIC, MDL

1. Introduction

Magnetoencephalography (MEG) is a powerful non-invasive neuroimaging technique that offers high temporal resolution for studying human brain function (Hämäläinen et al., 1993; Baillet, 2017). Localization of MEG sources has garnered significant interest in recent years since it can reveal the origins of neural signals and offer valuable insights into the complex workings of the human brain. By identifying the sources of neural activity, researchers can study the underlying mechanisms of cognition, perception, and other brain functions (Ahveninen et al., 2006; Giorgetta et al., 2013; Klepp et al., 2015; Pancholi et al., 2023). Additionally, source localization can aid in diagnosing and studying neurological disorders and identifying abnormal brain activity (Oishi et al., 2002; Westlake et al., 2012; Wilkinson et al., 2020; Xu et al., 2021; Giri, 2022; Giri et al., 2022).

MEG source localization methods typically involve solving an inverse problem, which entails estimating current sources within the brain based on the measured MEG data. This is challenging because the measured signals are influenced by several factors, such as the geometry and conductivity of the head, sensor noise, and the ill-posed nature of the problem. Mathematically, the localization problem can be cast as finding the location and moment of the set of dipoles whose field best matches the M/EEG measurements (Mosher et al., 1992). Localization methods can be broadly categorized into *distributed* and *discrete* solutions.

Distributed source imaging approaches aim to estimate a density map of active dipoles across the entire cortex. Commonly used methods include minimum norm estimators (MNE) (Hämäläinen et al., 1993, 1994), dynamic statistical parametric mapping (dSPM) (Dale et al., 2020), and standardized low-resolution electromagnetic tomography (sLORETA) (Pascual-Marqui et al., 2002). However, these methods assume a significantly larger number of unknown sources in a discrete surface or volumetric grid compared to the number of MEG sensors. The ill-posed nature of the problem poses a significant challenge, especially in the presence of multiple active regions in the brain (Darvas et al., 2004). Non-linear source estimation methods, such as Mixed Norm Estimate (MxNE) (Strohmeier et al., 2016) and time-frequency mixed-norm estimates (TF-MxNE) (Gramfort et al., 2013), address this issue by incorporating $l1$-norm penalty regularizers that favor sparse collections of focal dipolar sources. Other sparse approaches include hierarchical reconstructions of cortical and subcortical sources (Gramfort et al., 2012; Krishnaswamy et al., 2017; Rezaei et al., 2021). While these methods have shown some success, they tend to be computationally demanding and have limited accuracy when dealing with complex multi-dipole configurations.

On the other hand, *discrete multiple dipole localization* methods avoid the ill-posedness associated with distributed methods by finding a small set of equivalent current dipoles (ECDs) whose field best matches the M/EEG measurements in a least-squares sense (Mosher et al., 1992). Dipole localization methods offer a more classical approach to brain source localization and provide more intuitive interpretations of brain activity by estimating the location, orientation and amplitude of neural sources. The most well-known methods are beamformers (Van Veen et al., 1997; Vrba and Robinson, 2001) and MUltiple SIgnal Classification (MUSIC) (Mosher et al., 1992), and their recursive variants Recursively Applied and Projected MUSIC (RAP-MUSIC) (Mosher and Leahy, 1999), Truncated RAP-MUSIC (Mäkelä et al., 2018), and RAP Beamformer (Ilmoniemi and Sarvas, 2019). While recursive variants generally perform better than their non-recursive counterparts, they still face limitations such as reduced effectiveness, reliance on high signal-to-noise ratio (SNR), and potential cancellation of correlated sources. Recent advancements in this field have addressed some of these concerns, including Alternating Projections (AP) (Adler et al., 2022), double-scanning (DS-MUSIC) (Mäkelä et al., 2017; Ilmoniemi and Sarvas, 2019), hemispherical harmonics MUSIC (HSH-MUSIC) (Giri et al., 2018), head harmonics MUSIC (H^2 MUSIC) (Giri et al., 2019), and Flex-MUSIC (Hecker et al., 2023). Estimating the number of independent signal components is a prerequisite for dipole localization methods to accurately estimate dipole sources. However, determining the correct number of active sources contributing to the recorded signals remains a fundamental challenge in MEG data analysis (Wendel et al., 2009), significantly impacting the success of brain source localization. We focus on addressing this specific problem here.

Estimating the number of active sources in MEG data poses significant challenges due to multiple factors. First, MEG signals generally exhibit a low SNR, which makes it difficult to differentiate between simultaneously active sources. Second, the presence of correlated sources adds complexity by potentially causing multiple sources to be mistakenly identified as a single source. Last, errors in translational head modeling and variations in individual anatomy introduce additional noise and variability, hampering accurate estimation of the location and strength of underlying sources.

Early attempts to estimate the number of dipoles relied on subjective thresholds (Bartlett, 1954; Lawley, 1956; Chen et al., 1991). These approaches involved setting a threshold that separated the eigenvalues of the data covariance matrix from the complete set of eigenvalues. Chen et al. (1991) proposed a method that detected the number of sources by imposing an upper bound on the eigenvalue magnitudes of the correlation matrix derived from the array output. In addition to conventional eigenvalue-based techniques, a few methods have also employed eigenvectors for estimating the number of sources (Di and Tian, 1984; Jiang and Ingram, 2004).

To overcome the limitations of subjective thresholds, two main classes of methods have been developed for estimating the number of signal sources using the distribution of the eigenvalues of the data covariance matrix. The first class involves techniques based on principal component analysis (PCA) (Green et al., 1988; Yao et al., 2018), independent component analysis (ICA) (Ikeda and Toyama, 2000), and factor analysis (Malinowski, 1977a,b). The second class consists of information theoretic approaches (Wax and Kailath, 1985; Knösche et al., 1998), such as the Akaike information criterion (AIC) (Akaike, 1974) and the minimum description length (MDL) (Rissanen, 1978; Schwarz, 1978). The work from Wax and Kailath (1985) derived the eigenvalue forms of AIC and MDL methods, which can be directly applied to array signal processing problems. These methods aim to strike a balance between model fit and complexity using principles from information theory. However, these approaches assume source independence, which is not always valid in the brain. As a result, they tend to perform poorly (Zhang et al., 1989; Chen et al., 1991; Salman et al., 2015; Yao et al., 2018), especially in the presence of correlated sources, noise, low SNR, and limited time samples. Hence, there is a need for more robust and accurate methods to estimate the number of active sources in MEG signals.

To address these limitations, we propose a robust method for accurately estimating the number of active sources in the brain using the F-ratio statistical approach. Our method introduces formal decision criteria that sequentially increase the number of sources in the multiple dipole localization problem until all sources are found. Our method is based on the F-ratio test, which is commonly used in statistics to compare the variances of two samples. It is sensitive to differences in the variances of the samples and can be used to determine whether adding a source to the model significantly improves the fit of the model to the data. The F-ratio statistical approach allows for a comparison between a full model with a higher number of sources and a reduced model with fewer sources.

We validated the F-ratio-based method on simulated, real phantom, and human MEG data, and compared its performance to that of other state-of-the-art statistical approaches, such as AIC and MDL. We found that the F-ratio-based method outperformed competing methods in terms of accuracy and reliability. One crucial aspect we investigated was the selection of appropriate thresholds for the F-ratio values. We found that this selection played a critical role in determining the overall performance of our method. Through systematic analyses, we identified optimal thresholds that needed to be adjusted according to the number of sources and SNR levels. Importantly, these thresholds exhibited remarkable consistency across different inter-source correlations, translational modeling inaccuracies, and cortical anatomies. When fine-tuned with the optimal selection of thresholds, our F-ratio-based method emerged as a precise and robust tool for estimating the true number of active sources in MEG data.

2. Materials and methods

In this section, we provide a concise overview of the notations used to describe the measurement data, forward matrix, and sources. We also present the problem formulation for estimating multiple ECDs in the brain. Subsequently, we describe the F-ratio statistical procedure, which serves as the foundation to estimate the number of active sources in the brain, and outline the experimental procedures we use to assess performance.

2.1. Measurement model and notations

Consider an array of M MEG sensors detecting signals from Q ECD sources located at positions $\{\mathbf{p}_q\}_{q=1}^{Q}$. At time t, the MEG measurement vector $\mathbf{y}(t)$ can be described as a superposition of the contributions from Q source signals $\{s_q(t)\}_{q=1}^{Q}$ and additive noise:

$$\mathbf{y}(t) = \sum_{q=1}^{Q} \mathbf{l}(\mathbf{p}_q)s_q(t) + \mathbf{n}(t), \quad \text{where } \; Q < M \tag{1}$$

The topography $\mathbf{l}(\mathbf{p}_q)$ of the qth dipole at location $\mathbf{p}_q$ is defined as $\mathbf{l}(\mathbf{p}_q) = \mathbf{L}(\mathbf{p}_q)\mathbf{o}$, where $\mathbf{L}(\mathbf{p}_q) \in \mathbb{R}^{M\times 3}$ is the lead field matrix and $\mathbf{o} \in \mathbb{R}^{3\times 1}$ is the orientation vector. Depending on the problem, the orientation vector $\mathbf{o}$ may either be known, referred to as a *fixed-oriented* dipole, or it may be unknown, referred to as *freely-oriented*. Additionally, the measurements are subject to the presence of additive white Gaussian noise, which is represented by $\mathbf{n}(t) \in \mathbb{R}^{M\times 1}$.

Several source localization methods exist for estimating the Q ECD sources, with each dipole source characterized by its location, orientation, and amplitude. Recently, we introduced a method called Alternating Projections (AP) (Adler et al., 2022), which offers several advantages. AP source localization method is robust to forward model errors, can handle high inter-source correlation values, and is effective even in low SNR scenarios. It is important to note that estimating the true number of active sources Q is a fundamental requirement for all the aforementioned dipole localization methods to accurately estimate the dipole source parameters.

2.2. F-ratio based method

The F-test is a widely used statistical technique that leverages the F-ratio to assess the presence of a significant difference between the variances of two data sets. In the context of determining the true number of sources, this technique holds particular value. It enables us to test the hypothesis that incorporating an additional source results in a substantial improvement in the variance accounted for by the model. By employing the F-test, we can make informed decisions regarding the optimal number of sources to include in order to provide the most accurate explanation for the observed data.

In probability theory and statistics, the F-statistic, also known as the F-ratio, is defined as the ratio between two independent chi-square distributions, denoted as $\mathbf{X_1} \sim \chi^2_{\mathrm{DOF}_1}$ and $\mathbf{X_2} \sim \chi^2_{\mathrm{DOF}_2}$, where DOF_1 and DOF_2 represent the respective degrees of freedom. Mathematically, the F-ratio is expressed as:

$$\mathbf{F} = \frac{\mathbf{X_1}/\mathrm{DOF}_1}{\mathbf{X_2}/\mathrm{DOF}_2} \tag{2}$$

This formula provides a means to calculate the F-ratio by dividing the observed value of $\mathbf{X_1}$ normalized by its degrees of freedom, DOF_1, by the observed value of $\mathbf{X_2}$ normalized by its degrees of freedom, DOF_2. In this study, we use this idea to compare two hypothesized models based on the variance they explain. The first model, referred to as the "reduced model", explains the data with K number of sources:

$$\mathbf{y}(t) = \mathbf{y}_{\mathrm{R}}(t) + \mathbf{n}_{\mathrm{R}}(t), \tag{3}$$

$$\mathbf{y}_{\mathrm{R}}(t) = \sum_{q=1}^{K} \mathbf{l}(\mathbf{p}_q)s_{q_{\mathrm{R}}}(t) \tag{4}$$

where $\mathbf{y}_{\mathrm{R}}(t)$ represent the estimated signals and $\mathbf{n}_{\mathrm{R}}(t)$ represents noise of a reduced model. On the other hand, the second model, called the "full model," includes one more source compared to the reduced model, with $K+1$ sources:

$$\mathbf{y}(t) = \mathbf{y}_{\mathrm{F}}(t) + \mathbf{n}_{\mathrm{F}}(t), \tag{5}$$

$$\mathbf{y}_{\mathrm{F}}(t) = \sum_{q=1}^{K+1} \mathbf{l}(\mathbf{p}_q)s_{q_{\mathrm{F}}}(t) \tag{6}$$

where $\mathbf{y}_{\mathrm{F}}(t)$ represent the estimated signals and $\mathbf{n}_{\mathrm{F}}(t)$ represents noise of a full model. The estimation of $\mathbf{y}_{\mathrm{R}}(t)$ and $\mathbf{y}_{\mathrm{F}}(t)$ signals is achieved by solving an inverse problem using a dipole fitting method. By comparing the residual variance of these two models, we can assess their performance and determine the most appropriate model for the given data. Since we assume that the noise added to the measured signal is white Gaussian noise, it can be deduced that the sum of square errors between the measured signal $\mathbf{y}(t)$ and the estimated signals $\mathbf{y}_{\mathrm{R}}(t)$ and $\mathbf{y}_{\mathrm{F}}(t)$, denoted as

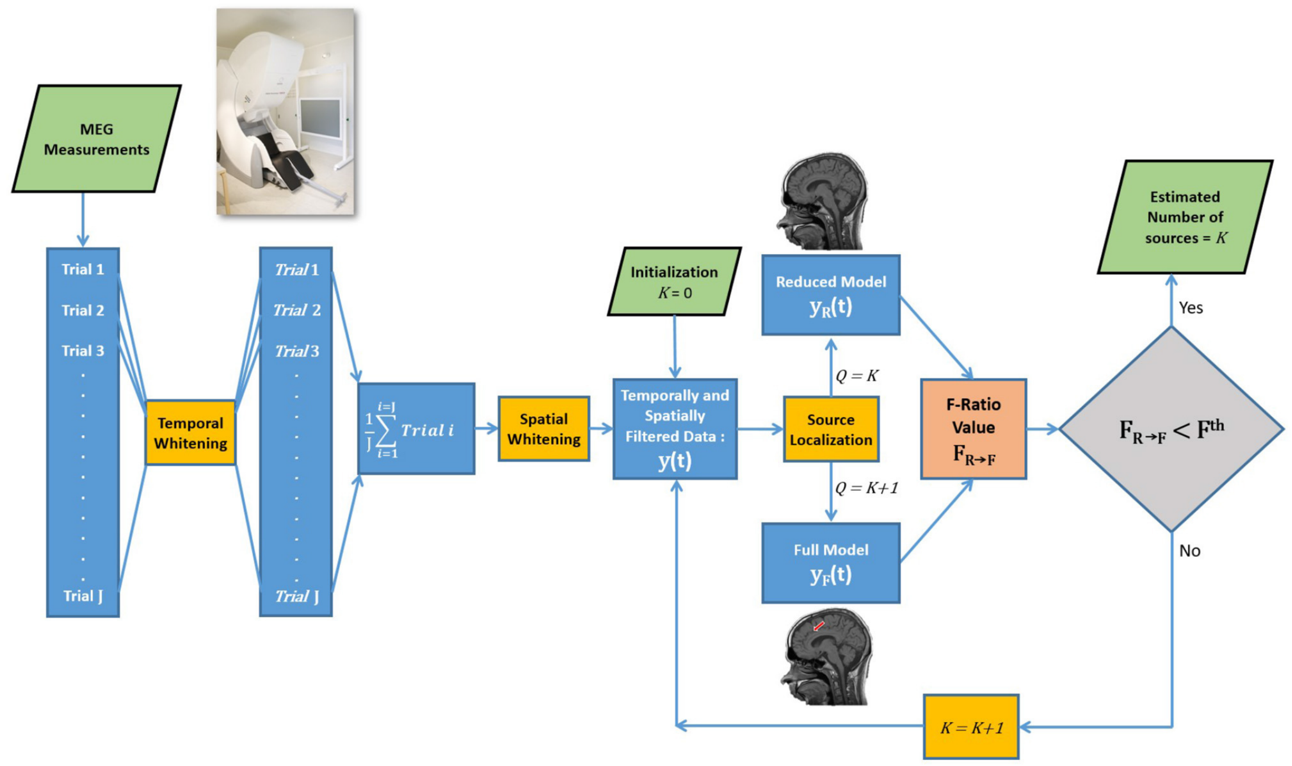

FIGURE 1
Flowchart of the F-ratio method for estimating the number of sources.

$\|\mathbf{y}(t) - \mathbf{y}_{R(t)}\|_2^2$ and $\|\mathbf{y}(t) - \mathbf{y}_F(t)\|_2^2$ respectively, follows chi-square distributions. Therefore, the F-ratio test can be written as Supek and Aine (1993):

$$\mathbf{F}_{R\to F} = \frac{\sum_{t=1}^{N} \|\|\mathbf{y}(t) - \mathbf{y}_R(t)\|\|_2^2}{\mathrm{DOF}_R} \Bigg/ \frac{\sum_{t=1}^{N} \|\|\mathbf{y}(t) - \mathbf{y}_F(t)\|\|_2^2}{\mathrm{DOF}_F} \tag{7}$$

where N is the number of time samples. For the fixed-oriented case, the degrees of freedom (DOF) for the reduced and full models are given by $\mathrm{DOF}_R = MN - (3+N)K$ and $\mathrm{DOF}_F = MN - (3+N)(K+1)$, respectively. For the freely-oriented case, the DOF for the reduced and full models are $\mathrm{DOF}_R = MN - (4+N)K$ and $\mathrm{DOF}_F = MN - (4+N)(K+1)$, respectively. These formulas account for a total of MN degrees of freedom, with three degrees of freedom deducted for position, one for orientation (in the freely-oriented case), and N for amplitude, for each dipole.

Note that the formulas for estimating the DOF assume independence among all data points, which is not the case in experimental data. To address this issue, in experimental data we implemented a two-step whitening process involving both temporal and spatial filtering. The first step involved temporal whitening, as depicted in the flowchart of the F-ratio method (Figure 1). The MEG data of each trial was whitened temporally using a six-order linear predictive coding (LPC) technique. This method helped alleviate temporal correlations within the data, reducing their impact on the results. Subsequently, the LPC-filtered trials were averaged. The second step was spatial whitening, which was achieved by applying a whitening filter derived from inverting the noise covariance matrix. This step further mitigated inter-dependencies among the data points, enhancing the reliability of the analysis. A more detailed discussion of the two-step whitening process is presented in Section 2.4.

It is important to note that the calculated F-ratio values are influenced by the residuals obtained after dipole fitting, and therefore, are dependent on the chosen source localization method used for solving the ECD localization problem in MEG. In our study, we specifically examined the behavior of the F-ratio statistical procedure when employing the AP localization method. The AP method solves the inverse problem iteratively and sequentially by minimizing the least-squares (LS) criterion. For a more detailed and comprehensive discussion of the AP method, we refer readers to Adler et al. (2022).

To estimate the number of sources, a systematic approach involving the comparison of a reduced model and a full model is illustrated in Figure 1. The formal comparison begins by initializing the reduced model with zero sources and the full model with one source to compute the F-ratio value. The decision regarding the number of sources involves comparing the resulting F-ratio value, denoted as $\mathbf{F}_{0\to1}$, with a threshold value, $\mathbf{F}^{\mathrm{th}}$. If the reduced model is rejected ($\mathbf{F}_{0\to1} > \mathbf{F}^{\mathrm{th}}$), indicating evidence of at least one source, the analysis proceeds to compare a reduced model with one source against a full model with two sources, represented as $\mathbf{F}_{1\to2}$. This sequential process continues, increasing the number of sources, until reaching a step where the reduced model cannot be rejected, providing an estimation of the true number of sources.

2.3. Performance evaluation with simulations

We evaluated the performance of the F-ratio method in diverse simulated scenarios, considering variations in the number of sources, SNR levels, inter-source correlations, translational modeling errors, and cortical anatomies.

The SNR was defined as the ratio between the Frobenius norm of the signal-magnetic-field spatiotemporal matrix and that of the noise matrix, following the approach described in Sekihara et al. (2001). To quantify inter-source correlation, we employed the Pearson's correlation coefficient. To establish the desired correlation among the sources, we utilized the Cholesky decomposition method. Initially, we generated fundamental cosine signals for each simulated source, with randomized phase and frequencies ranging from 10Hz to 30Hz. Next, we applied the Cholesky decomposition to factorize the symmetric positive definite target correlation matrix into the product of a lower triangular matrix and its conjugate transpose. By multiplying lower triangular matrix with the fundamental cosine signals, we generated a set of correlated dipole waveforms. This procedure ensured that the resulting source time courses closely matched the correlation coefficients specified by the target correlation matrix, thus incorporating the desired inter-source correlations in our simulations.

The sensor array geometry was based on the Megin Triux MEG system, which consists of a 306-channel probe unit with 204 planar gradiometer sensors and 102 magnetometer sensors. The MEG source space geometries were modeled using the cortical manifold extracted from MR data of adult humans, employing Freesurfer (Fischl et al., 2004). In our analysis, we used cortical anatomies from four different adult humans. Simulated sources were restricted to approximately 15,000 grid points distributed over the cortex. The reconstructed sources were estimated on a distinct grid of 50,000 points covering the cortex. To avoid the "inverse crime" problem, where identical parameters are used for data synthesis and inversion in an inverse problem, the simulation and reconstruction grids were non-overlapping with an average distance of 0.7 mm between neighboring points (Colton and Kress, 1998). The forward matrix for both grids was computed using the boundary element method implemented in OpenMEEG (Gramfort et al., 2010) within the BrainStorm software (Tadel et al., 2011). Simulated MEG data was generated by randomly selecting sources from the simulation grids. Gaussian white noise was then added to the MEG sensors to model instrumentation noise at specified SNR levels. In order to evaluate the effect of head model errors, we introduced translations to the reconstruction grid before computing the forward matrix. Last, we employed the AP method to solve the inverse problem in the *fixed oriented* case. All experiments were conducted with 100 Monte Carlo simulations to ensure statistical robustness.

2.4. Performance evaluation with a real phantom

We assessed the performance of the F-ratio method using the *freely-oriented* dipoles model with phantom data provided in the phantom tutorial (Taylor et al., 2016) of the Brainstorm software (Tadel et al., 2011). The phantom experiment was conducted using the Megin Neuromag system, which consists of a 306-channel probe unit with 204 planar gradiometer sensors and 102 magnetometer sensors.

The data comprised MEG recordings obtained from the sequential activation of 32 artificial dipoles. To activate the phantom dipoles, an internal signal generator was used along with an external multiplexer box that connected the signal to each individual dipole. Each dipole was activated 20 times with an amplitude of 200 nAm, resulting in a total of 20 trials for each experimental condition. It is important to note that the chosen amplitude of 200 nAm falls within the range typically observed in inter-ictal spikes associated with epilepsy, as observed in raw data (Oishi et al., 2002).

For each dipole and each trial, the MEG data was whitened temporally using a six-order LPC technique. In particular, baseline data of a 200 ms pre-stimulus interval was used to compute the LPC coefficients of sixth order. These coefficients were then averaged across sensors and subsequently applied to the post-stimulus data modeled as an moving average (MA) filter. The purpose of this step was to eliminate temporal dependencies in the post-stimulus data, as observed in the auto-regressive (AR) model of baseline data. Following this, the LPC-filtered post-stimulus measurements were averaged across the 20 trials. In addition to temporal prewhitening, spatial prewhitening was also performed on the average data using a regularized noise covariance matrix in the Brainstorm software (Tadel et al., 2011). The regularization process included adding an identity matrix scaled to 10% of the largest eigenvalue of the noise covariance matrix.

To simulate the concurrent activation of multiple sources, we combined averaged data from different dipoles since only one dipole could be activated at a time. To introduce variability and avoid perfect coherence, we added a random delay ranging from 0 to 50 ms for each dipole.

The reconstruction source space was defined as a sphere centered within the MEG sensor array, with a radius of 64.5 mm. It was sampled using a regular volumetric grid of points with a resolution of 2.5 mm, resulting in a total of 56,762 grid points. The forward matrix was estimated based on a single sphere head model using the BrainStorm software (Tadel et al., 2011). The performance of the F-ratio method was evaluated using the AP method for localizing dipoles in the *freely-oriented* case.

2.5. Performance evaluation with human MEG data

The effectiveness of the F-ratio method in practical scenarios was assessed using human MEG data recorded from a single human participant during an auditory task. Prior to participation, the subject provided written informed consent, and the study was approved by the local ethics committee (Institutional Review Board of the Massachusetts Institute of Technology), following the principles of the Declaration of Helsinki. During the experiment, binaural sounds (beeps) were delivered to the subject using tubal-insert earphones. These auditory stimuli are known to elicit specific brain responses that are localized in the bilateral primary auditory cortex. A total of 166 trials were recorded, with an interstimulus interval of 2150 ms between each auditory stimulus. The MEG data were acquired using a MEGIN Triux MEG system, which includes a 306-channel probe unit consisting of 102 magnetometers and 204 planar gradiometers.

The forward matrix was estimated using BrainStorm based on an overlapping spheres head model. The reconstruction source space samples the brain volume in an adaptive way, with a higher density near the surface where we expect a higher spatial resolution due to the proximity to the sensors. The density decreased gradually toward the center of the brain, resulting in a total of 33,073 grid points. This grid is constructed using a specific adaptive algorithm in Brainstorm: It begins with a brain envelope containing 10,000 vertices as the initial number. Then, each previous layer is successively shrunk and downsampled by a factor of 3. This operation is repeated for 17 layers or until no more vertices are available.

The performance of the F-ratio method was evaluated using the AP method for localizing dipoles in the *freely-oriented* case. Before localization, the raw data underwent prewhitening in both the temporal and spatial domains following the same procedure as in the real phantom data.

3. Results

3.1. Optimal modeling of MEG data requires the adjustment of F-ratio nominal thresholds

To investigate the behavior of the F-ratio method under different experimental conditions, we conducted a thorough simulation analysis. Our objective was to assess the accuracy of estimating the true number of sources by varying the threshold values across various experimental scenarios. These scenarios included different numbers of active sources, varying SNR levels, inter-source correlation values, translational modeling errors, and cortical anatomies.

We observed that the accuracy of estimating the true number of sources using a specific F-ratio threshold was strongly influenced by the actual number of sources Q. This relationship is depicted in Figures 2A–C, where the estimation accuracy varied significantly for different values of Q. Notably, as the number of true sources increased, a lower F-ratio threshold was required to achieve higher performance. Similarly, we discovered a strong correlation between the accuracy of estimating the true number of sources and the SNR level. Figures 2D–F demonstrates this dependency for various SNR values. As the SNR level increased, a lower F-ratio threshold became necessary to achieve higher accuracy in estimating the true number of sources.

In contrast, we made the important observation that the optimal F-ratio threshold remained independent of the inter-source correlation level. This finding is illustrated in Figures 2G–I, where we tested different inter-source correlation values (0.1, 0.5, and 0.9). The accuracy in estimating the number of sources peaked at the same threshold value for all correlation levels. This robustness indicates that the optimal F-ratio thresholds were not influenced by the inter-source correlation values of the active sources. Consequently, researchers may rely on a consistent threshold value regardless of the degree of correlation among the sources, enhancing the practical applicability and reliability of the F-ratio method. We obtained similarly robust results when testing the accuracy of estimating the true number of sources across different model errors (Figures 2J–L) and cortical anatomies (Figures 2M–O). In the case of model errors, we introduced registration errors by translating the reconstruction source space relative to the source simulation space. Specifically, we applied translations of 1 mm posterior (X-axis), right (Y-axis), and upward (Z-axis). Importantly, despite the presence of these registration errors, the F-ratio method remained highly robust. Similarly, when evaluating the F-ratio thresholds across the cortical anatomies of four different adult humans, we observed consistent and robust results.

In summary, our observations indicated that the performance of F-ratio thresholds varied significantly depending on the true number of sources and the SNR levels of the data. However, we found that F-ratio thresholds remained robust across different inter-source correlation values, translational model errors, and cortical anatomies. These findings highlight the need to adapt and optimize threshold procedures for the F-ratio test based on the specific number of sources and SNR levels in the data. In the next section, we determined these optimal thresholds.

3.2. Computation and evaluation of adjusted F-ratio thresholds in simulated data

In this section, we aimed to determine adjusted F-ratio thresholds for accurately estimating the number of active sources in MEG data. To accomplish this, we used a specific cortical anatomy as a reference (referred to as Anatomy 1). Optimal threshold values for Anatomy 1 were computed by identifying the F-ratio value that yielded the highest average accuracy in estimating the number of sources, considering the $\rho \in \{0.1, 0.5, 0.9\}$ inter-source correlations and 1mm translational modeling errors in x, y, z. It may be noted that our study specifically examined the robustness of the method against translational modeling errors as a representative example. The resulting adjusted F-ratio thresholds were obtained for various SNR levels and numbers of sources, as depicted in Figure 3. Our findings indicate that higher threshold values are necessary in scenarios characterized by a high SNR and a low number of sources.

To assess the effectiveness of the adjusted threshold values obtained for the reference anatomy, we conducted tests on three additional cortical anatomies (Figure 4). The performance of the adjusted F-ratio thresholds in estimating the number of sources was evaluated at 0 dB SNR and correlation levels $\rho \in \{0.1, 0.5, 0.9\}$. Remarkably, the results showed that the performance of the adjusted thresholds was comparable to that of the reference cortical anatomy (Anatomy 1). These findings demonstrate the reliability and robustness of the calculated optimal F-ratio thresholds across a wide range of simulation scenarios, including variations in the number of sources, SNR levels, inter-source correlation values, translational modeling errors, and cortical anatomies.

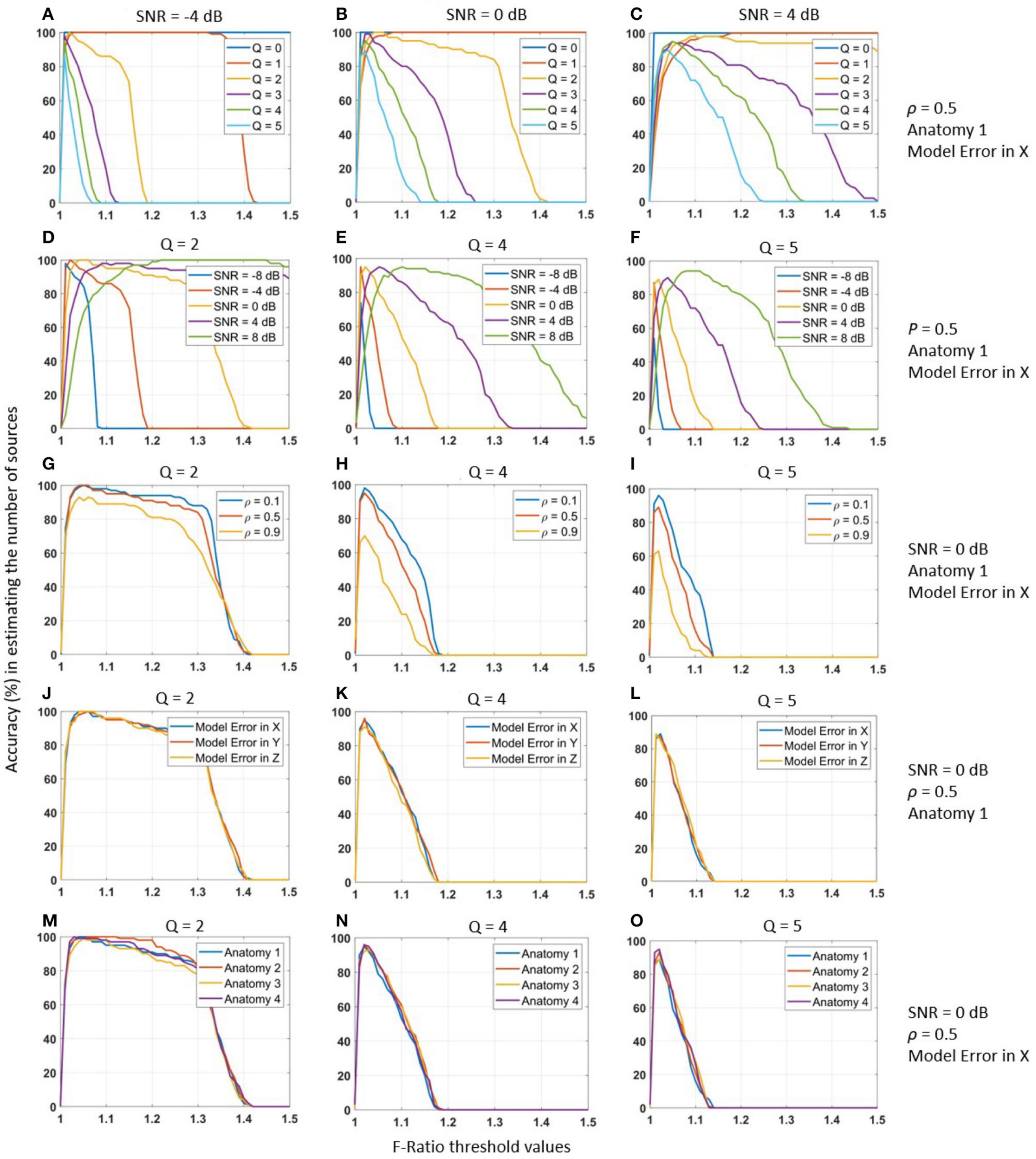

FIGURE 2
Accuracy (%) of the F-ratio method for estimating the number of active MEG sources (on vertical axis) under different threshold values (on horizontal axis). Performance evaluation was conducted across various experimental conditions: **(A–C)** varying number of true sources Q, **(D–F)** SNR levels from -8 to 8 dB, **(G–I)** inter-source correlation values ρ from 0.1 to 0.9, **(J–L)** different model errors, and **(M–O)** different cortical anatomies. Each experimental condition was tested using 100 Monte-Carlo repetitions to ensure statistical robustness. To account for head registration errors, we incorporated inaccuracies into the lead field matrix by applying a translation of 1mm posterior (X-axis), rightward (Y-axis), and upward (Z-axis).

We proceeded by conducting a comparative analysis between the proposed F-ratio method with adjusted thresholds and two commonly used methods, namely the information criterion AIC and MDL method, for estimating the number of sources. These methods rely on likelihood functions derived from information theory to assess and choose the optimal model. The comparison results of the F-ratio, AIC, and MDL methods across different SNR conditions and correlation levels are depicted in Figure 5. The

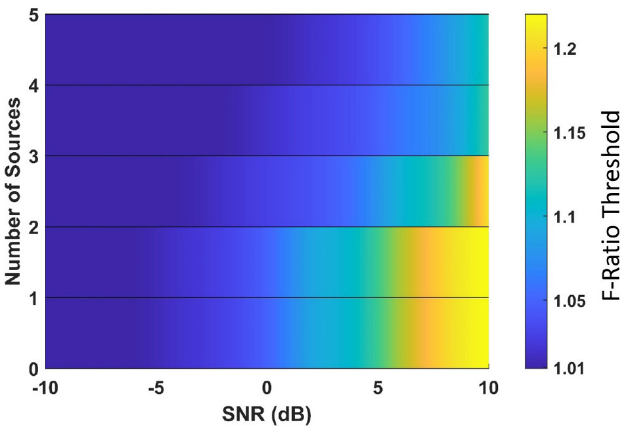

FIGURE 3
Optimal F-ratio threshold values, adjusted for the signal-to-noise ratio (SNR) level and the number of active sources in the MEG data.

results correspond to cortical anatomy 4 with 1 mm translational modeling error in X. Remarkably, the proposed F-ratio method with adjusted thresholds outperformed both the AIC and MDL methods in terms of accuracy and reliability.

3.3. Performance of the F-ratio method in estimating the number of active dipoles in phantom data

We assessed the performance of the F-ratio method in estimating the number of active dipoles in phantom data (Figure 6A). The locations of the 32 artificial dipoles of the MEGIN phantom are shown in Figure 6B. To simulate the activation of multiple MEG sources simultaneously, we combined the data obtained from individually activated dipoles. To avoid perfect coherence, a random delay ranging from 0 to 50 ms was introduced between the dipole time courses. Figure 6C illustrates an example of MEG sensor data from two active dipoles with a randomly selected temporal delay of 29 ms. The time courses are displayed following temporal and spatial prewhitening, and had an estimated SNR of 5.5 dB.

We conducted 100 Monte Carlo repetitions of phantom data simulations for each scenario involving 0 to 5 active sources. For each repetition, we applied the optimal F-ratio thresholds (presented in Figure 3) based on the estimated SNR of the phantom data and the corresponding number of tested sources. The rationale behind using the same optimal F-ratio value from simulations to both the phantom and experimental data lies in the observation that, while the performance of F-ratio thresholds varied significantly based on the number of sources and SNR levels, these thresholds remained largely invariant to variations in inter-source correlations, translational modeling inaccuracies, and different cortical anatomies.

The performance of the F-ratio method in accurately estimating the true number of active dipoles is shown in Figure 6D. The method successfully identified the correct number of sources up to 2, surpassing both the AIC and MDL methods. In contrast, the latter methods failed entirely, with no correct estimations among the 100 simulated scenarios (results not depicted). The AIC method yielded mean estimates of 41 for no true sources and 42 for 1 to 5 true number of sources, respectively, across 100 Monte Carlo repetitions. Similarly, the MDL method estimated the number of sources as 41 in all cases of 0 to 5 true numbers of sources across the same 100 Monte Carlo repetitions. It was found that AIC and MDL consistently overestimated the number of sources.

It is important to note that although the performance of the F-ratio method in experimental data was not as remarkable as in the simulated data, we attribute this to two factors. First, the specific configuration of the phantom dipoles played a critical role. The 32 phantom dipoles were closely spaced and shared similar orientations. In the 100 Monte Carlo repetitions, sources were randomly chosen with no constraints in their simultaneous activation. Consequently, there was a substantial probability of selecting adjacent sources, and this likelihood increased as the number of sources grew (3, 4, and 5). Additionally, the time courses of the phantom dipoles had random delays ranging from 0 to 50 ms, resulting in instances of minimal delay and strong correlation. The combined effect of proximate source selection and small time course delay exacerbated the challenge of accurately estimating the number of sources, particularly when dealing with a larger number of sources.

3.4. Performance of the F-ratio method in estimating the number of sources in human auditory data

To evaluate the effectiveness of the F-ratio method in human data, we utilized it to analyze brain responses captured during an auditory task. We employed the AP source localization method to fit dipoles within the time interval of 100–130 ms relative to the onset of the auditory stimuli, which approximately corresponded to the peak MEG response. The SNR within this interval was determined to be 5.78 dB.

Figure 7A illustrates the adjusted F-ratio thresholds at 5.78 dB SNR, along with the corresponding values estimated from the human data. By employing the F-ratio sequential procedure, we observed the rejection of the reduced models with zero or one source, while finding no evidence to reject (and thus accepting) a model with two distinct sources. To further validate these findings, we plotted the sum of squares of residuals for the competing models, as shown in Figure 7B. This plot reinforces our conclusion of the presence of two sources, as there was no significant reduction in the sum of squares of residuals beyond the model order of 2. Additionally, we visualized the dipoles detected using the AP localization method for the cases of 1, 2, and 3 sources (Figures 7C–E). In the case of the two-source model, the dipoles were localized bilaterally and coincided with the well-established regions in the primary auditory cortices.

It is worth mentioning that alternative methods such as the AIC and MDL yielded different estimates for the number of sources. Specifically, the AIC method suggested 33 sources, while the MDL method indicated only 31 sources. These estimates far exceed the

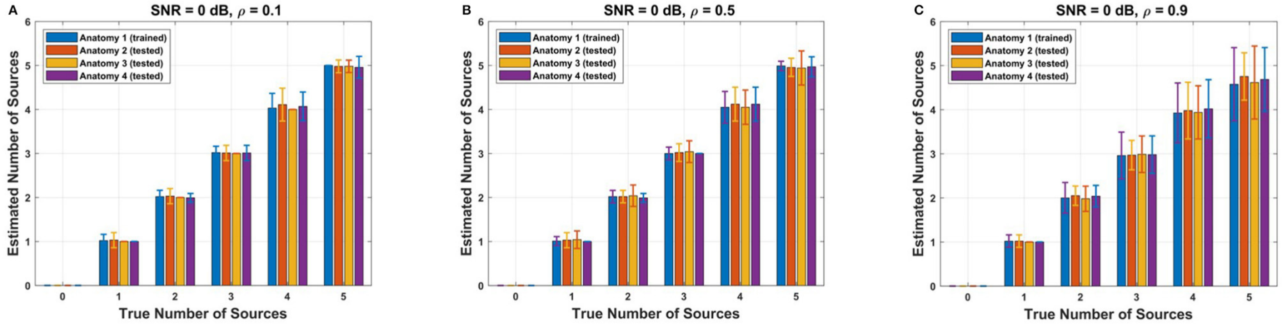

FIGURE 4
Performance of adjusted F-ratio thresholds in simulated data. The thresholds were optimized for Anatomy 1 and applied to three different anatomies (Anatomies 2, 3, and 4). The F-ratio method was employed to estimate the number of sources under varying levels of source correlation **(A)** $\rho = 0.1$, **(B)** $\rho = 0.5$, and **(C)** $\rho = 0.9$, while maintaining a signal-to-noise ratio of 0 dB.

expected number of active sources in human auditory responses and are not in line with the existing knowledge in the field.

Lastly, we conducted a further analysis on the human data with a reduced SNR of approximately 0 dB, achieved by averaging a reduced number of 44 trials (originally 166). As depicted in Supplementary Figure 1, this analysis highlights the robustness of the F-ratio test in accurately detecting 2 sources, consistent with the findings from the higher SNR case. It was found that AIC and MDL consistently overestimated the number of sources even in the presence of lower SNR. This suggests that the overestimation nature of AIC and MDL (in phantom and real data) might be related to the complex nature of human experimental data.

4. Discussion

We have proposed and validated an F-ratio-based method to detect the number of active sources in MEG data. We initially aimed to tune the method with a universal F-ratio threshold value that, once selected, could be applied across diverse simulation scenarios. However, we found that the performance of the F-ratio method was inherently dependent on the SNR and number of sources. Thus, we have concluded that it is not feasible to determine a single threshold value that guarantees optimal performance across all cases. Instead, we proposed a methodology that adjusts F-ratio threshold values based on the estimated SNR and the corresponding number of tested sources. Our results demonstrated the reliability and robustness of the calculated optimal F-ratio thresholds across a wide range of simulation scenarios, including variations in the number of sources, SNR levels, inter-source correlation values, modeling errors, and cortical anatomies.

However, it is crucial to acknowledge that the adjusted threshold values obtained in this study are specific to the MEG system analyzed and may need to be adjusted for other devices or modalities, such as EEG. When applying the F-ratio method in different devices, it would be necessary to determine appropriate threshold values that are specific to each case. Similarly, the effectiveness of the proposed method is inherently linked to the choice of the source localization technique. In this study, we employed the AP method to compute and validate the F-ratio thresholds. However, different source localization methods may yield varying results and require different threshold adjustments. Therefore, it is crucial to determine the optimal threshold values for a particular set of experimental settings and source localization method to ensure accurate estimation of the true number of active brain sources. Despite these considerations, our proposed method provides researchers with a precise tool to estimate the true number of active brain sources and effectively model brain function. By calculating threshold values that are tailored to the specific modality and source localization method, researchers can enhance the accuracy and reliability of their source estimation process.

A study by Supek and Aine (1993) aimed to evaluate the efficacy of three statistical measures, namely percent of variance, reduced chi-square, and F-ratio, in determining the correct number of sources (model order). The authors advocated for the reduced chi-square method as a reliable measure of goodness-of-fit, whereas they were less favorable to the percent of variance and F-ratio because they ignored noise contributions. Although we agree that the percent of variance has limited utility, we contend that the efficacy of the F-ratio method was underestimated. Indeed, the simulation results presented in Supek and Aine (1993) demonstrated that the F-ratio remained stable across different noise levels and successfully identified the true number of sources. However, it is important to note that the study was confined to simulations on a simple spherical head model, lacked assessments using real data, and did not provide clear threshold decision criteria for determining the correct number of sources. In this work, we proposed a methodology to estimate the number of sources by employing F-ratio threshold values based on the estimated SNR and the corresponding number of tested sources.

The Bayesian multi-dipole estimation method, Sequential Semi-Analytic Monte-Carlo Estimation (SESAME) (Sommariva and Sorrentino, 2014; Sorrentino et al., 2014; Luria et al., 2020) is an iterative Monte Carlo algorithm that approximates the posterior distribution for an a-priori unknown number of dipoles. The output of SESAME is a posterior distribution for a variable number of dipoles and their parameters. From this distribution, a cortical probability map is computed, quantifying for each voxel the posterior probability of containing a dipolar source. Additionally, the method provides a point estimate of the dipole location,

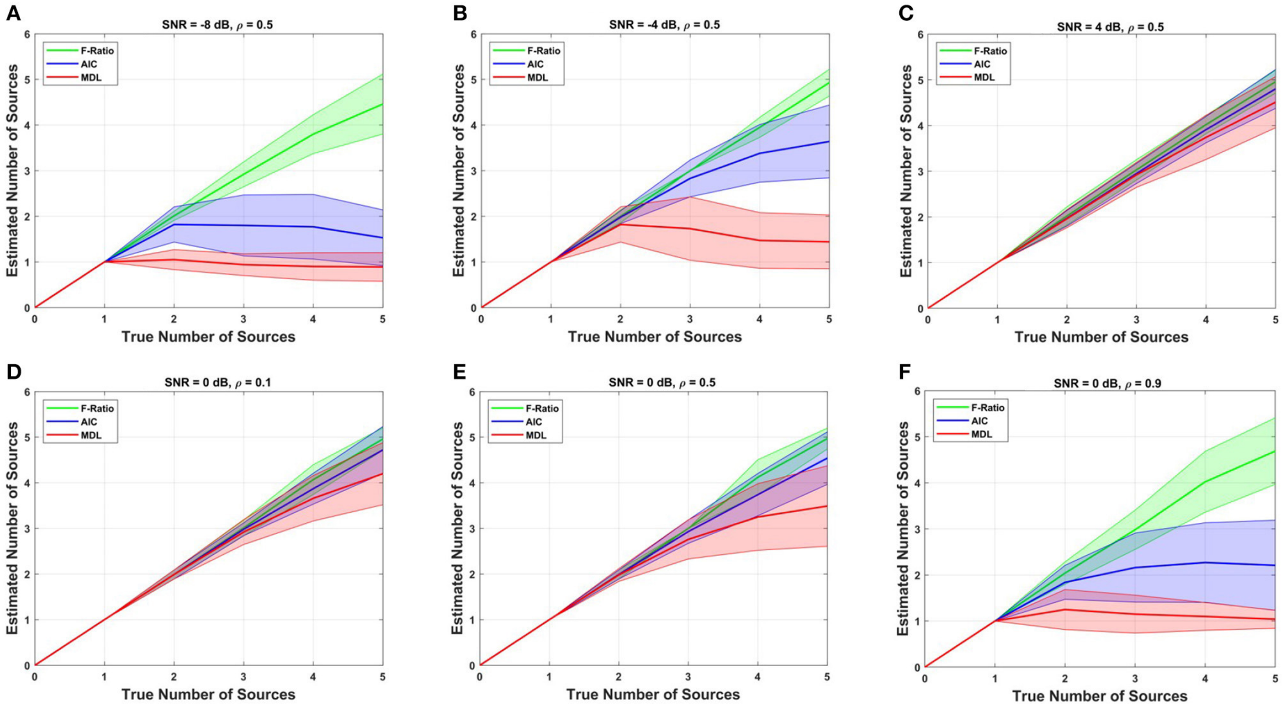

FIGURE 5
Comparison of the F-ratio, AIC, and MDL methods in simulated data for estimating the true number of dipoles at various SNR levels: **(A)** SNR = -8 dB, **(B)** SNR = -4 dB, and **(C)** SNR = 4 dB, and different levels of source correlation: **(D)** ρ = 0.1, **(E)** ρ = 0.5, and **(F)** ρ = 0.9.

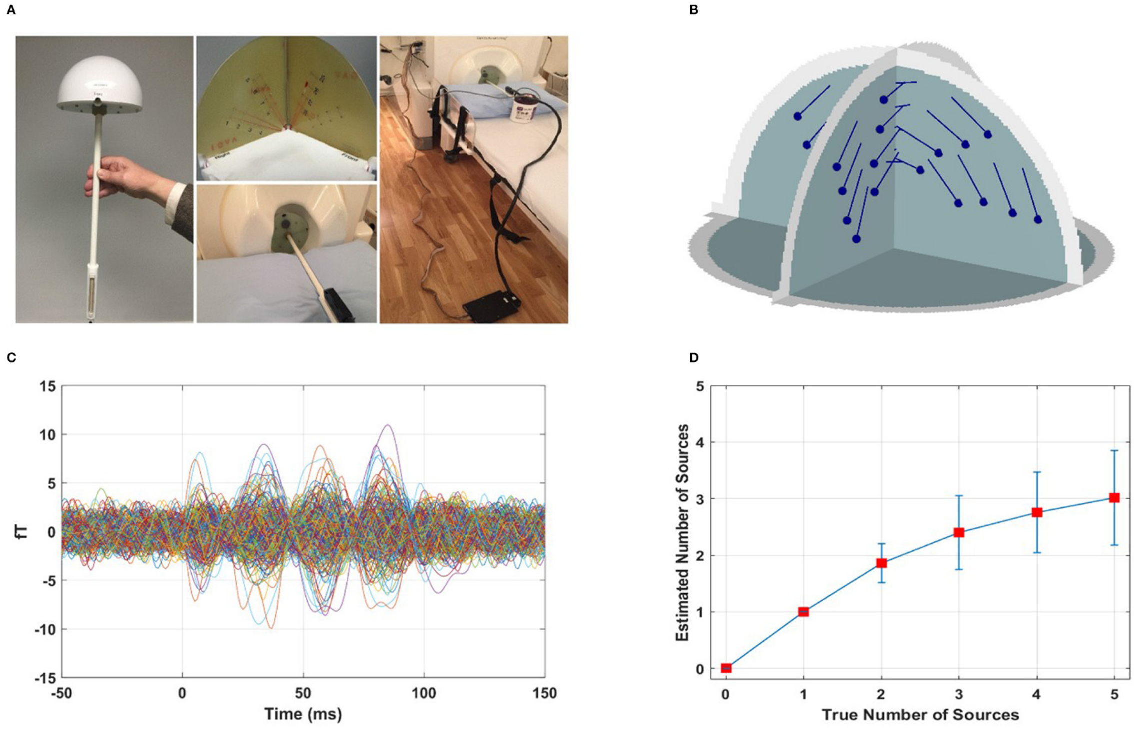

FIGURE 6
Performance of F-ratio method in phantom data. **(A)** Real phantom provided by the MEG vendor MEGIN (Taylor et al., 2016). **(B)** Location of the 32 artificial dipoles of the MEGIN phantom. **(C)** Example sensor measurements from two active dipoles with a temporal delay of 29 ms, following temporal and spatial prewhitening, corresponding to SNR 5.5 dB. **(D)** Performance of F-ratio method in estimating the number of active dipoles.

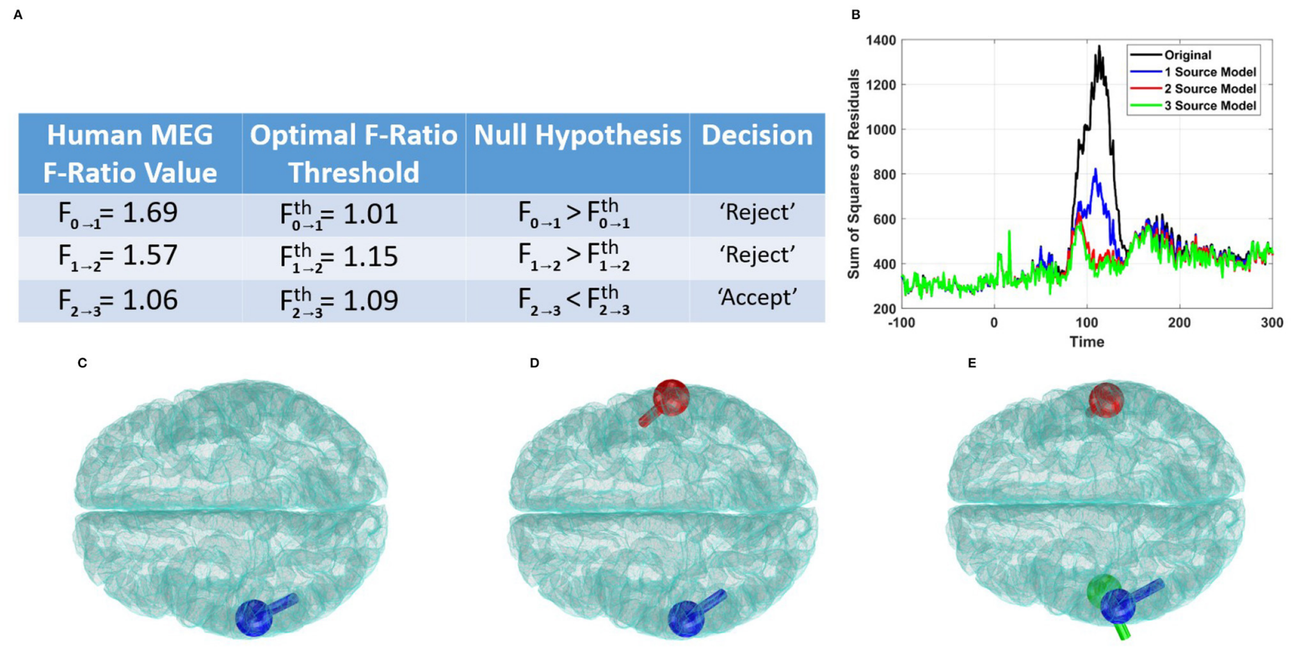

Human MEG F-Ratio Value	Optimal F-Ratio Threshold	Null Hypothesis	Decision
$F_{0\to1}$= 1.69	$F^{th}_{0\to1}$= 1.01	$F_{0\to1} > F^{th}_{0\to1}$	'Reject'
$F_{1\to2}$= 1.57	$F^{th}_{1\to2}$= 1.15	$F_{1\to2} > F^{th}_{1\to2}$	'Reject'
$F_{2\to3}$= 1.06	$F^{th}_{2\to3}$= 1.09	$F_{2\to3} < F^{th}_{2\to3}$	'Accept'

FIGURE 7
Performance of the F-ratio method in estimating the number of sources in human auditory data. **(A)** Comparison of obtained F-ratio values in human data with optimal F-ratio thresholds, supporting a model with two active sources. **(B)** Plot of the sum of squares of residuals for models with different numbers of active sources. **(C)** Localization of a single source. **(D)** Localization of two sources. **(E)** Localization of three sources.

determined as the peak of the cortical probability map. In future research, it would be valuable to compare the performance of SESAME against our proposed method.

It is essential to acknowledge the fact that the performance of the F-ratio method in phantom data was not as remarkable as in the simulated data, we attribute this to two factors. First, the specific configuration of the phantom dipoles played a critical role. The 32 phantom dipoles were closely spaced and shared similar orientations. Additionally, the time courses of the phantom dipoles had random delays ranging from 0 to 50 ms, resulting in instances of minimal delay and strong correlation. The combined effect of proximate source selection and small time course delay exacerbated the challenge of accurately estimating the number of sources, particularly when dealing with a larger number of sources.

In the literature, it is well known that the localization errors tend to increase when dealing with sources that have small spatial separation. This phenomenon has also observed in the AP method, as we reported in our previous work (Adler et al., 2019). Second, estimating the number of sources beyond two is generally an exceptionally challenging problem in MEG. Consequently, a significant body of work has focused on solving the problem of localizing up to two or three sources within simulation or controlled environments (Mosher et al., 1992; Mosher and Leahy, 1999; Mäkelä et al., 2018; Adler et al., 2019; Ilmoniemi and Sarvas, 2019; Giri et al., 2020).

Finally, it is important to mention that the MEG human experiment revealed the presence of two active sources. Notably, the F-ratio method consistently exhibited excellent performance in simulations and phantom experiments with this specific number of sources. However, it is crucial to acknowledge that as the number of sources increases, the suitability of the F-Ratio method might diminish, necessitating further investigation in future studies.

5. Conclusion

We have validated our F-ratio-based method on simulated, real phantom, and human MEG data. In comparison to other state-of-the-art statistical approaches like AIC and MDL, which rely on certain assumptions that often do not hold in real-world situations, our method demonstrated superior performance in terms of accuracy and reliability. One crucial aspect we emphasized is the selection of appropriate thresholds for the F-ratio values, which significantly impacts the overall performance of the method. We identified optimal thresholds and showed that these thresholds needed to be adjusted for the number of sources and SNR levels. Notably, these thresholds exhibited remarkable consistency across different inter-source correlations, head translation modeling errors, and cortical anatomies. Overall, by fine-tuning the selection of thresholds, our F-ratio-based method provides researchers with a precise and robust tool for accurately estimating the true number of active sources in MEG data. Further research is needed to explore and validate the proposed method in different modalities and with various source localization techniques. By refining the threshold determination process and investigating its applicability across different experimental conditions, we can extend the utility of this method to a wider range of neuroimaging studies and enhance our understanding of the underlying mechanisms of brain function.

Data availability statement

The datasets presented in this study can be found in online repositories. The names of the repository/repositories and accession number(s) can be found below: https://github.com/Amita-Giri/FRatio-based-Method-for-Source-Enumeration.

Ethics statement

The studies involving humans were approved by Institutional Review Board of the Massachusetts Institute of Technology. The studies were conducted in accordance with the local legislation and institutional requirements. The participants provided their written informed consent to participate in this study.

Author contributions

AG and DP developed the methodology. AG performed the coding, data analysis, and wrote the first manuscript draft. DP made major contributions to the writing of the final manuscript. AA and DP provided funding, resources, and supervision. All authors contributed to conception of the method, interpreted and discussed the results, critically reviewed the manuscript, and approved the submitted version.

Funding

This work was supported by the National Eye Institute of the NIH under award number 1R01EY033638 (to DP), the National Institute on Aging of the NIH under award numbers RF1AG074204 and RF1AG079324 (to JM and DP), and the United States-Israel Binational Science Foundation grant 2020805 (to AA).

Conflict of interest

The authors declare that the research was conducted in the absence of any commercial or financial relationships that could be construed as a potential conflict of interest.

Publisher's note

Supplementary material

The Supplementary Material for this article can be found online at: https://www.frontiersin.org/articles/10.3389/fnhum.2023.1235192/full#supplementary-material

References

Adler, A., Wax, M., and Pantazis, D. (2019). Localization of MEG and EEG Brain Signals by Alternating Projection. *arXiv. [Preprint]*. arXiv:1908.11416.

Adler, A., Wax, M., and Pantazis, D. (2022). "Brain source localization by alternating projection," in *2022 IEEE 19th International Symposium on Biomedical Imaging* (ISBI), (IEEE), p. 1–5.

Ahveninen, J., Jääskeläinen, I. P., Raij, T., Bonmassar, G., Devore, S., Hämäläinen, M., et al. (2006). Task-modulated "what" and "where" pathways in human auditory cortex. *Proc. Nat. Acad. Sci.* 103, 14608–14613. doi: 10.1073/pnas.0510480103

Akaike, H. (1974). A new look at the statistical model identification. *IEEE Trans. Automat. Contr.* 19, 716–723. doi: 10.1109/TAC.1974.1100705

Baillet, S. (2017). Magnetoencephalography for brain electrophysiology and imaging. *Nat. Neurosci.* 20, 327–339. doi: 10.1038/nn.4504

Bartlett, M. S. (1954). A note on the multiplying factors for various χ 2 approximations. *J. Royal Stat. Soc. Series B (Methodological).* 1954, 296–298. doi: 10.1111/j.2517-6161.1954.tb00174.x

Chen, W., Wong, K. M., and Reilly, J. P. (1991). Detection of the number of signals: a predicted eigen-threshold approach. *IEEE Trans. Signal Proc.* 39, 1088–1098. doi: 10.1109/78.80959

Colton, D. L., and Kress, R. (1998). *Inverse Acoustic and Electromagnetic Scattering Theory*. Cham: Springer.

Dale, A.M., Liu, A. K., Fischl, B. R., Buckner, R. L., Belliveau, J. W., Lewine, J. D., et al. (2020). Dynamic statistical parametric mapping: combining fMRI and MEG for high-resolution imaging of cortical activity. *Neuron* 26, 55–67. doi: 10.1016/S0896-6273(00)81138-1

Darvas, F., Pantazis, D., Kucukaltun-Yildirim, E., and Leahy, R. (2004). Mapping human brain function with meg and eeg: methods and validation. *Neuroimage* 23, S289–S299. doi: 10.1016/j.neuroimage.2004.07.014

Di, A., and Tian, L. (1984). "Matrix decomposition and multiple source location," in ICASSP'84. IEEE International Conference on Acoustics, Speech, and Signal Processing. San Diego, CA: IEEE, 722–725.

Fischl, B., Salat, D. H., Van Der Kouwe, A. J., Makris, N., Ségonne, F., Quinn, B. T., et al. (2004). Sequence-independent segmentation of magnetic resonance images. *Neuroimage* 23, S69–S84. doi: 10.1016/j.neuroimage.2004.07.016

Giorgetta, C., Grecucci, A., Bonini, N., Coricelli, G., Demarchi, G., Braun, C., et al. (2013). Waves of regret: A meg study of emotion and decision-making. *Neuropsychologia* 51, 38–51. doi: 10.1016/j.neuropsychologia.2012.10.015

Giri, A. (2022). *Spatial and anatomical harmonics domain based brain source localization*. PhD thesis, IIT Delhi. doi: 10.21203/rs.3.rs-953226/v1

Giri, A., Kumar, L., and Gandhi, T. (2018). "EEG dipole source localization in hemispherical harmonics domain," in *2018 Asia-Pacific Signal and Information Processing Association Annual Summit and Conference (APSIPA ASC)*. Honolulu, HI: IEEE, 679–684.

Giri, A., Kumar, L., and Gandhi, T. (2019). "Head harmonics based EEG dipole source localization," in *2019 53rd Asilomar Conference on Signals, Systems, and Computers*. Pacific Grove, CA: IEEE, 2149–2153.

Giri, A., Kumar, L., and Gandhi, T. K. (2020). Brain source localization in head harmonics domain. *IEEE Trans. Instrum. Meas.* 70, 1–10. doi: 10.1109/TIM.2020.3026511

Giri, A., Kumar, L., Kurwale, N., and Gandhi, T. K. (2022). Anatomical harmonics basis based brain source localization with application to epilepsy. *Sci. Rep.* 12, 11240. doi: 10.1038/s41598-022-14500-7

Gramfort, A., Kowalski, M., and Hämäläinen, M. (2012). Mixed-norm estimates for the m/eeg inverse problem using accelerated gradient methods. *Phys. Med. Biol.* 57, 1937. doi: 10.1088/0031-9155/57/7/1937

Gramfort, A., Papadopoulo, T., Olivi, E., and Clerc, M. (2010). OpenMEEG: opensource software for quasistatic bioelectromagnetics. *Biomed. Eng. Online* 9, 1–20. doi: 10.1186/1475-925X-9-45

Gramfort, A., Strohmeier, D., Haueisen, J., Hämäläinen, M. S., and Kowalski, M. (2013). Time-frequency mixed-norm estimates: Sparse m/eeg imaging with non-stationary source activations. *Neuroimage* 70, 410–422. doi: 10.1016/j.neuroimage.2012.12.051

Green, A. A., Berman, M., Switzer, P., and Craig, M. D. (1988). A transformation for ordering multispectral data in terms of image quality with implications for noise removal. *IEEE Trans. Geosci. Remote Sens*. 26:65–74. doi: 10.1109/36.3001

Hämäläinen and Ilmoniemi,Hämäläinen, M. S., and Ilmoniemi, R. J. (1994). Interpreting magnetic fields of the brain: minimum norm estimates. *Med. Biol. Eng. Comput.*32, 35–42. doi: 10.1007/BF02512476

Hämäläinen, M., Hari, R., Ilmoniemi, R. J., Knuutila, J., and Lounasmaa, O. (1993). Magnetoencephalography theory, instrumentation, and applications to noninvasive studies of the working human brain. *Rev. Mod. Phys*. 65, 413–497. doi: 10.1103/RevModPhys.65.413

Hecker, L., Tebartz van Elst, L., and Kornmeier, J. (2023). Source localization using recursively applied and projected MUSIC with flexible extent estimation. *Front. Neurosci.* 17:1170862. doi: 10.3389/fnins.2023.1170862

Ikeda, S., and Toyama, K. (2000). Independent component analysis for noisy data—MEG data analysis. *Neural Networks* 13, 1063–1074. doi: 10.1016/S0893-6080(00)00071-X

Ilmoniemi, R., and Sarvas, J. (2019). *Brain Signals: Physics and Mathematics of MEG and EEG*. Cambridge, MA: MIT Press.

Jiang, J.-S., and Ingram, M. A. (2004). "Robust detection of number of sources using the transformed rotational matrix," in *2004 IEEE Wireless Communications and Networking Conference (IEEE Cat. No. 04TH8733)*. Atlanta, GA: IEEE, 501–506.

Klepp, A., Niccolai, V., Buccino, G., Schnitzler, A., and Biermann-Ruben, K. (2015). Language-motor interference reflected in MEG beta oscillations. *Neuroimage* 109, 438–448. doi: 10.1016/j.neuroimage.2014.12.077

Knösche, T. R., Berends, E., Jagers, H., and Peters, M. J. (1998). Determining the number of independent sources of the EEG: a simulation study on information criteria. *Brain Topogr*. 11, 111–124. doi: 10.1023/A:1022202521439

Krishnaswamy, P., Obregon-Henao, G., Ahveninen, J., Khan, S., Babadi, B., Iglesias, J. E., et al. (2017). Sparsity enables estimation of both subcortical and cortical activity from meg and eeg. *Proc. Nat. Acad. Sci*. 114, E10465–E10474. doi: 10.1073/pnas.1705414114

Lawley, D. (1956). Tests of significance for the latent roots of covariance and correlation matrices. *Biometrika*. 43, 128–136. doi: 10.1093/biomet/43.1-2.128

Luria, G., Duran, D., Visani, E., Rossi Sebastiano, D., Sorrentino, A., Tassi, L., et al. (2020). Towards the automatic localization of the irritative zone through magnetic source imaging. *Brain Topogr*. 33, 651–663. doi: 10.1007/s10548-020-00789-y

Mäkelä, N., Stenroos, M., Sarvas, J., and Ilmoniemi, R. J. (2017). Locating highly correlated sources from MEG with (recursive)(R) DS-MUSIC. *bioRxiv [Preprint]*. doi: 10.1101/230672

Mäkelä, N., Stenroos, M., Sarvas, J., and Ilmoniemi, R. J. (2018). Truncated RAP-MUSIC (TRAP-MUSIC) for MEG and EEG source localization. *Neuroimage* 167, 73–83. doi: 10.1016/j.neuroimage.2017.11.013

Malinowski, E. R. (1977a). Determination of the number of factors and the experimental error in a data matrix. *Anal. Chem*. 49, 612–617. doi: 10.1021/ac50012a027

Malinowski, E. R. (1977b). Theory of error in factor analysis. *Anal. Chem*. 49, 606–612. doi: 10.1021/ac50012a026

Mosher, J., Lewis, P., and Leahy, R. (1992). Multiple dipole modeling and localization from spatio-temporal MEG data. *IEEE Trans. Biomed. Eng*. 39, 541–557. doi: 10.1109/10.141192

Mosher, J. C., and Leahy, R. M. (1999). Source localization using recursively applied and projected (RAP) MUSIC. *IEEE Trans. Signal Proc*. 47, 332–340. doi: 10.1109/78.740118

Oishi, M., Otsubo, H., Kameyama, S., Morota, N., Masuda, H., Kitayama, M., et al. (2002). Epileptic spikes: magnetoencephalography versus simultaneous electrocorticography. *Epilepsia* 43, 1390–1395. doi: 10.1046/j.1528-1157.2002.10702.x

Pancholi, S., Giri, A., Jain, A., Kumar, L., and Roy, S. (2023). "Source aware deep learning framework for hand kinematic reconstruction using EEG signal," in *IEEE Transactions on Cybernetics, Vol. 53* (IEEE), 4094–4106. doi: 10.1109/TCYB.2022.3166604

Pascual-Marqui, R. D. (2002). Standardized low-resolution brain electromagnetic tomography (sloreta): technical details. *Methods Find. Exp. Clin. Pharmacol*. 24, 5–12.

Rezaei, A., Lahtinen, J., Neugebauer, F., Antonakakis, M., Piastra, M. C., Koulouri, A., et al. (2021). Reconstructing subcortical and cortical somatosensory activity via the RAMUS inverse source analysis technique using median nerve SEP data. *Neuroimage* 245, 118726. doi: 10.1016/j.neuroimage.2021.118726

Rissanen, J. (1978). Modeling by shortest data description. *Automatica*. 14, 465–471. doi: 10.1016/0005-1098(78)90005-5

Salman, T., Badawy, A., Elfouly, T. M., Mohamed, A., and Khattab, T. (2015). "Estimating the number of sources: An efficient maximization approach," in *2015 International Wireless Communications and Mobile Computing Conference (IWCMC)*. Dubrovnik: IEEE, 199–204.

Schwarz, G. (1978). Estimating the dimension of a model. *Ann. Statist*. 461–464. doi: 10.1214/aos/1176344136

Sekihara, K., Nagarajan, S. S., Poeppel, D., Marantz, A., and Miyashita, Y. (2001). Reconstructing spatio-temporal activities of neural sources using an MEG vector beamformer technique. *IEEE Trans. Biomed. Eng*. 48, 760–771. doi: 10.1109/10.930901

Sommariva, S., and Sorrentino, A. (2014). Sequential Monte Carlo samplers for semi-linear inverse problems and application to magnetoencephalography. *Inverse Probl*. 30, 114020. doi: 10.1088/0266-5611/30/11/114020

Sorrentino, A., Luria, G., and Aramini, R. (2014). Bayesian multi-dipole modelling of a single topography in MEG by adaptive sequential Monte Carlo samplers. *Inverse Probl*. 30, 045010. doi: 10.1088/0266-5611/30/4/045010

Strohmeier, D., Bekhti, Y., Haueisen, J., and Gramfort, A. (2016). The iterative reweighted mixed-norm estimate for spatio-temporal MEG/EEG source reconstruction. *IEEE Trans. Med. Imaging* 35, 2218–2228. doi: 10.1109/TMI.2016.2553445

Supek, S., and Aine, C. J. (1993). Simulation studies of multiple dipole neuromagnetic source localization: model order and limits of source resolution. *IEEE Trans. Biomed.l Eng*. 40, 529–540. doi: 10.1109/10.237672

Tadel, F., Baillet, S., Mosher, J. C., Pantazis, D., and Leahy, R. M. (2011). Brainstorm: a user-friendly application for MEG/EEG analysis. *Comput. Intell. Neurosci*. 2011, 1–13. doi: 10.1155/2011/879716

Taylor, K., Tadel, F., and Mosher, J. C. (2016). *MEG Current Phantom (Elekta-Neuromag)*. Available online at: https://neuroimage.usc.edu/brainstorm/Tutorials/PhantomElekta

Van Veen, B. D., Van Drongelen, W., Yuchtman, M., and Suzuki, A. (1997). Localization of brain electrical activity via linearly constrained minimum variance spatial filtering. *IEEE Trans. Biomed. Eng*. 44, 867–880. doi: 10.1109/10.623056

Vrba, J., and Robinson, S. E. (2001). Signal processing in magnetoencephalography. *Methods* 25, 249–271. doi: 10.1006/meth.2001.1238

Wax, M., and Kailath, T. (1985). Detection of signals by information theoretic criteria. *IEEE Trans. Acoust*. 33, 387–392. doi: 10.1109/TASSP.1985.1164557

Wendel, K., Väisänen, O., Malmivuo, J., Gencer, N. G., Vanrumste, B., Durka, P., et al. (2009). EEG/MEG source imaging: methods, challenges, and open issues. *Comput. Intell. Neurosci*. 2009, 656092. doi: 10.1155/2009/656092

Westlake, K. P., Hinkley, L. B., Bucci, M., Guggisberg, A. G., Findlay, A. M., Henry, R. G., et al. (2012). Resting state alpha-band functional connectivity and recovery after stroke. *Exp. Neurol*. 237, 160–169. doi: 10.1016/j.expneurol.2012.06.020

Wilkinson, C. M., Burrell, J. I., Kuziek, J. W., Thirunavukkarasu, S., Buck, B. H., and Mathewson, K. E. (2020). Predicting stroke severity with a 3-min recording from the muse portable EEG system for rapid diagnosis of stroke. *Sci. Rep*. 10, 1–11. doi: 10.1038/s41598-020-75379-w

Xu, M., Sanz, D. L., Garces, P., Maestu, F., Li, Q., and Pantazis, D. (2021). A graph gaussian embedding method for predicting alzheimer's disease progression with MEG brain networks. *IEEE Trans. Biomed. Eng*. 68, 1579–1588. doi: 10.1109/TBME.2021.3049199

Yao, Z., Zhang, Y., Bai, Z., and Eddy, W. F. (2018). Estimating the number of sources in magnetoencephalography using spiked population eigenvalues. *J. Am. Stat. Assoc*. 113, 505–518. doi: 10.1080/01621459.2017.1341411

Zhang, Q.-T., Wong, K. M., Yip, P. C., and Reilly, J. P. (1989). Statistical analysis of the performance of information theoretic criteria in the detection of the number of signals in array processing. *IEEE Trans. Acoust*. 37, 1557–1567. doi: 10.1109/29.35394

Frontiers in Human Neuroscience

TYPE Original Research
PUBLISHED 20 October 2023
DOI 10.3389/fnhum.2023.1239105

OPEN ACCESS

EDITED BY
Johannes Vorwerk,
UMIT TIROL – Private University for Health Sciences and Health Technology, Austria

REVIEWED BY
Seok Lew,
Olivet Nazarene University, United States
Maria-Carla Piastra,
University of Twente, Netherlands

*CORRESPONDENCE
Yu Huang
✉ andypotatohy@gmail.com

RECEIVED 12 June 2023
ACCEPTED 09 October 2023
PUBLISHED 20 October 2023

CITATION
Guillen A, Truong DQ, Datta A and Huang Y (2023) Optimized high-definition tDCS in patients with skull defects and skull plates. *Front. Hum. Neurosci.* 17:1239105.
doi: 10.3389/fnhum.2023.1239105

Optimized high-definition tDCS in patients with skull defects and skull plates

Alexander Guillen[1], Dennis Q. Truong[1], Abhishek Datta[1,2] and Yu Huang[1]*

[1]Research and Development, Soterix Medical, Inc, Woodbridge, NJ, United States, [2]The City College of New York, New York, NY, United States

Introduction: Transcranial direct current stimulation (tDCS) has been shown to benefit patients with brain lesions or traumatic brain injury (TBI). These patients usually have skull defects with different sizes and electrical conductivities. There is very little data in the literature that show how to optimally stimulate these patients with the presence of skull defects.

Methods: Here we leveraged high-resolution (1 mm) realistic head models to explore the best montages targeting right beneath the skull defects with different sizes and conductivities. Specifically, open-source software ROAST was used to solve for the lead field on the publicly available MIDA model. Four different skull defects/plates were modeled with the center above the right primary motor cortex: a larger defect (10 cm diameter) modeled as either titanium or acrylic plate, and a smaller defect (2.5 cm diameter) modeled as either acute state filled with cerebrospinal fluid (CSF) or chronic state with scar tissue. Optimized stimulation with maximal intensity was run using ROAST targeting the right primary motor cortex.

Results: We show that optimized high-definition montages can achieve an average of 0.3 V/m higher stimulation intensities at the target compared to un-optimized montages (M1-SO or 4×1). Large skull defects with titanium or acrylic plates significantly reduce the stimulation intensity by about 80%, while small defects with acute (CSF) or chronic (scar) tissues significantly increase the stimulation intensity by about 200%. Furthermore, one can use M1-SO to achieve almost the same stimulation strength as the optimized montage if the skull has a large defect with titanium plate, and there is no significant difference in stimulation intensity between 4×1 montage and the optimized montage for small skull defects with scar tissue.

Discussion: Based on this work, future modeling studies leveraging individual anatomy of skull defects may help guide tDCS practice on patients with skull defects and skull plates.

KEYWORDS

transcranial direct current stimulation (tDCS), skull defect, skull plate, tramatic brain injury, computational models and optimization

Introduction

As an emerging neuromodulation technique, transcranial direct current stimulation (tDCS) has been shown to have therapeutic effects for a wide range of neurological disorders such as major depression (Bikson et al., 2008), epilepsy (Fregni et al., 2006b; Auvichayapat et al., 2013), Parkinson's disease (Fregni et al., 2006a), chronic pain (Fregni et al., 2007), and stroke (Meinzer et al., 2016). It is shown that tDCS has the potential to promote motor recovery and improve cognitive functions after traumatic brain injury (TBI) (Kim et al., 2019; Schwertfeger et al., 2023;

Ziesel et al., 2023). High-definition (HD) tDCS leverages several small disc electrodes (~6 mm radius) to achieve better focality compared to conventional pad electrodes (Datta et al., 2009). We have previously developed algorithms to optimally guide electrode placement so that a specific brain region can be stimulated with HD-tDCS with either maximal intensity or maximal focality (Dmochowski et al., 2011; Huang et al., 2018). However, all these studies are based on intact skulls. Skull defects and use of skull plates can significantly alter the injected electric current, as shown in previous computational studies (Datta et al., 2010; Sun et al., 2021). To the best of our knowledge, there is still no data reported in the literature that shows if we can efficiently stimulate brain regions below the skull defects or skull plates by optimizing the electrode montages. This is important for patients with TBI as they usually have defects in their skull (also known as the decompressive craniectomy), and tDCS has shown benefits to recovery after TBI (Kim et al., 2019; Schwertfeger et al., 2023; Ziesel et al., 2023). In this study, we aim to computationally investigate how skull defects or plates affect the current flow induced by optimized HD-tDCS. Specifically, we built a realistic, high-resolution computational model following previous methodology (Huang et al., 2019). To find out how different sizes and electrical conductivities of skull defects / plates affect the patterns of current flow, we altered the original model of normal anatomy into four variants that modeled a larger and a smaller skull defect with different conductivities. As the most common locations of the skull defect are unilateral with an opening on the left or right hemisphere (Fatima et al., 2019; Lambride et al., 2020), we modeled the skull defect above the right primary motor cortex. We then performed optimized HD-tDCS (Dmochowski et al., 2011) targeting the right primary motor cortex and compared the achieved electric field at the target with those from an intact skull anatomy. We found that optimization always increases the stimulation at the target below the skull defects. Large skull defects reduce the stimulation intensity while small defects increase the intensity. We hope that our results will provide some general guidelines for future tDCS on patients with skull defects and skull plates.

Methods

Construction of head and skull lesion models

A high-resolution (0.5 mm) head model publicly available at the IT'IS Foundation known as MIDA (Multimodal Imaging-Based Detailed Anatomical Model, Iacono et al., 2015) was used in this study. The original MIDA model has segmentation for 153 brain structures. As the goal of this work is to evaluate how skull defects affect optimized HD-tDCS, we are interested in a head model that includes the major head tissues. Therefore, we merged most of these structures into six tissue types: white matter, gray matter, cerebrospinal fluid (CSF), skull, scalp, and air cavities. This was done in ScanIP (Simpleware Ltd., Exeter, UK). The model was also downsampled to 1 mm resolution for faster speed in computing the lead field (see Section of "Optimized HD-tDCS").

Patients with a large skull defect (up to a diameter of 10 cm) that can be associated with decompressive craniectomy (Guo et al., 2022) usually have a skull plate implanted for cosmetic purposes and to also protect against external trauma, as the original skull cannot be placed back (Sekhar and Fessler, 2016). A small skull defect (diameter of ~2.5 cm) is either filled with CSF in the acute state or scar tissues in chronic state (Jacobs et al., 2001; Soltanian-Zadeh et al., 2003). Based on these, we modeled the skull defects as follows: (1) 10-cm diameter defect modeled as a titanium plate; (2) 10-cm diameter defect modeled as an acrylic plate; (3) 2.5-cm diameter defect modeled as acute injury (filled with the CSF); (4) 2.5-cm diameter defect modeled as chronic scar tissue. Note in this paper we use "defect" to refer to the openings on the skull that are either implanted with a plate or filled with CSF or scar tissue. The defect was first modeled as a cylinder and placed manually in ScanCAD (Simpleware Ltd., Exeter, UK) with the center above the right primary motor cortex and normal to the local scalp surface. The intersection of the cylinder and the skull segmentation was then classified as the defect and was assigned a different electrical conductivity when computing the lead field (see the next subsection).

Optimized HD-tDCS

A customized version of the open-source software ROAST (Huang et al., 2019; Huang, 2020) was used to solve for the forward model (also known as the lead field) needed for optimized HD-tDCS (Dmochowski et al., 2011). Specifically, the customized ROAST takes the segmentation of six tissues from the MIDA model. 74 electrodes of 6 mm radius following international 10–10 convention (Klem et al., 1999) were placed on the scalp. To avoid complications in automatically placing electrodes near or behind the ear-lobes, we omitted positions TP9 and TP10. The entire volume was then discretized into a finite element mesh, and the forward problem was solved for each bipolar montage with electrode Iz as the reference. See Huang et al. (2013, 2019) for more details. If the skull defect was added into the model, then in total seven tissues were modeled. This entire process was done fully automated in the customized ROAST. Default conductivities in ROAST were assigned to the six tissues (in S/m: white matter – 0.126, gray matter – 0.276, CSF – 1.65, skull – 0.01, scalp – 0.465, air cavities – 2.5×10^{-14}; Huang et al., 2013), and skull defects were assigned with the following conductivities (in S/m): (1) titanium – 7.4×10^{5}; (2) acrylic – 2.0×10^{-13}; (3) CSF – 1.65; (4) scar – 0.34 (Datta et al., 2010). Optimized HD-tDCS was performed to stimulate the right primary motor cortex (MNI coordinates $x = 48$, $y = -8$, $z = 50$) below the skull defect with highest possible intensity and stimulating current on the scalp not exceeding the safety limit of 2 mA (Dmochowski et al., 2013). This was done also in ROAST using the "roast_target()" function. The achieved electric field magnitude at the target location was recorded for each skull defect model and the normal head model (without any skull defect). We released the customized version of ROAST at the Github repository (Huang, 2020).

Comparison between models and montages

For all the skull defect models and the normal model, we also simulated the electric field distribution for two un-optimized electrode montages in ROAST: M1-SO and 4×1. For the M1-SO montage, conventional pad electrodes were used with the anode placed on top of the right primary cortex (electrode C4) and the cathode placed at Fp1. For the 4×1 montage, 6-mm radius anode was placed at C4, with cathodes surrounding at FC2, FC6, CP2, and CP6. In both cases, the total injected current was 2 mA.

We compared the achieved electric field magnitude at the right primary motor cortex across different models (4 skull defect models and the normal model) and montages (optimized, M1-SO, 4×1). To test the robustness of optimized HD-tDCS and sample more data points from the models to compare, we also shifted the target location, re-ran the optimization, and compared the achieved field magnitude across models and montages. We shifted the target location in four directions: anterior by 2 cm, posterior by 2 cm, left by 2 cm, and right by 1 cm (instead of 2 cm which is out of the brain). Mann–Whitney U test was used to assess the significance of the difference between models.

Results

Construction of head and skull lesion models

The merged segmentation of the head tissues from the MIDA model, with the skull defects, is shown in Figure 1. Note that we centered the skull defect right above the right primary motor cortex (Figure 2D).

Optimized HD-tDCS

Figure 3 shows the electric field from each model under different montages. It is notable that optimized stimulation always boosts the intensity at the target compared to un-optimized montages, no matter whether the skull has a defect or not. Specifically, for the location directly under the skull defect [circle marker, MNI coordinates (48, −8, 50)], optimized stimulation in a normal-skull model boosts the stimulation intensity at the target by 0.18 V/m (4×1 montage) and 0.09 V/m (M1-SO montage). For the large defect with a titanium plate, the increase is 0.07 V/m for 4×1 montage and 0.01 V/m for M1-SO montage. For the large defect with an acrylic plate, the increase is 0.18 V/m (4×1) and 0.12 V/m (M1-SO). For the small defect with CSF, the increase is 0.22 V/m for both 4×1 and M1-SO montages. For the small defect with scar tissue, the increase is 0.25 V/m (4×1) and 0.29 V/m (M1-SO).

Comparison between models and montages

Skull defects change the stimulation intensity. As shown in Figure 3, for the optimized montage, electric field at the right primary motor cortex decreases from 0.33 V/m to 0.07 V/m for the large titanium plate, to 0.18 V/m for the large acrylic plate, and increases to 0.78 V/m for the small defect with CSF, and to 0.93 V/m for the small defect with scar tissue. Mann–Whitney U test shows that the changes

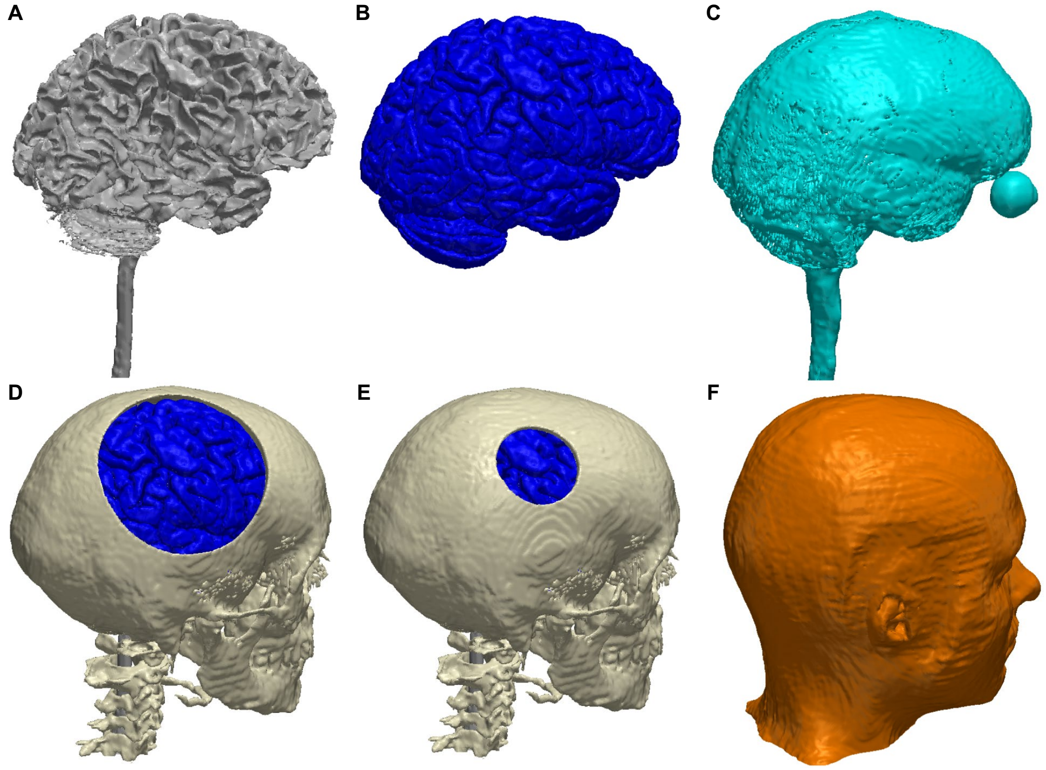

FIGURE 1
3D renderings of the major tissue types in the MIDA head model: **(A)** white matter; **(B)** gray matter; **(C)** CSF; **(D)** skull with a large defect (10-cm diameter, gray matter can be seen through the defect); **(E)** skull with a small defect (2.5-cm diameter); **(F)** scalp.

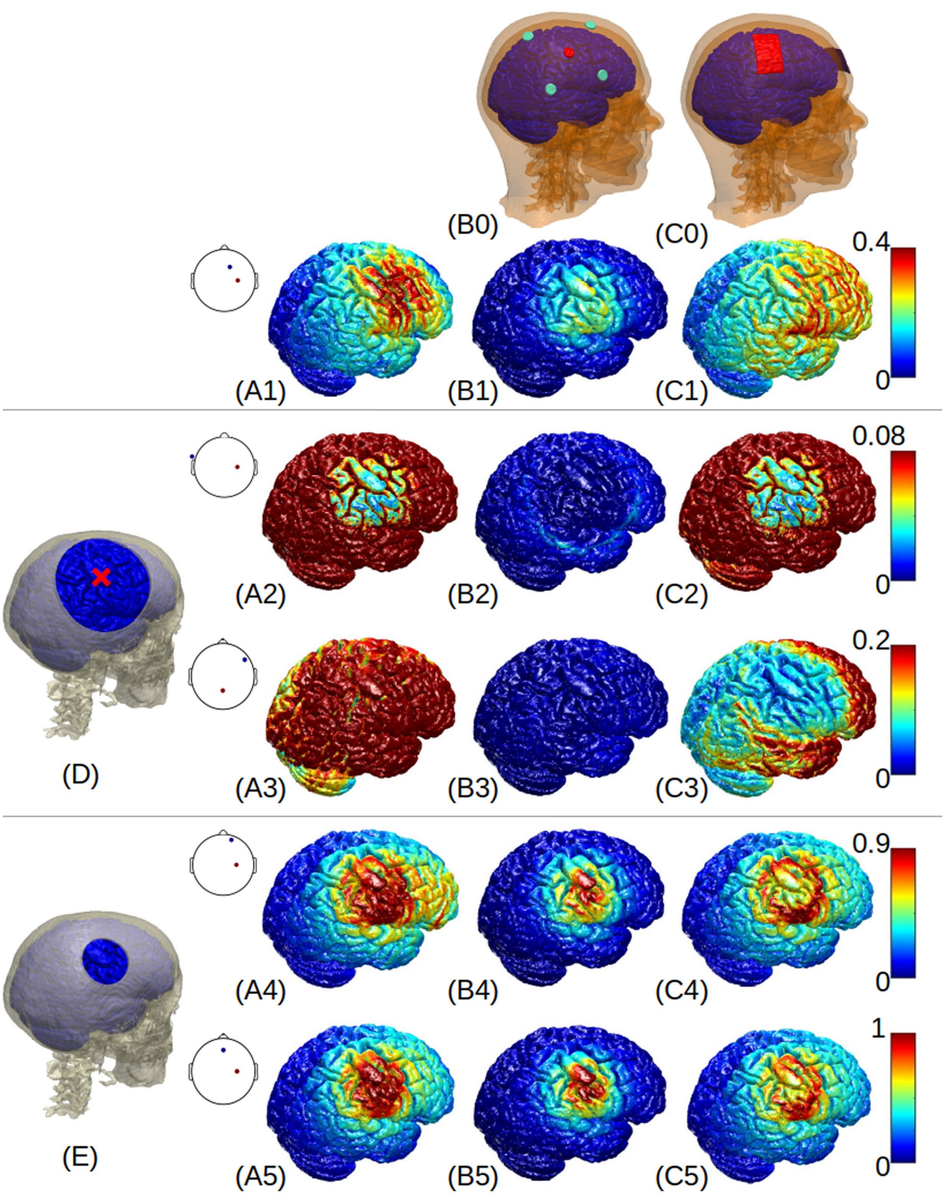

FIGURE 2
3D renderings of electric field around the right primary motor cortex (indicated by the red cross in **(D)**) generated by the normal-anatomy model **(A1-C1)**, large skull defect with titanium conductivity **(A2-C2)**, large defect with acrylic conductivity **(A3-C3)**, small defect with CSF conductivity **(A4-C4)**, and small defect with scar tissue **(A5-C5)**. Column **(A)** shows the results from optimized HD-tDCS with the optimal montages shown as insets at each panel; Columns **(B)** and **(C)** show the results from 4×1 and M1-SO montages, respectively. The skull defects are shown in panels **(D)** and **(E)**. A colormap for each row is shown on the right side, with a unit of V/m.

in stimulation intensities by skull defects are significant for all the four skull-defect models ($p < 0.01$).

Figure 2 visualizes the electric field distribution. Again we see that, compared to the normal anatomy, large skull defects with titanium or acrylic plates reduce the electric field at the right primary motor cortex, while small defects with CSF or scar tissue increase the electric field. This is true for all the montages. The small skull defect seems to increase the focality of the stimulation (Figures 2A4–C4, A5–C5), while the large defect seems to blur the stimulation focality (Figures 2A2–C2, A3–C3). The large titanium plate shunts away electric current (Figures 2A2, C2), and the large acrylic plate insulates the current (Figure 2B3).

When considering all the five locations (target and four shifted locations, Figure 3), Mann–Whitney U test showed that the boost by optimized stimulation is significant for all the cases ($p < 0.05$), except two scenarios: (1) for large defect with a titanium plate, the difference in stimulation intensity is not significant between optimized montage and the conventional M1-SO montage ($p = 0.42$, Figure 3B); (2) for small defect with scar tissue, optimized montage does not significantly increase the stimulation from 4×1 montage ($p = 0.06$, Figure 3E).

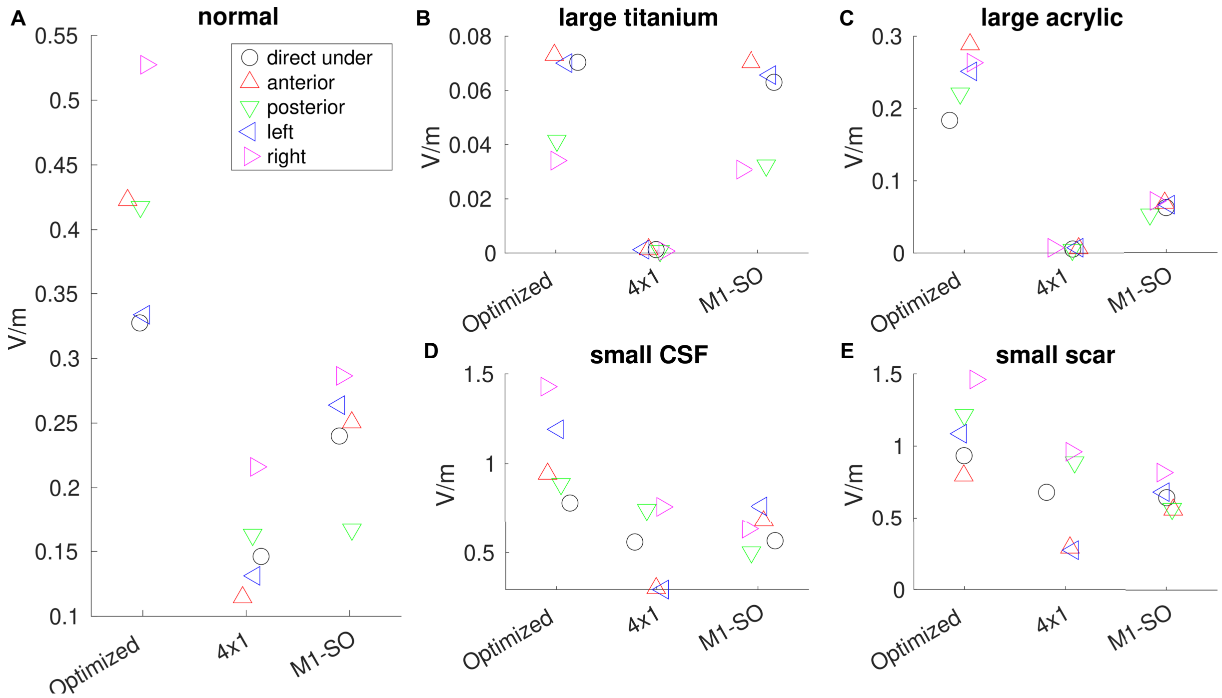

FIGURE 3
Electric field (V/m) read out from each model under different montages (optimized, 4×1, and M1-SO). **(A)** model with normal anatomy; **(B)** large skull defect with titanium conductivity; **(C)** large defect with acrylic conductivity; **(D)** small defect with CSF conductivity; **(E)** small defect with scar tissue. Electric fields are read out from the right primary motor cortex (circle marker) which is directly under the skull defect with MNI coordinates (48, −8, 50), as well as from locations anterior (up-pointing triangle), posterior (down-pointing triangle), left (left-pointing triangle), or right (right-pointing triangle) to the right primary motor cortex.

Discussion

To the best of our knowledge, this work is the first computational study to compare optimized HD-tDCS with conventional electrode montages on a head model with a skull defect. Existing work in the literature mostly focus on how the forward models of electroencephalogram (EEG) is affected by skull defects (Lau et al., 2016), skull segmentation (Lanfer et al., 2012), skull conductivity (Antonakakis et al., 2019b), and skull suture (McCann and Beltrachini, 2022). The only work we found that studied how skull defects affect optimized tDCS is Antonakakis et al. (2019a), but it only looked at small burr holes on the skull instead of skull plates. Our previous work (Datta et al., 2010) studied how skull defects affect the current flow but did not compare between un-optimized and optimized montage stimulating the cortex under the defect. Here we investigated how different sizes and conductivities of skull defects affect the current flow on the cortex beneath the defects, for both un-optimized and optimized stimulation. We found that large defects with titanium or acrylic plates significantly reduces the electric current reaching the target area beneath the defect by about 80%, while small defects with CSF or scar tissue significantly increases the stimulation by about 200%. Optimization always increases the stimulation intensities at the target area, no matter if the skull has a defect or not, even though this increase is not significant when a large defect with titanium plate or a small defect with scar tissue is present on the skull.

From the safety standpoint, the increase in electric field by 200% does not raise any potential theoretical safety issue. Using epicranial electrode stimulation in rats, Liebetanz and colleagues demonstrated that the threshold for tissue damage is at least two orders of magnitude away from the scalp charge density applied in humans (Liebetanz et al., 2009). Further, one may expect similar electric field deviation even in intact anatomy across individual heads (Datta et al., 2012). If the study objective requires maintaining the same electric field magnitude, a simple abating strategy would be to reduce the scalp injected current in proportion to the increase. Finally, optimized HD-tDCS has already been safely delivered to stroke subjects including cases where the cortical electric field was found to triple in comparison to conventional tDCS delivery (Dmochowski et al., 2013; Richardson et al., 2015).

To address the 80% decrement, a compelling clinical strategy would be to increase the scalp injected current. Higher intensity tDCS (i.e., delivery of 3–4 mA scalp current) has been recently shown to be safe (Workman et al., 2020; Hsu et al., 2023). While doubling the scalp intensity would only cover for the 50% decrement, what is clear is that scaling scalp current offers an option to get closer to what may be considered as "efficacious dose." Ultimately, clinicians would have to make the decision based on the potential risk–benefit, as tDCS may be one of the few interventions available considering the high vulnerability of patients with skull defects and plates.

Note that the strategies above are only general guidelines on tDCS on patients with skull defects or plates, as they are only based on the results from the single subject model we obtained here. Future modeling studies leveraging individualized geometry of the skull defects/plates obtained from patients MRI and CT scans will be needed to further provide personalized guidelines and plans on improving the outcomes from tDCS therapy.

Besides the average of 0.3 V/m increase of stimulation intensities at the target compared to un-optimized montages, the utility of optimization is best exemplified by targeting a region directly under the large skull acrylic plate. In general, the very low conductivity of acrylic makes it difficult to deliver meaningful electric field intensity directly underneath the plate (Datta et al., 2010). However, using optimized HD-tDCS, we are able to obtain ~0.18 V/m and as mentioned above, potentially deliver an efficacious dose by a simple scaling of scalp current. This is in stark contrast to the traditional montages, where the very low induced target electric field makes pursuing them unworthy.

There are some limitations of this work. First, we only modeled the skull defect at one single location which is mostly motivated by the clinical scenario (Fatima et al., 2019; Lambride et al., 2020). However, the same physics and optimization algorithm apply to defects at other locations on the skull. Second, we simplified the shape of the defect, while in reality the defect could have a complicated shape. Future work will collect image data from patients with skull defects to model the actual geometry of skull defects. Third, only one individual head was modeled. Considering inter-individual variability, future work will repeat the modeling process on more heads with skull defects to confirm if the results are replicable on other individual heads. Lastly, all the results were obtained from computational models, which need to be confirmed by experimental measurements following previous methodology (Huang et al., 2017).

Data availability statement

The original contributions presented in the study are included in the article/supplementary material, further inquiries can be directed to the corresponding author.

Author contributions

AG contributes to build the initial head model and draft of the manuscript. DT contributes to build the initial head model and editing of the manuscript. AD contributes to the concept of this work, and editing of the manuscript. YH contributes to the concept of this work, implementation of the model optimization, analysis of results, and editing of the manuscript. All authors contributed to the article and approved the submitted version.

Funding

YH is supported by grants from the National Institute of Health (NIH): 1R44MH126833-01A1 and Department of Education (ED): 91990022C0043.

Conflict of interest

AG, DT, AD, and YH were employed by Research and Development, Soterix Medical, Inc.

Publisher's note

References

Antonakakis, M., Rampp, S., Kellinghaus, C., Wolters, C. H., and Moeddel, G., (2019a). Individualized targeting and optimization of multi-channel transcranial direct current stimulation in drug-resistant epilepsy, in: 2019 IEEE 19th international conference on bioinformatics and bioengineering (BIBE). Presented at the 2019 IEEE 19th international conference on bioinformatics and bioengineering (BIBE), pp. 871–876.

Antonakakis, M., Schrader, S., Wollbrink, A., Oostenveld, R., Rampp, S., Haueisen, J., et al. (2019b). The effect of stimulation type, head modeling, and combined EEG and MEG on the source reconstruction of the somatosensory P20/N20 component. *Hum. Brain Mapp.* 40, 5011–5028. doi: 10.1002/hbm.24754

Auvichayapat, N., Rotenberg, A., Gersner, R., Ngodklang, S., Tiamkao, S., Tassaneeyakul, W., et al. (2013). Transcranial direct current stimulation for treatment of refractory childhood focal epilepsy. *Brain Stimulat.* 6, 696–700. doi: 10.1016/j.brs.2013.01.009

Bikson, M., Bulow, P., Stiller, J., Datta, A., Battaglia, F., Karnup, S., et al. (2008). Transcranial direct current stimulation for major depression: a general system for quantifying transcranial electrotherapy dosage. *Curr. Treat. Options Neurol.* 10, 377–385. doi: 10.1007/s11940-008-0040-y

Datta, A., Bansal, V., Diaz, J., Patel, J., Reato, D., and Bikson, M. (2009). Gyri –precise head model of transcranial DC stimulation: improved spatial focality using a ring electrode versus conventional rectangular pad. *Brain Stimulat.* 2, 201–207. doi: 10.1016/j.brs.2009.03.005

Datta, A., Bikson, M., and Fregni, F. (2010). Transcranial direct current stimulation in patients with skull defects and skull plates: high-resolution computational FEM study of factors altering cortical current flow. *NeuroImage* 52, 1268–1278. doi: 10.1016/j.neuroimage.2010.04.252

Datta, A., Truong, D., Minhas, P., Parra, L. C., and Bikson, M. (2012). Inter-individual variation during transcranial direct current stimulation and normalization of dose using MRI-derived computational models. *Front. Psychiatry Front. Res. Found.* 3:91. doi: 10.3389/fpsyt.2012.00091

Dmochowski, J. P., Datta, A., Bikson, M., Su, Y., and Parra, L. C. (2011). Optimized multi-electrode stimulation increases focality and intensity at target. *J. Neural Eng.* 8:046011. doi: 10.1088/1741-2560/8/4/046011

Dmochowski, J. P., Datta, A., Huang, Y., Richardson, J. D., Bikson, M., Fridriksson, J., et al. (2013). Targeted transcranial direct current stimulation for rehabilitation after stroke. *NeuroImage* 75, 12–19. doi: 10.1016/j.neuroimage.2013.02.049

Fatima, N., Al Rumaihi, G., Shuaib, A., and Saqqur, M. (2019). The role of decompressive Craniectomy in traumatic brain injury: a systematic review and meta-analysis. *Asian J. Neurosurg.* 14, 371–381. doi: 10.4103/ajns.AJNS_289_18

Fregni, F., Boggio, P. S., Santos, M. C., Lima, M., Vieira, A. L., Rigonatti, S. P., et al. (2006a). Noninvasive cortical stimulation with transcranial direct current stimulation in Parkinson's disease. *Mov. Disord.* 21, 1693–1702. doi: 10.1002/mds.21012

Fregni, F., Freedman, S., and Pascual-Leone, A. (2007). Recent advances in the treatment of chronic pain with non-invasive brain stimulation techniques. *Lancet Neurol.* 6, 188–191. doi: 10.1016/S1474-4422(07)70032-7

Fregni, F., Thome-Souza, S., Nitsche, M. A., Freedman, S. D., Valente, K. D., and Pascual-Leone, A. (2006b). A controlled clinical trial of cathodal DC polarization in patients with refractory epilepsy. *Epilepsia* 47, 335–342. doi: 10.1111/j.1528-1167.2006.00426.x

Guo, Z., Ding, W., Cao, D., Chen, Y., and Chen, J. (2022). Decompressive Craniectomy vs. Craniotomy Only for Traumatic Brain Injury: A Propensity-Matched Study of Long-Term Outcomes in Neuropsychology. *Front. Neurol.* 13:813140. doi: 10.3389/fneur.2022.813140

Hsu, G., Shereen, A. D., Cohen, L. G., and Parra, L. C. (2023). Robust enhancement of motor sequence learning with 4 mA transcranial electric stimulation. Brain Stimul. *Basic Transl. Clin. Res. Neuromodulation* 16, 56–67. doi: 10.1016/j.brs.2022.12.011

Huang, Y.A., (2020). *ROAST: A simulator for TES*. Available at: https://github.com/andypotatohy/roast/tree/master.

Huang, Y., Datta, A., Bikson, M., and Parra, L. C. (2019). Realistic volumetric-approach to simulate transcranial electric stimulation—ROAST—a fully automated open-source pipeline. *J. Neural Eng.* 16:056006. doi: 10.1088/1741-2552/ab208d

Huang, Y., Dmochowski, J. P., Su, Y., Datta, A., Rorden, C., and Parra, L. C. (2013). Automated MRI segmentation for individualized modeling of current flow in the human head. *J. Neural Eng.* 10:066004. doi: 10.1088/1741-2560/10/6/066004

Huang, Y., Liu, A. A., Lafon, B., Friedman, D., Dayan, M., Wang, X., et al. (2017). Measurements and models of electric fields in the in vivo human brain during transcranial electric stimulation. *elife* 6:e18834. doi: 10.7554/eLife.18834

Huang, Y., Thomas, C., Datta, A., and Parra, L.C., (2018). Optimized tDCS for targeting multiple brain regions: an integrated implementation, in: 2018 40th annual international conference of the IEEE engineering in medicine and biology society (EMBC). Presented at the 2018 40th annual international conference of the IEEE engineering in medicine and biology society (EMBC), pp. 3545–3548

Iacono, M. I., Neufeld, E., Akinnagbe, E., Bower, K., Wolf, J., Vogiatzis Oikonomidis, I., et al. (2015). MIDA: a multimodal imaging-based detailed anatomical model of the human head and neck. *PLoS One* 10:e0124126. doi: 10.1371/journal.pone.0124126

Jacobs, M. A., Zhang, Z. G., Knight, R. A., Soltanian-Zadeh, H., Goussev, A. V., Peck, D. J., et al. (2001). A model for multiparametric mri tissue characterization in experimental cerebral ischemia with histological validation in rat: part 1. *Stroke* 32, 943–949. doi: 10.1161/01.str.32.4.943

Kim, W.-S., Lee, K., Kim, S., Cho, S., and Paik, N.-J. (2019). Transcranial direct current stimulation for the treatment of motor impairment following traumatic brain injury. *J. NeuroEngineering Rehabil.* 16:14. doi: 10.1186/s12984-019-0489-9

Klem, G. H., Lüders, H. O., Jasper, H. H., and Elger, C. (1999). The ten-twenty electrode system of the international federation. The International Federation of Clinical Neurophysiology. *Electroencephalogr. Clin. Neurophysiol. Suppl.* 52, 3–6.

Lambride, C., Christodoulou, N., Michail, A., Vavourakis, V., and Stylianopoulos, T. (2020). Decompressive craniectomy of post-traumatic brain injury: an in silico modelling approach for intracranial hypertension management. *Sci. Rep.* 10:18673. doi: 10.1038/s41598-020-75479-7

Lanfer, B., Scherg, M., Dannhauer, M., Knösche, T. R., Burger, M., and Wolters, C. H. (2012). Influences of skull segmentation inaccuracies on EEG source analysis. *NeuroImage* 62, 418–431. doi: 10.1016/j.neuroimage.2012.05.006

Lau, S., Güllmar, D., Flemming, L., Grayden, D. B., Cook, M. J., Wolters, C. H., et al. (2016). Skull defects in finite element head models for source reconstruction from magnetoencephalography signals. *Front. Neurosci.* 10:10:141. doi: 10.3389/fnins.2016.00141

Liebetanz, D., Koch, R., Mayenfels, S., König, F., Paulus, W., and Nitsche, M. A. (2009). Safety limits of cathodal transcranial direct current stimulation in rats. *Clin. Neurophysiol. Off. J. Int. Fed. Clin. Neurophysiol.* 120, 1161–1167. doi: 10.1016/j.clinph.2009.01.022

McCann, H., and Beltrachini, L. (2022). Impact of skull sutures, spongiform bone distribution, and aging skull conductivities on the EEG forward and inverse problems. *J. Neural Eng.* 19:016014. doi: 10.1088/1741-2552/ac43f7

Meinzer, M., Darkow, R., Lindenberg, R., and Flöel, A. (2016). Electrical stimulation of the motor cortex enhances treatment outcome in post-stroke aphasia. *Brain* 139, 1152–1163. doi: 10.1093/brain/aww002

Richardson, J., Datta, A., Dmochowski, J., Parra, L. C., and Fridriksson, J. (2015). Feasibility of using high-definition transcranial direct current stimulation (HD-tDCS) to enhance treatment outcomes in persons with aphasia. *NeuroRehabilitation* 36, 115–126. doi: 10.3233/NRE-141199

Schwertfeger, J. L., Beyer, C., Hung, P., Ung, N., Madigan, C., Cortes, A. R., et al. (2023). A map of evidence using transcranial direct current stimulation (tDCS) to improve cognition in adults with traumatic brain injury (TBI). *Front. Neuroergonomics.* 4:1170473. doi: 10.3389/fnrgo.2023.1170473

Sekhar, L.N., and Fessler, R.G, (2016). *Atlas of neurosurgical techniques: Brain 2nd* Thieme, New York Stuttgart Delhi Rio de Janeiro.

Soltanian-Zadeh, H., Pasnoor, M., Hammoud, R., Jacobs, M. A., Patel, S. C., Mitsias, P. D., et al. (2003). MRI tissue characterization of experimental cerebral ischemia in rat. *J. Magn. Reson. Imaging JMRI* 17, 398–409. doi: 10.1002/jmri.10256

Sun, W., Dong, X., Yu, G., Shuai, L., Yuan, Y., and Ma, C. (2021). Transcranial direct current stimulation in patients after decompressive craniectomy: a finite element model to investigate factors affecting the cortical electric field. *J. Int. Med. Res.* 49:0300060520942112. doi: 10.1177/0300060520942112

Workman, C. D., Kamholz, J., and Rudroff, T. (2020). Increased leg muscle fatigability during 2 mA and 4 mA transcranial direct current stimulation over the left motor cortex. *Exp. Brain Res.* 238, 333–343. doi: 10.1007/s00221-019-05721-w

Ziesel, D., Nowakowska, M., Scheruebel, S., Kornmueller, K., Schäfer, U., Schindl, R., et al. (2023). Electrical stimulation methods and protocols for the treatment of traumatic brain injury: a critical review of preclinical research. *J. NeuroEng Rehabil.* 20:51. doi: 10.1186/s12984-023-01159-y

frontiers | Frontiers in Human Neuroscience

TYPE Original Research
PUBLISHED 26 October 2023
DOI 10.3389/fnhum.2023.1239114

EDITED BY
Johannes Vorwerk,
UMIT TIROL - Private University for Health Sciences and Health Technology, Austria

REVIEWED BY
Matthew Ryan Krause,
McGill University Health Centre, Canada
Florian H. Kasten,
UMR5549 Centre de Recherche Cerveau et Cognition (CerCo), France

*CORRESPONDENCE
Yu Huang
✉ andypotatohy@gmail.com

RECEIVED 12 June 2023
ACCEPTED 03 October 2023
PUBLISHED 26 October 2023

CITATION
Huang Y (2023) Visualizing interferential stimulation of human brains.
Front. Hum. Neurosci. 17:1239114.
doi: 10.3389/fnhum.2023.1239114

Visualizing interferential stimulation of human brains

Yu Huang*

Research and Development, Soterix Medical Inc., Woodbridge, NJ, United States

Introduction: Transcranial electrical stimulation (TES) is limited in focally stimulating deep-brain regions, even with optimized stimulation montages. Recently, interferential stimulation (IFS), also known as transcranial temporal interference stimulation (TI, TIS, or tTIS), has drawn much attention in the TES community as both computational and experimental studies show that IFS can reach deep-brain areas. However, the underlying electrodynamics of IFS is complicated and difficult to visualize. Existing literature only shows static visualization of the interfered electric field induced by IFS. These could result in a simplified understanding that there is always one static focal spot between the two pairs of stimulation electrodes. This static visualization can be frequently found in the IFS literature. Here, we aimed to systematically visualize the entire dynamics of IFS.

Methods and results: Following the previous study, the lead field was solved for the MNI-152 head, and optimal montages using either two pairs of electrodes or two arrays of electrodes were found to stimulate a deep-brain region close to the left striatum with the highest possible focality. We then visualized the two stimulating electrical currents injected with similar frequencies. We animated the instant electric field vector at the target and one exemplary off-target location both in 3D space and as a 2D Lissajous curve. We finally visualized the distribution of the interfered electric field and the amplitude modulation envelope at an axial slice going through the target location. These two quantities were visualized in two directions: radial-in and posterior–anterior.

Discussion: We hope that with intuitive visualization, this study can contribute as an educational resource to the community's understanding of IFS as a powerful modality for non-invasive focal deep-brain stimulation.

KEYWORDS

interferential stimulation, temporal interference, visualization, computational modeling, transcranial electric stimulation

Introduction

As a non-invasive brain stimulation method, transcranial electrical stimulation (TES) has been shown to improve cognitive functions and help treat some neurological diseases such as major depression (Bikson et al., 2008), epilepsy (Fregni et al., 2006b; Auvichayapat et al., 2013), Parkinson's disease (Fregni et al., 2006a), chronic pain (Fregni et al., 2007), and stroke (Meinzer et al., 2016). However, TES is not able to focally stimulate deep-brain regions, even with optimized stimulation montages (Dmochowski et al., 2011; Huang and Parra, 2019). Recently, interferential stimulation (IFS), also known as transcranial temporal interference stimulation (TI, TIS, or tTIS), has drawn much attention in the TES community as both computational and experimental studies show that IFS can reach deep-brain areas (Grossman et al., 2017; Huang et al., 2020; Huang and Datta, 2021; Violante et al., 2022). When optimized, it can achieve higher focality than conventional TES (Huang et al., 2020). However, the underlying electrodynamics of IFS is complicated and difficult to visualize. This is because the interfered electric field is amplitude modulated and contains both a fast-oscillating carrier signal in the kilohertz range and a slowly oscillating modulation envelope in ~10 Hz. The premise of IFS is that neurons only respond to slower oscillation due to their property of low-pass filtering (Grossman et al., 2017). To the best of our knowledge, except for a conference poster that acknowledges the rotational property of the interfered electric field (Turovets et al., 2018), existing literature only shows static visualization of the interfered electric field induced by IFS (Grossman et al., 2017; Rampersad et al., 2019; Lee et al., 2020; Esmaeilpour et al., 2021; von Conta et al., 2021; Violante et al., 2022). These simplified visualizations sometimes may bring misunderstanding of the underlying physics to the research community. For example, the graphical abstract of Grossman et al. (2017) is only a schematic that fails to illustrate the actual dynamics, which may lead one to believe that there is only one static focal spot between the two pairs of stimulation electrodes (**Figure 1A**). This can be frequently found in the IFS literature (Mirzakhalili et al., 2020; von Conta et al., 2021; Piao et al., 2022; Violante et al., 2022). See **Figure 1** for a compilation of these visualizations of IFS. Although the electric field was modeled in these studies using state-of-the-art software packages, these schematic illustrations do not represent the complete dynamics. Here, we aimed to visualize the entire dynamic process of IFS including both the fast-oscillating carrier signals and the slowly oscillating modulation envelope, in the hope of contributing to the community with vivid educational resources on IFS as a powerful modality for non-invasive focal deep-brain stimulation.

Materials and methods

Construction of the head model

The forward head model was built on the ICBM152 (v6) template from the Montreal Neurological Institute (MNI, Montreal, Canada) (Mazziotta et al., 2001; Grabner et al., 2006), following the previously published methods (Huang et al., 2013). Briefly, the ICBM152 (v6) template magnetic resonance image (MRI) was segmented by the New Segment toolbox (Ashburner and Friston, 2005) in Statistical Parametric Mapping 8 (SPM8, Wellcome Trust Centre for Neuroimaging, London, UK) implemented in MATLAB (MathWorks, Natick, MA, USA). Segmentation errors such as discontinuities in the cerebrospinal fluid (CSF) and noisy voxels were corrected first by a customized Matlab script (Huang et al., 2013) and then by hand in interactive segmentation software Simpleware ScanIP (Simpleware Ltd., Exeter, UK). As TES modeling work has demonstrated the need to include the entire head down to the neck for realistic current flow, in particular in deep-brain areas and the brainstem (Huang et al., 2013), the field of view (FOV) of the ICBM152 (v6) MRI was extended down to the neck by registering and reslicing the standard head published in Huang et al. (2013) to the voxel space of ICBM152 (see Huang et al., 2016 for details). High-definition electrodes (6 mm radius) following the convention of the standard 10–10 international system (Klem et al., 1999) were placed on the scalp surface by a custom MATLAB script (Huang et al., 2013). Two rows of electrodes below the ears and four additional electrodes around the neck were also placed to allow for the targeting of deeper cortical areas and the use of distant reference electrodes in TES. A total of 93 electrodes were placed. A finite element model (FEM, Logan, 2007) was generated from the segmentation data by the ScanFE module in ScanIP. Laplace's equation was then solved (Griffiths, 1999) in Abaqus 6.11 (SIMULIA, Providence, RI, USA) for the electric field distribution in the head. With one fixed reference electrode Iz as cathode, the electric field was solved for all other 92 electrodes with 1 mA current injected for each of them, giving 92 solutions for electric field distribution representing the forward model of the ICBM152 head.

Optimization of the IFS montage

We employed previously published methods to optimize the montages for IFS. Specifically, we optimized the focality of modulation depth (MD) along the radial-in direction (Eq. 3 below) at the target with either two pairs of electrodes or two arrays of electrodes. Briefly, for the two pairs of electrodes, the optimization simply searches for the best two pairs that give the highest MD focality (Lee et al., 2020; Huang and Datta, 2021); for the two arrays of electrodes, the algorithm implements sequential quadratic programming to maximize the MD at the target while minimizing the energy of MD at the off-target areas (Huang et al., 2020). The target we picked is a deep location close to the left striatum with MNI coordinates of [−16, 10, 2] (Hampshire et al., 2019).

Visualization of IFS dynamics

Suppose the optimized montages for the two stimulating currents are $\mathbf{s}_1\sin(\omega_1 t)$ and $\mathbf{s}_2\sin(\omega_2 t + \pi)$, where $\mathbf{s}_1$ and $\mathbf{s}_2$ are vectors of length 93 that encode the distribution of the current sources for each frequency ω_1 and ω_2, respectively. Here, we choose a phase difference of 180 degrees simply for visualization purposes. The total electric field in the brain induced by these two stimulating currents is

$$\mathbf{E}(\mathbf{r}, t) = \sin(\omega_1 t)^{*}\mathbf{A}(\mathbf{r})\mathbf{s}_1 + \sin(\omega_2 t + \pi)^{*}\mathbf{A}(\mathbf{r})\mathbf{s}_2, \qquad (1)$$

where $\mathbf{A}(\mathbf{r})$ is the forward model of TES obtained above [also known as the lead field in the literature of EEG source localization (Dmochowski et al., 2017)]. $\mathbf{r}$ stands for any spatial location in the brain, and t is the time. The envelope of the interfering signal $\mathbf{E}(\mathbf{r}, t)$ along a specific direction $\mathbf{d}(\mathbf{r})$ can be computed by the absolute value of the analytic signal:

$$|\mathbf{E}^{\sim}(\mathbf{r}, t)| = |\mathbf{d}(\mathbf{r})^{T}\mathbf{E}(\mathbf{r}, t) + jH[\mathbf{d}(\mathbf{r})^{T}\mathbf{E}(\mathbf{r}, t)]|, \qquad (2)$$

where j is the unit imaginary number, H[] is the Hilbert transform, and $\mathbf{d}(\mathbf{r})$ is a unit vector with $|\mathbf{d}(\mathbf{r})| = 1$. The MD is defined as the

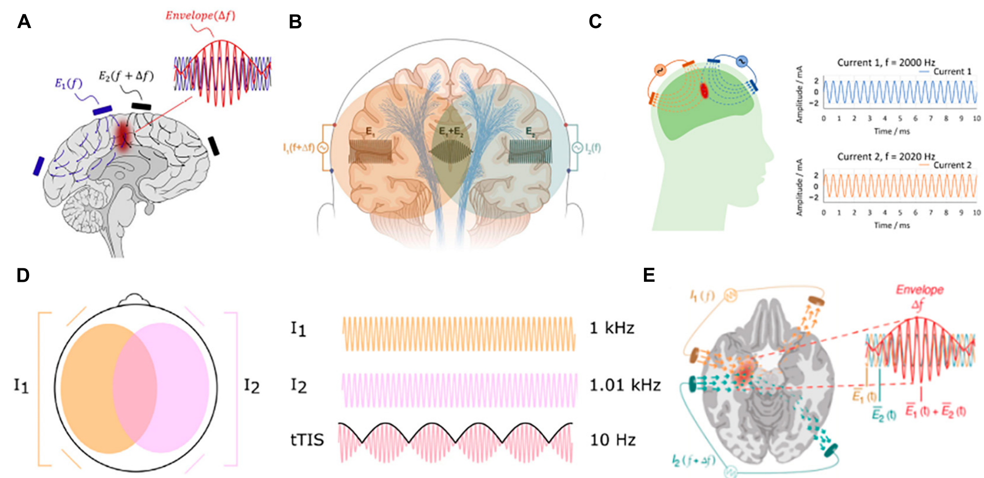

FIGURE 1
Compilation of commonly used visualization of IFS in the literature. **(A)** Grossman et al. (2017); **(B)** Mirzakhalili et al. (2020); **(C)** Piao et al. (2022); **(D)** von Conta et al. (2021); **(E)** Violante et al. (2022).

depth of this envelope (Huang and Parra, 2019), i.e.,

$$\mathrm{MD}(\mathbf{r}) = \max_t(|\mathbf{E}^{\sim}(\mathbf{r},t)|) - \min_t(|\mathbf{E}^{\sim}(\mathbf{r},t)|) = 2\min(|\mathbf{d}(\mathbf{r})^{\mathrm{T}}\mathbf{A}(\mathbf{r})\mathbf{s}_1|, |\mathbf{d}(\mathbf{r})^{\mathrm{T}}\mathbf{A}(\mathbf{r})\mathbf{s}_2|). \quad (3)$$

Note $\mathrm{MD}(\mathbf{r})$ is a static value that does not change with time and is the quantity we optimize (Huang et al., 2020; Huang and Datta, 2021). For visualization purposes, here we are interested in the instantaneous value of the MD, i.e.,

$$\mathrm{MD}(\mathbf{r},t) = |\mathbf{E}^{\sim}(\mathbf{r},t)| - \min_t(|\mathbf{E}^{\sim}(\mathbf{r},t)|). \quad (4)$$

We also visualize the dynamics of the two stimulating currents, and the dynamics of the total electric field $\mathbf{E}(\mathbf{r},t)$ in 3D space as well as along a specific direction $\mathbf{d}(\mathbf{r})^T\mathbf{E}(\mathbf{r},t)$. We also visualize the distributions of $\mathbf{d}(\mathbf{r})^T\mathbf{E}(\mathbf{r},t)$ and $\mathrm{MD}(\mathbf{r},t)$ in a 2D brain slice. We visualize all these quantities for two specific directions $\mathbf{d}(\mathbf{r})$: radial-in (pointing to the center of the brain, i.e., MNI coordinates of [0, 0, 0]) and posterior–anterior (PA, pointing to the front of the head), and at both the target location (left striatum) and a randomly chosen off-target location. We made animations to show the dynamics in action. For visualization purposes, we chose the two frequencies of the two stimulating currents to be only 10 Hz and 12 Hz and animated the dynamics for only 1 s.

Results

Visualization of electric field from two pairs of electrodes

Figure 2 shows a snapshot of the dynamical process of IFS at a time point of $t = 0.272$ s, indicated by the black vertical lines in panels A, B, E, and F. The optimal montage of two pairs of electrodes shown in panels A and B is determined by exhaustively searching through all the possible combinations from the 93 candidate electrodes (gray circles in panels A and B) (Lee et al., 2020; Huang and Datta, 2021). The optimal two pairs of electrodes are shown in **Table 1**. This optimal montage generates a maximal focal stimulation in terms of the MD as shown in panel I for the target location shown as a black circle.

The frequencies of the two stimulating currents are set as 10 Hz and 12 Hz for visualization purposes (**Figures 2A, B**). Each of these two currents induces an electric field (E-field) in the brain, and the two E-fields interfere with each other to generate a total E-field represented by the blue arrows in panels C and D. Due to the superposition of the two E-field vectors induced by the two stimulating currents, the total field always resides in the blue plane spanned by them, and the head of the total field traces a Lissajous curve in the blue plane. See **Figure 3** for a zoomed-in version of the Lissajous curve, and the path the total field follows on that curve; also see **Supplementary Video 1** for the complete animation. Unlike IFS, the conventional transcranial stimulation using alternating current generates an E-field that only oscillates along a 1D line, without any rotation of the field vector that traces a Lissajous curve in the 3D space.

Here, we are particularly interested in the projection of the total E-field along two exemplary directions: (1) the radial-in direction pointing to the center of the brain and (2) the posterior–anterior (PA) direction pointing toward the front of the head. These two directions are represented by the red and green lines, respectively, in **Figures 2C, D** and zoomed-in in **Figure 3**, where the projected E-fields are depicted by the red and green arrows. The alternating E-fields along these two directions are shown in **Figures 2E, F**, for the target and off-target locations shown in **Figure 2G** as a black circle and cross, respectively. The distributions of the instant E-field along radial and PA directions in an axial slice through the target location are shown in **Figures 2G, H**. The MD is the amplitude of the slowly oscillating envelope of the total E-field (e.g., black dashed line in **Figure 2E**). The distribution of the instant MD along radial and PA directions in the axial slice is in **Figures 2I, J**.

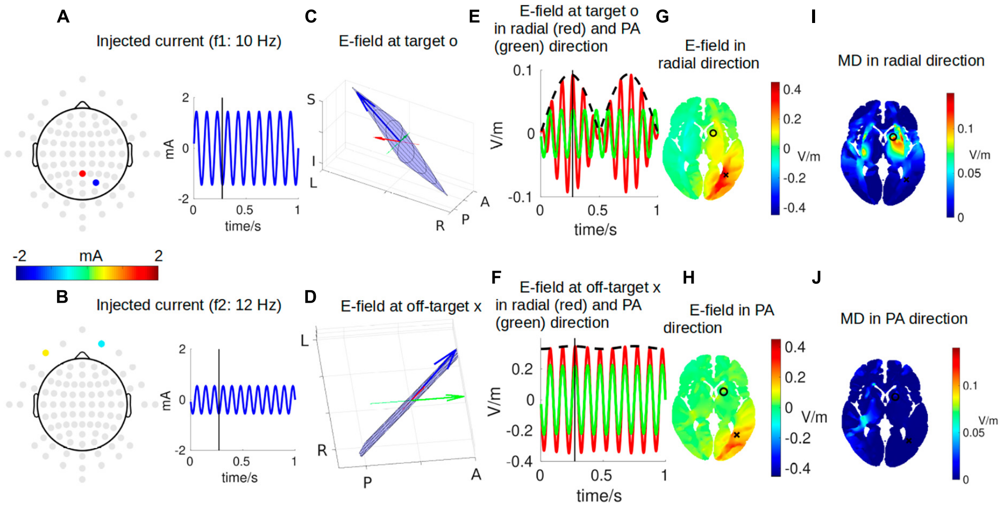

FIGURE 2
One instant in time during IFS stimulating the target location close to the left striatum with MNI coordinates of [−16, 10, 2] [indicated by a black circle in panel **(G)**]. **(A,B)** The optimal montages of two pairs of electrodes stimulating the target with the highest possible focality [as shown in panel **(I)**]. Note the topoplots in panels **(A,B)** show the amplitudes of the sinusoidal currents injected as shown by the right (gray circles are all candidate electrodes for the algorithm to consider when searching for the optimal montage). **(C,D)** The electric field (E-field) vector in 3D space (blue arrow). The head of the blue arrow moves in space and draws a Lissajous curve (black curve) in the 2D plane (blue plane) spanned by the two E-fields individually induced by the two stimulating currents. The orientation of the modeled head is indicated by letters on the three axes (L, left; R, right; P, posterior; A, anterior; I, inferior; S, superior). See Figure 3 for a zoomed-in version for more details. Specifically, we are interested in the E-field projected onto radial-in direction (red arrow) and posterior–anterior (PA) direction (green arrow). These three arrows are constantly moving, and panels **(C,D)** show the snapshots at the instant indicated by the black vertical lines in panels **(A,B,E,F)**. **(E)** E-field at the target along the radial direction (red) and PA direction (green). The black dashed line represents the envelope that defines the modulation depth (MD). **(F)** Same as **(E)** but for E-field at an off-target location indicated by a black cross in panel G. **(G,H)** Distribution of E-field along radial and PA directions in an axial slice through the target (black circle) and off-target (black cross) locations. **(I,J)** Distribution of MD along radial and PA directions in the same axial slice. Panels **(G,H,I,J)** are constantly changing, and shown here again are the snapshots at the instant indicated by the black vertical lines in panels **(A,B,E,F)**. For the complete animation, please see Supplementary Video 1.

TABLE 1 **Optimal montages targeting the left striatum with MNI coordinates of [−16, 10, 2] using either two pairs of electrodes (Huang and Datta, 2021) or two arrays of electrodes (Huang et al., 2020).**

	Frequency 1	Frequency 2
Two pairs of electrodes	Pz (1.45), PO4 (−1.45)	Ex15 (0.55), Ex18 (−0.55)
Two arrays of electrodes	T8 (0.357), Ex18 (0.170), F4 (0.169), FC6 (0.126), Fp2 (0.092), Ex10 (0.052), FC4 (0.030), PO4 (0.004), AF7 (−0.002), F3 (−0.002), Ex3 (−0.003), FT9 (−0.004), AF3 (−0.006), FC1 (−0.007), C2 (−0.008), Cz (−0.010), Nk2 (−0.012), C4 (−0.014), Exz (−0.024), P8 (−0.029), CP6 (−0.075), F8 (−0.804)	CP5 (0.875), TP8 (0.027), Fp2 (0.022), FT10 (0.018), AF4 (0.018), FC6 (0.016), F4 (0.011), T8 (0.007), C6 (0.002), AF8 (0.002), F6 (0.001), CP4 (−0.006), F1 (−0.020), CP2 (−0.059), O10 (−0.062), C2 (−0.080), P4 (−0.084), Fz (−0.097), AF3 (−0.115), Exz (−0.185), Ex11 (−0.291)

Numbers in the parentheses are the amplitudes (in mA) of the sinusoidal currents, with positive and negative values meaning currents going into and out of the head, respectively. Ex# electrodes are from the two additional rows of electrodes below the ears, and Nk2 is the electrode placed on the back of the neck (see Huang et al., 2013, for details).

To summarize the relationship between different dynamics, the individual stimulating currents (Figures 2A, B) induce two fast-oscillating E-fields in the brain. These two E-fields interfere and generate a total E-field at the target location (blue arrow in Figure 2C). Projection of this E-field along the radial-in direction (red arrow in Figure 2C) traces the red waveform shown in Figure 2E, whose envelope (black dashed wave in Figure 2E) oscillates slowly and generates neuronal effects.

Note that the intensity of the instant E-field in the radial direction is weaker at the target than that at the off-target (0.09 vs. 0.34 V/m; Figure 2G), but the instant MD at the target is much higher than that at the off-target location (0.09 vs. 0.02 V/m; Figure 2I). This can also be seen from the red wave in Figure 2F whose envelope does not oscillate that much compared to that in Figure 2E. In fact, the MD is determined by the weaker of the two E-fields individually induced by the two stimulating currents (Eq. 3). At the off-target location, even though the total E-field is 0.34 V/m, the two stimulating currents individually induce an E-field of 0.33 V/m and 0.01 V/m. Therefore, the MD is very small. On the other hand, at the target location, the two stimulating currents individually induce an E-field of 0.04 V/m and 0.05 V/m, leading to a higher MD of 0.09 V/m (as seen in the black dashed line in Figure 2E) even though the instant E-field is smaller than that at the off-target location. We also note that we specifically optimized the MD along the radial direction (Figure 2I), and thus, the MD in the PA direction is weak for both the target and off-target locations (green waves in Figures 2E, F; also see Figure 2J). The animation (Supplementary Video 1) shows the entire dynamics. The E-field oscillates slowly in the animation as the frequencies of the system are only 10–12 Hz. In reality, the oscillation is much faster when the injected currents are in the 1 kHz range; that is, the carrier signal will oscillate at the kHz range, and the envelope oscillates at the ∼10 Hz range.

Note the MD in Figures 2I, J is usually illustrated as hotspots of stimulation right in the middle of the two pairs of electrodes in the literature (Figure 1). We found, however, that the hotspot

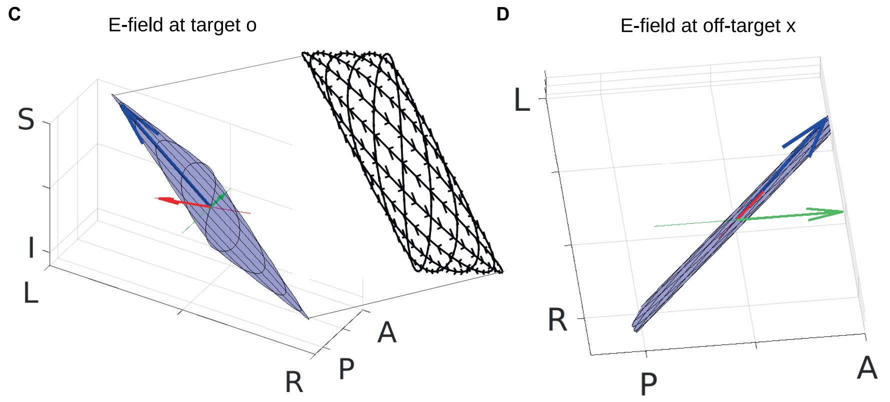

FIGURE 3
Zoom-in of panels **(C,D)** in Figure 2. Total electric field (E-field) is indicated by the blue arrow. Radial and posterior–anterior (PA) directions are indicated by the red and green lines, respectively, with projections of the E-field onto these two directions shown by red and green arrows. Blue planes represent the planes where the total E-field resides, and black curves are Lissajous curves drawn by the head of the moving blue arrows. The inset of panel **(C)** shows the Lissajous curves viewed in the PA direction (not drawn to scale), with small black arrows on the curves indicating the path of the head of the moving blue arrow. See **Supplementary Video 1** for the entire dynamics. Orientation of the modeled head is indicated by letters on the three axes (L, left; R, right; P, posterior; A, anterior; I, inferior; S, superior).

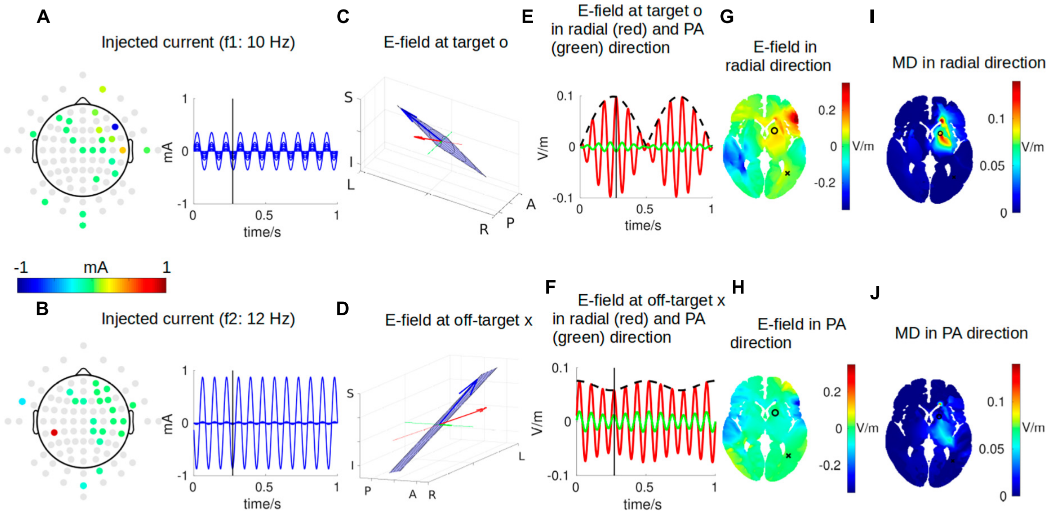

FIGURE 4
Same as Figure 2 but for two arrays of electrodes instead of two pairs of electrodes for focally stimulating the target. See **Supplementary Video 2** for the entire animation.

(Figure 2I) does not exactly lie in the middle of the two pairs of electrodes, and there is more than one hotspot in the brain (e.g., the smaller hotspot in the left hemisphere in Figure 2I). In fact, the location of the hotspot cannot be intuitively determined from the electrode montage, and we employed numerical search to find the montage that gives the most focal MD at the predefined target. Also, the MD is sensitive to the specific direction as shown in Figures 2I, J.

Visualization of electric field from two arrays of electrodes

A similar snapshot at the same time point of $t = 0.272$ s for two arrays of stimulating electrodes is shown in Figure 4. The array solutions are obtained using algorithms presented in Huang et al. (2020) to maximize the focality of MD along the radial-in direction at the target. The optimal two arrays of electrodes are shown in Table 1. When these montages are used, we achieve better focality of MD in radial-in direction at the target than that from using two pairs of electrodes. In fact, the smaller hotspot in the left hemisphere shown in Figure 2I disappears with array solutions shown in Figure 4I. Quantitatively, at a similar level of instant MD at the target (0.09 V/m), the focality of the MD is 3.72 cm from two arrays of electrodes (Figure 4I) and 4.93 cm from two pairs of electrodes (Figure 2I). Here, focality is defined as the cubic root of the volume in the brain that achieves over half of the MD at the target location (Huang and Parra, 2019), and thus, smaller number means higher focality.

Discussion

This study attempts to give a complete visualization of the complicated dynamics of the underlying physics in IFS, including both the fast-oscillating carrier signals and the slowly oscillating modulation envelope as only static figures are available in the literature illustrating the core concept behind IFS. As the animation shows, the instant E-field at every single point in the brain oscillates and rotates fast in the 3D space. The premise of IFS is that neurons only respond to the slower oscillations of the envelope of these fast-changing E-fields, which is quantified by the modulation depth (MD) (Grossman et al., 2017; Huang and Parra, 2019). The hotspot of the MD does not exactly lie in the middle between the two pairs of stimulating electrodes as shown commonly in the literature. The animation shows how the MD is generated from the E-field and how it depends on the directions of interest. It also shows that the locations of the hotspot of MD cannot be intuitively determined, and more than one hotspot may present in the brain, with more focal hotspots if two arrays of electrodes are used. Note that the two directions we chose here (radial-in and posterior–anterior) are only exemplary for the purpose of visualization. The actual stimulation effects are highly correlated with the directions of the electric field relative to the cortical sheet (Rahman et al., 2013). However, the same physics applies to any direction of the electric field (Huang and Parra, 2019).

To the best of our knowledge, only a recent publication on IFS visualizes the complicated dynamics, but still in static figures (Wang et al., 2023). Here, we further show everything in action to give the readers a complete picture. We note that as the instant E-field rotates in the 3D space, it generates different strengths of MD along different directions. Existing optimization algorithms for IFS (Huang et al., 2020; Lee et al., 2020) only consider the spatial focality of the MD in a predefined direction, while ignoring the specificity of the modulation in different directions. In other words, it does not consider whether the optimal montage will also generate some strength of MD in directions other than the one being optimized that may modulate neurons in those directions. Future computational study will improve this by adding direction specificity to the cost function being optimized that only encodes spatial focality. In addition, multi-scale models that incorporate neuronal geometry are needed to investigate how the MD in different directions affects neurons at the target location (Wang et al., 2023). Finally, all these computational results of optimal IFS montages need to be validated by experimental recordings.

Data availability statement

The original contributions presented in this study are included in this article/**Supplementary material**, further inquiries can be directed to the corresponding author.

Author Contributions

The author confirms being the sole contributor of this work and has approved it for publication.

Funding

YH was supported by the grants from National Institute of Health (NIH): 1R44MH126833-01A1 and Department of Education (ED): 91990022C0043.

Conflict of interest

YH was employed by Soterix Medical Inc.

Publisher's note

Supplementary material

The Supplementary Material for this article can be found online at: https://www.frontiersin.org/articles/10.3389/fnhum.2023.1239114/full#supplementary-material

SUPPLEMENTARY VIDEO 1
Full animation of the IFS dynamics stimulating the target location with two pairs of electrodes. Please refer to **Figure 2** in the main manuscript for detailed explanation of each panel.

SUPPLEMENTARY VIDEO 2
Full animation of the IFS dynamics stimulating the target location with two arrays of electrodes. Please refer to **Figure 4** in the main manuscript for detailed explanation of each panel.

References

Ashburner, J., and Friston, K. J. (2005). Unified segmentation. *Neuroimage* 26, 839–851. doi: 10.1016/j.neuroimage.2005.02.018

Auvichayapat, N., Rotenberg, A., Gersner, R., Ngodklang, S., Tiamkao, S., Tassaneeyakul, W., et al. (2013). Transcranial direct current stimulation for treatment of refractory childhood focal epilepsy. *Brain Stimulat.* 6, 696–700. doi: 10.1016/j.brs.2013.01.009

Bikson, M., Bulow, P., Stiller, J., Datta, A., Battaglia, F., Karnup, S., et al. (2008). Transcranial direct current stimulation for major depression: A general system for quantifying transcranial electrotherapy dosage. *Curr. Treat. Options Neurol.* 10, 377–385. doi: 10.1007/s11940-008-0040-y

Dmochowski, J. P., Datta, A., Bikson, M., Su, Y., and Parra, L. C. (2011). Optimized multi-electrode stimulation increases focality and intensity at target. *J. Neural Eng.* 8:046011. doi: 10.1088/1741-2560/8/4/046011

Dmochowski, J. P., Koessler, L., Norcia, A. M., Bikson, M., and Parra, L. C. (2017). Optimal use of EEG recordings to target active brain areas with transcranial electrical stimulation. *Neuroimage* 157, 69–80. doi: 10.1016/j.neuroimage.2017.05.059

Esmaeilpour, Z., Kronberg, G., Reato, D., Parra, L. C., and Bikson, M. (2021). Temporal interference stimulation targets deep brain regions by modulating neural oscillations. *Brain Stimulat.* 14, 55–65. doi: 10.1016/j.brs.2020.11.007

Fregni, F., Boggio, P. S., Santos, M. C., Lima, M., Vieira, A. L., Rigonatti, S. P., et al. (2006a). Noninvasive cortical stimulation with transcranial direct current stimulation in Parkinson's disease. *Mov. Disord.* 21, 1693–1702. doi: 10.1002/mds.21012

Fregni, F., Freedman, S., and Pascual-Leone, A. (2007). Recent advances in the treatment of chronic pain with non-invasive brain stimulation techniques. *Lancet Neurol.* 6, 188–191. doi: 10.1016/S1474-4422(07)70032-7

Fregni, F., Thome-Souza, S., Nitsche, M. A., Freedman, S. D., Valente, K. D., and Pascual-Leone, A. (2006b). A controlled clinical trial of cathodal DC polarization in patients with refractory epilepsy. *Epilepsia* 47, 335–342. doi: 10.1111/j.1528-1167.2006.00426.x

Grabner, G., Janke, A. L., Budge, M. M., Smith, D., Pruessner, J., and Collins, D. L. (2006). Symmetric atlasing and model based segmentation: An application to the hippocampus in older adults. *Med. Image Comput. Comput. Assist. Interv.* 9, 58–66.

Griffiths, D. J. (1999). *Introduction to electrodynamics*, 3rd Edn. Upper Saddle River, NJ: Prentice Hall.

Grossman, N., Bono, D., Dedic, N., Kodandaramaiah, S. B., Rudenko, A., Suk, H.-J., et al. (2017). Noninvasive deep brain stimulation via temporally interfering electric fields. *Cell* 169, 1029–1041.e16. doi: 10.1016/j.cell.2017.05.024

Hampshire, A., Daws, R. E., Neves, I. D., Soreq, E., Sandrone, S., and Violante, I. R. (2019). Probing cortical and sub-cortical contributions to instruction-based learning: Regional specialisation and global network dynamics. *Neuroimage* 192, 88–100. doi: 10.1016/j.neuroimage.2019.03.002

Huang, Y., and Datta, A. (2021). "Comparison of optimized interferential stimulation using two pairs of electrodes and two arrays of electrodes," in *Presented at the 2021 43rd Annual International Conference of the IEEE Engineering in Medicine & Biology Society (EMBC)*, Mexico, 4180–4183. doi: 10.1109/EMBC46164.2021.9631012

Huang, Y., and Parra, L. C. (2019). Can transcranial electric stimulation with multiple electrodes reach deep targets? *Brain Stimulat.* 12, 30–40. doi: 10.1016/j.brs.2018.09.010

Huang, Y., Datta, A., and Parra, L. C. (2020). Optimization of interferential stimulation of the human brain with electrode arrays. *J. Neural Eng.* 17:036023. doi: 10.1088/1741-2552/ab92b3

Huang, Y., Dmochowski, J. P., Su, Y., Datta, A., Rorden, C., and Parra, L. C. (2013). Automated MRI segmentation for individualized modeling of current flow in the human head. *J. Neural Eng.* 10:066004. doi: 10.1088/1741-2560/10/6/066004

Huang, Y., Parra, L. C., and Haufe, S. (2016). The New York Head—A precise standardized volume conductor model for EEG source localization and tES targeting. *Neuroimage* 140, 150–162. doi: 10.1016/j.neuroimage.2015.12.019

Klem, G. H., Lüders, H. O., Jasper, H. H., and Elger, C. (1999). The ten-twenty electrode system of the International Federation. The International Federation of Clinical Neurophysiology. *Electroencephalogr. Clin. Neurophysiol. Suppl.* 52, 3–6.

Lee, S., Lee, C., Park, J., and Im, C.-H. (2020). Individually customized transcranial temporal interference stimulation for focused modulation of deep brain structures: A simulation study with different head models. *Sci. Rep.* 10:11730. doi: 10.1038/s41598-020-68660-5

Logan, D. L. (2007). *A First Course in the Finite Element Method*. Boston, MA: Cengage Learning.

Mazziotta, J., Toga, A., Evans, A., Fox, P., Lancaster, J., Zilles, K., et al. (2001). A four-dimensional probabilistic atlas of the human brain. *J. Am. Med. Inform. Assoc.* 8, 401–430.

Meinzer, M., Darkow, R., Lindenberg, R., and Flöel, A. (2016). Electrical stimulation of the motor cortex enhances treatment outcome in post-stroke aphasia. *Brain* 139, 1152–1163. doi: 10.1093/brain/aww002

Mirzakhalili, E., Barra, B., Capogrosso, M., and Lempka, S. F. (2020). Biophysics of temporal interference stimulation. *Cell Syst.* 11, 557–572.e5. doi: 10.1016/j.cels.2020.10.004

Piao, Y., Ma, R., Weng, Y., Fan, C., Xia, X., Zhang, W., et al. (2022). Safety evaluation of employing temporal interference transcranial alternating current stimulation in human studies. *Brain Sci.* 12:1194. doi: 10.3390/brainsci12091194

Rahman, A., Reato, D., Arlotti, M., Gasca, F., Datta, A., Parra, L. C., et al. (2013). Cellular effects of acute direct current stimulation: Somatic and synaptic terminal effects. *J. Physiol.* 591, 2563–2578. doi: 10.1113/jphysiol.2012.247171

Rampersad, S., Roig-Solvas, B., Yarossi, M., Kulkarni, P. P., Santarnecchi, E., Dorval, A. D., et al. (2019). Prospects for transcranial temporal interference stimulation in humans: A computational study. *Neuroimage* 202:116124. doi: 10.1016/j.neuroimage.2019.116124

Turovets, S., Corazza, M. F., Tucker, D., and Luu, P. (2018). "Temporal interference transcranial electrical stimulation in humans: Actual doses and steerability," in *Poster at the NYC Neuromodulation Conference and NANS Summer Series*, New York, NY.

Violante, I. R., Alania, K., Cassarà, A. M., Neufeld, E., Acerbo, E., Carron, R., et al. (2022). Non-invasive temporal interference electrical stimulation of the human hippocampus. *BioRxiv [Preprint]* doi: 10.1101/2022.09.14.507625

von Conta, J., Kasten, F. H., Æurèiæ-Blake, B., Aleman, A., Thielscher, A., and Herrmann, C. S. (2021). Interindividual variability of electric fields during transcranial temporal interference stimulation (tTIS). *Sci. Rep.* 11:20357. doi: 10.1038/s41598-021-99749-0

Wang, B., Aberra, A. S., Grill, W. M., and Peterchev, A. V. (2023). Responses of model cortical neurons to temporal interference stimulation and related transcranial alternating current stimulation modalities. *J. Neural Eng.* 19:066047. doi: 10.1088/1741-2552/acab30

frontiers | Frontiers in Human Neuroscience

TYPE Original Research
PUBLISHED 12 February 2024
DOI 10.3389/fnhum.2024.1279183

EDITED BY
Xin Zhang,
Chinese Academy of Medical Sciences and
Peking Union Medical College, China

REVIEWED BY
Ricardo Nuno Braço Forte Salvador,
Neuroelectrics, Spain
Théodore Papadopoulo,
Research Centre Inria Sophia Antipolis
Méditerranée, France
David S. Holder,
University College London, United Kingdom

*CORRESPONDENCE
Maria Carla Piastra
✉ m.c.piastra@utwente.nl

RECEIVED 17 August 2023
ACCEPTED 25 January 2024
PUBLISHED 12 February 2024

CITATION
Piastra MC, Oostenveld R, Homölle S, Han B, Chen Q and Oostendorp T (2024) How to assess the accuracy of volume conduction models? A validation study with stereotactic EEG data. *Front. Hum. Neurosci.* 18:1279183. doi: 10.3389/fnhum.2024.1279183

How to assess the accuracy of volume conduction models? A validation study with stereotactic EEG data

Maria Carla Piastra[1,2]*, Robert Oostenveld[3,4], Simon Homölle[3], Biao Han[5], Qi Chen[5] and Thom Oostendorp[2]

[1]Clinical Neurophysiology, Faculty of Science and Technology, Technical Medical Centre, University of Twente, Enschede, Netherlands, [2]Department of Cognitive Neuroscience, Donders Institute for Brain, Cognition and Behaviour, Radboud University Medical Center, Nijmegen, Netherlands, [3]Donders Institute for Brain, Cognition and Behaviour, Radboud University, Nijmegen, Netherlands, [4]NatMEG, Karolinska Institutet, Stockholm, Sweden, [5]School of Psychology, South China Normal University, Guangzhou, China

Introduction: Volume conduction models of the human head are used in various neuroscience fields, such as for source reconstruction in EEG and MEG, and for modeling the effects of brain stimulation. Numerous studies have quantified the accuracy and sensitivity of volume conduction models by analyzing the effects of the geometrical and electrical features of the head model, the sensor model, the source model, and the numerical method. Most studies are based on simulations as it is hard to obtain sufficiently detailed measurements to compare to models. The recording of stereotactic EEG during electric stimulation mapping provides an opportunity for such empirical validation.

Methods: In the study presented here, we used the potential distribution of volume-conducted artifacts that are due to cortical stimulation to evaluate the accuracy of finite element method (FEM) volume conduction models. We adopted a widely used strategy for numerical comparison, i.e., we fixed the geometrical description of the head model and the mathematical method to perform simulations, and we gradually altered the head models, by increasing the level of detail of the conductivity profile. We compared the simulated potentials at different levels of refinement with the measured potentials in three epilepsy patients.

Results: Our results show that increasing the level of detail of the volume conduction head model only marginally improves the accuracy of the simulated potentials when compared to *in-vivo* sEEG measurements. The mismatch between measured and simulated potentials is, throughout all patients and models, maximally 40 microvolts (i.e., 10% relative error) in 80% of the stimulation-recording combination pairs and it is modulated by the distance between recording and stimulating electrodes.

Discussion: Our study suggests that commonly used strategies used to validate volume conduction models based solely on simulations might give an overly optimistic idea about volume conduction model accuracy. We recommend more empirical validations to be performed to identify those factors in volume conduction models that have the highest impact on the accuracy of simulated potentials. We share the dataset to allow researchers to further investigate the mismatch between measurements and FEM models and to contribute to improving volume conduction models.

KEYWORDS

volume conduction, EEG, stereotactic EEG, empirical validation, finite element method, head model

1 Introduction

Volume conduction models of the head are widely used for source reconstruction of electro- (EEG) and magnetoencephalography (MEG) activity (Malmivuo and Plonsey, 1995; Nunez and Srinivasan, 2006; Hansen et al., 2010), and are used to understand and optimize the effects of electrical (Neuling et al., 2012; Rampersad et al., 2014) and magnetic brain stimulation (Janssen et al., 2013) applied intra- and extracranially with transcranial electrical, deep brain, and magnetic stimulation (tES, DBS, and TMS). Although there are numerous model studies that quantified the accuracy of numerical approximations of electric potentials (in the EEG case) and magnetic fields (in the MEG case) by comparing different simulated models, there are fewer studies that investigated differences between actual measurements in humans and simulated potentials and fields (Rush and Driscoll, 1968; Bangera et al., 2010; Huang et al., 2017).

Previous work shows that the accuracy of the potential resulting from volume conduction models relies on a number of factors, such as the geometrical representation of the model (Vorwerk et al., 2014), the conductivity of the different tissues (Oostendorp et al., 2000; Aydin et al., 2014), the representation of the sensors (Pursiainen et al., 2012; Vermaas et al., 2020a), the representation of the sources [e.g., dipoles (De Munck et al., 1988) or bipoles (Vermaas et al., 2020b)], and the method used to solve the mathematical problem [e.g., with analytical formulas (de Munck and Peters, 1993; Zhang, 1995; Mosher et al., 1999), boundary element methods (Fuchs et al., 2001; Oostenveld and Oostendorp, 2002; Akalin-Acar and Gençer, 2004; Kybic et al., 2005; Stenroos and Sarvas, 2012; Makarov et al., 2020), finite difference methods (Montes-Restrepo et al., 2013; Morales et al., 2018; Moridera et al., 2021), and finite element methods (Marin et al., 1998; Schimpf et al., 2002; Miinalainen et al., 2019)].

The geometrical, electrical, and numerical aspects of volume conduction models are inherently interlinked. For example, the BEM assumes the geometry to be comprised of nested compartments with homogenous and isotropic conductivity, resulting in a geometrical description of the boundaries between compartments by triangulated surface meshes, where most BEM implementations require the surfaces not to touch or intersect, and where triangles should have a desired aspect ratio (Sun et al., 2012). Another example is the assumption of white matter conductivity being anisotropic, which limits the choice of the numerical method to FEM or FDM. The specific link between geometrical and electrical volume conduction model aspects is exemplified by including high-resolution anatomical details in the model, such as CSF, the compact and spongiform bone parts of the skull, blood vessels, or the dura mater, which require the geometrical description to have a spatial resolution that is high enough to be able to assign the detailed conductivities (Engwer et al., 2017; Piastra et al., 2018).

A strategy often adopted in validation studies that involve computer simulations is to focus on one or two of these factors and keep the remaining aspects fixed. In Nüßing et al. (2016), for example, the geometry of the head model was kept constant and the mathematical method to solve the forward problem was varied. In Piastra et al. (2018), the numerical method and the source model were changed, whereas the geometry was kept constant. In Vorwerk et al. (2014), the geometrical description and the numerical method were kept constant, and the conductivity profile was varied. Here, we adopt the same strategy as, e.g., in Vorwerk et al. (2014), keeping the identical geometry and numerical method, and explore the effects of increasing the level of detail in the head model by including more compartments with different conductivities. Going beyond existing simulation studies, we empirically compared the simulated potentials to measured potentials.

An interesting opportunity to empirically validate the forward model accuracy is provided by stereotactic EEG (sEEG) measurements during electric stimulation mapping, a technique used in the pre-surgical evaluation of epilepsy patients. Electrical stimulation mapping is essential for epilepsy surgery planning (Ritaccio et al., 2018), where pharmaco-resistant epileptic patients that are considered for resective surgery are implanted with intracranial (sEEG or electrocorticography (ECoG) electrodes to guide surgical resections of epileptiform tissue while sparing the eloquent cortex. In particular, by detecting behavioral changes, electrical stimulation is used to identify the epileptogenic zone or to localize the eloquent cortex which is to be spared in the subsequent resection. Electrical stimulation can also be combined with simultaneous recording of brain activity, resulting in cortical stimulation evoked potentials (CSEPs) that allow studying the spread of the induced activity, similar to how transcranial magnetic stimulation (TMS) evoked potentials are studied with scalp EEG (Bonato et al., 2006; Conde et al., 2019).

In the current study, we challenged the commonly employed strategy to improve volume conduction models based on the comparison between one simulation to another simulation, by validating volume conduction models using empirical data recorded from sEEG during stimulation. Rather than looking at the (biological) neuronal propagation of the activity of the CSEPs, we used the (physical) spatial potential distribution of the passively volume-conducted stimulation artifact. We compared the measured potential to the simulated potential that was computed with state-of-the-art FEM models based on the individuals' anatomical CT and MRI data of three epileptic patients. We investigate how the mismatch between recorded and simulated potentials depends on the level of detail in the FEM model, i.e., tissue conductivity, and on the distance between stimulating and recording sites.

2 Materials and methods

2.1 Ethics statement

Participants were recruited at the Guangdong Sanjiu Brain Hospital. The placement of the depth electrodes and the cortical stimulation were based solely on the clinical needs for the treatment of the patients and were thus independent of the purpose of the present study. This study did not add any invasive procedure to the intracranial recordings. The MRI, CT, and sEEG were all approved by the Ethics Committee of the School of Psychology, South China Normal University (SCNU-PSY-2020-1-050), and the Ethics Committee of Guangdong Sanjiu Brain Hospital. All the participants gave their written informed consent prior to the experiments in accordance with the Declaration of Helsinki.

TABLE 1 Conductivity values (in S/m) of the three isotropic head models created and used in this study, with five (5C), four (4C), and three compartments (3C).

Tissue	5C (S/m)	4C (S/m)	3C (S/m)	References
White matter	0.14	–	–	Ramon et al., 2003
Gray matter	0.33	–	–	Ramon et al., 2003
Brain	:	0.33	0.33	Ramon et al., 2003
CSF	1.79	1.79	–	Baumann et al., 1997
Skull	0.01	0.01	0.01	Dannhauer et al., 2011
Scalp	0.43	0.43	0.43	Ramon et al., 2003, Dannhauer et al., 2011

The column (:) indicates that the compartment has been split, e.g., the brain compartment divided between gray and white matter, while the dash (-) indicates that the relative compartment has been neglected in the head model.

2.2 Participants and data acquisitions

This study used data recorded for pre-surgical evaluation in three patients suffering from refractory epilepsy. The three participants (referred to as s1, s2, and s3) were 18, 21, and 25 years old. The three patients had 11, 9, and 15 semi-rigid multi-lead electrode shafts implanted, respectively. The electrode shafts had a diameter of 0.8 mm and contained 10–16 contacts that were 2 mm wide and 1.5 mm apart, with a total of 146, 124, and 186 electrodes per participant.

Intracranial sEEG recordings were conducted using commercial video-intracranial monitoring systems (Nihon Kohden). The data were bandpass filtered from 0.1 to 300 Hz and sampled at 1,000 Hz, using a reference electrode located in the white matter. During the CSEP recording procedures, around 40 electric stimulations were induced per patient in 20, 38, and 26 pairs of neighboring electrodes, respectively, while the sEEG signal was recorded on all remaining contacts. The total recording time was 17 m 15 s, 29 m 39 s, and 19 m 35 s, respectively.

Prior to the sEEG electrode implantation, T1 weighted spoiled gradient-recalled (SPGR) MRIs were acquired with a 3T scanner (GE Discovery MR750). Post-implantation CT images were acquired with a Philips Brilliance 64 scanner. The MRI resolution was 1.0 × 1.0 × 1.0, 0.5 × 0.5 × 0.5, and 0.5 × 0.5 × 0.5 mm for participants 1, 2, and 3, respectively, and the field of view (FOV) was 256 × 256 × 172, 390 × 435 × 418, and 374 × 424 × 377 for participants 1, 2, and 3, respectively. The CT resolution was 0.5 × 0.5 × 0.5 mm for all participants, and the FOV was 512 × 512 × 368, 390 × 435 × 418, and 374 × 424 × 377 for participants 1, 2, and 3, respectively.

2.3 Processing the sEEG data

All signal analysis was performed using FieldTrip (Oostenveld et al., 2011). The sEEG data was high-pass filtered at 10 Hz, segmented around the stimulation moments, and baseline corrected. Noisy channels were excluded following different criteria: variance of the after-peak signal higher than 10 millivolts, electrode positioned in the skull or scalp, and electrode close to or involved in the stimulation. The sEEG data were subsequently re-referenced to a bipolar montage (Allen et al., 1992), and the average of the peaks occurring at the moment of the electric stimulations was extracted.

2.4 Processing the anatomical MRI and CT data

Each participant's pre-implantation T1-weighted MRI scan was coregistered with the post-implantation CT scan, using rigid affine transformations derived from FSL's FLIRT algorithm (Jenkinson et al., 2002). The positions of sEEG electrodes were manually identified on the CT scan using the procedure outlined in Stolk et al. (2018). Some electrode contacts were located outside the brain and therefore not used in further analysis.

The MRI and CT scans of each patient were used to construct three individualized head models for each participant: a simple three-compartment isotropic head model (3C), where scalp, skull, and brain are included, a four-compartment isotropic head model (4C), where the cerebrospinal fluid (CSF) is additionally distinguished, and a more detailed volume conductor head model with five isotropic compartments (5C), i.e., scalp, skull, CSF, gray matter, and white matter.

To facilitate the segmentation procedure, the pre-implantation T1-weighted MRI scan and post-implantation CT scan were resampled so that the voxels of the anatomical data are cubic with 1 mm resolution. Furthermore, the images were truncated at 36, 30, and 35 mm below the spinal cord opening of participants 1, 2, and 3, respectively, following the suggestions in Lanfer et al. (2012).

As the T1-weighted anatomical MRI provides poor contrast to delineate the skull from the surrounding tissue, we segmented the skull from the CT scan by thresholding the CT scan, keeping the biggest connected components (performed in MATLAB), manually deleting electrodes and CT artifacts, and, finally, applying a smooth erode-dilate filter [performed in Seg3D (CIBC, 2016)]. The resulting skull geometry was closed, apart from the spinal cord opening, and skull burr holes drilled during surgery were excluded in the model.

The scalp, gray, and white matter compartments were segmented from the T1-weighted MRI scan using the SPM12 (Penny et al., 2011) routine implemented in FieldTrip. Finally, a series of binary operations was performed in Seg3D to combine the volumetric masks deduced from the two segmentations. In particular, the CSF compartment was constructed by subtracting the dilated inner skull mask from the scalp, skull, and gray and white matter masks. The dilation of the inner skull compartment was necessary to remove artificial holes at both the outer and inner skull interfaces generated by merging the skull segmentation from the CT and the one from the MRI. Since no DTI scans were acquired, we excluded the anisotropic conductivity tensors in the model (Tuch et al., 2001; Aydin et al., 2017).

Once the masks were assembled, a 1 mm volumetric hexahedral mesh was created (with a nodeshift of 0.3), resulting in ∼3.5 million nodes and 3.5 million hexahedrons. For the three-compartment (3C) and four-compartment (4C) head models, only the tissue labels (and hence conductivities) were modified, while the mesh remained the same as the one for the five-compartment (5C) head model. The specific features of the three models are gathered in Table 1.

2.5 FEM simulations

The FEM simulations computing the electric potential difference distributions were performed using the DUNEuro software (Schrader et al., 2021). As Pursiainen et al. (2012) and Vermaas et al. (2020a) show that the spatial extent and geometry of electrodes do not play a significant role, we modeled the sensors as point-sensors. The stimulating electrode pairs were modeled as point-dipoles located at the midpoints between the neighboring anode and cathode.

2.6 Validation analysis/strategy

Figure 1 gives a schematic representation of the analysis pipeline. We computed the absolute difference between measured and simulated potentials for all combinations of the stimulation electrode pairs and all recording electrode pairs. Since the electrical stimulation pulse duration is only 0.3 ms and the sampling rate is 1,000 Hz (i.e., each sample represents 1 ms), the recording does not capture the full temporal detail of the rising and falling flank of the electrical stimulation and we were not able to retrieve the actual peak amplitude of the stimulation artifact in the data. We, therefore, determined a scaling factor that minimized the absolute error between simulated and measured potentials, i.e., 200, for all the participants and multiplied the simulated potentials by this factor.

As we have around 30 stimulating electrode pairs which were each recorded with about 150 electrode pairs (channels), there are about 4,500 model simulations per participant and per volume conduction model to be compared to their corresponding measurements. We summarized the model errors over all stimulation sites and all recording sites by computing the cumulative distribution of the absolute differences between measured and simulated potentials. In addition, we normalized the absolute difference with the root mean square (RMS) over time and channels of the preprocessed signal, thus obtaining a relative difference between measured and simulated potentials. The RMS values are ∼610, 332, and 96 μV, for participants 1, 2, and 3, respectively. We investigated how the absolute and relative difference between measured and simulated potentials depends on the level of detail of the head model. In Figure 2, the absolute cumulative distribution curve and the relative error are visualized as boxplots.

Furthermore, we studied how the relative error depends on the distance between stimulating and recording sites. To do so, we computed the distances between stimulation and recording sites, divided them into 5 mm bins, resulting in 9, 11, and 14 bins, respectively for the three participants, and visualized boxplots of the relative difference for each volume conduction model and for each participant (Figure 3).

3 Results

3.1 Difference between measured and simulated potentials for the three head models and participants

For each of the participants and for each of the volume conduction models we compared the measured potential to the simulated potentials for all combinations of stimulation and recording electrodes. Figure 2 shows the cumulative distribution (in the percentage of the total number of stimulating-recording electrode pairs) of the absolute error (top) and boxplots of the relative error (bottom) difference between the measured and simulated potentials in the three head models, i.e., 3C, 4C, and 5C, for the three participants, i.e., s1, s2, s3. From Figure 2 we can see that in 80% of the stimulation-recording electrode pair combinations, there is an absolute error of ≤5 (for s3), 15 (for s1), and 35 (for s2) μV (Figure 2A), which corresponds to a relative error with median values of less than 1, 2.8 and 2.4%, respectively, (Figure 2B).

From Figure 2, we furthermore observe that the difference between the three head models (3C, 4C, 5C; line thickness) is considerably smaller than the difference between the three participants (s1, s2, s3; line color). In general, there is hardly any dependency of the error on the level of detail of the volume conduction head model used in the FEM simulation, since the cumulative distribution curves relative to 3C, 4C, and 5C are nearly overlapping for most participants.

3.2 Dependance of the simulation errors on the distance between stimulating and recording sites

In Figures 3A–C, we used a boxplot to visualize the relative error between measured and simulated potentials for different distances (in mm) between stimulating and recording electrode pairs, for the three head models and the three participants, i.e., s1, s2, and s3, respectively. Furthermore, we showed histograms of the distance distribution for each participant (gray bar plot on top of the boxplots).

From Figure 3, we observe that the relative error depends on the distance between the stimulating and recording electrode pairs. In particular, we can see that in all three participants, the error is very high for small distances and decreases for larger distances. For participant 2 and, to a smaller degree, also for participant 1, we can further notice that the relative error increases for distances larger than 65 mm. This effect is not present for participant 3 (Figure 3C).

All in all, without considering the closest stimulating-recording electrode combinations, i.e., the 0–5 mm bin, the medians of the relative errors are below 15% for all of the three participants. In particular, very low (2%) relative errors can be found for stimulating-recording electrode distances between 35 and 45 mm. Note that the distance histograms are very different

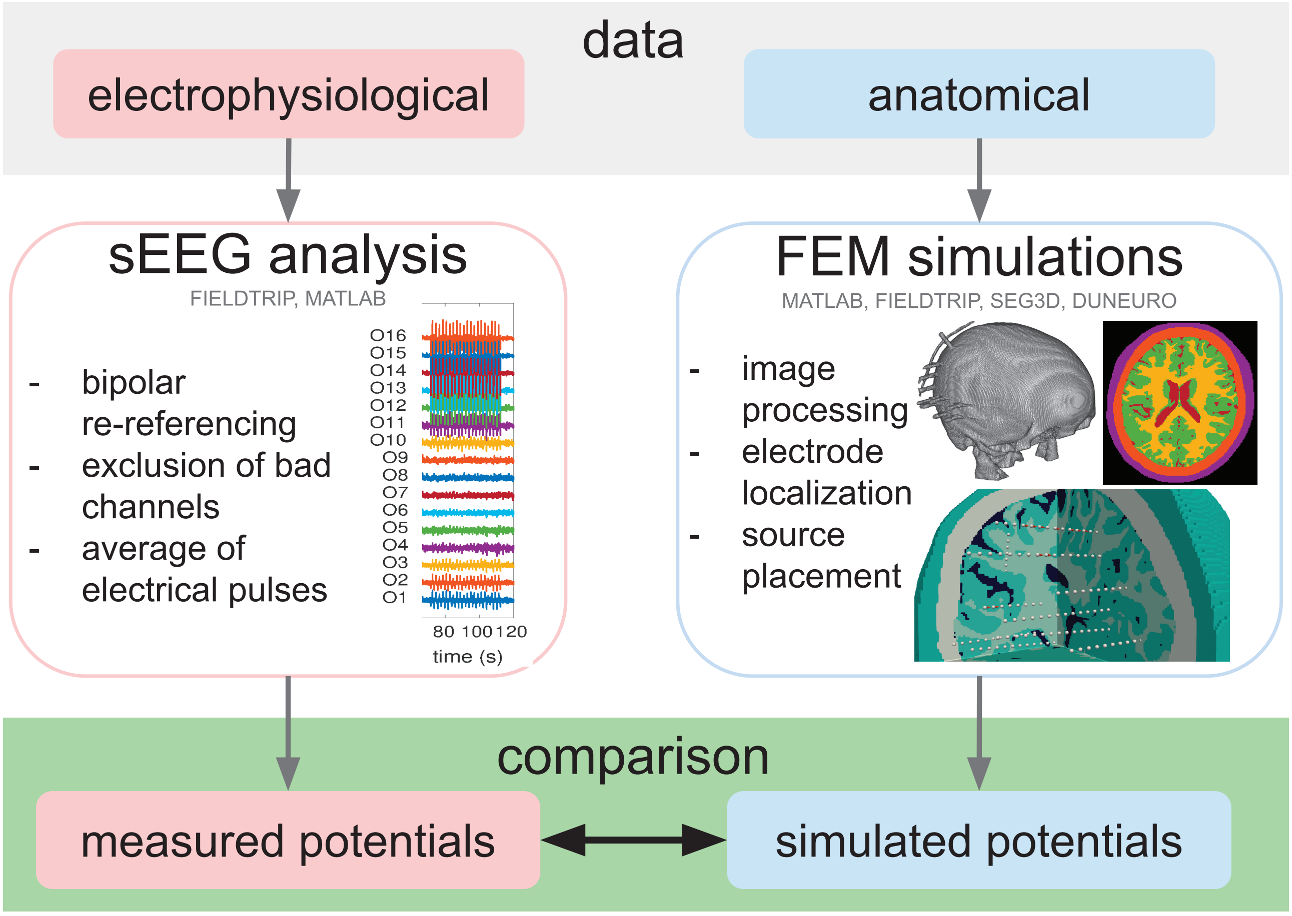

FIGURE 1
Schematic representation of the analysis pipeline. Following the collection of electrophysiological (sEEG) and anatomical (MRI and CT) data, the sEEG analysis was performed to obtain the measured potentials (red box), and the volume conduction simulations were set up, starting from the MRI and CT image processing, the electrode localization, and the source placement. Subsequently, the simulated potentials were computed (blue box) and the measured and simulated potentials were finally compared (green box). The software tools used in each step are indicated.

among participants, which is not surprising considering that each epileptic patient has an individualized electrode implantation plan aligned with the clinical requirements and the suspected epileptogenic zones.

4 Discussion

In our study, we found that increasing the level of detail of the volume conduction head model only marginally improves the accuracy of the simulated potentials, when compared to *in-vivo* sEEG measurements of three epileptic patients undergoing electric stimulation mapping. In 80% of the stimulation-recording combination pairs, the relative error is around 10%; for stimulating-recording electrode distances between 35 and 45 mm, the relative error is 2%.

Many possible factors can explain why the difference among patients is much larger than the differences among models. One main difference lies in the different electrode implantation, the positioning and the number of electrodes are individualized and based on the collective assumptions of the epileptic network of the patient. This means that not only the density of sampling but also the within-tissue location of the electrodes are different. This can be partially seen, for example, in the three gray bar plots of Figure 3.

Another possible explanation for bigger differences among patients is the choice of fixed values for the conductivity profiles, whose modeling represents, in our opinion, the most delicate aspect to discuss. The standard approach used to include tissue conductivity in the volume conduction model relies on the MRI-based classification of the human head into a limited number of compartments; whereas FEM allows each volume element to have its own conductivity, we therefore only make use of a limited number of conductivity values. On top of this simplified compartmentalization, conductivity values are typically assigned independent of the individual characteristics of the participant. Moreover, template conductivity values are not consistent throughout the literature (McCann et al., 2019). Finally, there is no consensus on the method or technology that should be used to deduce or estimate such values (Ferrée et al., 2000; Verhoeven et al., 2015; Ranta et al., 2017; Acar and Makeig, 2022; Altakroury et al., 2022).

In literature, several direct and indirect volume conduction validation attempts have been carried out. In the pioneering work of Rush and Driscoll (1968), for example, simulated EEG potentials were tested both with a phantom, i.e., an electrolytic tank

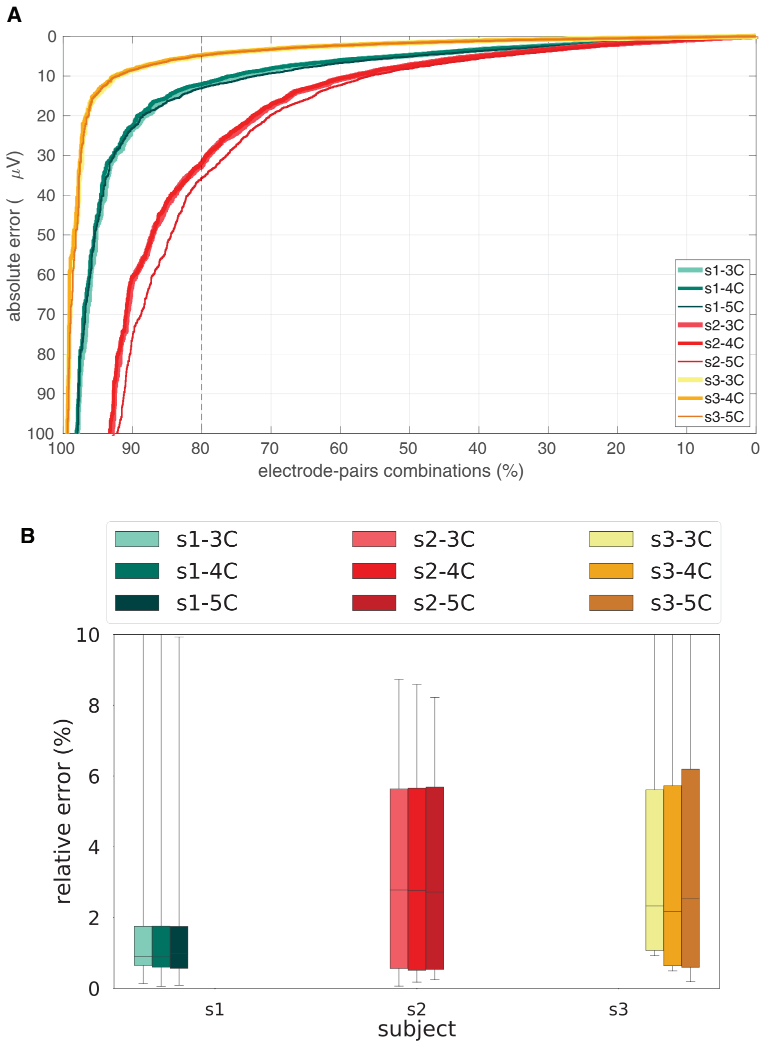

FIGURE 2
Absolute and relative errors per participant and head model. **(A)** Cumulative distributions in the percentage of the total number of stimulating-recording electrode pairs of the absolute difference between measured and simulated potentials in the three head models, i.e., 3C, 4C, and 5C, for the three participants, i.e., s1, s2, s3. The dashed vertical line represents 80% of the stimulation-recording combination pairs. **(B)** Boxplots of the relative difference between measured and simulated potentials in the three head models, i.e., 3C, 4C, and 5C, for the three participants, i.e., s1, s2, s3.

containing a human skull, and by comparison with *in-vivo* data from within the brain of a monkey (Burger and Van Milaan, 1943) and from the surface of a human head (Hayes, 1950). Given the technology available nowadays, it would be interesting to repeat such validation studies with, for example, 3D-printed phantoms that more accurately mimic the complexity of human head tissues (Avery et al., 2017; Zhang et al., 2017; Tsizin et al., 2018; Morales-Quezada et al., 2019; Kuratko et al., 2022).

Both in our study and in Bangera et al. (2010), it is found that increasing the level of detail of the volume conduction model does not improve the accuracy of the iEEG forward simulations within the skull compartment. Bangera et al. made use of stereo EEG recordings of four epileptic patients to assess which level of detail should be adopted in volume conduction modeling of the inner skull head. Similar to our work, they computed FEM solutions in a variety of head models with an increasing number of compartments included in both isotropic and anisotropic models. Differently from Bagera, where they restricted their claims to intracranial EEG forward solutions accuracy, the overall goal of our study is to have a critical eye on how the accuracy of forward simulations is assessed in literature, independent of whether intra or extracranial compartments are included in the model.

In a reciprocal sense (see, e.g., Vallaghé et al., 2008; Wagner et al., 2016), validation conducted for transcranial electrical stimulation (tES) simulations can be associated with and compared to forward solutions validations. In Opitz et al. (2016), for example, sEEG recordings during extracranial tES stimulations were acquired and analyzed in monkeys and humans. In their study, the focus is on assessing the intracranial amplitude of the potential induced by tES, and did not study the effect of variations in the volume conductor model, e.g. by varying the number of compartments. In Datta et al. (2013), the attempt on characterizing scalp voltages generated by tES to validate participant-specific FEM models of current flow for clinical dose is presented. They

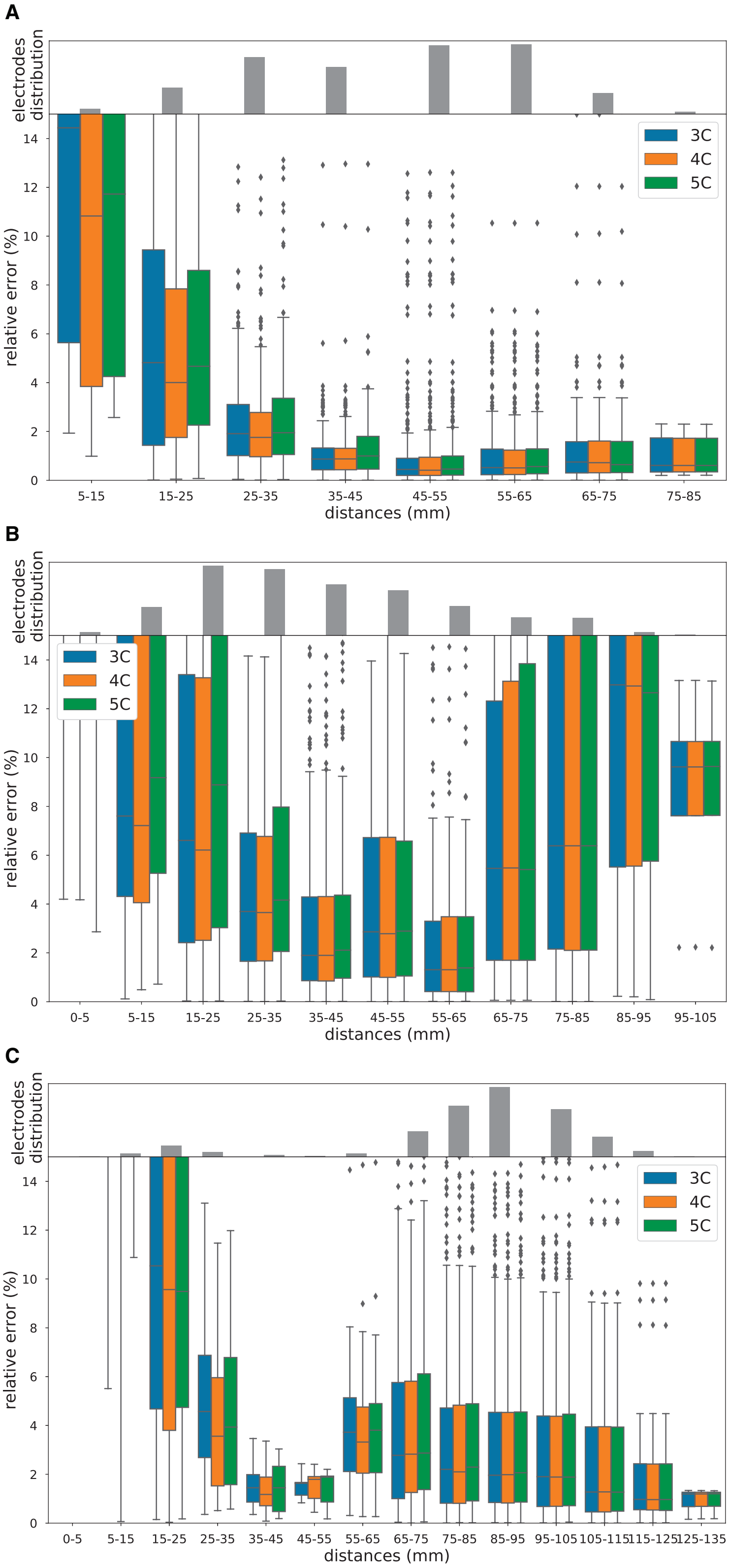

FIGURE 3
Relative errors and distances. Boxplot of the relative errors in percentage between measured and simulated potentials in 3C (in blue), 4C (in orange), and 5C (in green), for increasing distances between stimulating and recording electrode pairs, for participant 1 **(A)**, participant 2 **(B)** and participant 3 **(C)**. The gray bar plots on top of the boxplots are the histograms of the distances. Note the different scaling of the *y*-axis.

concluded that the FEM model accurately predicted the distinct voltage distributions and correlated the induced scalp voltages with current flow through the cortex, without directly validating the model prediction of brain current flow.

In recent work of Huang et al. (2017), the influence of different volume conduction head models is quantified in a tES/sEEG validation. Despite multiple refinements in the head model, Huang et al. (2017) did not find consistently that a more complex model improves the simulation performance across the ten participants analyzed in their work. Our findings are therefore also in line with their conclusions.

One indirect way to validate volume conduction models is to compare source reconstruction results with known intracranial sources, in terms of source location, magnitude, and orientation. In several studies (e.g., in Cohen et al., 1990; Murakami et al., 2016; Mikulan et al., 2020; Unnwongse et al., 2023), such validation has been performed without, nevertheless, studying the influence of the forward model accuracy on the source reconstruction results. In contrast, Leahy et al. (1998) performed such validation in a three-layered human phantom, concluding that the influence of using a realistic head model instead of a sphere for computing the forward solution was found to be minimal on the location mismatch. In addition, Gullmar et al. (2006) and Lau et al. (2016) made use of *in-vivo* measurements of a rabbit implanted with actual dipoles to study the influence of white matter anisotropic conductivity (Gullmar et al., 2006), and skull defects (Lau et al., 2016), on EEG (Gullmar et al., 2006), and MEG (Lau et al., 2016), source reconstruction. Gullmar et al. (2006) found a strong influence of the anisotropy on the magnitude in the forward as well as in the inverse solution and on the orientation of dipoles in the inverse solution. They concluded that source localization procedures in animals will improve by including white matter anisotropy. In Lau et al. (2016), the forward simulation of the MEG signals reproduced the experimentally observed characteristic magnitude and topography changes due to skull defects. They conclude that detailed finite element head models can improve the localization of brain function, specifically after surgery.

Despite our best efforts, there remains some model inaccuracy that are related to data limitations. For example, partial volume effects might lead to inaccurate brain structure quantification in MRIs or electrode identification in CTs.

Moreover, there are features of the sEEG signal we cannot fully take into account in our study due to limitations in recording hardware. Both the onset and the offset of the pulse are affected by capacitive filtering effects that last more than a millisecond. As a result, the pulse (which has a duration of 0.3 ms) ends well before the capacitive effect from the start has subsided. In addition, since the sample period (1 ms) is longer than the pulse duration, the recorded potential cannot be related directly to the stimulation strength. As already mentioned, we, therefore, adopted a scaling factor of 200 to fit the simulated potentials into the measured potentials which compensates for the uncertain, but fixed, relation between the stimulation strength and the average of the recorded potentials. Since the technical features of the stimulation and recording setup were the same for all participants, we believe it is appropriate to assume the same scaling factor for all participants. The scaling factor does not affect the main conclusion of this work, since we would notice a consistent global rescaling of the error curves and bars in Figure 2, but the relation between curves with different head models would be untouched. We are nevertheless planning to perform a similar study with higher sample rates and longer pulse durations.

As to model inaccuracies, we know that assuming point-like dipoles introduces modeling errors at small distances, see Figure 3, which can be reduced if monopole models are adopted instead. We recently developed a tool, i.e., FEMfuns (Vermaas et al., 2020b), that is able to model monopolar sources in volume conduction simulations, and we are planning to use it in the future. Nevertheless, this inaccuracy does not explain why more detailed head models do not lead to more accurate FEM solutions in our study. We believe that a U-shaped behavior with a subsequent descent slope might be present in all subjects, but only part of this shape is visible given the electrode configuration, i.e., distance. In all subjects, the errors are the highest for the smallest distances and decrease until reaching a minimum at around 35-65 mm. Subsequently, the errors are increasing again for higher distances, describing a U-shape. What is visible for subjects 2 and 3 (and not for subject 1) is that after around 95 mm for subject 2 and 75 mm for subject 3, the errors are decreasing with higher distances. While the U-shaped behavior of the errors in the vicinity of the sources (i.e., dipolar vs monopolar source model) and in the proximity of conductivity jumps (at higher distances) is clear, further analysis is required to understand the behavior of the errors for further higher distances.

Though they could only be important for intracranial recording simulations, CSF shunting effects in the electrodes' vicinity are not sufficiently captured by our volume conduction model. Similar to what is demonstrated in Vermaas et al. (2020a), more accurate features of the electrodes, such as volumetric extent, shape, and electrical properties, can be neglected since we are looking at distances higher than the dimension of the electrodes themselves. However, by not including the electrode structure, we are neglecting a possible CSF layer that is around the electrodes and relative shunting effects. During surgery, holes are drilled in the skull and the electrode shaft is inserted into the brain, allowing CSF to flow between the shaft and neighboring tissue.

There exist more sophisticated numerical methods to solve the quasi-static approximation of Maxwell's equations. Recently, for example, the discontinuous Galerkin FEM (Engwer et al., 2017; Piastra et al., 2018) was shown to alleviate modeling inaccuracies that occur in head geometries when using classical FE methods, e.g., so-called "skull leakage effects" for skull compartments with a thickness in the range of the mesh resolution (Engwer et al., 2017). Since we are focusing on the model accuracy in the inner skull compartment, our study does not fall in the scenario where the DG-FEM can be beneficial and therefore we do not expect these numerical solutions to substantially improve the accuracy in our study.

All in all, in the last decades, a lot of effort has been directed toward improving volume conduction models in terms of geometrical approximation (Vorwerk et al., 2014), source representation (Riera et al., 2012; Gratiy et al., 2013) and discretization (Haueisen et al., 1997; von Ellenrieder et al., 2006), and numerical accuracy (Engwer et al., 2017; Miinalainen et al., 2019), each individually showing incremental improvements. However, comparing the mismatch between measured and simulated potentials found in our study, the improvements in FEM models achieved in recent years that we were able to incorporate in our forward models appear relatively marginal and result in a limited accuracy compared to real data.

Considering our results, we feel that the commonly employed strategy to improve volume conduction models based on the comparison between one simulation to another simulation might not be the most efficient, we rather might want to reorient and channel more efforts toward actual measurements and empirical validations. We believe that empirical validations are more likely to reveal which aspects of the data, of the model assumptions and/or methodological details have the most impact to improve model potential distributions, for example, working with higher resolution imaging data and model geometries, better use of template anatomical models to deal with details that are too small to be imaged, and improved approaches for conductivity estimation such as Bayesian (Stahlhut et al., 2011) or deep learning techniques (Rashed et al., 2020).

Finally, we share the dataset of this study to allow researchers to shed new light on the reasons behind the high mismatch and to contribute to improving volume conduction models.

5 Conclusions

From our empirical comparison of FEM volume conduction model simulations with *in-vivo* measured sEEG potentials, we conclude that even with state-of-the-art model, increasing the level of detail of the volume conduction head model only marginally improves the accuracy of the simulated potentials when compared to the measurements. We argue that commonly employed methods for validating volume conduction models that rely solely on simulations should be supplemented with empirical validations based on actual data, as these will highlight the volume conduction model elements that have the greatest influence on the accuracy of simulated potentials.

Data availability statement

The data and code that support the findings of this study are available from the Donders Repository (https://doi.org/10.34973/j0jh-9j28).

Ethics statement

The studies involving humans were approved by Ethics Committee of the School of Psychology, South China Normal University (SCNU-PSY-2020-1-050), and the Ethics Committee of Guangdong Sanjiu Brain Hospital. The studies were conducted in accordance with the local legislation and institutional requirements. The participants provided their written informed consent to participate in this study.

Author contributions

MCP: Conceptualization, Formal analysis, Investigation, Methodology, Project administration, Software, Visualization, Writing – original draft, Writing – review & editing, Validation. RO: Methodology, Software, Writing – review & editing, Conceptualization, Supervision. SH: Writing – review & editing, Investigation, Software. BH: Data curation, Writing – review & editing, Resources. QC: Writing – review & editing, Data curation, Funding acquisition. TO: Conceptualization, Funding acquisition, Methodology, Supervision, Writing – review & editing, Investigation.

Funding

The author(s) declare financial support was received for the research, authorship, and/or publication of this article. This work was supported by the Dutch Research Council grant STW (grant no. P14-12) and the EU Horizon 2020 Marie Skłodowska-Curie Actions (MSCA)-ITN-2014-ETN Programme, project “ChildBrain” (grant no. 641652).

Acknowledgments

We thank the patients and doctors at Guangdong Sanjiu Brain Hospital who contributed to this study.

Conflict of interest

The authors declare that the research was conducted in the absence of any commercial or financial relationships that could be construed as a potential conflict of interest.

The author(s) declared that they were an editorial board member of Frontiers, at the time of submission. This had no impact on the peer review process and the final decision.

Publisher’s note

References

Acar, Z. A., and Makeig, S. (2022). "Evaluation of skull conductivity using scale head tissue conductivity estimation using EEG," in *2022 44th Annual International Conference of the IEEE Engineering in Medicine and Biology Society (EMBC)* (Glasgow), 4826–4829. doi: 10.1109/EMBC48229.2022.9872004

Akalin-Acar, Z., and Gençer, N. G. (2004). An advanced boundary element method (BEM) implementation for the forward problem of electromagnetic source imaging. *Phys. Med. Biol.* 49:5011. doi: 10.1088/0031-9155/49/21/012

Allen, P., Fish, D., and Smith, S. (1992). Very high-frequency rhythmic activity during sEEG suppression in frontal lobe epilepsy. *Electroencephalogr. Clin. Neurophysiol.* 82, 155–159. doi: 10.1016/0013-4694(92)90160-J

Altakroury, H., Koessler, L., Ranta, R., Hofmanis, J., Coulbois, S. C., Maillard, L., et al. (2022). Evaluation of performance for human in-vivo conductivity estimation from EEG and sEEG recorded in simultaneous with intracerebral electrical stimulation. *arXiv [Preprint].* arXiv:2203.05191.

Avery, J., Aristovich, K., Low, B., and Holder, D. (2017). Reproducible 3D printed head tanks for electrical impedance tomography with realistic shape and conductivity distribution. *Physiol. Meas.* 38, 1116–1131. doi: 10.1088/1361-6579/aa6586

Aydin, Ü., Rampp, S., Wollbrink, A., Kugel, H., Cho, J. H., Knösche, T. R., et al. (2017). Zoomed mRI guided by combined EEG/MEG source analysis: a multimodal approach for optimizing presurgical epilepsy work-up and its application in a multi-focal epilepsy patient case study. *Brain Topogr.* 30, 417–433. doi: 10.1007/s10548-017-0568-9

Aydin, Ü., Vorwerk, J., Küpper, P., Heers, M., Kugel, H., Galka, A., et al. (2014). Combining EEG and MEG for the reconstruction of epileptic activity using a calibrated realistic volume conductor model. *PLoS ONE* 9:e93154. doi: 10.1371/journal.pone.0093154

Bangera, N. B., Schomer, D. L., Dehghani, N., Ulbert, I., Cash, S., Papavasiliou, S., et al. (2010). Experimental validation of the influence of white matter anisotropy on the intracranial EEG forward solution. *J. Comput. Neurosci.* 29, 371–387. doi: 10.1007/s10827-009-0205-z

Baumann, S. B., Wozny, D. R., Kelly, S. K., and Meno, F. (1997). The electrical conductivity of human cerebrospinal fluid at body temperature. *IEEE Trans. Biomed. Eng.* 44, 220–223. doi: 10.1109/10.554770

Bonato, C., Miniussi, C., and Rossini, P. (2006). Transcranial magnetic stimulation and cortical evoked potentials: a TMS/EEG co-registration study. *Clin. Neurophysiol.* 117, 1699–1707. doi: 10.1016/j.clinph.2006.05.006

Burger, H., and Van Milaan, J. (1943). Measurements of the specific resistance of the human body to direct current. *Acta Med. Scand.* 114, 584–607. doi: 10.1111/j.0954-6820.1943.tb11253.x

CIBC (2016). *Seg3D: Volumetric Image Segmentation and Visualization. Scientific Computing and Imaging Institute (SCI)*. Available online at: http://www.seg3d.org (accessed January 30, 2024).

Cohen, D., Cuffin, B. N., Yunokuchi, K., Maniewski, R., Purcell, C., Cosgrove, G. R., et al. (1990). MEG versus EEG localization test using implanted sources in the human brain. *Ann. Neurol.* 28, 811–817. doi: 10.1002/ana.410280613

Conde, V., Tomasevic, L., Akopian, I., Stanek, K., Saturnino, G. B., Thielscher, A., et al. (2019). The non-transcranial tms-evoked potential is an inherent source of ambiguity in tms-EEG studies. *Neuroimage* 185, 300–312. doi: 10.1016/j.neuroimage.2018.10.052

Dannhauer, M., Lanfer, B., Wolters, C. H., and Knösche, T. R. (2011). Modeling of the human skull in EEG source analysis. *Hum. Brain Mapp.* 32, 1383–1399. doi: 10.1002/hbm.21114

Datta, A., Zhou, X., Su, Y., Parra, L. C., and Bikson, M. (2013). Validation of finite element model of transcranial electrical stimulation using scalp potentials: implications for clinical dose. *J. Neural Eng.* 10:036018. doi: 10.1088/1741-2560/10/3/036018

de Munck, J. C., and Peters, M. J. (1993). A fast method to compute the potential in the multisphere model. *IEEE Trans. Biomed. Eng.* 40, 1166–1174. doi: 10.1109/10.245635

De Munck, J. C., Van Dijk, H., and Spekreijse, B. W. (1988). Mathematical dipoles are adequate to describe realistic generators of human brain activity. *IEEE Trans. Biomed. Eng.* 35, 960–966. doi: 10.1109/10.8677

Engwer, C., Vorwerk, J., Ludewig, J., and Wolters, C. H. (2017). A discontinuous galerkin method to solve the EEG forward problem using the subtraction approach. *SIAM J. Sci. Comput.* 39, B138–164. doi: 10.1137/15M1048392

Ferrée, T. C., Eriksen, K. J., and Tucker, D. M. (2000). Regional head tissue conductivity estimation for improved EEG analysis. *IEEE Trans. Biomed. Eng.* 47, 1584–1592. doi: 10.1109/10.887939

Fuchs, M., Wagner, M., and Kastner, J. (2001). Boundary element method volume conductor models for EEG source reconstruction. *Clin. Neurophysiol.* 112, 1400–1407. doi: 10.1016/S1388-2457(01)00589-2

Gratiy, S. L., Pettersen, K. H., Einevoll, G. T., and Dale, A. M. (2013). Pitfalls in the interpretation of multielectrode data: on the infeasibility of the neuronal current-source monopoles. *J. Neurophysiol.* 109, 1681–1682. doi: 10.1152/jn.01047.2012

Gullmar, D., Haueisen, J., Eiselt, M., Gießler, F., Flemming, L., Anwander, A., et al. (2006). Influence of anisotropic conductivity on EEG source reconstruction: investigations in a rabbit model. *IEEE Trans. Biomed. Eng.* 53, 1841–1850. doi: 10.1109/TBME.2006.876641

Hansen, P., Kringelbach, M., and Salmelin, R. (2010). *MEG: An Introduction to Methods*. Oxford: Oxford University Press. doi: 10.1093/acprof:oso/9780195307238.001.0001

Haueisen, J., Böttner, A., Funke, M. E., Brauer, H., and Nowak, H. (1997). Effect of boundary element discretization on forward calculation and the inverse problem in electroencephalography and magnetoencephalography. *Biomed. Tech.* 42, 240–248. doi: 10.1515/bmte.1997.42.9.240

Hayes, K. J. (1950). The current path in electric convulsion shock. *Arch. Neurol. Psychiatry* 63, 102–109. doi: 10.1001/archneurpsyc.1950.02310190108008

Huang, Y., Liu, A. A., Lafon, B., Friedman, D., Dayan, M., Wang, X., et al. (2017). Measurements and models of electric fields in the *in vivo* human brain during transcranial electric stimulation. *Elife* 6:e18834. doi: 10.7554/eLife.18834

Janssen, A., Rampersad, S., Lucka, F., Lanfer, B., Lew, S., Aydin, Ü., et al. (2013). The influence of sulcus width on simulated electric fields induced by transcranial magnetic stimulation. *Phys. Med. Biol.* 58:4881. doi: 10.1088/0031-9155/58/14/4881

Jenkinson, M., Bannister, P., Brady, M., and Smith, S. (2002). Improved optimization for the robust and accurate linear registration and motion correction of brain images. *Neuroimage* 17, 825–841. doi: 10.1006/nimg.2002.1132

Kuratko, D., Lacik, J., Koudelka, V., Vejmola, C., Wjcik, D. K., Raida, Z., et al. (2022). Forward model of rat electroencephalogram: comparative study of numerical simulations with measurements on rat head phantoms. *IEEE Access* 10, 92023–92035. doi: 10.1109/ACCESS.2022.3202206

Kybic, J., Clerc, M., Faugeras, O. D., Keriven, R., and Papadopoulo, T. (2005). Fast multipole acceleration of the MEG/EEG boundary element method. *Phys. Med. Biol.* 50, 4695–4710. doi: 10.1088/0031-9155/50/19/018

Lanfer, B., Scherg, M., Dannhauer, M., Knösche, T. R., Burger, M., and Wolters, C. H. (2012). Influences of skull segmentation inaccuracies on EEG source analysis. *Neuroimage* 62, 418–431. doi: 10.1016/j.neuroimage.2012.05.006

Lau, S., Güllmar, D., Flemming, L., Grayden, D. B., Cook, M. J., Wolters, C. H., et al. (2016). Skull defects in finite element head models for source reconstruction from magnetoencephalography signals. *Front. Neurosci.* 10:141. doi: 10.3389/fnins.2016.00141

Leahy, R., Mosher, J., Spencer, M., Huang, M., and Lewine, J. (1998). A study of dipole localization accuracy for MEG and EEG using a human skull phantom. *Electroencephalogr. Clin. Neurophysiol.* 107, 159–173. doi: 10.1016/S0013-4694(98)00057-1

Makarov, S. N., Hämäläinen, M. S., Okada, Y. C., Noetscher, G. M., Ahveninen, J., and Nummenmaa, A. (2020). Boundary element fast multipole method for enhanced modeling of neurophysiological recordings. *IEEE Trans. Biomed. Eng.* 68, 308–318. doi: 10.1109/TBME.2020.2999271

Malmivuo, J., and Plonsey, R. (1995). *Bioelectromagnetism: Principles and Applications of Bioelectric and Biomagnetic Fields.* Oxford University Press, USA. doi: 10.1093/acprof:oso/9780195058239.001.0001

Marin, G., Guérin, C., Baillet, S., Garnero, L., and Meunier, G. (1998). Influence of skull anisotropy for the forward and inverse problem in EEG: simulation studies using fem on realistic head models. *Hum. Brain Mapp.* 6, 160–188. doi: 10.1002/(SICI)1097-0193(1998)6:4<250::AID-HBM5>3.0.CO;2-2

McCann, H., Pisano, G., and Beltrachini, L. (2019). Variation in reported human head tissue electrical conductivity values. *Brain Topogr.* 32, 825–858. doi: 10.1007/s10548-019-00710-2

Miinalainen, T., Rezaei, A., Us, D., Nüßing, A., Engwer, C., Wolters, C. H., et al. (2019). A realistic, accurate and fast source modeling approach for the EEG forward problem. *Neuroimage* 184, 56–67. doi: 10.1016/j.neuroimage.2018.08.054

Mikulan, E., Russo, S., Parmigiani, S., Sarasso, S., Zauli, F. M., Rubino, A., et al. (2020). Simultaneous human intracerebral stimulation and hd-EEG, ground-truth for source localization methods. *Sci. Data* 7:127. doi: 10.1038/s41597-020-0467-x

Montes-Restrepo, V., van Mierlo, P., Strobbe, G., Staelens, S., Vandenberghe, S., Hallez, H., et al. (2013). Influence of skull modeling approaches on EEG source localization. *Brain Topogr.* 27, 95–111. doi: 10.1007/s10548-013-0313-y

Morales, E. C., Acosta-Medina, C. D., Castellanos-Domínguez, G., and Mantini, D. (2018). A finite-difference solution for the EEG forward problem in inhomogeneous anisotropic media. *Brain Topogr.* 32, 229–239. doi: 10.1007/s10548-018-0683-2

Morales-Quezada, L., El-Hagrassy, M. M., Costa, B., McKinley, R. A., Lv, P., Fregni, F., et al. (2019). Transcranial direct current stimulation optimization-from physics-based computer simulations to high-fidelity head phantom fabrication and measurements. *Front. Hum. Neurosci.* 13:388. doi: 10.3389/fnhum.2019.00388

Moridera, T., Rashed, E. A., Mizutani, S., and Hirata, A. (2021). High-resolution EEG source localization in segmentation-free head models based on finite-difference method and matching pursuit algorithm. *Front. Neurosci.* 15:695668. doi: 10.3389/fnins.2021.695668

Mosher, J. C., Leahy, R. M., and Lewis, P. S. (1999). EEG and MEG: forward solutions for inverse methods. *IEEE Trans. Biomed. Eng.* 46, 245–259. doi: 10.1109/10.748978

Murakami, H., Wang, Z. I., Marashly, A., Krishnan, B., Prayson, R. A., Kakisaka, Y., et al. (2016). Correlating magnetoencephalography to stereo-electroencephalography in patients undergoing epilepsy surgery. *Brain* 139, 2935–2947. doi: 10.1093/brain/aww215

Neuling, T., Wagner, S., Wolters, C. H., Zaehle, T., and Herrmann, C. S. (2012). Finite-element model predicts current density distribution for clinical applications of tdcs and tacs. *Front. Psychiatry* 3:83. doi: 10.3389/fpsyt.2012.00083

Nunez, P. L., and Srinivasan, R. (2006). *Electric Fields of the Brain: The Neurophysics of EEG*. Cary, NC: Oxford University Press. doi: 10.1093/acprof:oso/9780195050387.001.0001

Nüßing, A., Wolters, C. H., Brinck, H., and Engwer, C. (2016). The unfitted discontinuous galerkin method for solving the EEG forward problem. *IEEE Trans. Biomed. Eng.* 63, 2564–2575. doi: 10.1109/TBME.2016.2590740

Oostendorp, T. F., Delbeke, J., and Stegeman, D. F. (2000). The conductivity of the human skull: results of *in vivo* and *in vitro* measurements. *IEEE Trans. Biomed. Eng.* 47, 1487–1492. doi: 10.1109/TBME.2000.880100

Oostenveld, R., Fries, P., Maris, E., and Schoffelen, J.-M. (2011). Fieldtrip: open source software for advanced analysis of MEG, EEG, and invasive electrophysiological data. *Comput. Intell. Neurosci.* 2011, 1–9. doi: 10.1155/2011/156869

Oostenveld, R., and Oostendorp, T. F. (2002). Validating the boundary element method for forward and inverse EEG computations in the presence of a hole in the skull. *Hum. Brain Mapp.* 17, 179–192. doi: 10.1002/hbm.10061

Opitz, A., Falchier, A., Yan, C.-G., Yeagle, E. M., Linn, G. S., Megevand, P., et al. A. D., et al. (2016). Spatiotemporal structure of intracranial electric fields induced by transcranial electric stimulation in humans and nonhuman primates. *Sci. Rep.* 6:31236. doi: 10.1038/srep31236

Penny, W. D., Friston, K. J., Ashburner, J. T., Kiebel, S. J., and Nichols, T. E. (2011). *Statistical parametric Mapping: The Analysis of Functional Brain Images*. Amsterdam: Elsevier.

Piastra, M. C., Nüßing, A., Vorwerk, J., Bornfleth, H., Oostenveld, R., Engwer, C., et al. (2018). The discontinuous galerkin finite element method for solving the MEG and the combined MEG/EEG forward problem. *Front. Neurosci.* 12:30. doi: 10.3389/fnins.2018.00030

Pursiainen, S., Lucka, F., and Wolters, C. H. (2012). Complete electrode model in EEG: relationship and differences to the point electrode model. *Phys. Med. Biol.* 57:999. doi: 10.1088/0031-9155/57/4/999

Ramon, C., Schimpf, P. H., Haueisen, J., Holmes, M. D., and Ishimaru, A. (2003). Role of soft bone, CSF and gray matter in EEG simulations. *Brain Topogr.* 16, 245–248. doi: 10.1023/B:BRAT.0000032859.68959.76

Rampersad, S. M., Janssen, A. M., Lucka, F., Aydin, Ü., Lanfer, B., Lew, S., et al. (2014). Simulating transcranial direct current stimulation with a detailed anisotropic human head model. *IEEE Trans. Neural Syst. Rehabil. Eng.* 22, 441–452. doi: 10.1109/TNSRE.2014.2308997

Ranta, R., Cam, S. L., Tyvaert, L., and Louis-Dorr, V. (2017). Assessing human brain impedance using simultaneous surface and intracerebral recordings. *Neuroscience* 343, 411–422. doi: 10.1016/j.neuroscience.2016.12.013

Rashed, E. A., Gomez-Tames, J., and Hirata, A. (2020). Deep learning-based development of personalized human head model with non-uniform conductivity for brain stimulation. *IEEE Trans. Med. Imaging* 39, 2351–2362. doi: 10.1109/TMI.2020.2969682

Riera, J. J., Ogawa, T., Goto, T., Sumiyoshi, A., Nonaka, H., Evans, A. C., et al. (2012). Pitfalls in the dipolar model for the neocortical EEG sources. *J. Neurophysiol.* 108, 956–975. doi: 10.1152/jn.00098.2011

Ritaccio, A. L., Brunner, P., and Schalk, G. (2018). Electrical stimulation mapping of the brain: basic principles and emerging alternatives. *J Clin. Neurophysiol.* 35, 86. doi: 10.1097/WNP.0000000000000440

Rush, S., and Driscoll, D. A. (1968). Current distribution in the brain from surface electrodes. *Anesth. Analg.* 47, 717–723. doi: 10.1213/00000539-196811000-00016

Schimpf, P. H., Ramon, C., and Haueisen, J. (2002). Dipole models for the EEG and MEG. *IEEE Trans. Biomed. Eng.* 49, 409–418. doi: 10.1109/10.995679

Schrader, S., Westhoff, A., Piastra, M. C., Miinalainen, T., Pursiainen, S., Vorwerk, J., et al. (2021). Duneuro a software toolbox for forward modeling in bioelectromagnetism. *PLoS ONE* 16:e0252431. doi: 10.1371/journal.pone.0252431

Stahlhut, C., Mørup, M., Winther, O., and Hansen, L. K. (2011). Simultaneous EEG source and forward model reconstruction (sofomore) using a hierarchical Bayesian approach. *J. Signal Process. Syst.* 65, 431–444. doi: 10.1007/s11265-010-0527-0

Stenroos, M., and Sarvas, J. (2012). Bioelectromagnetic forward problem: isolated source approach revis(it)ed. *Phys. Med. Biol.* 57, 3517–3535. doi: 10.1088/0031-9155/57/11/3517

Stolk, A., Griffin, S., van der Meij, R., Dewar, C., Saez, I., Lin, J. J., et al. (2018). Integrated analysis of anatomical and electrophysiological human intracranial data. *Nat. Protoc.* 13, 1699–1723. doi: 10.1038/s41596-018-0009-6

Sun, H., Darmofal, D. L., and Haimes, R. (2012). On the impact of triangle shapes for boundary layer problems using high-order finite element discretization. *J. Comput. Phys.* 231, 541–557. doi: 10.1016/j.jcp.2011.09.018

Tsizin, E., Mund, T., and Bronstein, A. (2018). "Printable anisotropic phantom for EEG with distributed current sources," in *Proc. IEEE Int. Symp. Biomed. Imag. (ISBI)* (Washington DC), 4–7.

Tuch, D. S., Wedeen, V. J., Dale, A. M., George, J. S., and Belliveau, J. W. (2001). Conductivity tensor mapping of the human brain using diffusion tensor mRI. *Proc. Nat. Acad. Sci.* 98, 11697–11701. doi: 10.1073/pnas.171473898

Unnwongse, K., Rampp, S., Wehner, T., Kowoll, A., Parpaley, Y., von Lehe, M., et al. (2023). Validating EEG source imaging using intracranial electrical stimulation. *Brain Commun.* 5:fcad023. doi: 10.1093/braincomms/fcad023

Vallaghé, S., Papadopoulo, T., and Clerc, M. (2008). The adjoint method for general EEG and MEG sensor-based lead field equations. *Phys. Med. Biol.* 54:135. doi: 10.1088/0031-9155/54/1/009

Verhoeven, T., Strobbe, G., van Mierlo, P., Buteneers, P., Vandenberghe, S., Dambre, J., et al. (2015). "A Bayesian model to estimate individual skull conductivity for EEG source imaging," in *International Workshop on Seizure Predictions 7* (Melbourne, VIC). Available online at: http://hdl.handle.net/1854/LU-6934868

Vermaas, M., Piastra, M., Oostendorp, T., Ramsey, N., and Tiesinga, P. (2020a). When to include ecog electrode properties in volume conduction models. *J. Neural Eng.* 17:056031. doi: 10.1088/1741-2552/abb11d

Vermaas, M., Piastra, M. C., Oostendorp, T. F., Ramsey, N. F., and Tiesinga, P. H. (2020b). Femfuns: a volume conduction modeling pipeline that includes resistive, capacitive or dispersive tissue and electrodes. *Neuroinformatics* 18, 569–580. doi: 10.1007/s12021-020-09458-8

von Ellenrieder, N., Muravchik, C. H., and Nehorai, A. (2006). Effects of geometric head model perturbations on the EEG forward and inverse problems. *IEEE Trans. Biomed. Eng.* 53, 421–429. doi: 10.1109/TBME.2005.869769

Vorwerk, J., Cho, J.-H., Rampp, S., Hamer, H., Knösche, T. R., and Wolters, C. H. (2014). A guideline for head volume conductor modeling in EEG and MEG. *Neuroimage* 100, 590–607. doi: 10.1016/j.neuroimage.2014.06.040

Wagner, S., Lucka, F., Vorwerk, J., Herrmann, C. S., Nolte, G., Burger, M., et al. (2016). Using reciprocity for relating the simulation of transcranial current stimulation to the EEG forward problem. *Neuroimage* 140, 163–173. doi: 10.1016/j.neuroimage.2016.04.005

Zhang, J., Yang, B., Li, H., Fu, F., Shi, X., Dong, X., et al. (2017). A novel 3D-printed head phantom with anatomically realistic geometry and continuously varying skull resistivity distribution for electrical impedance tomography. *Sci. Rep.* 7:4608. doi: 10.1038/s41598-017-05006-8

Zhang, Z. (1995). A fast method to compute surface potentials generated by dipoles within multilayer anisotropic spheres. *Phys. Med. Biol.* 40:335. doi: 10.1088/0031-9155/40/3/001

frontiers | Frontiers in Human Neuroscience

TYPE Original Research
PUBLISHED 29 February 2024
DOI 10.3389/fnhum.2024.1201574

OPEN ACCESS

EDITED BY
Kanak Kalita,
Vel Tech Dr. RR & Dr. SR Technical University,
India

REVIEWED BY
Umit Aydin,
University of Reading, United Kingdom
Ghazaleh Soleimani,
Medical School, University of Minnesota,
United States

*CORRESPONDENCE
Fernando Galaz Prieto
✉ fernando.galazprieto@tuni.fi

RECEIVED 06 April 2023
ACCEPTED 16 February 2024
PUBLISHED 29 February 2024

CITATION
Galaz Prieto F, Samavaki M and Pursiainen S (2024) Lattice layout and optimizer effect analysis for generating optimal transcranial electrical stimulation (tES) montages through the metaheuristic L1L1 method.
Front. Hum. Neurosci. 18:1201574.
doi: 10.3389/fnhum.2024.1201574

Lattice layout and optimizer effect analysis for generating optimal transcranial electrical stimulation (tES) montages through the metaheuristic L1L1 method

Fernando Galaz Prieto*, Maryam Samavaki and
Sampsa Pursiainen

Computing Sciences, Faculty of Information Technology, Tampere University, Tampere, Finland

Introduction: This study focuses on broadening the applicability of the metaheuristic L1-norm fitted and penalized (L1L1) optimization method in finding a current pattern for multichannel transcranial electrical stimulation (tES). The metaheuristic L1L1 optimization framework defines the tES montage via linear programming by maximizing or minimizing an objective function with respect to a pair of hyperparameters.

Methods: In this study, we explore the computational performance and reliability of different optimization packages, algorithms, and search methods in combination with the L1L1 method. The solvers from Matlab R2020b, MOSEK 9.0, Gurobi Optimizer, CVX's SeDuMi 1.3.5, and SDPT3 4.0 were employed to produce feasible results through different linear programming techniques, including Interior-Point (IP), Primal-Simplex (PS), and Dual-Simplex (DS) methods. To solve the metaheuristic optimization task of L1L1, we implement an exhaustive and recursive search along with a well-known heuristic direct search as a reference algorithm.

Results: Based on our results, and the given optimization task, Gurobi's IP was, overall, the preferable choice among Interior-Point while MOSEK's PS and DS packages were in the case of Simplex methods. These methods provided substantial computational time efficiency for solving the L1L1 method regardless of the applied search method.

Discussion: While the best-performing solvers show that the L1L1 method is suitable for maximizing either focality and intensity, a few of these solvers could not find a bipolar configuration. Part of the discrepancies between these methods can be explained by a different sensitivity with respect to parameter variation or the resolution of the lattice provided.

KEYWORDS

transcranial electrical stimulation (tES), optimization, linear programming, L1-norm, Interior-Point, metaheuristics

1 Introduction

Transcranial Electrical Stimulation (tES) is a non-invasive brain stimulation method used for stimulating neuronal activity, treating psychiatric disorders, and studying neuronal behavior by transmitting a constant low-intensity current pattern through a set of electrode patches attached to the scalp of the subject to modulate cortical excitability (Nitsche and Paulus, 2000). In tES, a volumetric current density in the brain is generated by injecting through the scalp a current pattern that can be described via different properties, including the number of active electrodes, their physical description (e.g., positioning, shape, permittivity, and impedance values), the applied stimulus waveform (e.g., amplitude, pulse shape, pulse width, and polarity), the number of stimulation sessions, and the time interval (Peterchev et al., 2012). Since different electrode montages result in distinct brain current flow, clinicians and researchers can adjust the montage to target or avoid specific brain regions in an application-specific manner.

An increasingly popular form of tES is the Transcranial Direct Current Stimulation (tDCS) method (Paulus, 2011; Moreno-Duarte et al., 2014; Thair et al., 2017; Reed and Cohen Kadosh, 2018). Compared to other non-invasive stimulation methods, the advantages of tDCS can be attributed to its inexpensive and approachable characteristics. Unlike the intricate machinery required for Transcranial Magnetic Stimulation (TMS) or the specialized frequency considerations in Transcranial Alternating Current Stimulation (tACS), tDCS involves a simpler setup—a direct current passed through scalp electrodes. This simplicity not only reduces the cost of equipment but also enhances portability, making tDCS more accessible for various settings, including home use. The simplicity and minimal training required contribute to its user-friendly nature enabling a broader range of individuals to utilize or participate in studies involving this method. Whereas tDCS is classically applied in a two-channel configuration (Kaufmann et al., 2021), its focality can be enhanced via multiple channels, which has motivated the introduction of advanced optimization methods for finding an optimal multi-channel montage (Fernandez-Corazza et al., 2020).

tES modeling involves constructing computational representations of the head and brain anatomy, simulating the distribution of electric fields. This process integrates factors such as electrode placement, tissue conductivity, and finite element method simulations to visualize and analyze the spatial distribution of the electric field within the brain. Generating a high-resolution forward model is critical for building an explicit patient-specific head model, determining optimal positioning of electrodes, and predicting electric field generation across the brain for specific stimulation configurations (Faria et al., 2011; Rampersad et al., 2013; Wagner et al., 2013). Using such a forward model, multi-electrode stimulation can be optimized via specifically designed mathematical methodology (Dmochowski et al., 2011; Ruffini et al., 2014; Guler et al., 2016; Wagner et al., 2016; Fernandez-Corazza et al., 2020), such as the recently developed convex optimization schemes including the Distributed Constrained Maximum Intensity (D-CMI) (Khan et al., 2022), and the metaheuristic L1-norm regularized L1-norm fitting (L1L1) (Galaz Prieto et al., 2022) which aim at an individualized distributional fit for a given target activity.

In this study, we aim to broaden the applicability of the linear programming (LP)-based L1L1 method for finding tES electrode montages computationally in a comprehensive manner, i.e., by evaluating the metaheuristic results and total computing time through different mathematical optimization algorithms and packages; this includes Interior-Point (IP) (Mehrotra, 1992), Primal-Simplex (PS), and Dual-Simplex (DS) (Boyd and Vandenberghe, 2004) as alternative LP algorithms, and Matlab (R2020b) from MathWorks (Zhang, 1999), MOSEK Optimization Suite (Release 9.0) (Mosek, 2019), Gurobi Optimization (9.5.1) (Gurobi Optimization LLC, 2022), SDPT3 (4.0) (Tütüncü et al., 2003), and SeDuMi (1.3.5) (Sturm, 1999; Frenk et al., 2000; Polik et al., 2007) as alternative packages. The latter two open-source alternatives are available in the CVX optimization toolbox (Grant and Boyd, 2014). We also investigate the metaheuristic hyperparameter optimization (HPO) task of L1L1 via exhaustive search (Bianchi et al., 2009) and recursive search (Je and Park, 2013) with heuristic direct search as a reference algorithm (Bogani et al., 2009).

Our results suggest that the performance differences between the above-mentioned optimization packages, algorithms, and search methodology can be crucial regarding the optimization results, focality stimulation current, and the availability of active channels in the montage. Moreover, exhaustive and recursive search methods can also be considered preferable to heuristic direct search in terms of their overall reliability and predictability.

2 Materials and methods

In tES, a real $L \times 1$ current pattern $\mathbf{y}$ is injected into the subject's head through a set of contact electrodes attached to the scalp. These electrodes, ranging from 0.5 to 4.0 milliamperes (mA) (Zaghi et al., 2010; Khadka et al., 2020; Workman et al., 2020), form what is known as an electrode montage and are responsible for distributing the injected volumetric current density–measured in ampere per square meter (A/m^2)–throughout the scalp, skull, cerebrospinal fluid (CSF), and brain components, including cortical and subcortical brain structures. The governing linear system is of the form

$$\hat{\mathbf{L}}\mathbf{y} = \hat{\mathbf{x}}, \tag{1}$$

where $\hat{\mathbf{L}}$ is a real $N \times L$ lead field matrix (forward mapping) that describes the relationship between the $\mathbf{y}$, and $\hat{\mathbf{x}}$ is a real $N \times 1$ discretized volume current density vector. The linear system (Equation 1) is re-interpreted component-wise as the focused field $\hat{\mathbf{L}}_1\mathbf{y} = \hat{\mathbf{x}}_1$, where the target field has non-zero values, and the nuisance field $\hat{\mathbf{L}}_2\mathbf{y} = \mathbf{0}$, where it vanishes. Detailed mathematical definition of the lead field matrix refer to *Appendix A. Forward model* in Galaz Prieto et al. (2022).

The optimization problem needs to find the best matching between $\mathbf{y}$, and the focused field via $\mathbf{L}\mathbf{y} = \mathbf{x}$, where the projection of the focused field into the direction of the target constitutes the first component as

$$\mathbf{L} = \begin{pmatrix} \mathbf{L}_1 \\ \mathbf{L}_2 \end{pmatrix} = \begin{pmatrix} \mathbf{P}\hat{\mathbf{L}}_1 \\ \hat{\mathbf{L}}_2 \end{pmatrix} \quad \text{and} \quad \mathbf{x} = \begin{pmatrix} \mathbf{x}_1 \\ \mathbf{0} \end{pmatrix} = \begin{pmatrix} \mathbf{P}\hat{\mathbf{x}}_1 \\ \mathbf{0} \end{pmatrix}$$

with $\mathbf{P}$ denoting a matrix that projects a vector into the direction of $\hat{\mathbf{x}}_1$. The target amplitude $\|\mathbf{x}_1\|_2$ is set as 3.85 A/m^2 which is an approximation of the excitation current threshold for nerve fibers of the upper limb area of the motor cortex (Kowalski et al., 2002).

2.1 L1-norm fitted and regularized optimization

The goal in L1-norm Fitted and Regularized (L1L1) optimization method (Galaz Prieto et al., 2022) is to minimize

$$\min_{\mathbf{y}} \left\{ \left\| \begin{pmatrix} \mathbf{L}_1\mathbf{y} - \mathbf{x}_1 \\ \Psi_\varepsilon[\nu^{-1}\mathbf{L}_2\mathbf{y}] \end{pmatrix} \right\|_1 + \alpha\zeta\,\|\mathbf{y}\|_1 \right\}, \qquad (2)$$
$$\text{s.t.} \qquad \mathbf{y} \preceq \gamma\,\mathbf{1}, \quad \|\mathbf{y}\|_1 \leq \mu, \quad \sum_{\ell=1}^{L} y_\ell = 0.$$

The injection on every active ℓ-th electrode channel is limited to $\gamma \leq 2.0$ mA, the total injection current dose flowing through the tES head cap is within the safety limit $\mu \leq 4.0$ mA, and the total sum of electric current from every active electrode channel in y_ℓ, where $\ell \in \{1, \cdots, L\}$, must be equal to zero. The regularization parameter α sets the level of L1-regularization with respect to the scaling value $\zeta = \|\mathbf{L}\|_1$. The function

$$\Psi_\varepsilon[\mathbf{w}]_m = \max\{\, |w_m|, \varepsilon \,\} \quad \text{for} \quad m = \{1, 2, \cdots, M\},$$

where $\mathbf{w} = (w_1, w_2, \cdots, w_M)$, sets the nuisance field threshold $0 \leq \varepsilon \leq 1$ with respect to the scaling value $\nu = \|\mathbf{x}\|_\infty$, meaning that entries $(\mathbf{L}_2\mathbf{y})_m$ with an absolute value below $\varepsilon\nu$ do not actively contribute to the minimization process due to the threshold. We refer to the set $\{\, m : |(\mathbf{L}_2\mathbf{y})_m| \geq \varepsilon\nu \,\}$ as the *constraint support*, i.e., the index set contributing to the value of the objective function. Detailed formulation of the linear programming system (Equation 2) can be found in Galaz Prieto et al. (2022).

The current density Γ of the focused field is defined as

$$\Gamma = \frac{\mathbf{x}_1^T \mathbf{L}_1 \mathbf{y}}{\|\mathbf{x}_1\|_2} \quad \text{and} \quad \Gamma_{\max} = \arg\max_{\mathbf{y},\alpha,\varepsilon} \Gamma\,,$$

and the focality of the stimulus Θ is defined as the following current ratio

$$\Theta = \frac{\Gamma}{\|\mathbf{L}_2\mathbf{y}\|_2/\sqrt{M}} \quad \text{and} \quad \Theta_{\max} = \arg\max_{\mathbf{y},\alpha,\varepsilon} \Theta.$$

The metacriterion $\Gamma \geq \Gamma_0$ is applied to maintain appropriate intensity at the target location. Namely, without a lower bound for the intensity, the intensity of the maximizer is likely to vanish.

2.2 Two-stage metaheuristic lattice search

To derive a multi-channel tES montage following the aforementioned equations, the optimization framework takes into account the following indications: (A) a procedure for selecting the most relevant electrodes in the montage for a given region of interest; (B) a definition of the tuning parameters which will maximize or minimize the objective function; and (C) a method to evaluate said parameters and retrieve data (search method). In this study, 128 electrodes were attached to the scalp following the international 10-10 EEG hardware system with an impedance of 2.0 kOhm (kiloohms). Physiological impediments in the head model, fluctuation in conductivity tissue, and behavior of the injected current aspects are excluded. The framework of this search is as follows:

(A) The *two-stage* determines which of the tES channels in the neurostimulator headgear should be set as active or inactive based on the field distribution on the head surface for a given current source in the brain. After calculating the lead field matrix, the user specifies an approximate region of interest through forward dipole modeling (Bauer et al., 2015; Medani et al., 2015; Pursiainen et al., 2016). This is the highlighted region from which the two-stage procedure shall prioritize the electrode selection as follows:

  (A.1). During the first stage, the optimization model sets all channels with an initial current of zero value and determines a volumetric current density influenced by the electric properties, direction, and positioning of the dipole modeling. Then, the optimization model filters the montage down to a (user-defined) number of electrodes that contribute the most to the maximal safety tES current injection based on the initial range of α and ε values provided. The corresponding electric potential from the now-limited montage with channels y_ℓ is normalized to meet the intended maximum current injection μ value while the remaining electrodes are opted out of further calculations. We constraint the total number of active electrodes available to $\ell = 20$ inspired by commercial tES systems (Roy et al., 2019; Tost et al., 2021).

  (A.2). In the second stage, the optimization re-runs using only the active electrodes obtained previously. In this stage, the objective function can be retroactively modified to retrieve a customized montage that favors an intense volumetric current density Γ or a maximal stimulation focality given a target current Θ. The final result is then thresholded to a non-zero number of currents in the pattern.

(B) Using *metaheuristic* methodology means developing an algorithm that can produce near-optimal results in a computationally feasible time (Bianchi et al., 2009). In the present context, the objective is to iteratively adjust the parameters α and ε to ascertain a solution that minimally impairs the objective function. The aim is to secure a heightened amplitude within the targeted focus field while concurrently mitigating undesirable signals (the nuisance field). We define a parameter space by specifying ranges for α_m from -100 to -20 dB and ε_n from -160 to 0 dB, employing logarithmic increments. Plotting these parameter values on a Cartesian plane elucidates the search space κ, subject to a set of constraints delineated by the linear programming paradigm at hand.

(C) The *lattice search* aspect defines the instructions on how to retrieve information from the search space κ for solving (Equation 2). This task can be considered as a hyperparameter optimization (HPO) exercise (Feurer and Hutter, 2019; Yang and Shami, 2020) for building a predictive model that performs best when using the most fitting α_m and ε_n parameters. The following exploration techniques are evaluated for finding these parameters: *exhaustive search, direct search*, and *recursive search*.

(C.1) The *exhaustive search*, or grid search, systematically evaluates every possible candidate solution within the search space κ, i.e., the Cartesian product of each α_m and ε_n value in existence (Figure 1A). The final candidate solution is the combination that best minimizes the objective function. We applied a coarse grid of size $\kappa = 15$ and compared it against a finer grid of size $\kappa = 40$.

(C.2) By *direct search*, we refer to the Generalized direct search (GPS) (Bogani et al., 2009) available in the Matlab's optimization toolbox. It aims at finding a point in the hyperparameter space without knowledge of any gradient. The method begins with a given search window $D^{(i)}$ and an initial estimate $\psi^{(i)}_{(\alpha,\varepsilon)}$ acting as a pivot. The location of this window is centralized over the pivot along with its four orthogonal neighbor points in the Euclidian distance $w^{(i)}$, i.e.,

$$D^{(i)} = \{\psi^{(i)}_{(\alpha_m,\varepsilon_n)}, \psi^{(i)}_{(\alpha_m,\varepsilon_{n+w^{(i)}})},$$
$$\psi^{(i)}_{(\alpha_{m+w^{(i)}},\varepsilon_n)}, \psi^{(i)}_{(\alpha_m,\varepsilon_{n-w^{(i)}})}, \psi^{(i)}_{(\alpha_{m-w^{(i)}},\varepsilon_n)}\}.$$

Figure 1B depicts the mesh and its behavior. At each i-th iteration within the mesh, if a neighboring point performs better than the center point, the window reallocates this point as the new pivot. If none of these points yields a better output, then the length of the mesh w is reduced, and a new set of neighbor points is adopted. That is,

$$w^{(i+1)} = \begin{cases} w^{(i)}, & \text{if } \psi^{(i+1)}_{(\alpha_m,\varepsilon_n)} \leq \psi^{(i)}_{(\alpha_m,\varepsilon_n)}, \\ w^{(i)}/2, & \text{if none satisfies.} \end{cases}$$

The cycle repeats until the number of i iterations is reached or the algorithm is unable to find any better point.

(C.3) The *recursive search* is a modified version of the three-step search block-matching algorithm (Je and Park, 2013) that resembles a combination of the previously mentioned methods; it defines the subset of the hyperparameter space as in (C.1), and converges towards the most fitting solution by recursively reducing the region of feasibility similar to (C.2). In this study, we adapted the algorithm for tuning α and ε by dividing these finite sets into two linearly-spaced vectors with $\{\tilde{\kappa}\}$ points, recursively through a number of M iterations, taking their minimum and maximal values as their lower and upper bounds, i.e.,

$$\tilde{\alpha}^{(M+1)} = \{(\alpha^{(M)}_{\tilde{\kappa}} - \alpha^{(M)}_1)/(\tilde{\kappa} - 1)\}, \text{ and}$$
$$\tilde{\varepsilon}^{(M+1)} = \{(\varepsilon^{(M)}_{\tilde{\kappa}} - \varepsilon^{(M)}_1)/(\tilde{\kappa} - 1)\}, \text{ respectively.}$$

Thus, the method updates the hyperparameter space by replacing it with a narrower subspace instead of shrinking the search window (Figure 1C). At each M-th iteration, the search window, with initial size $w_i = \beta_i{}^2$, finds the center of the subspace such that

$$\frac{1}{\beta_i}\psi^{(i)} \leq \psi^{(i)} \leq \beta_i\psi^{(i)},$$

where $\psi^{(i)}$ is the central point at the i-th grid and the optimal solution from the previous (or initial) feasible region $\beta^{-1}_{i-1}\psi^{(i-1)} \leq \psi^{(i-1)} \leq \beta_{i-1}\psi^{(i-1)}$. A search window of size w_{i+1} is centered at the location of $\psi^{(i)}$, i.e., $\beta_i = s\beta_{i-1}$ with $s > 0$,

$$w_M = \beta^2_M = \left(\frac{u_0}{l_0}\right)^{1/K} \quad \text{and} \quad s = \left(\frac{l_0}{u_0}\right)^{\frac{K-1}{KM}},$$

where u_0 and l_0 are the upper and lower limits from the initial hyperparameter space, respectively, and K equals a user-defined reference lattice size for a single non-recursive search. We evaluate and compare this method by setting $\tilde{\kappa} = \{3, 5, 7, 9\}$, with $M = \{1, \cdots, 3\}$ in each case. With this set of equations, the workload of an exhaustive search is reduced to $O(M\tilde{K}^2)$, where $\tilde{K}$ is a smaller grid size, i.e, $\tilde{K} < \frac{K}{\sqrt{M}}$.

Additionally, we estimated the limits for the lattice-induced deviation of $\Theta_{\max}$ and $\Gamma_{\max}$ via a second-order Taylor's polynomial approximation (Sauer, 2018), With this strategy, the deviation is obtained with respect to a hypothetical lattice with twice the resolution compared to the actual one.

2.3 Reciprocity principle

The Reciprocity Principle (Fernandez-Corazza et al., 2020) is an explicit approach for obtaining maximum current density, $\Gamma_{\max}$, based on the reciprocity of the electromagnetic field propagation. Specifically, the maximum stimulation amplitude is obtained with a two-patch tES electrode montage corresponding to the two greatest EEG electrode voltages generated by a desired target current in the brain. The principle considers the connection between the forward and reverse propagation of the electromagnetic field, which is predicted by the lead field matrix.

2.3.1 Formulation of the reciprocity principle for a tES lead field matrix

While gradient propagation in general electromagnetism is not always reciprocal, it can be shown that a bipolar montage in tES corresponds to the greatest absolute back-projected currents in the vector $\mathbf{L}^{\mathbf{T}}\mathbf{x}_1$. The reciprocity principle can be formulated, for a restricted system, as

$$\mathbf{L}\mathbf{R}_K\mathbf{y}_K = \mathbf{x}, \tag{3}$$

where $\mathbf{R}_K$ denotes a real $N \times K$ $(K \leq N)$ restriction matrix whose nonzero entries $r_{i_j,j} = 1$ correspond to an ordered subset of electrodes

$$\mathcal{S} = i_j : j = 1, 2, \cdots, K, \text{ with } |(\mathbf{L}^T_1\mathbf{x}_1)_{i_1}| \geq |(\mathbf{L}^T_1\mathbf{x}_1)_{i_2}| \geq \cdots$$
$$\geq |(\mathbf{L}^T_1\mathbf{x}_1)_{i_K}|.$$

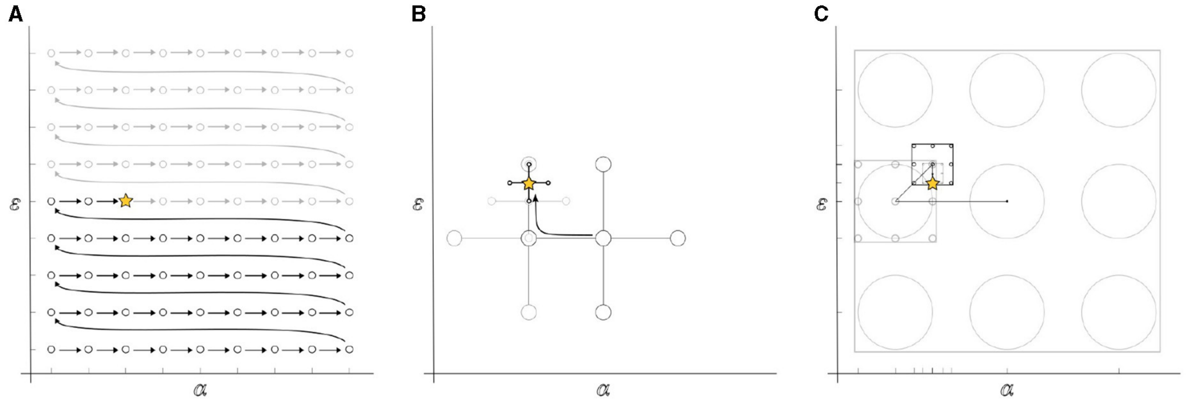

FIGURE 1
Schematic illustration of the Hyperparameter Optimization (HPO) techniques applied; **(A)** the exhaustive search method evaluates the entire hyperparameter space, case by case; **(B)** The direct search method employs a pattern that shrinks in size towards the direction in which the objective function decays; and **(C)** the recursive search divides the space into subspaces based on the size of the search lattice, shrinking and repositioning the lattice towards the most fitting solution in a recursive manner.

The reciprocity principle follows by writing the intensity as $\Gamma = \sigma_K \mathbf{y}_K^T \mathbf{s}_K$ with $\sigma_K = \|\mathbf{R}_K \mathbf{L}_1^T \mathbf{x}_1\|_1 / \|\mathbf{x}_1\|_2$ and $\mathbf{s}_K = \mathbf{R}_K \mathbf{L}_1^T \mathbf{x}_1 / \|\mathbf{R}_K \mathbf{L}_1^T \mathbf{x}_1\|_1$ describing that Γ can be interpreted as a projection of $\mathbf{y}_K$ on $\sigma_K\, \mathbf{s}_K$. Thus, the maximum of Γ is achieved when $\mathbf{y}_K$ is parallel to $\mathbf{s}_K$. The maximizer is then up-scaled to match the applied current dose μ, i.e., $\mathbf{y}_K = \mu\, \mathbf{s}_K$. Therefore, the corresponding maximum intensity is $\Gamma = \mu\, \sigma_K\, \|\mathbf{s}_K\|_2^2$. The optimal maximizer montage is

$$\max_K \mu\, \sigma_K \|\mathbf{s}_K\|_2^2\,,$$

where, by definition, $\|\mathbf{s}_K\|_1 = 1$ for any $K = 1, 2, \ldots, N$, and the entries of $\mathbf{s}_K$ are ordered in descending order with respect to their absolute value. Assuming that these entries are given by $\lambda_1 \geq \lambda_2 \geq \cdots \geq \lambda_K \geq 0$, respectively, it holds that $\|\mathbf{s}_K\|_1 = \sum_{j=1}^{K} \lambda_j$, $\|\mathbf{s}_{K-1}\|_1 = (\lambda_j - 1)^{-1} \sum_{j=1}^{K-1} \lambda_j$, and

$$\begin{aligned}\|\mathbf{s}_K\|_2^2 - \|\mathbf{s}_{K-1}\|_2^2 = \frac{\lambda_K}{1-\lambda_K}\left(\lambda_K^2 - \lambda_K + \frac{2-\lambda_K}{1-\lambda_K}\sum_{j=1}^{K-1}\lambda_j^2\right) \geq \\ \frac{\lambda_K}{1-\lambda_K}\left(\lambda_K^2 - \lambda_K + 2\sum_{j=1}^{K-1}\lambda_j^2\right) \\ \geq \frac{\lambda_K}{1-\lambda_K}\left(K\lambda_K^2 - \lambda_K + \sum_{j=1}^{K-1}\lambda_j^2\right)\,.\end{aligned}$$

The equality follows a straightforward substitution, the first inequality is based on

$$\frac{2-\lambda_K}{1-\lambda_K} = 1 + \frac{1}{1-\lambda_K} \geq 2,$$

and the second one is obtained as $(K-1)\lambda_K^2 \leq \sum_{j=1}^{K-1} \lambda_{i_j}^2$. Following from the discriminant, together with the Arithmetic Mean–Quadratic Mean inequality

$$\frac{1}{K-1}\sum_{j=1}^{K-1}\lambda_j^2 \geq \left(\frac{1}{1-K}\sum_{j=1}^{K-1}\lambda_j\right)^2,$$

The second factor in Equation (3) does not have roots if

$$K\sum_{j=1}^{K-1}\lambda_j^2 \geq \left(\sum_{j=1}^{K-1}\lambda_j\right)^2 \geq \frac{1}{4}\,, \quad \text{i.e.,} \quad \sum_{j=1}^{K-1}\lambda_j \geq \frac{1}{2}\,.$$

This assumption is valid since a montage with only two active channels cannot contain more than two halves of the total dose (otherwise, the sum of said currents will be less than zero). Hence, $\|\mathbf{s}_K\|_2^2 - \|\mathbf{s}_{K-1}\|_2^2 \geq 0$ for any montage, and the maximum of Γ is obtained with the bipolar pattern that corresponds to the first two entries i_1 and i_2 in the set $\mathcal{S}$.

2.4 Mathematical optimization software

We solve the optimization task (Equation 2) using the Interior-Point (IP), the Primal-Simplex (PS), and the Dual-Simplex (DS) methods. The class of the IP methods is sub-divided into the primal-dual algorithms (predictor-corrector) (Fiacco and McCormick, 1964; Mehrotra, 1992) and the barrier methods, which determine the feasible set via a barrier function. While IP methods utilize Newton's method to operate in the interior of a feasible set (Boyd and Vandenberghe, 2004), simplex methods seek solutions by considering the feasible set as a convex polytope and moving along its edges. While this strategy uses less memory than the interior-point strategy, it has lower predictability for large-problem convergence.

The concepts of primal- and dual-simplex refer to the formulation of the linear programming problem; by presenting the entries of the current pattern $\mathbf{y}$ as differences of non-negative variables ($y_i = s_i - p_i$, $s_i, p_i \geq 0$) and the equality constraint via two inequalities (condition $a = 0$ is satisfied, $a \leq 0$ and $-a \leq 0$), the task can be brought back to the following standard primal formulation:

$$\max_{\mathbf{z}} \mathbf{c}^T\mathbf{z} \quad \text{subject to} \quad \mathbf{A}\mathbf{z} \leq \mathbf{b}, \quad \mathbf{z} \geq 0\,,$$

TABLE 1 Description of the Linear Programming (LP) solvers applied for solving the L1L1 optimization problem through the Interior-Point (IP), Primal-Simplex (PS), and Dual-Simplex (DS) algorithms.

Solver	Interface	Method	Code
Matlab 2020b	Optimization toolbox	Interior-Point (Primal-Dual)	Matlab IP
		Primal-Simplex	Matlab PS
		Dual-Simplex	Matlab DS
MOSEK 9.0	MOSEK toolbox	Interior-Point (Primal-Dual)	MOSEK IP
		Primal-Simplex	MOSEK PS
		Dual-Simplex	MOSEK DS
Gurobi Optimizer	Gurobi toolbox	Interior-Point (Barrier Method)	Gurobi IP
		Primal-Simplex	Gurobi PS
		Dual-Simplex	Gurobi DS
SDPT3 4.0	CVX 2.1	Interior-Point (Primal-Dual)	SDPT3 IP
SeDuMi 1.3.5	CVX 2.1	Interior-Point (Primal-Dual)	SeDuMi IP

All solvers were embedded with Matlab's version R2020b and called by the optimizer of the Zeffiro Interface (ZI) toolbox. Matlab, MOSEK, CVX's SDPT3, and CVX's SeDuMi apply primal-dual routines, and Gurobi uses the barrier method.

whose dual is given by

$$\min_{\hat{\mathbf{z}}} \mathbf{b}^T\hat{\mathbf{z}} \quad \text{subject to} \quad \mathbf{A}^T\hat{\mathbf{z}} \geq \mathbf{c}, \quad \hat{\mathbf{z}} \geq 0\,.$$

The IP algorithms applied in this study include Gurobi's parallel barrier method and the primal-dual routines from Matlab, MOSEK, SDPT3, and SeDuMi. The simplex methods include MOSEK's PS and DS, Gurobi's PS and DS, and Matlab's DS algorithm. Matlab's Optimization Toolbox has two IP solvers, of which we apply the interior-point legacy (IPL), whose origin is in the Linear-Programming Interior Point Solvers (LIPSOL) package (Zhang, 1999). All the solvers, their types, and their abbreviations used in this study are described in Table 1.

2.5 Numerical domain and computing platform

As the domain of the numerical simulations, we applied a realistic tetrahedral 1.0 mm FE mesh based on an open T1-weighted Magnetic Resonance Imaging (MRI) dataset[1]. Through FreeSurfer Software Suite[2], we segmented the data to find the complex surface boundaries between different tissue compartments, including the skin, skull, cerebrospinal fluid (CSF), gray and white matter, and subcortical structures such as brain stem, thalamus, amygdala, and ventricles (Fischl, 2012). Their conductivity values, which influence the accuracy of the forward solution (Montes-Restrepo et al., 2014), were set according to (Dannhauer et al., 2011). We discretized the volumetric current density to solve the inverse problem using 563 spatial nodes evenly distributed in the gray and white matter compartments of the cerebrum and cerebellum with approximately 1.3 cm (centimeters) distance between two neighboring nodes, associating each node with three divergence-free Cartesian field components.

Through dipole modeling (Bauer et al., 2015; Medani et al., 2015; Pursiainen et al., 2016), we define the region of interests from which the multi-channel tES montage should be derived. We selected the primary somatosensory cortex in the postcentral gyrus (Figure 2A), the primary auditory cortex of the posterior superior temporal gyrus (Figure 2B), and the primary visual cortex in the occipital lobe (Figure 2C) as the target areas. Each dipole is normally oriented with respect to the surface of the gray matter to satisfy the normal constraint of brain activity in the cerebral cortex (Creutzfeldt et al., 1962). Each L1L1 method-based current pattern obtained represents an approximative solution to the optimization problem (Equation 2) corresponding to one of the aforementioned areas.

We performed the numerical simulations using a Dell 5820 workstation with a 10-core Intel Core i9-10900X processor and 256 GB of RAM. The L1L1 solver was implemented in Matlab-based Zeffiro Interface toolbox[3] (He et al., 2019) which builds a high-resolution finite element (FE) mesh and generates a tES lead field matrix (Galaz Prieto et al., 2022) for a given surface-based head segmentation incorporating the Complete Electrode Model's (CEM) boundary conditions (Pursiainen et al., 2012, 2017).

3 Results

The exhaustive search proved to be a reliable method for experimental benchmarking when the required tES montage requires careful design for clinical applications. By presenting the exhaustive search results in the form of a heatmap with a coarse grid of $\kappa = 15$ (Figure 3A), we can pinpoint the (α, ε) region where the focused current amplitude reaches its maximum. Despite a significantly increased number of evaluations, with a finer grid of $\kappa = 40$ (Figure 3B), we can further determine a more detailed optimal area. This area corresponds to the Cartesian product of α_m ranging from -71 to -50 dB and ε_n from 0 to -98 dB. In this context, a high current injection montage, denoted by $\Gamma_{\max}$ (yellow star), is positioned at the peak of the amplitude, while focality-based montages, $\Theta_{\max}$ (purple star), adhere closely. However, these focality-based montages are slightly deviated due to the influence of the nuisance field, despite being relatively close, as determined by a threshold condition corresponding to 75% of the maximum amplitude achievable with the two-patch bipolar tES montage. In comparison between these grid resolutions, one can observe slight enhancements in amplitude, increased optimization accuracy, and improved numerical stability in the latter case. These aspects are far more noticeable with Dual- and Primal-Simplex methods than with the Interior-Point, which yields overall smoother results with fewer drastic deviations.

Figure 4 delineates the performance nuances among optimization strategies. The whiskers along the stems signify a second-order Taylor's polynomial estimate, reflecting the maximum deviation within half lattice units distance from

---

[1] https://brain-development.org/ixi-dataset/

[2] https://surfer.nmr.mgh.harvard.edu/

[3] https://github.com/sampsapursiainen/zeffiro_interface

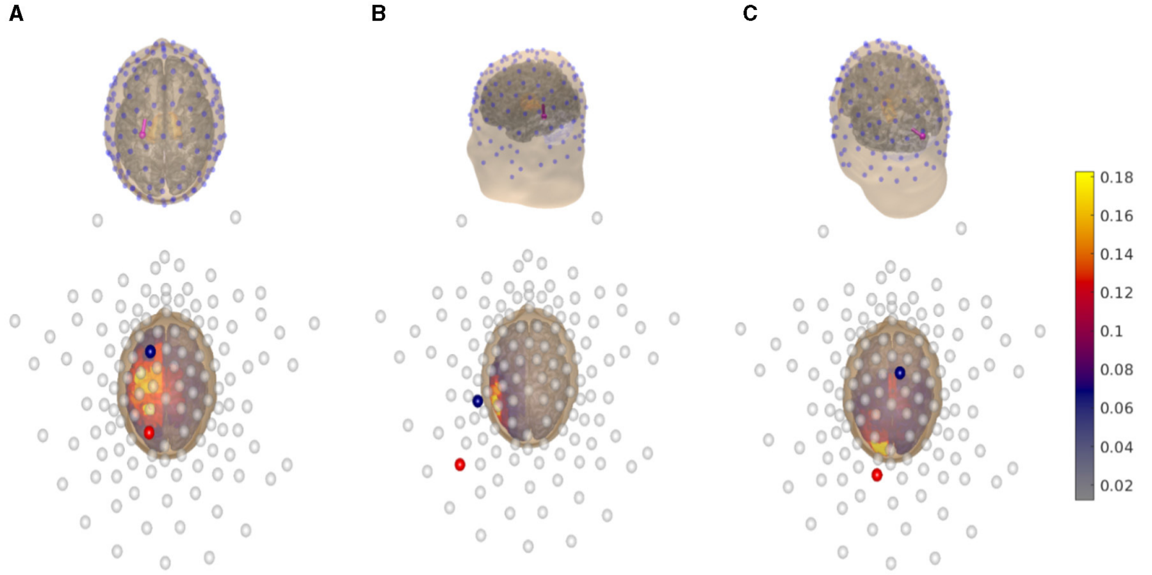

FIGURE 2
Top row: 3D view of the head model coupled with a 128-channel electrode array (blue dots) following a 10-10 EEG hardware configuration. A synthetic dipole, (magenta spherical arrow), which simulates a current distribution, is placed at the **(A)** primary somatosensory cortex in the postcentral gyrus, **(B)** primary auditory cortex in posterior superior temporal gyrus, and **(C)** primary visual cortex in the occipital lobe, respectively. **Bottom row:** 2D plane view of the head model displaying the electric field distribution generated by an optimal tES montage following the reciprocity principle which maximizes the focused volumetric current density. The direction of the injection current pattern generated by the montage matches the dipole's orientation. The anodal channels (red spheres) are found by the posterior, while the cathodal channels (blue spheres) by the parietal or frontal sections. The empty circles indicate inactive channels. The volumetric current density is given in Amperes per square meter (A/m^2).

the optimizer. The reciprocity principle reference for $\Gamma_{\max}$ is represented by a horizontal black dashed line, and the number of non-zero (NNZ) channels required for a tES montage is depicted on the right side of each corresponding stem. The solvers are sorted in ascending order based on their performance, with the exhaustive search $\kappa = 40$ grid (blue) serving as the point of reference. Both the direct and recursive search techniques adeptly uncover optimal (α, ε) solutions for $\Theta_{\max}$ and $\Gamma_{\max}$, yielding a substantial reduction in total computing time compared to the specified hyperparameter space.

Due to the heuristic nature of the direct search, and to assert the efficacy of the said technique, we performed a series of trial runs by setting the initial point to the center of the search space. In these trials, the number of objective function evaluations varied, ranging from 25 to 54 trials, with a 33.8 mean among the evaluations (see Table 2). While the number of function evaluations was slightly higher, the quality of the results was nearly on par with those obtained with the recursive search with a search window of $\tilde{K} = 3$. With IP solvers, the search runs were mostly successful, while PS and DS tended to fail to find a feasible optimizer candidate.

Due to its relatively fast performance among interior-point methods, we applied MOSEK IP to evaluate topographical maps of stimulus focality $\Theta_{\max}$ (Figure 5A) and current density $\Gamma_{\max}$ (Figure 5B) for an exhaustive search $\kappa = 15$ and a recursive search $\tilde{K} = 3$. Overall, the results of the recursion were close to the outcome of the exhaustive search. Thus, the topographical differences between the different approaches of this study were observed to be minor.

By limiting the search space only to a narrower subspace is a simple countermeasure for dealing with the disadvantages of the exhaustive search. With a $\kappa = 15$ grid as a reference, it can take approximately 850 seconds to perform a complete search for the first stage, while the second stage only takes roughly 15% of that time since it uses a limited lead field following from the limited number of active electrodes. As an alternative approach, the direct and recursive search seemed to perform well compared to the number of objective function evaluations made during the search process (Figure 6). In particular, MOSEK turned out to be the superior choice, with MOSEK DS being the fastest one. The computing time for Gurobi IP was close to that of MOSEK IP, and Gurobi DS, PS, and Matlab IPL and DS required approximately three times the time. The slowest-performing SDPT3 and SeDuMi took as much as six times the run time of MOSEK IP. Overall, the simplex methods applied to the L1L1 optimization scheme deliver faster yet less accurate solutions than Interior-Point (IP) for focality-based montages, while minor differences can be found for intensity-based solutions.

4 Discussion

In this study, we analyzed the numerical and computational performance of exhaustive search, direct search, and recursive search techniques to find an optimal stimulation focality Θ and current density Γ for solving the L1L1 optimization problem for non-invasive transcranial electrical stimulation (tES) current injection. This analysis was motivated by our earlier results in (Galaz Prieto et al., 2022) which suggested that the L1L1 method

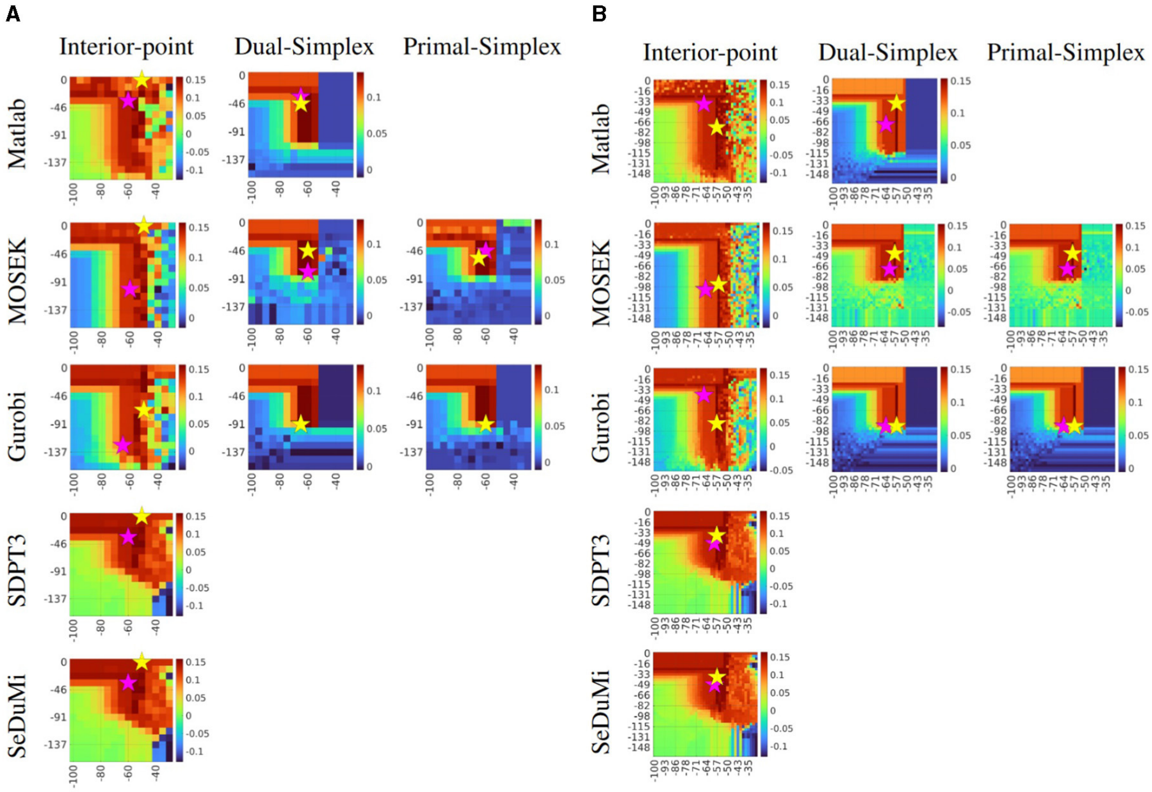

FIGURE 3
Performance comparison of the exhaustive search for solving the L1-norm fitted and penalized (L1L1) optimization method with current density Γ as the objective function. The coarse **(A)** search space $\kappa = 15$ produces 225 evaluations, and the finer **(B)** search space $\kappa = 40$ with 1600 evaluations, both using regularization parameter α (x-axis) and the nuisance threshold level ε (y-axis). The candidate solutions with respect to current density $\Gamma_{\max}$ and focality $\Theta_{\max}$ are marked with a yellow and purple star, respectively. The maximizers are generally found around from area in which α is between -71 to -50 dB dB (decibels) and ε from 0 to -98 dB. Notice that in the case of using the Gurobi package, with a Simplex algorithm, both optimal candidate solutions for either a stimulus focality or a current density both optimal solutions are taking the same (α, ε) tuning parameters due to the sharp steepness from the coarse search space. The volumetric current density on every chart is given in Amperes per square meter (A/m^2).

provides a theoretically attractive approach for obtaining a high-gain focal stimulus as compared to complex L2-norm fitting and regularized least squares techniques (Dmochowski et al., 2011; Wagner et al., 2016).

The reciprocity principle, as outlined by Fernandez-Corazza et al. (2020), served as a reference technique. Its validity was shown for the present tES lead field matrix **L** (see Section 2.3.1). When focusing on a specific target region, the current injection pattern from a two-patch tES montage aligns with the maximum intensity achievable through this principle. Essentially, this involves selecting the two electrodes with the highest absolute back-projected currents. With the absence of nuisance field constraints, the L1L1 solution was observed to agree with the reciprocity principle if the aforementioned algorithmic aspects were handled appropriately.

Decisive aspects for a successful outcome of L1L1 were found to be the choice of the optimization package, algorithm, and search routine, which significantly affect both the performance of the metaheuristic optimization process and output. To enlighten this aspect, we covered the performance of several Interior-Point (IP) (Mehrotra, 1992), Dual-Simplex (DS), and Primal-Simplex (PS) (Boyd and Vandenberghe, 2004) methods from different open-source and commercial optimization toolboxes. We tested the L1L1 method using the commercial solvers of MOSEK Optimization Suite (Release 9) (Mosek, 2019) and Gurobi Optimization (9.5.1) (Gurobi Optimization LLC, 2022), and compared them to the open-source alternatives (Grant and Boyd, 2014) SDPT3 (4.0) (Tütüncü et al., 2003) and SeDuMi (1.3.5) (Sturm, 1999; Frenk et al., 2000; Polik et al., 2007) as well as Matlab R2020b's (MathWorks) Interior-Point-Legacy (IPL) algorithm, which originates from the open LIPSOL (Zhang, 1999) toolbox. We selected the IPL algorithm since we experienced stagnation with Matlab's main IP algorithm, which did not return any appropriate results.

Based on the results, we consider Gurobi IP to be the preferable choice in both optimization stages, considering $\Theta_{\max}$ and $\Gamma_{\max}$ in each tested target region of interest and, as it was also overall the fastest of the IP solvers. While the best-performing solvers show that the L1L1 method is suitable for maximizing focality and intensity, a few did not find the bipolar current pattern that maximizes $\Gamma_{\max}$. Notably, SDTP3 did not find a bipolar pattern at all, verifying our earlier hypothesis (Galaz Prieto et al., 2022) that the performance of L1L1 might be highly solver-based. Part of the discrepancies between the optimization methods can be explained by a different sensitivity with respect to parameter variation or the resolution of the lattice.

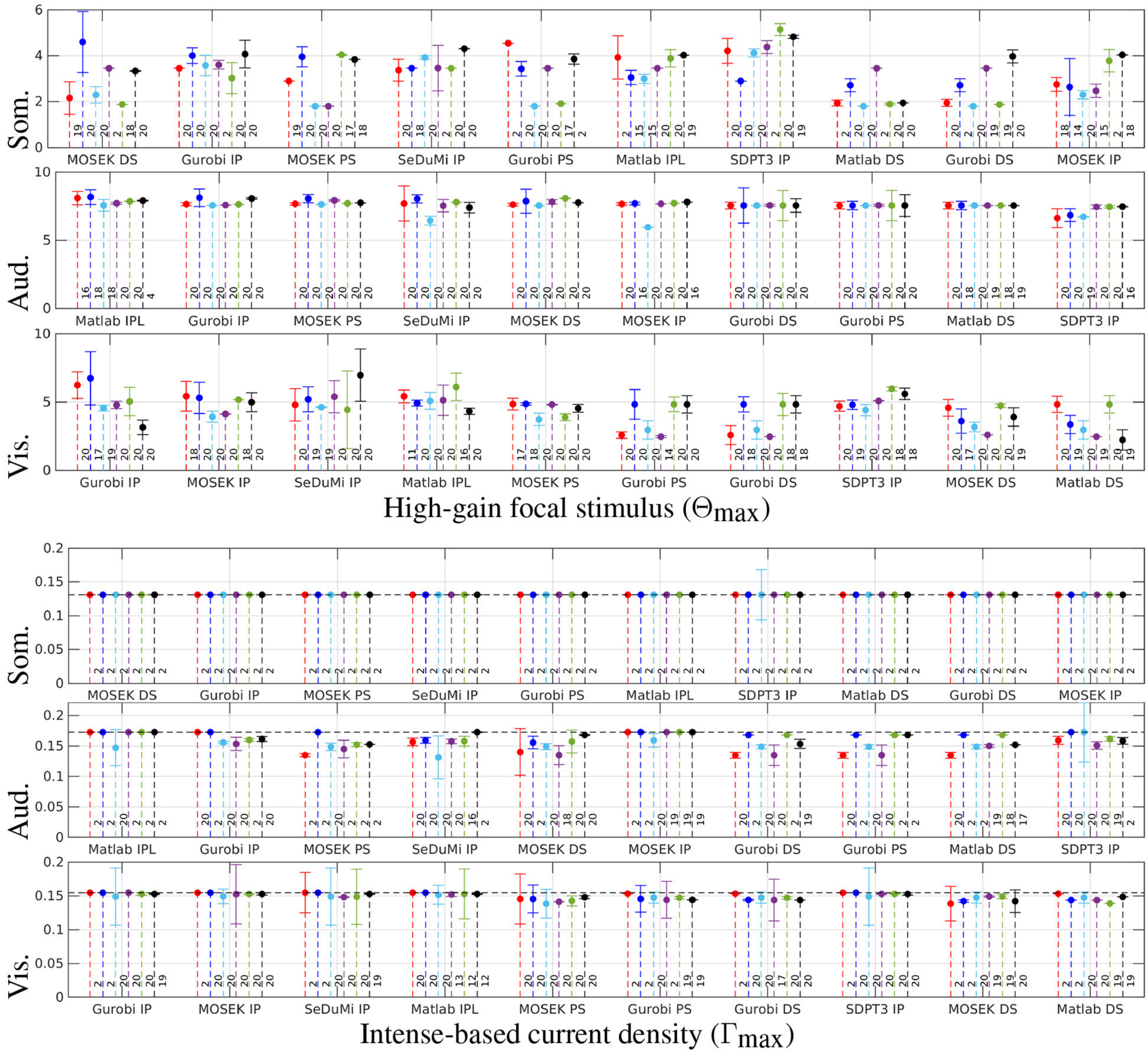

FIGURE 4
Stem plots results from the two-stage metaheuristic lattice search using exhaustive search with coarse grid of $\kappa = 15$ (red) and fine grid of $\kappa = 40$ (blue), and a recursive one with $\tilde{K} = \{3, 5, 7, 9\}$ (cyan, magenta, green, and black, respectively) considering the somatosensory (Som.), auditory (Aud.) and visual (Vis.) regions of interest. The whiskers in the stem plot indicate a second-order Taylor's polynomial estimate for the maximum deviation within a half-lattice unit distance from the optimizer. The intense current injection ($\Gamma_{\max}$) calculated using the reciprocity principle is shown with a horizontal black dashed line as a reference. The number of non-zero (NNZ) channels in the Transcranial Electrical Stimulation (tES) montage is shown on the right side next to the corresponding stem. The solvers are sorted in descending order from left to right based on their performance with $\kappa = 40$.

From a computational complexity standpoint, the exhaustive search method can be applied for benchmarking purposes. In contrast, a recursive search proves an advantageous alternative and is competitively on par with the direct search technique, each one applied in this study. This equivalence arises from both methods converging toward the most suitable regularization parameter α and nuisance threshold ε values in a comparably controlled manner. Notably, the computational complexity of recursive search remains consistent across various optimization runs, in contrast to the variability observed in the direct search. Results comparable to those obtained through exhaustive search can be attained with a reduced-resolution search window of, say, size $\tilde{K} = 3$, representing a substantial acceleration in comparison to exhaustive search. Furthermore, the recursive approach demonstrates both numerical stability and convergence towards exhaustive search results, both at individual data points and in the overall topographical context, as the probing lattice size increases.

4.1 Limitations and future work

Unlike earlier linear programming (LP) formulations for tES optimization problems, our use of the metaheuristic process enabled us to explore parameters freely, without imposing rigid

TABLE 2 Comparison of stimulation focality $\Theta_{\max}$ and intensity $\Gamma_{\max}$ results obtained between exhaustive, direct, and recursive search methods.

Search	Resolution	Levels	Window	Evaluations	Somatosensory		Auditory		Visual	
					$\Theta_{\max}$	$\Gamma_{\max}$	$\Theta_{\max}$	$\Gamma_{\max}$	$\Theta_{\max}$	$\Gamma_{\max}$
Exhaustive	Fixed	-	15	225	2.93	0.1315	6.47	0.1486	4.98	0.1488
Exhaustive	Fixed	-	40	1600	3.93	0.1315	7.69	0.1725	4.98	0.1574
Direct	Adaptive	-	-	28-54*	3.45	0.1315	7.75	0.1725	4.99	0.1488
Recursive	Adaptive	3	3	27	2.99	0.1315	6.47	0.1486	5.11	0.1514
	Adaptive	3	5	75	3.45	0.1315	6.92	0.1725	5.17	0.1545
	Adaptive	3	7	147	3.88	0.1315	7.10	0.1725	5.17	0.1545
	Adaptive	3	9	243	4.02	0.1315	7.68	0.1725	3.91	0.1545

The behavior of the search space (Resolution), number of resolution levels (Levels), search window size (Window), and the number of objective function evaluations (Evaluation) per optimization run are given. Non-applicable features are marked with the (-) symbol.

[*] In direct search, the number of objective function evaluations varied between different optimization runs.

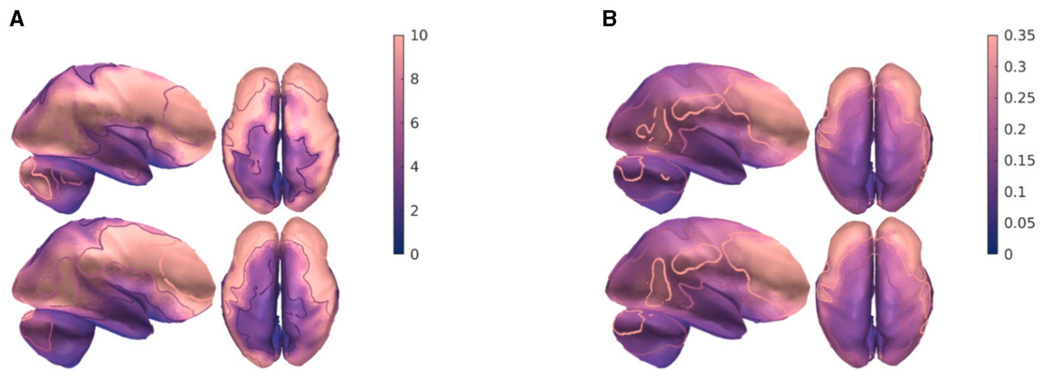

FIGURE 5
Comparison of the topographical maps for **(A)** maximum focality $\Theta_{\max}$ and **(B)** current density $\Gamma_{\max}$ using exhaustive search $\kappa = 15$ (top-row), and recursion with $\tilde{K} = 3$ (bottom-row). The contours show 20, 40, and 75% equicurves with respect to their maximum entry. Maps have been computed using the MOSEK with the Interior-point method.

a priori constraints on the nuisance field, as observed in Wagner et al. (2016). In L1L1, we optimally set the nuisance field through hyperparameter optimization embedded in a two-stage metaheuristic lattice search procedure. Interpreted as an enhancement for localizing both pattern and volumetric density of the stimulus, L1-norm fitting and regularization outperform the least-squares methodology introduced in Dmochowski et al. (2011, 2017). However, this improvement comes at a greater computational cost, prompting our in-depth investigation into various algorithmic aspects of metaheuristic optimization in this study. Our present findings underscore the critical role of computational considerations when integrating hyperparameters and metacriteria into the tES optimization problem, aspects overlooked in the studies mentioned earlier.

Our results concerning L1L1 are limited to numerically simulated tES only, meaning that neither the performance of the method in other modalities than tES nor the effects of uncertainty causing inter-subject variability (Laakso et al., 2015) have not been fully covered yet. Those might include, for example, any discrepancies between the estimated and actual values of electrical conductivity, such as skull conductivity (Schmidt et al., 2015), strategy to specify a montage (Kaufmann et al., 2021), as well as uncertainty about the targeted region in the brain, e.g., a possible spread of an epileptic focus (Simula et al., 2022). While the expected level of uncertainty can be controlled via the range of the hyperparameter ε, a future study on its effect will obviously need to be conducted.

Of the applied liner programming methods, interior-point is an overall preferable option over the simplex methods, which can be considered beneficial characteristic when hardware performance is limited, e.g., for a potential Field-Programmable Gate Array (FPGA) implementation (Bayliss et al., 2006; Gensheimer et al., 2014). Another comparative method, the Alternating Direction Method of Multipliers (ADMM) (Lin et al., 2021), was not included in this investigation as achieving an appropriate convergence seemed more difficult due to its dependence on a step-length parameter. While the current results enlighten how the different algorithms would perform with different nuisance threshold levels, an independent study would be needed to determine the optimal level given the mathematical uncertainty.

Possible future work directions can be to open up the function of L1L1 on a broader scale, this include applying it for deep brain stimulation (DBS), where the electrical stimulus is not transcranial. Likewise, an advanced optimization technique is needed to target subcortical nuclei of the brain; for instance, in the recent study (Anderson et al., 2018), where the Interior-Point

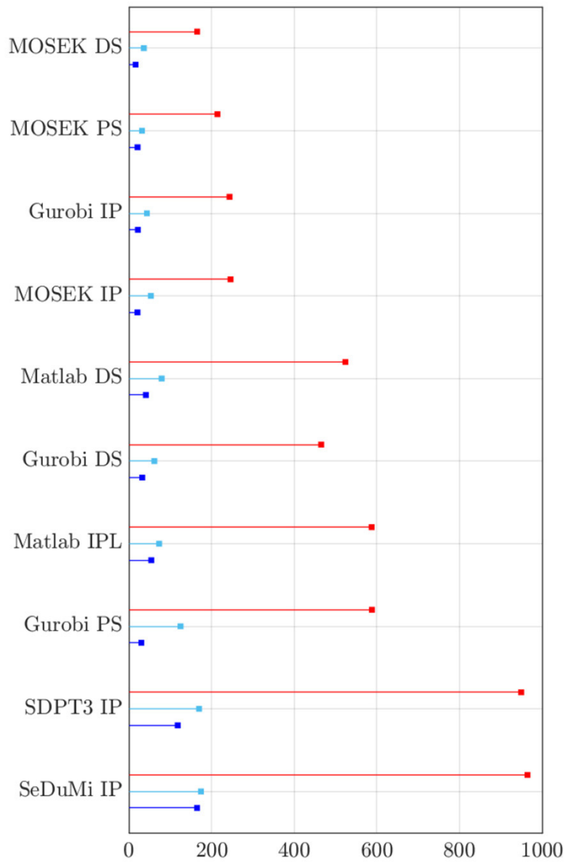

FIGURE 6
Total amount of computing time for finding the most fitting candidate solution through the two-stage metaheuristic lattice search on every optimization solver and method in this study. In order of stem (top-to-bottom): exhaustive search with search space $\kappa = 15$ (red), direct search (cyan), and recursive search with $\tilde{K} = 3$ (blue). Noticeably, the non-commercial solvers from CVX (SDPT3 and SeDuMi) are significantly slower than those produced by Matlab, Gurobi and MOSEK.

algorithm has been applied. Yet another interesting direction is to consider *a priori* information for the design and application of the L1L1 algorithm, for example, an epileptic focus based on non-invasive measurements such as video-EEG of epileptic activity applied to determine approximate stimulation locations. Finally, the mathematical implications of this study can be further enriched by incorporating transcranial direct current stimulation and functional magnetic resonance imaging (tDCS-fMRI) (Esmaeilpour et al., 2020). By utilizing tDCS-fMRI data sets to explore real-time neural changes caused by electrical stimulation–such as in the studies by Callan et al. (2016) for investigating resting state networks linked to visual stimuli, or in the research conducted by Mark et al. (2023) for monitoring brain activity of pilots undergoing aviation training–further enriches the necessity of an effective inverse problem study equipped with optimization methods for simulating and understanding the signal-to-noise (SNR) impacts with a level of mathematical uncertainty, as some of these deficiencies were mentioned on their study limitations.

Data availability statement

The original contributions presented in the study are included in the article/supplementary material, further inquiries can be directed to the corresponding author.

Author contributions

FG: Conceptualization, Data curation, Formal analysis, Investigation, Methodology, Software, Visualization, Writing—original draft. MS: Formal analysis, Project administration, Supervision, Validation, Software, Visualization, Writing—original draft, Writing—review & editing. SP: Conceptualization, Data curation, Formal analysis, Funding acquisition, Investigation, Methodology, Project administration, Resources, Software, Supervision, Validation, Visualization, Writing—review & editing.

Funding

FG, MS, and SP were supported by the Research Council of Finland through the Center of Excellence in Inverse Modelling and Imaging 2018–2025 (decision 353089), the researcher exchange (DAAD) project "Non-invasively reconstructing and inhibiting activity in focal epilepsy" (decision 354976), the ERA PerEpi project (decision 344712), and Flagship of Advanced Mathematics for Sensing, Imaging and Modelling (decision 359185).

Acknowledgments

The authors would like to thank Prof. Dr. rer. nat. Carsten Wolters, researchers and clinicians from the Institute for Biomagnetism and Biosignalanalysis (IBB), and the PerEpi consortium for their continuous support, discussions, and feedback regarding non-invasive brain stimulation topics, regression analysis, and the seminars prepared during the elaboration of this study.

Conflict of interest

The authors declare that the research was conducted in the absence of any commercial or financial relationships that could be construed as a potential conflict of interest.

Publisher's note

References

Anderson, D. N., Osting, B., Vorwerk, J., Dorval, A. D., and Butson, C. R. (2018). Optimized programming algorithm for cylindrical and directional deep brain stimulation electrodes. *J. Neural Eng.* 15, 026005. doi: 10.1088/1741-2552/aaa14b

Bauer, M., Pursiainen, S., Vorwerk, J., Köstler, H., and Wolters, C. H. (2015). Comparison study for Whitney (Raviart-Thomas) type source models in finite element method based EEG forward modeling. *IEEE Trans. Biomed. Eng.* 62, 2648–2656. doi: 10.1109/TBME.2015.2439282

Bayliss, S., Constantinides, G. A., Luk, W., et al. (2006). "An FPGA implementation of the simplex algorithm," in *2006 IEEE International Conference on Field Programmable Technology* (Bangkok: IEEE), 49–56.

Bianchi, L., Dorigo, M., Gambardella, L. M., and Gutjahr, W. J. (2009). A survey on metaheuristics for stochastic combinatorial optimization. *Nat. Comput.* 8, 239–287. doi: 10.1007/s11047-008-9098-4

Bogani, C., Gasparo, M., and Papini, A. (2009). Generalized pattern search methods for a class of nonsmooth optimization problems with structure. *J. Comput. Appl. Math.* 229, 283–293. doi: 10.1016/j.cam.2008.10.047

Boyd, S., and Vandenberghe, L. (2004). *Convex Optimization*. Cambridge: Cambridge University Press.

Callan, D. E., Falcone, B., Wada, A., and Parasuraman, R. (2016). Simultaneous tdcs-fMRI identifies resting state networks correlated with visual search enhancement. *Front. Hum. Neurosci.* 10, 72. doi: 10.3389/fnhum.2016.00072

Creutzfeldt, O. D., Fromm, G. H., and Kapp, H. (1962). Influence of transcortical dc currents on cortical neuronal activity. *Exp. Neurol.* 5, 436–452. doi: 10.1016/0014-4886(62)90056-0

Dannhauer, M., Lanfer, B., Wolters, C. H., and Knösche, T. R. (2011). Modeling of the human skull in EEG source analysis. *Hum. Brain Mapp.* 32, 1383–1399. doi: 10.1002/hbm.21114

Dmochowski, J. P., Datta, A., Bikson, M., Su, Y., and Parra, L. C. (2011). Optimized multi-electrode stimulation increases focality and intensity at target. *J. Neural Eng.* 8, 046011. doi: 10.1088/1741-2560/8/4/046011

Dmochowski, J. P., Koessler, L., Norcia, A. M., Bikson, M., and Parra, L. C. (2017). Optimal use of eeg recordings to target active brain areas with transcranial electrical stimulation. *Neuroimage* 157, 69–80. doi: 10.1016/j.neuroimage.2017.05.059

Esmaeilpour, Z., Shereen, A. D., Ghobadi-Azbari, P., Datta, A., Woods, A. J., Ironside, M., et al. (2020). Methodology for tdcs integration with fmri. *Hum. Brain Mapp.* 41, 1950–1967. doi: 10.1002/hbm.24908

Faria, P., Hallett, M., and Miranda, P. C. (2011). A finite element analysis of the effect of electrode area and inter-electrode distance on the spatial distribution of the current density in tdcs. *J. Neural Eng.* 8, 066017. doi: 10.1088/1741-2560/8/6/066017

Fernandez-Corazza, M., Turovets, S., and Muravchik, C. H. (2020). Unification of optimal targeting methods in transcranial electrical stimulation. *Neuroimage* 209, 116403. doi: 10.1016/j.neuroimage.2019.116403

Feurer, M., and Hutter, F. (2019). "Hyperparameter optimization," in *Automated Machine Learning*. (Cham: Springer), 3–33.

Fiacco, A. V., and McCormick, G. P. (1964). The sequential unconstrained minimization technique for nonlinear programing, a primal-dual method. *Manage. Sci.* 10:360–366. doi: 10.1287/mnsc.10.2.360

Fischl, B. (2012). Freesurfer. *Neuroimage* 62, 774–781. doi: 10.1016/j.neuroimage.2012.01.021

Frenk, H., Roos, K., Terlaky, T., and Zhang, S. (2000). "Central region method," in *High Performance Optimization*, 157–194.

Galaz Prieto, F., Rezaei, A., Samavaki, M., and Pursiainen, S. (2022). L1-norm vs. l2-norm fitting in optimizing focal multi-channel tes stimulation: linear and semidefinite programming vs. weighted least squares. *Comput. Methods Programs Biomed.* 226:107084. doi: 10.1016/j.cmpb.2022.107084

Gensheimer, F., Ruzika, S., Scholl, S., and Wehn, N. (2014). "A simplex algorithm for lp decoding hardware," in *2014 IEEE 25th Annual International Symposium on Personal, Indoor, and Mobile Radio Communication (PIMRC)* (Washington, DC: IEEE), 790–794

Grant, M., and Boyd, S. (2014). *CVX: Matlab Software for Disciplined Convex Programming, Version 2.1*. Available online at: http://cvxr.com/cvx

Guler, S., Dannhauer, M., Erem, B., Macleod, R., Tucker, D., Turovets, S., et al. (2016). Optimization of focality and direction in dense electrode array transcranial direct current stimulation (tdcs). *J. Neural Eng.* 13, 036020. doi: 10.1088/1741-2560/13/3/036020

Gurobi Optimization LLC (2022). *Gurobi Optimizer Reference Manual*. Available online at: https://www.gurobi.com

He, Q., Rezaei, A., and Pursiainen, S. (2019). Zeffiro user interface for electromagnetic brain imaging: A gpu accelerated fem tool for forward and inverse computations in matlab. *Neuroinformatics* 18, 237–250. doi: 10.1007/s12021-019-09436-9

Je, C., and Park, H.-M. (2013). Optimized hierarchical block matching for fast and accurate image registration. *Signal Proc. Image Commun.* 28, 779–791. doi: 10.1016/j.image.2013.04.002

Kaufmann, E., Hordt, M., Lauseker, M., Palm, U., and Noachtar, S. (2021). Acute effects of spaced cathodal transcranial direct current stimulation in drug resistant focal epilepsies. *Clini, Neurophysiol*, 132, 1444–1451. doi: 10.1016/j.clinph.2021.03.048

Khadka, N., Borges, H., Paneri, B., Kaufman, T., Nassis, E., Zannou, A. L., et al. (2020). Adaptive current tdcs up to 4ma. *Brain Stimul.* 13, 69–79. doi: 10.1016/j.brs.2019.07.027

Khan, A., Antonakakis, M., Vogenauer, N., Haueisen, J., and Wolters, C. H. (2022). Individually optimized multi-channel tdcs for targeting somatosensory cortex. *Clini. Neurophysiol.* 134, 9–26. doi: 10.1016/j.clinph.2021.10.016

Kowalski, T., Silny, J., and Buchner, H. (2002). Current density threshold for the stimulation of neurons in the motor cortex area. *Bioelectromagnetics*. 23, 421–428. doi: 10.1002/bem.10036

Laakso, I., Tanaka, S., Koyama, S., De Santis, V., and Hirata, A. (2015). Inter-subject variability in electric fields of motor cortical tdcs. *Brain Stimul.* 8, 906–913. doi: 10.1016/j.brs.2015.05.002

Lin, T., Ma, S., Ye, Y., and Zhang, S. (2021). An admm-based interior-point method for large-scale linear programming. *Optimizat. Methods Softw.* 36, 389–424. doi: 10.1080/10556788.2020.1821200

Mark, J. A., Ayaz, H., and Callan, D. E. (2023). Simultaneous fmri and tdcs for enhancing training of flight tasks. *Brain Sci.* 13, 1024. doi: 10.3390/brainsci13071024

Medani, T., Lautru, D., Ren, Z., Schwartz, D., and Sou, G. (2015). "Modelling of brain sources using the modified saint Venant's method in FEM resolution of EEG forward problem," in *Conference IEEE EMBS Conference on Neural Engineering 2015, 7th International IEEE EMBS Conference on Neural Engineering* (Montpellier, France: IEEE).

Mehrotra, S. (1992). On the implementation of a primal-dual interior point method. *SIAM J. Optimizat.* 2, 575–601. doi: 10.1137/0802028

Montes-Restrepo, V., Van Mierlo, P., Strobbe, G., Staelens, S., Vandenberghe, S., and Hallez, H. (2014). Influence of skull modeling approaches on eeg source localization. *Brain Topogr.* 27, 95–111. doi: 10.1007/s10548-013-0313-y

Moreno-Duarte, I., Gebodh, N., Schestatsky, P., Guleyupoglu, B., Reato, D., Bikson, M., et al. (2014). "Chapter 2-transcranial electrical stimulation: Transcranial direct current stimulation (tdcs), transcranial alternating current stimulation (tacs), transcranial pulsed current stimulation (tpcs), and transcranial random noise stimulation (trns)," in *The Stimulated Brain*, R. Cohen Kadosh (San Diego: Academic Press), 35–59.

MOSEK ApS (2019). Mosek Optimization Toolbox for Matlab. *Users Guide and Reference Manual, Version*. MOSEK, 4, 1.

Nitsche, M. A., and Paulus, W. (2000). Excitability changes induced in the human motor cortex by weak transcranial direct current stimulation. *J. Physiol.* 527, 633–639. doi: 10.1111/j.1469-7793.2000.t01-1-00633.x

Paulus, W. (2011). Transcranial electrical stimulation (tes - tdcs; trns, tacs) methods. *Neuropsychol. Rehabil.* 21, 602–617. doi: 10.1080/09602011.2011.557292

Peterchev, A. V., Wagner, T. A., Miranda, P. C., Nitsche, M. A., Paulus, W., Lisanby, S. H., et al. (2012). Fundamentals of transcranial electric and magnetic stimulation dose: Definition, selection, and reporting practices. *Brain Stimul.* 5, 435–453. doi: 10.1016/j.brs.2011.10.001

Polik, I., Terlaky, T., and Zinchenko, Y. (2007). "Sedumi: a package for conic optimization," in *IMA Workshop on Optimization and Control, Univ. Minnesota, Minneapolis*. Minnesota, Minneapolis: Citeseer.

Pursiainen, S., Agsten, B., Wagner, S., and Wolters, C. H. (2017). Advanced boundary electrode modeling for tes and parallel tes/eeg. *IEEE Trans. Neural Syst. Rehabilitat. Eng.* 26, 37–44. doi: 10.1109/TNSRE.2017.2748930

Pursiainen, S., Lucka, F., and Wolters, C. H. (2012). Complete electrode model in EEG: relationship and differences to the point electrode model. *Phys. Med. Biol.*, 57, 999–1017. doi: 10.1088/0031-9155/57/4/999

Pursiainen, S., Vorwerk, J., and Wolters, C. H. (2016). Electroencephalography (EEG) forward modeling viaH(div) finite element sources with focal interpolation. *Phys. Med. Biol.* 61, 8502–8520. doi: 10.1088/0031-9155/61/24/8502

Rampersad, S., Stegeman, D., and Oostendorp, T. (2013). Op 11 optimized tdcs electrode configurations for five targets determined via an inverse fe modeling approach. *Clini. Neurophysiol.* 124, e61–e62. doi: 10.1016/j.clinph.2013.04.078

Reed, T., and Cohen Kadosh, R. (2018). Transcranial electrical stimulation (tes) mechanisms and its effects on cortical excitability and connectivity. *J. Inherit. Metab. Dis.* 41, 1123–1130. doi: 10.1007/s10545-018-0181-4

Roy, A., Boroda, E., Waldron, E., Lim, K., and Henry, T. (2019). Integration of prefrontal transcranial direct current stimulation with cognitive training for treatment of memory dysfunction in epilepsy. *Brain Stimulat.* 12, 481. doi: 10.1016/j.brs.2018.12.571

Ruffini, G., Fox, M. D., Ripolles, O., Miranda, P. C., and Pascual-Leone, A. (2014). Optimization of multifocal transcranial current stimulation for weighted cortical pattern targeting from realistic modeling of electric fields. *Neuroimage* 89, 216–225. doi: 10.1016/j.neuroimage.2013.12.002

Sauer, T. (2018). *Numerical Analysis*. London: Pearson.

Schmidt, C., Wagner, S., Burger, M., van Rienen, U., and Wolters, C. H. (2015). Impact of uncertain head tissue conductivity in the optimization of transcranial direct current stimulation for an auditory target. *J. Neural Eng.* 12, 046028. doi: 10.1088/1741-2560/12/4/046028

Simula, S., Daoud, M., Ruffini, G., Biagi, M. C., Bénar, C.-G., Benquet, P., et al. (2022). Transcranial current stimulation in epilepsy: a systematic review of the fundamental and clinical aspects. *Front. Neurosci.* 16, 909421. doi: 10.3389/fnins.2022.909421

Sturm, J. F. (1999). Using sedumi 1.02, a matlab toolbox for optimization over symmetric cones. *Optimization methods and software* 11:625–653. doi: 10.1080/10556789908805766

Thair, H., Holloway, A. L., Newport, R., and Smith, A. D. (2017). Transcranial direct current stimulation (tdcs): A beginner's guide for design and implementation. *Front. Neurosci.* 11, 641. doi: 10.3389/fnins.2017.00641

Tost, A., Migliorelli, C., Bachiller, A., Medina-Rivera, I., Romero, S., García-Cazorla, Á., et al. (2021). Choosing strategies to deal with artifactual eeg data in children with cognitive impairment. *Entropy* 23, 1030. doi: 10.3390/e23081030

Tütüncü, R. H., Toh, K.-C., and Todd, M. J. (2003). Solving semidefinite-quadratic-linear programs using sdpt3. *Mathemat. Program.* 95, 189–217. doi: 10.1007/s10107-002-0347-5

Wagner, S., Burger, M., and Wolters, C. H. (2016). An optimization approach for well-targeted transcranial direct current stimulation. *SIAM J. Appl. Math.* 76, 2154–2174. doi: 10.1137/15M1026481

Wagner, S., Rampersad, S. M., Aydin, U., Vorwerk, J., Oostendorp, T. F., Neuling, T., et al. (2013). Investigation of tdcs volume conduction effects in a highly realistic head model. *J. Neural Eng.* 11, 016002. doi: 10.1088/1741-2560/11/1/016002

Workman, C. D., Fietsam, A. C., and Rudroff, T. (2020). Different effects of 2 ma and 4 ma transcranial direct current stimulation on muscle activity and torque in a maximal isokinetic fatigue task. *Front. Hum. Neurosci.* 14, 240. doi: 10.3389/fnhum.2020.00240

Yang, L., and Shami, A. (2020). On hyperparameter optimization of machine learning algorithms: Theory and practice. *Neurocomputing* 415, 295–316. doi: 10.1016/j.neucom.2020.07.061

Zaghi, S., Acar, M., Hultgren, B., Boggio, P. S., and Fregni, F. (2010). Noninvasive brain stimulation with low-intensity electrical currents: Putative mechanisms of action for direct and alternating current stimulation. *Neuroscientist* 16, 285–307. doi: 10.1177/1073858409336227

Zhang, Y. (1999). User's guide to lipsol linear-programming interior point solvers v0. 4. *Optimizat. Methods Softw.* 11, 385–396. doi: 10.1080/10556789908805756

Frontiers in Human Neuroscience

TYPE Original Research
PUBLISHED 12 March 2024
DOI 10.3389/fnhum.2024.1335212

EDITED BY
George Alexandrakis,
University of Texas at Arlington, United States

REVIEWED BY
Joonas Iivanainen,
Aalto University, Finland
Seppo P. Ahlfors,
Massachusetts General Hospital and Harvard Medical School, United States

*CORRESPONDENCE
Johannes Vorwerk
✉ johannes.vorwerk@umit-tirol.at

RECEIVED 08 November 2023
ACCEPTED 22 January 2024
PUBLISHED 12 March 2024

CITATION
Vorwerk J, Wolters CH and Baumgarten D (2024) Global sensitivity of EEG source analysis to tissue conductivity uncertainties. *Front. Hum. Neurosci.* 18:1335212.
doi: 10.3389/fnhum.2024.1335212

Global sensitivity of EEG source analysis to tissue conductivity uncertainties

Johannes Vorwerk[1]*, Carsten H. Wolters[2,3] and Daniel Baumgarten[1]

[1]Institute of Electrical and Biomedical Engineering, UMIT TIROL—Private University for Health Sciences and Health Technology, Hall in Tirol, Austria, [2]Institute for Biomagnetism and Biosignalanalysis, University of Münster, Münster, Germany, [3]Otto Creutzfeldt Center for Cognitive and Behavioral Neuroscience, University of Münster, Münster, Germany

Introduction: To reliably solve the EEG inverse problem, accurate EEG forward solutions based on a detailed, individual volume conductor model of the head are essential. A crucial—but often neglected—aspect in generating a volume conductor model is the choice of the tissue conductivities, as these may vary from subject to subject. In this study, we investigate the sensitivity of EEG forward and inverse solutions to tissue conductivity uncertainties for sources distributed over the whole cortex surface.

Methods: We employ a detailed five-compartment head model distinguishing skin, skull, cerebrospinal fluid, gray matter, and white matter, where we consider uncertainties of skin, skull, gray matter, and white matter conductivities. We use the finite element method (FEM) to calculate EEG forward solutions and goal function scans (GFS) as inverse approach. To be able to generate the large number of EEG forward solutions, we employ generalized polynomial chaos (gPC) expansions.

Results: For sources up to a depth of 4 cm, we find the strongest influence on the signal topography of EEG forward solutions for the skull conductivity and a notable effect for the skin conductivity. For even deeper sources, e.g., located deep in the longitudinal fissure, we find an increasing influence of the white matter conductivity. The conductivity variations translate to varying source localizations particularly for quasi-tangential sources on sulcal walls, whereas source localizations of quasi-radial sources on the top of gyri are less affected. We find a strong correlation between skull conductivity and the variation of source localizations and especially the depth of the reconstructed source for quasi-tangential sources. We furthermore find a clear but weaker correlation between depth of the reconstructed source and the skin conductivity.

Discussion: Our results clearly show the influence of tissue conductivity uncertainties on EEG source analysis. We find a particularly strong influence of skull and skin conductivity uncertainties.

KEYWORDS

EEG, forward modeling, finite element method, source analysis, sensitivity analysis, uncertainty quantification

1 Introduction

Electroencephalography (EEG) is a frequently used tool for functional brain imaging in both research and clinical care (Brette and Destexhe, 2012). A huge advantage of EEG over, e.g., functional magnetic resonance imaging (fMRI), is its time resolution in the millisecond range. To localize the brain activity underlying a measured signal it is necessary to solve the EEG inverse problem (Knösche and Haueisen, 2022). As a prerequisite for solving the EEG inverse problem, it is necessary to model the propagation of the electric fields evoked by brain activity through the head tissues, which are measured as the EEG signal at the head surface (EEG forward problem). Accurately solving the EEG forward problem is one important factor to reliably solve the EEG inverse problem (others are, e.g., the choice of an adequate inverse method).

The EEG forward problem is commonly solved using numerical methods, such as the boundary element method (BEM; Kybic et al. 2005) or the finite element method (FEM; Yan et al. 1991; Buchner et al. 1997), and, therefore, requires a discretized volume conductor model of the head, i.e., a 3d representation of the head distinguishing the different conductive tissues. It was shown that the use of accurate, individual head models distinguishing five or more tissues (skin, skull, cerebrospinal fluid/CSF, gray matter, white matter) is important to obtain accurate EEG forward solutions (Vorwerk et al., 2014; Nielsen et al., 2023), which, in consequence, are essential for accurate EEG inverse solutions (Ramon et al., 2006; Cho et al., 2015; Neugebauer et al., 2017; Asadzadeh et al., 2020; Azizollahi et al., 2020). However, besides the geometrical accuracy of the head model, also the values chosen for the tissue's electrical conductivities influence the obtained EEG forward solution. Neglecting interindividual variations of these conductivities in the computation of the EEG forward solution may therefore lead to inaccurate EEG inverse solutions (Vanrumste et al., 2000; Chen et al., 2010; Akalin Acar and Makeig, 2013; Aydin et al., 2014; Vorwerk et al., 2019a). Such interindividual variations may, e.g., occur due to age or disease state (Akhtari et al., 2002; McCann et al., 2019; Antonakakis et al., 2020). Conductivity calibration based on electrical impedance tomography (EIT), EEG, or combined EEG/MEG has been proposed as a means to alleviate the influence of conductivity uncertainties (Huang et al., 2007; Acar et al., 2016; Fernández-Corazza et al., 2017). Most of these studies focused on fitting the skull conductivity, but it is unclear whether the dependency on the skull conductivity is similarly strong for all source positions and whether fitting the skull conductivity is thus always the optimal choice.

Sensitivity studies allow estimating to what extent variations of the tissue conductivities influence the results of EEG forward solutions. So far, studies found that variations of skin and skull conductivities have the strongest influence for the EEG (Gençer and Acar, 2004; Vallaghé and Clerc, 2008; Vorwerk et al., 2019a). However, to the best of our knowledge, existing EEG sensitivity studies only investigated a few source positions that were assumed to be representative. Especially in highly-detailed head volume conductor models, as they are more and more frequently used nowadays (Buzzell et al., 2017; Piai et al., 2017; Staljanssens et al., 2017; Gao et al., 2019; Zaky et al., 2023), the choice of the source positions might have a strong influence on the results of the sensitivity analysis.

In this study, we investigate the sensitivity of EEG forward solutions to conductivity variations for sources distributed over the whole cortex surface. Furthermore, we investigate the sensitivity of EEG inverse solutions to the same conductivity variations, and determine to what extent changes of the EEG inverse solution correlate with the sensitivity of the EEG forward solutions to tissue conductivity variations.

2 Materials and methods

2.1 Head model

We generated a head model based on the segmentations provided for the *New York Head* (https://www.parralab.org/nyhead/). The segmentations of brain and non-brain tissues are based on the symmetric ICBM-152 v2009 and the symmetric ICBM-152 v6 average atlases, respectively (https://nist.mni.mcgill.ca/atlases/), whereas the lower parts of the head are from a separate segmentation (Huang et al., 2016). We slightly modified the segmentations to ensure a minimal thickness of the gray matter of 2.5 mm. Furthermore, we reduced the number of tissue compartments to five (white matter, gray matter, CSF, skull, skin). We used SimNIBS 4 (https://simnibs.github.io/simnibs/; Puonti et al. 2020) for head mesh generation and to obtain gray matter, white matter, and central cortex surfaces for both hemispheres that will be used for source space construction and visualization. We chose to generate an especially fine mesh structure in the gray and white matter volumes; the resulting tetrahedral head mesh consisted of 3,473,632 nodes and 20,703,247 elements (see Figure 1, left). We used the electrode positions provided with the New York Head to create a realistic sensor configuration corresponding to a 10-10 layout, resulting in 80 electrode positions.

2.2 Source spaces and EEG forward simulations

We created the source space for this study based on the central surface of the cortex obtained from SimNIBS, which is the estimated surface in the middle of gray matter/CSF and gray/white matter boundaries. It has to be observed that this central surface represents a closed surface for each hemisphere, i.e., the hemispheres are split at the corpus callosum. Furthermore, these surfaces also cover some deep brain regions that could be attributed to subcortical brain structures such as the thalamus or the basal ganglia, whereas brainstem and cerebellum are excluded. Due to the symmetry of the underlying segmentation, we only considered the left hemisphere. For reasons of computational efficiency, we downsampled the surface to 34,997 vertices.

To achieve high numerical accuracy in our forward simulations, we ensured that for all source positions the closest node of the head mesh is fully contained in the gray matter compartment, i.e., all mesh elements this node is part of have to belong to the gray matter compartment (Vorwerk et al., 2019b). Source positions for which this was initially not the case were shifted toward the closest node fully contained in the gray matter compartment until this condition was fulfilled. For each source position, we calculated the surface normal as a physiologically plausible source direction at this position. We refer to this source space as *sources_cortex*. For visualization purposes, we created an inflated version of the central cortex surface underlying this source space.

To avoid an inverse crime when evaluating the sensitivity of EEG source analysis to conductivity uncertainties, we created a second source space based on the dual mesh of the source space *sources_cortex*. This means that the source positions for this

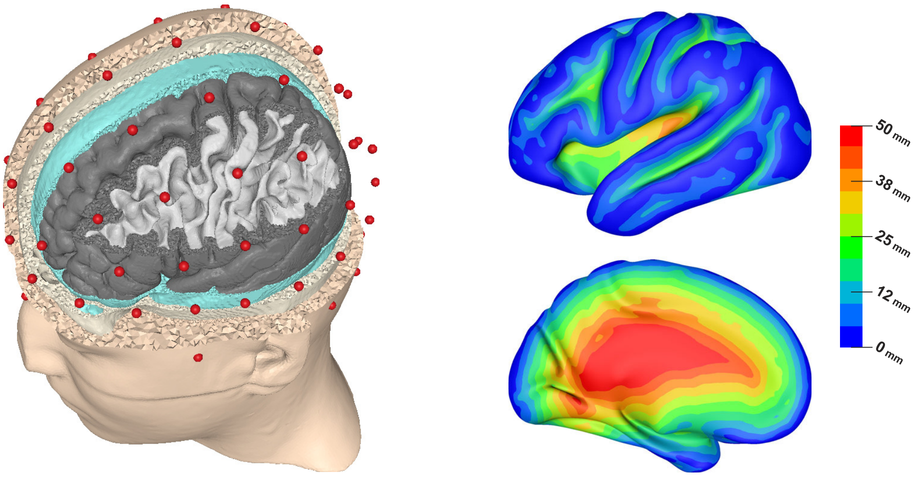

FIGURE 1
Visualization of the FEM head model showing electrode positions (red) and (from outside to inside) skin, skull, CSF, gray matter, and white matter surfaces **(left)**. Lateral and medial view of source depth (distance to inner skull surface) visualized on inflated left cortex surface **(right)**.

second source space are the triangle centers of the cortex surface on which the original source space *sources_cortex* is based. The resulting source space consists of 69,990 vertices; we refer to this source space as *sources_cortex**. *sources_cortex** is used for all inverse calculations, whereas *sources_cortex* is used for the forward simulations. Again, we ensured that the closest node of the volume conductor model for all source positions of *sources_cortex** is fully contained in the gray matter compartment. On average, the distance between a node of *sources_cortex** and the closest node in *sources_cortex* is 0.8 mm, which is the average minimal localization error, accordingly.

We used the FEM multipole approach for all forward simulations, as it was shown to achieve high numerical accuracy with a high computational efficiency (Vorwerk et al., 2019b). The multipole approach was implemented based on the FieldTrip-SimBio pipeline (Vorwerk et al., 2018).

2.3 EEG forward problem sensitivity analysis

We mostly rely on Monte Carlo approaches for our sensitivity analysis. To handle the large number of forward simulations for different conductivity values necessary for the sensitivity/uncertainty analysis, we employ generalized polynomial chaos (gPC) expansions (Vorwerk et al., 2019a). Based on predefined probability distributions and precomputed forward solutions generated for corresponding sets of conductivities, gPC expansions allow to rapidly approximate accurate forward simulations for arbitrary conductivity values. We used UQLab 2.0 to perform the gPC calculations in this study (https://www.uqlab.com/; Marelli and Sudret 2014). The details of the used gPC approach are described in Vorwerk et al. (2019a).

As in Vorwerk et al. (2019a), we chose uniform distributions for all tissue conductivities considered uncertain. The uniform distribution represents minimal knowledge about the distribution of these conductivities. The intervals within which each conductivity could vary are shown in Table 1; the CSF conductivity was not considered uncertain as it was shown to have a negligible inter-individual variation (Baumann et al., 1997).

With four tissue conductivities varying uniformly within the ranges indicated in Table 1, it is of interest to estimate the contribution of each of the four uncertain tissue conductivities to the overall variation of the EEG forward solution. Therefore, we use Sobol indices (Sobol, 2001). These are defined as

$$S_{i_1,\ldots,i_s} = \frac{\mathbb{V}(i_1,\ldots,i_s)}{\mathbb{V}}, \qquad (1)$$

i.e., the Sobol index $S_{i_1,\ldots,i_s}$ is defined as the ratio between the variance caused by the interaction of the subset of input parameters $\{i_1,\ldots,i_s\} \subset \{1,\ldots,n\}$ and the overall variance. It is important to note that $\mathbb{V}(i_1,\ldots,i_s)$ only includes the variance caused by the interaction of the subset of indices $i_1,\ldots,i_s$ but not the contributions that can be attributed to a single variable or a smaller subset of these variables. For example, for a second-order Sobol index $S_{i,j}$, the variance $\mathbb{V}(i,j)$ does not include the variances $\mathbb{V}(i)$ and $\mathbb{V}(j)$ that can be attributed to either i or j individually.

In this study, we focus on first- and second-order Sobol indices, i.e., the share of variance caused by the uncertainty of a single uncertain tissue conductivity or the share of variance caused by the uncertainty of two conductivities that cannot be attributed to the uncertainties of a single conductivity, respectively. We further consider total-effect or full Sobol indices, S_i^T, for which all Sobol indices involving a certain input parameter i are summed up:

$$S_i^T = S_i + \sum_{i\neq j} S_{i,j} + \sum_{\substack{i\neq j,k \\ j<k}} S_{i,j,k} + \ldots. \qquad (2)$$

The Sobol indices were computed with UQLab using a Monte Carlo approach with 50,000 samples per parameter. We found that this number of samples guaranteed a more than sufficient convergence of the Sobol indices for the requirements of this study. To calculate the Sobol indices, the *Janon estimator* was used (Janon et al., 2014, Equation 2.6), which has optimal asymptotic variance and is robust against model perturbations. Further details regarding the calculation of the Sobol indices are provided as

TABLE 1 Tissue conductivity intervals (mS/m).

Tissue	Min. σ_{min}	Max. σ_{max}	Standard σ_{st}	References
Skin	280.0	870.0	430.0	Haueisen et al., 1997; Ramon et al., 2004
Skull	1.6	33.0	10.0	Akhtari et al., 2002; Hoekema et al., 2003; Dannhauer et al., 2011
CSF	1,769.6	1,810.4	1,790.0	Baumann et al., 1997
GM	220.0	670.0	330.0	Haueisen et al., 1997; Ramon et al., 2004
WM	90.0	290.0	140.0	Haueisen et al., 1997; Ramon et al., 2004

Supplementary material. Furthermore, we would like to refer the interested reader to the original publication of Janon et al. (2014) or the UQLab User Manual (https://uqftp.ethz.ch/uqlab_doc_pdf/2.0.0/UserManual_Sensitivity.pdf) for additional information.

In the sensitivity analysis of EEG forward simulations, we have the challenge that we do not have a single output parameter, but each computed electrode potential is a separate output parameter. To allow for a comprehensible and easily interpretable evaluation of the Sobol indices, we introduce the relative difference measure (RDM) and the magnitude error (MAG) (Meijs et al., 1989). Computing these error measures in comparison to a reference solution, it is possible to express the topography and magnitude change of the set of electrode potentials through a single parameter for each source position. Interpreting RDM and MAG as functions of the conductivities, we can then compute the Sobol indices for the changes of RDM and MAG, expressing the influence of changes in each tissue conductivity on signal topography and magnitude. A similar approach was previously used by Vallaghé and Clerc (2008). As a reference solution, we use the forward solution for the standard conductivity values indicated in Table 1.

RDM and MAG are defined as follows:

$$\begin{aligned} RDM(u^{test}, u^{ref}) &= \left\| \frac{u^{test}}{\|u^{test}\|_2} - \frac{u^{ref}}{\|u^{ref}\|_2} \right\|_2, \\ MAG(u^{test}, u^{ref}) &= \frac{\|u^{test}\|_2}{\|u^{ref}\|_2}, \end{aligned} \tag{3}$$

where u^{test} corresponds to the vector of electrode potentials for varied conductivities and u^{ref} corresponds to the vector of electrode potentials for standard conductivities.

The RDM represents the change in signal topography in comparison to the reference solution, which was shown to be linked to source localization accuracy, whereas the MAG defines the change in signal magnitude. In most applications of EEG source analysis, only the change of signal topography is of relevance, whereas there are only a few cases where the exact source magnitude is of interest. Thus, we mainly focus on the RDM evaluations in this study.

2.4 EEG source analysis sensitivity analysis

To evaluate the influence of conductivity uncertainties on EEG inverse solutions, we performed forward simulations for 1,000 randomly drawn sets of conductivities. Following, for each source position, we calculate inverse solutions using the source *space sources_cortex** and a leadfield matrix obtained with standard conductivity values. This scenario corresponds to the common problem of EEG source analysis that the actual tissue conductivities that influence the measurement result are unknown, while the EEG source analysis is performed using conductivity values from the literature. The resulting 1,000 source localizations per source position can then be evaluated to investigate the sensitivity of the EEG inverse solution to conductivity variations.

As an inverse method, we used goal function scans (GFS) with a free source orientation, i.e., the source position i in the source space for which

$$GoF = 1 - \left(\frac{\|u_{\text{meas}} - L_i L_i^{+} u_{\text{meas}}\|_2}{\|u_{\text{meas}}\|_2} \right)^2 \tag{4}$$

is maximal is selected as the reconstructed source location. Here, u_{meas} is the (simulated) measurement result, $\| \cdot \|_2$ is the Euclidian norm, $L_i = L(\mathbf{x}_i)$ is the $\#sensors \times 3$ leadfield matrix for position $\mathbf{x}_i$, i.e., a matrix containing the forward simulation results for dipoles with moments oriented in each of the three cartesian directions at the source position, and L_i^{+} its Moore-Penrose inverse. In a single dipole scenario, as it is given in our simulation study, the GFS reliably finds the source position that optimally explains the data (Knösche, 1997; Fuchs et al., 1998).

To evaluate the influence of the conductivity uncertainties on the source localization, we calculate and visualize the average localization error, i.e., the distance between source localization and original source position, for the 1,000 sets of conductivities at each source position. This allows to understand how much the conductivity variations affect the accuracy of the source localization for each source position. We further calculate and visualize the ratio between the difference in source depth and the localization error and again take the average over all sets of conductivities to analyze to what extent the localization error can be explained by a change in source depth. Here, "change in source depth" denotes the absolute value of the difference between the source depth of the original source and the source depth of the reconstructed source.

To understand the influence of the variation of each tissue conductivity on the source localization, we calculate and visualize the correlation between deviations of each conductivity from the average conductivity and distance of the source reconstruction to the center of the point cloud of source localizations, and the correlation between each conductivity and the source depth. Again, these measures are calculated for each source position in *sources_cortex*.

The Sobol indices computed as described in Section 2.3 only indicate which tissue conductivities contribute most to the variation of an output parameter, but not how strongly this output parameter varies overall. To understand the dependency between RDM and source analysis accuracy, we calculate the RDM for all source positions and all 1,000 considered sets of conductivities, and visualize the average RDM and the correlation between localization error and RDM for each position in source space *sources_cortex*.

2.5 Evaluation

We employ two kinds of evaluation in this study. On the one hand, we visualize the results directly on an inflated cortex surface. This allows to visually identify the most affected brain areas. On the other hand, we plot the median Sobol indices and the corresponding 50% confidence interval, i.e., the interval between upper and lower quartile, as a function of the source depth. In this case, the source depth is calculated as the distance from the source position to the inner skull surface. These plots allow to identify in how far the source depth affects the sensitivity of the forward solution toward the different conductivities. Similar plots are also created for the correlation between the tissue conductivities and source localization error/source depth as a function of the source depth.

Figure 1 (right) allows to understand the distribution of source depths, which is necessary to interpret these plots. Unlike in spherical models, there is no unique definition of source depth in realistically shaped head models. In this study, we chose to define source depth as the distance of a source position to the inner skull surface. We chose this definition over the also frequently used distance to the outer skin surface, as it led to better interpretable results when plotting effect measures as a function of source depth. In result, some source positions that would usually be considered as "deep", e.g., in the medial temporal lobe, are classified as rather superficial in our study, as they are close to the base of the skull. Furthermore, Figure 1 (right) shows that source depths smaller than 5 mm correspond to sources on top of gyri, which can be assumed to mostly have a quasi-radial orientation. An exception are sources at the inferior surfaces of frontal and temporal lobe, which have a rather quasi-tangential orientation. Sources up to a depth of 30 mm correspond to sources inside of sulci, which are assumed to be mostly located on sulcal walls and have a quasi-tangential orientation in consequence. However, for source depths of about 15–30 mm this also includes sources at the bottom of sulci, which again have a rather quasi-radial orientation. Sources at depths of 30 mm and deeper mostly correspond to source positions in the insula, the longitudinal fissure and subcortical regions.

As our plots are based on the median and upper and lower quartile, the results should be stable against outliers and especially the median should represent the results for the dominant type of sources at each source depth well. This would correspond to quasi-radial sources for source depths smaller than 5 mm, quasi-tangential sources for source depths of about 5–30 mm, and sources in the insula and the longitudinal fissure for larger source depths.

3 Results

3.1 EEG forward problem

3.1.1 Signal topography

In this section, we analyze the sensitivity of the topography of EEG forward solutions toward tissue conductivity variations. Therefore, we calculated the Sobol indices of the RDM in comparison to a reference solution (see Equation 3). Figure 2 shows that the skull conductivity clearly has the strongest influence on the signal topography for nearly all source depths. Looking at the first-order and the second-order skin-skull interaction Sobol indices (Figure 2, left), we find a median skull conductivity Sobol index of about 60% for source positions with a depth of up to 35 mm, which includes basically all source positions except those deep in the longitudinal fissure and in subcortical regions (see Figure 1, right). Besides, we also find a strong influence of the skin-skull interaction for rather superficial sources. The median of this second-order Sobol index is at about 20% for the most superficial sources and gradually decreases for deeper sources. All other Sobol indices are below 10% for superficial and medium-deep sources. For sources deeper than 35 mm, e.g., sources deep in the longitudinal fissure, the sensitivity toward the white matter conductivity clearly increases, whereas the skull and skin-skull Sobol indices decrease.

The full Sobol indices (Figure 2, right), i.e., the sum of all variations attributed to one parameter (see Equation 2), underline the dominant influence of the skull conductivity for all sources that are not very deep even more. The median full skull conductivity Sobol index is higher than 80% for source depths smaller than 30 mm. As a result of the skin-skull conductivity interaction, also the full skin conductivity Sobol index is significant at a value of 30% for the most superficial sources. For deep sources, again, the sensitivity toward the white matter conductivity clearly increases.

The visualization of first- and second-order Sobol indices on the cortex surface underlines the influence of the skull conductivity (Figure 3). For large parts of the cortex surface, the Sobol index for the skull conductivity is clearly above 60% (Figure 3, second row). Lower Sobol indices are mainly found on top of gyri and at the bottom of sulci where the Sobol index drops to about 40%. Due to the choice of source orientations normal to the cortex surface, these source positions correspond to quasi-radial sources. Furthermore, the medial view shows small Sobol indices for source positions deep in the longitudinal fissure. For the skin-skull second-order Sobol index, we find sensitivities of about 30% for very superficial sources, whereas the sensitivity gradually decreases for deeper sources. For the skin conductivity, we find generally rather low Sobol indices of around 10% and lower. Here, lower values are especially found for deeper sources at the bottom of sulci and in some areas on top of gyri; higher values are consistently found on sulcal walls. For gray and white matter conductivities, the Sobol indices are almost zero for large parts of the cortex surface. However, strong outliers are found especially on gyral crowns and at sulci bottoms, where these Sobol indices are clearly increased. This corresponds to the positions for which the skull conductivity Sobol index was decreased and where we assume quasi-radial sources. Furthermore, we find increased Sobol indices for gray and

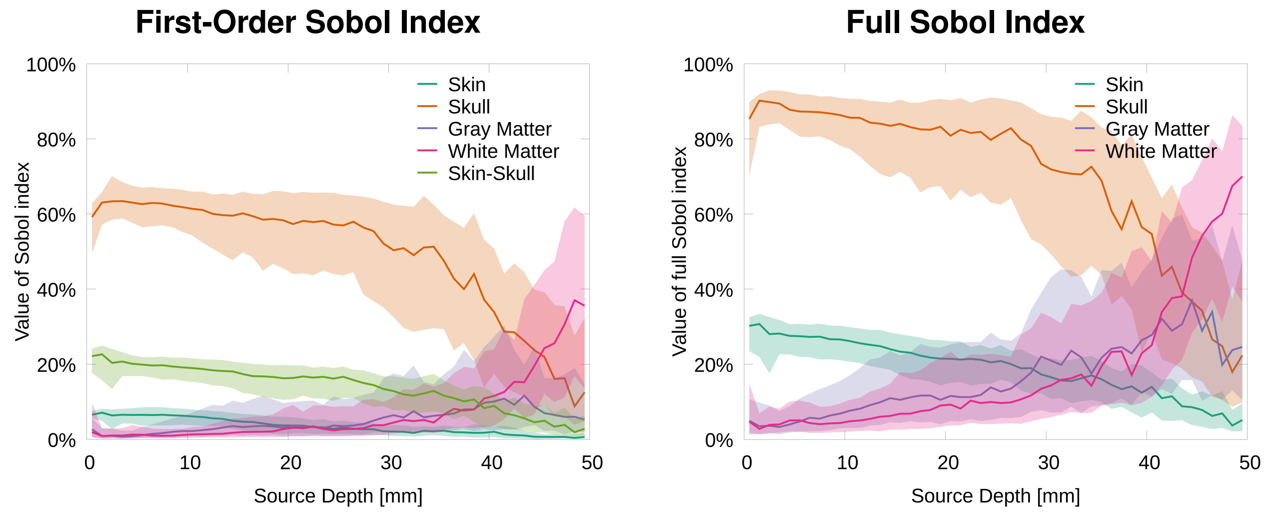

FIGURE 2
Median and 50% confidence interval of first-order and skin-skull second-order **(left)** and full **(right)** Sobol indices for signal topography/RDM plotted as a function of source depth.

white matter conductivities deep in the longitudinal fissure and in subcortical regions as can be seen in the medial view.

Visualizing the full Sobol indices (Figure 4), the predominance of the sensitivity toward the skull conductivity gets even more clear. Only for a few areas this sensitivity drops below 75%. Due to the addition of the skin-skull Sobol index, also the full skin Sobol index has a value of around 50% for large parts of the cortex surface. We especially find a notable decrease in the sensitivity to the skin conductivity on top of gyri and at the bottom of sulci. Gray and white matter conductivities again only show a significant sensitivity in a few areas, such as some gyral crowns and sulci bottoms.

3.1.2 Signal magnitude

To evaluate the influence of conductivity uncertainties on the signal magnitude, we calculated the Sobol indices for the MAG (see Equation 3). Figure 5 shows the strongest influence for skull and gray matter conductivities. Furthermore, we observe that first-order and full Sobol indices are almost identical, as the higher-order interactions are negligible for the signal magnitude. Therefore, we only discuss the full Sobol indices here and also only provide the cortex plots for the full Sobol indices.

For the most superficial sources, we find the strongest influence for the skull conductivity with a Sobol index of about 50%. For the influence of the gray matter conductivity, we find a Sobol index of about 25% and for the skin conductivity of about 20%. The influence of the white matter conductivity is negligible and stays below 10% at all source depths. For slightly deeper sources of about 5 mm depth, the influence of skin and skull conductivity slightly increases, whereas that of gray matter slightly drops. With increasing source depth, the influence of the gray matter conductivity gradually increases up to a Sobol index of about 40% for sources with a depth of 20 mm and more, whereas the influence of skull and skin conductivities drops to Sobol indices below 40 and 20%, respectively, for sources with a depth of 20 mm and more.

The visualization on the cortex surface (Figure 6) shows the strongest influence of the skull conductivity on the signal magnitude for sources on top of gyri with Sobol indices above 50%. This influence gradually decreases to values around 35% for sources deeper inside the sulci. For the gray matter conductivity, we see the exact opposite with the weakest influence and Sobol indices of about 20–25% on top of gyri and a gradual increase toward values of up to 50% at the bottom of sulci and deep in the longitudinal fissure. For the skin conductivity, we find the same decrease from the top of gyri to the bottom of sulci as for the skull conductivity, just at a clearly reduced level with Sobol indices of about 25% and lower. For the white matter conductivity, we do not find a significant influence except for some deep brain regions visible in the medial view.

3.2 EEG inverse problem

Analyzing the influence of conductivity variations on EEG source analysis, we first focus on the general localization errors caused by simultaneous variations of all four tissue conductivities considered uncertain and analyze the direction of these localization errors, i.e., in how far these can be explained by an incorrect depth of the reconstructed source position. To understand the relationship between the results obtained in the forward simulation study, we further compare the distribution of the average localization error and the average RDM as well as the correlation between RDM and localization error at each source position. Subsequently, we analyze the correlation between localization errors and conductivity variations to understand which conductivities have the strongest influence on the localization errors.

Figure 7 (top) shows that source positions inside the sulci are clearly more sensitive to localization errors due to conductivity uncertainties than superficial source positions on top of the gyri. We find average localization errors of up to 10 mm for sources deep inside of sulci, whereas the average localization errors remain below 5 mm for superficial sources. For rather superficial sources in the longitudinal fissure we find large localization errors as well, whereas the localization errors for deep brain regions that

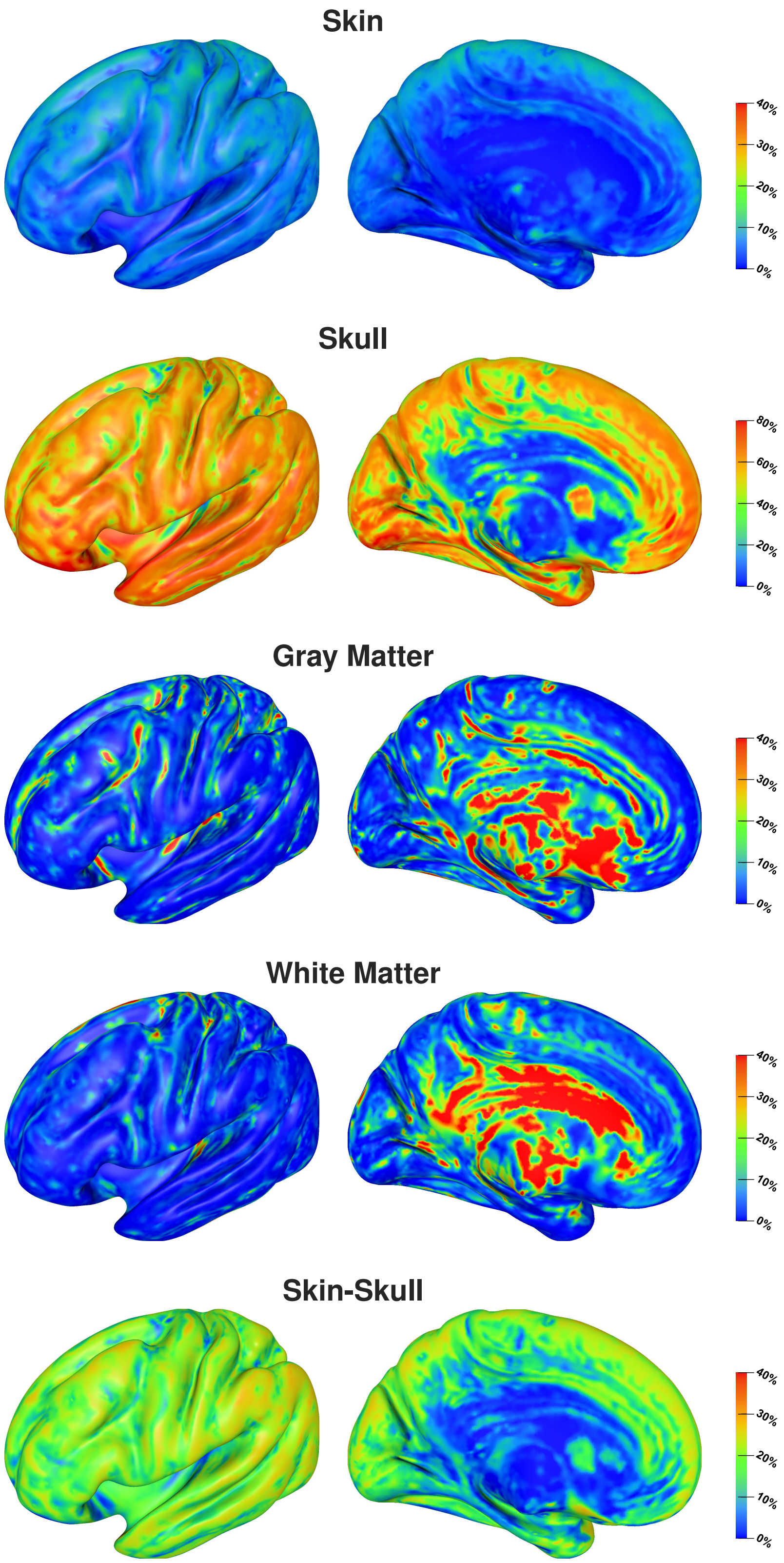

FIGURE 3
First-order and skin-skull second-order Sobol indices for signal topography visualized on inflated cortex surface; (fronto-)lateral **(left column)** and medial **(right column)** view. Please observe the different scalings of the colorbar.

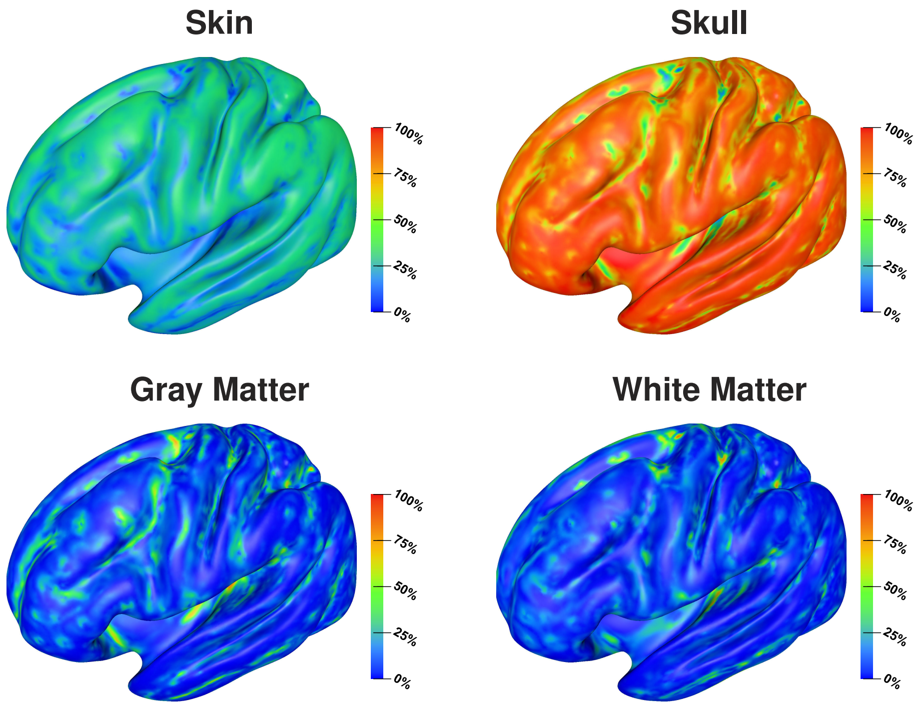

FIGURE 4
Full Sobol indices for signal topography visualized on inflated cortex surface; (fronto-)lateral view.

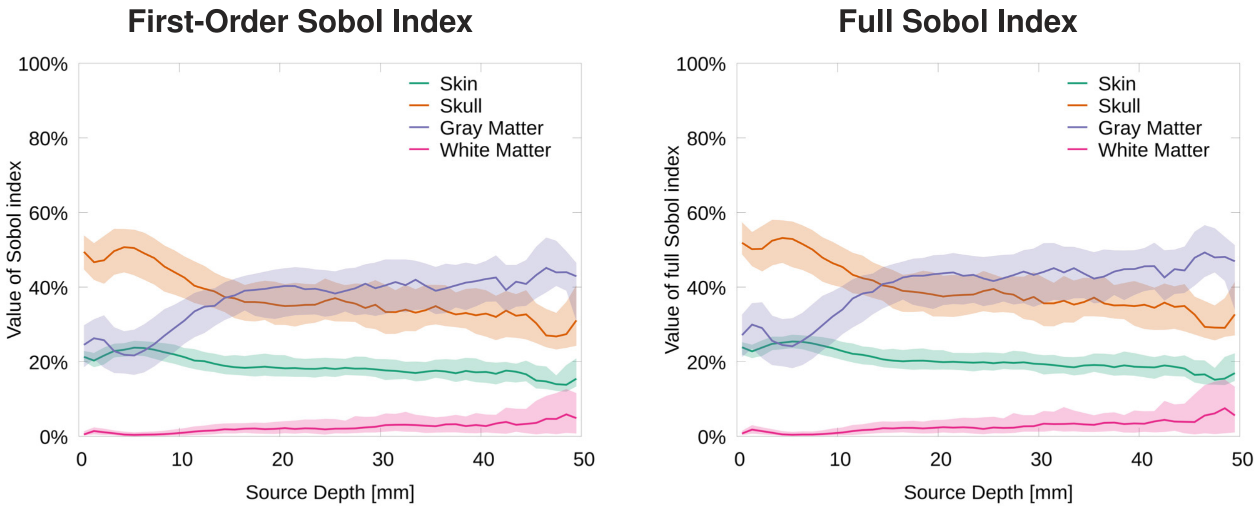

FIGURE 5
Median and 50% confidence interval of first-order **(left)** and full **(right)** Sobol indices for signal magnitude/MAG plotted as a function of source depth.

could be attributed to subcortical structures are small. Visualizing the ratio between change in source depth, i.e., the absolute value of the difference between depth of the original source position and depth of the reconstructed source position, and localization error, i.e., the distance between the original source position and the reconstructed source position, Figure 7 (bottom) shows that for the quasi-tangential sources on the sulcal walls and for sources in the longitudinal fissure the localization error is nearly completely caused by changes in source depth, whereas this is slightly less distinct for the quasi-radial sources at the bottoms of the sulci. For the quasi-radial sources on top of gyri, only a small fraction of the localization error can be explained by changes in source depth.

Comparing the average localization error (Figure 7, top) and the average RDM for each source position (Figure 8, top) there seems to be no direct relation between the size of the topography

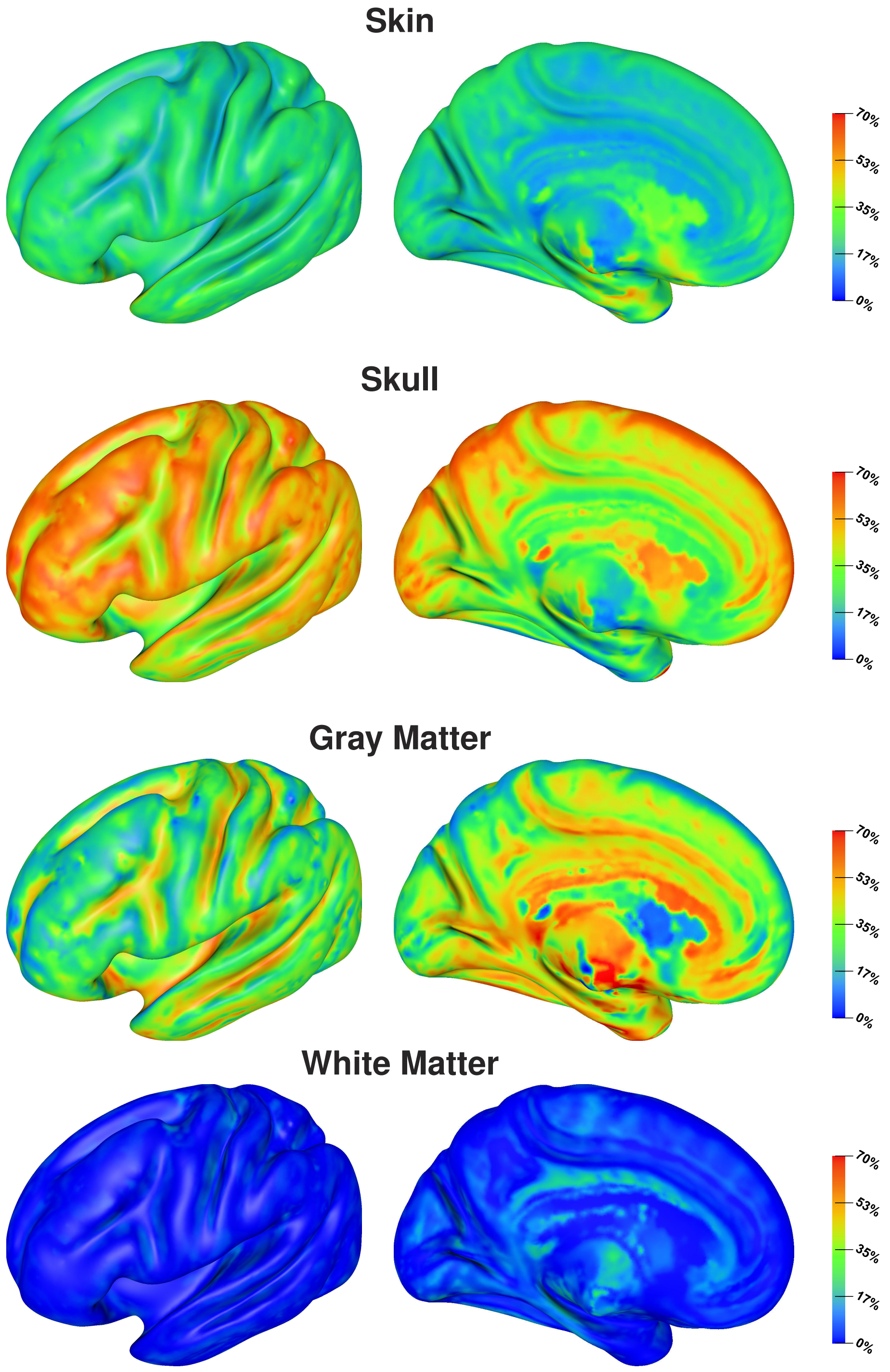

FIGURE 6
Full Sobol indices for signal magnitude visualized on inflated cortex surface; (fronto-)lateral **(left column)** and medial **(right column)** view.

errors at a source position due to conductivity variations and the resulting average localization error. The largest average RDMs are found on top of gyri, which are the source positions at which the average localization error is minimal. However, analyzing the correlation between RDM and localization error at each source position (Figure 8, bottom), we find a clear, positive correlation for the source positions for which we also find large localization errors (compare Figure 8, bottom, and Figure 7, top). For sources that are less affected by localization errors in general, we only find a weaker correlation between RDM and localization errors.

To understand which tissue conductivities drive the overall localization errors and the changes in source depth, we calculated two different correlation coefficients. For the localization error, we calculated correlation coefficients between the absolute value of the deviation of a tissue conductivity from the mean conductivity

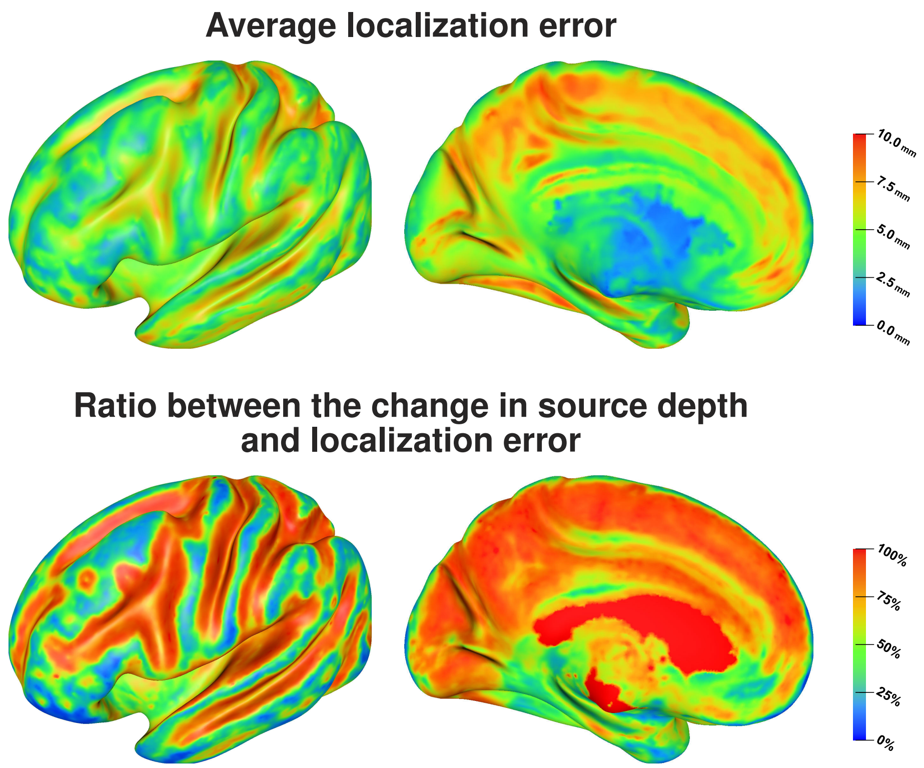

FIGURE 7
Average localization error **(top)** and the average ratio between the change in source depth and localization error **(bottom)** visualized on inflated cortex surface; (fronto-)lateral **(left column)** and medial **(right column)** view.

for this tissue, $|\sigma_i - (\sigma_{max} - \sigma_{min})/2|$, and the distance of the source localization from the center of the point cloud of source localizations for each source position, $\|\mathbf{x_i} - \frac{1}{n}\sum_j \mathbf{x_j}\|_2$ (Figure 9, left). Taking the absolute value of the deviation was necessary here to be able to properly calculate a correlation, as the localization error can only be measured as a distance to a reference position (in our case the center of the point cloud of source localizations), i.e., the distance is always positive, regardless of whether the conductivity was increased or decreased. For the source depth, it was directly possible to calculate the correlation coefficients between tissue conductivities and depth of the corresponding reconstructed sources (Figure 9, right).

We find that changes in the skull conductivity have the by far strongest influence on localization errors, with a correlation coefficient of around 0.6 for all source depths. All other correlation coefficients have small values below 0.1 with the skin conductivity having the second highest correlation especially for sources deeper than 1 cm (Figure 9, top). We find a strong negative correlation between skull conductivity and source depth, especially for sources deeper than 1 cm. At the same time, we find a positive correlation of up to 0.3 between changes in skin conductivity and source depth. This means that using a higher skull conductivity for the simulated source leads to a more superficial source localization based on standard conductivities, whereas a higher skin conductivity leads to a deeper source localization. As shown in previous studies, changes in skin and skull conductivities have opposite effects and the effect of the skull conductivity is stronger.

We find an increasing variation in the correlation of skull conductivity and source depth for sources 20 mm and deeper. This is presumably caused by sources already being located relatively deep in sulci, for which a further increase in source depth within the sulci upon a decrease of the skull conductivity is not possible. These sources might then be mislocalized in a different brain structure but at a similar source depth, e.g., in a neighboring sulci, resulting in a reduced correlation coefficient.

Visualizing the correlation coefficients of skin and skull conductivities and source depth shows the strongest correlations for sources inside the sulci and especially on sulcal walls (Figure 10). This correlates to the source positions for which the localization error was mainly driven by an incorrect depth of the reconstructed sources (see Figure 7, bottom). The still relatively high correlation coefficients for sources on top of gyri can be of less relevance, since these source positions were previously found to be more robust against localization errors (see Figure 7, top), so the correlations were probably caused by rather small variations of the source localizations. For deep brain areas the medial view shows inverted correlation coefficients for both skin and skull conductivity. However, due to the generally small average localization errors in these areas (Figure 7, top) and the small influence of skin and skull conductivity on the signal topography for these sources (Figure 3) they presumably have only little influence in practice.

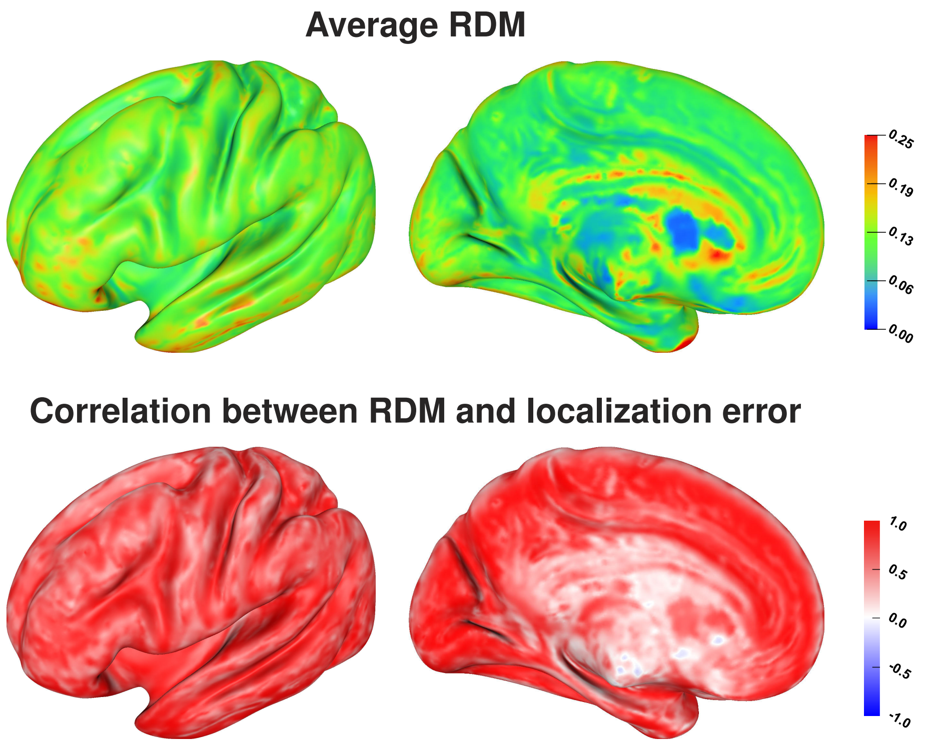

FIGURE 8
Average RDM **(top)** and correlation between RDM and localization error, i.e., distance between reconstructed and original source position, **(bottom)** visualized on inflated cortex surface; (fronto-)lateral **(left column)** and medial **(right column)** view.

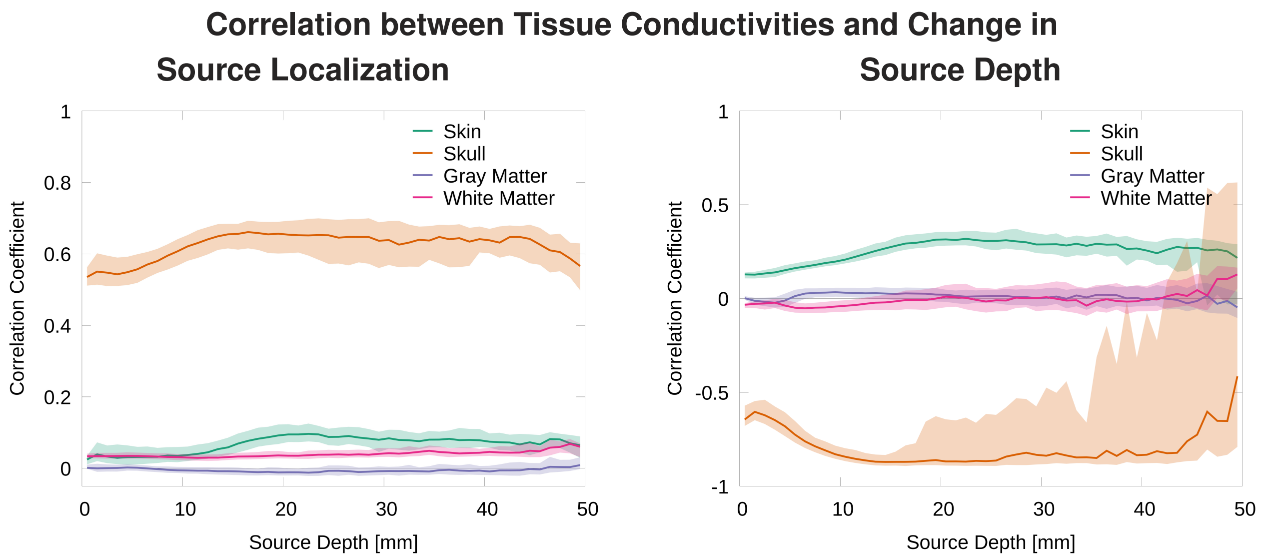

FIGURE 9
Median and 50% confidence interval of the correlation coefficient between deviation of tissue conductivities from mean, $|\sigma_i - (\sigma_{max} - \sigma_{min})/2|$, and distance to average source localization **(left)** and correlation coefficient between tissue conductivity and depth of localized source **(right)** plotted as a function of source depth.

4 Discussion

4.1 EEG forward problem

In this study, we investigated the sensitivity of EEG forward and inverse solutions to conductivity uncertainties. Making use of Sobol indices, we found that variations of the skull conductivity have the by far strongest influence on the topography of EEG forward solutions (Figures 2–4). Furthermore, we found a notable influence of skin conductivity variations, especially through the second-order skin-skull interaction. For very deep sources (source depth of more than 40 mm), which corresponds to sources deep in

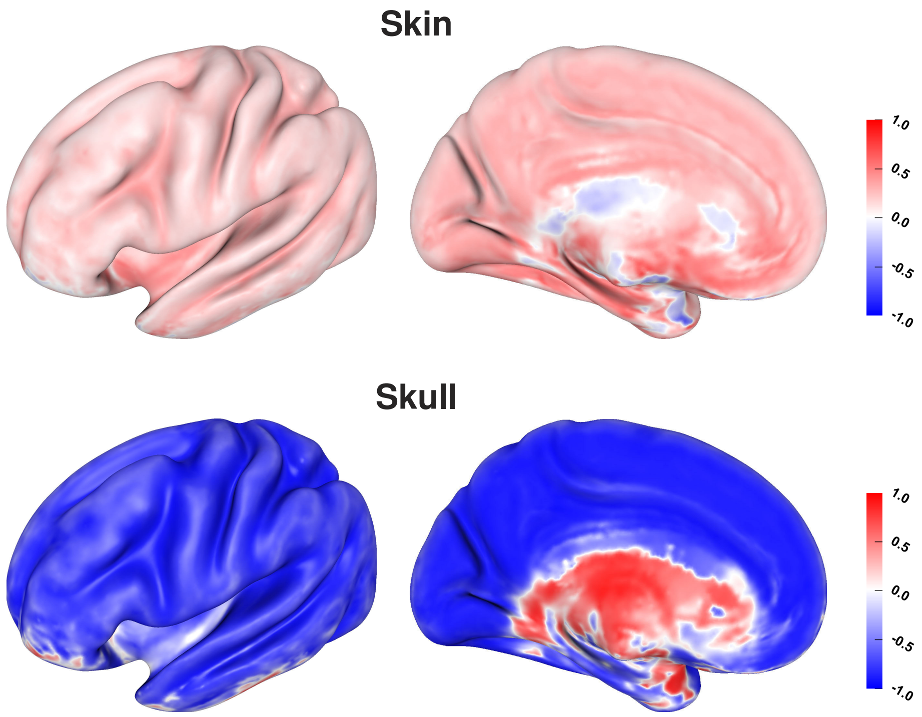

FIGURE 10
Correlation coefficient between tissue conductivity and depth of source localization for skin **(top)** and skull conductivity **(bottom)** visualized on inflated cortex surface; (fronto-)lateral **(left column)** and medial **(right column)** view.

the longitudinal fissure and in subcortical structures, the sensitivity to white and gray matter conductivity variations increases clearly. For the signal magnitude, we find a strong sensitivity to variations of skull and gray matter conductivities, with an especially strong influence of the skull conductivity for superficial, quasi-radial sources (Figures 5, 6). Furthermore, we find a notable influence of the skin conductivity which is almost constant for all source depths.

These results confirm the results of prior sensitivity studies (Gençer and Acar, 2004; Vallaghé and Clerc, 2008; Vorwerk et al., 2019a). Using realistic three- and four-layer models, Vallaghé and Clerc (2008) found the strongest sensitivity for the skin-skull interaction, whereas we found the strongest sensitivity for variations of the skull conductivity in our study with a clearly lower sensitivity to the skin-skull interaction. However, for EEG source analysis, the variations of skin and skull conductivity were shown to have almost identical effects on localization errors but with opposing directions, and the influence of the skull conductivity was found to be stronger than that of the skin conductivity (Figure 10, Vorwerk et al. 2019a). Thus, it is hard to distinguish between the first-order effects of variations of skin and skull conductivity and the second-order skin-skull sensitivity in a sensitivity study, but the practical implications are the same.

Whereas prior studies investigated the sensitivity of the EEG forward solution toward conductivity variations only for a few sources, we present results for sources positioned on the whole cortex surface and variations of four tissue conductivity in our study. Vallaghé and Clerc (2008) and Vorwerk et al. (2019a) both analyzed a source in the postcentral gyrus, for which it is not directly clear in how far the results are representative for general source positions. Our study shows that the results for such a source can indeed be generalized for most sources on sulcal walls, whereas we find a slightly different sensitivity distribution for sources on top of gyri and at the bottom of sulci. For such sources, the sensitivity toward skin and skull conductivity may be reduced and a higher sensitivity toward variations of gray and white matter conductivities can be found. This corresponds to the results of Gençer and Acar (2004), who found a strong dependency of the sensitivity values on the dipole direction.

4.2 EEG inverse problem

We find the strongest influence of conductivity variations for sources inside of sulci, especially on sulcal walls, and in the longitudinal fissure on EEG source localizations. For these sources, we observe a strong change of the depth of the source reconstruction as a result of conductivity variations (Figure 7). We find average localization errors of up to 1 cm, which corresponds to an extent of the point cloud of source localizations of up to 2 cm. A large amount of these localization errors is caused by incorrect reconstructions of the source depth, i.e., the sources are localized more superficial or deeper on the sulcal wall than the original source position, which makes these mislocalizations relatively predictable. The localization of sources on top of gyri, which mostly have a quasi-radial or partially quasi-radial source orientation, is clearly less affected by conductivity variations. However, only a small amount of these localization errors is caused by an incorrect reconstruction of the source depth, and thus has to be mainly caused by mislocalizations in a direction tangential to the inner skull surface, which could be a mislocalization of the source position along the top of the gyri or to the top of a neighboring gyri. In consequence, this makes these mislocalizations—if they occur—potentially harder to predict than those for quasi-tangential sources.

At all source depths except for very deep brain areas, we find a strong correlation between the localization error and the change in skull conductivity (Figure 10). Investigating the correlation between tissue conductivity variations and the change in source depth, we find a strong negative correlation with the skull conductivity and a positive correlation with the skin conductivity. This means that underestimating the skull conductivity leads to a too shallow source reconstruction and overestimating to a too deep source reconstruction. The opposite effect is found for the skin conductivity. Changes in gray and white matter conductivity neither affected the general localization error nor the source depth.

Our results are in line and expand upon prior studies investigating the influence of tissue conductivity variations on EEG source localizations (Vanrumste et al., 2000; Chen et al., 2010; Akalin Acar and Makeig, 2013; Aydin et al., 2014; Vorwerk et al., 2019a; McCann and Beltrachini, 2022). These studies mostly focused on the effect of variations of the skull conductivity or only investigated single source positions. Our study shows that the effects of skin conductivity variations on the depth of source reconstructions found in Vanrumste et al. (2000) and Aydin et al. (2014) can be generalized for almost all source positions with limitations for very superficial sources. Furthermore, our study confirmed the opposing effects of variations of skin and skull conductivity and confirmed the effect of the skin conductivity on the depth of the reconstructed source found in Vorwerk et al. (2019a) for general source positions. Finally, we also found that the effects of gray and white matter conductivity variations on source localizations remain negligible even for very deep cortical sources, e.g., in the insula.

4.3 Limitations

To obtain results that are universally applicable, we made use of a head model based on an averaged MRI template in this study. Therefore, any effects due to individual anatomical variations should be excluded. The stability of our results over the whole cortex suggests that these can largely be transferred to individual head models, of course, except in cases with significant variations of the anatomy such as skull openings, brain resections, or lesions (Oostenveld and Oostendorp, 2002; Brodbeck et al., 2009; Rullmann et al., 2009; Lanfer et al., 2012).

The head model used in this study has two major simplifications compared to six-layer state-of-the-art head models with anisotropic white matter conductivity. We did not include white matter anisotropy in our study, as no such data are available for the New York Head. Given the small influence of variations of the white matter conductivity found for nearly all source positions in this study, it can be assumed that this simplification did not have any significant effect on the outcome of our study. Furthermore, we did not include the distinction between skull compacta and spongiosa, but modeled a homogeneous skull compartment instead. Prior studies have shown that neglecting this distinction can especially affect the accuracy of the EEG forward solution in temporal regions (Vorwerk et al., 2014; Nielsen et al., 2023), below suture lines (McCann and Beltrachini, 2022), or at the skull base (Montes-Restrepo et al., 2014). Since we did not consider this distinction in both the forward and inverse calculations, there should be no direct impact on the results of this study. However, considering variations of skull compacta and spongiosa conductivities separately would add another layer of complexity and might be of interest in future studies. To keep the computational complexity within bounds one might neglect variations of gray and white matter conductivities in turn, which were found to have only a minor influence in our study.

Both in the forward and inverse studies, we focused on single dipole scenarios, i.e., extended source models were not investigated. In general, the results of our inverse study should translate for all inverse methods that allow for an accurate localization of single dipoles. This includes not only dipole scans and dipole fits, but also beamforming methods (Sekihara and Nagarajan, 2008; Westner et al., 2022) and some current-density reconstruction methods, e.g., Bayesian methods (Lucka et al., 2012; Costa et al., 2017; Rezaei et al., 2020), minimum norm estimates (MNE) with depth weighting (Fuchs et al., 1999), or LORETA variations (Pascual-Marqui et al., 2002). Contrary to this, Stenroos and Hauk (2013) have shown that classical MNEs are robust against skull conductivity errors. However, this comes at the cost of an increased localization error for sources that are not superficial (Stenroos and Hauk, 2013, Figure A1), since MNE suffers from depth-bias, i.e., the peak of the reconstructed current density is generally localized too superficial for deep sources (Fuchs et al., 1999; Lucka et al., 2012). Thus, MNEs are not a suitable inverse approach in scenarios where deeper sources are assumed. In other scenarios, e.g., group studies in which widespread brain activation is reconstructed and compared between subjects, the benefit of the robustness against skull conductivity variations might outweigh the disadvantage of the depth-bias. In general, the effect of conductivity variations on the reconstruction of extended sources was not investigated in this study. However, it can be assumed that our results can be generalized to such cases as long as the source is still predominantly dipolar.

Finally, it has to be noted that our choice of the intervals within which the tissue conductivities may vary (Table 1) represents a worst-case scenario. Not only were these intervals chosen rather widely, but it can also be assumed that the real distribution of the conductivities is not uniform but more focused around the literature value (McCann et al., 2019). In practice, the tissue conductivity uncertainties could potentially be more realistically modeled through, e.g., β- or Normal distributions (Gutiérrez et al., 2004; Saturnino et al., 2019). However, these distributions require additional parameters, which, again, are not known a priori and need to be estimated based on the literature.

5 Conclusion

In this study, we found that the topography of EEG forward solutions for source positions on the whole cortex surface is mostly sensitive to variations of skull and skin conductivity. The magnitude of EEG forward solutions is also very sensitive to the skull conductivity, but almost similarly sensitive to the gray matter conductivity and to a smaller degree also to the skin conductivity. Analyzing the EEG inverse problem, we find that these changes in the EEG forward solutions translate to localization errors particularly for sources inside of sulci, with the strongest effect on sources on the sulcal walls. For these sources, the localization errors clearly correlate with variations in skull and skin conductivity resulting in changes in the source depth of the reconstructed sources. Sources on top of gyri showed the strongest topography changes for varying tissue conductivities, but these changes resulted in smaller source reconstruction errors than for sources inside of sulci. We are convinced that these results help to better estimate the uncertainty inherent to EEG source localizations. Furthermore, our study shows the additional value of skull conductivity calibration, as the inter-individual variation of the skull conductivity is one of the main sources of EEG source analysis uncertainties affecting almost all cortex areas.

Data availability statement

The datasets presented in this study can be found in online repositories. The names of the repository/repositories and accession number(s) can be found below: https://www.parralab.org/nyhead/.

Author contributions

JV: Conceptualization, Funding acquisition, Investigation, Methodology, Writing – original draft, Writing – review & editing. CW: Conceptualization, Funding acquisition, Supervision, Writing - review & editing. DB: Conceptualization, Funding acquisition, Resources, Supervision, Writing - review & editing.

Funding

The author(s) declare financial support was received for the research, authorship, and/or publication of this article. This research was funded in whole, or in part, by the Austrian Science Fund (FWF), projects P 35949 (JV) and I 3790-B27 (JV and DB), the Tyrolian Science Fund (TWF), project F.45065 (JV), the Bundesministerium für Gesundheit (BMG), as project ZMI1-2521FSB006 under the frame of ERA PerMed as project ERAPERMED2020-227 (CW), the Deutsche Forschungsgemeinschaft (DFG), project WO1425/10-1 (CW), and by DAAD project 57663920 (CW). For the purpose of open access, the author has applied a CC BY public copyright licence to any Author Accepted Manuscript version arising from this submission.

Conflict of interest

The authors declare that the research was conducted in the absence of any commercial or financial relationships that could be construed as a potential conflict of interest.

The author(s) declared that they were an editorial board member of Frontiers, at the time of submission. This had no impact on the peer review process and the final decision.

Publisher's note

Supplementary material

The Supplementary Material for this article can be found online at: https://www.frontiersin.org/articles/10.3389/fnhum.2024.1335212/full#supplementary-material

References

Acar, Z. A., Acar, C. E., and Makeig, S. (2016). Simultaneous head tissue conductivity and EEG source location estimation. *Neuroimage* 124, 168–180. doi: 10.1016/j.neuroimage.2015.08.032

Akalin Acar, Z., and Makeig, S. (2013). Effects of forward model errors on EEG source localization. *Brain Topogr*. 26, 378–396. doi: 10.1007/s10548-012-0274-6

Akhtari, M., Bryant, H., Mamelak, A., Flynn, E., Heller, L., Shih, J., et al. (2002). Conductivities of three-layer live human skull. *Brain Topogr*. 14, 151–167. doi: 10.1023/A:1014590923185

Antonakakis, M., Schrader, S., Aydin, Ü., Khan, A., Gross, J., Zervakis, M., et al. (2020). Inter-subject variability of skull conductivity and thickness in calibrated realistic head models. *Neuroimage* 223:117353. doi: 10.1016/j.neuroimage.2020.117353

Asadzadeh, S., Rezaii, T. Y., Beheshti, S., Delpak, A., and Meshgini, S. (2020). A systematic review of EEG source localization techniques and their applications on diagnosis of brain abnormalities. *J. Neurosci. Methods* 339, 108740. doi: 10.1016/j.jneumeth.2020.108740

Aydin, Ü., Vorwerk, J., Küpper, P., Heers, M., Kugel, H., Galka, A., et al. (2014). Combining EEG and MEG for the reconstruction of epileptic activity using a calibrated realistic volume conductor model. *PLoS ONE* 9:e93154. doi: 10.1371/journal.pone.0093154

Azizollahi, H., Aarabi, A., and Wallois, F. (2020). Effect of structural complexities in head modeling on the accuracy of EEG source localization in neonates. *J. Neural Eng*. 17:056004. doi: 10.1088/1741-2552/abb994

Baumann, S. B., Wozny, D. R., Kelly, S. K., and Meno, F. M. (1997). The electrical conductivity of human cerebrospinal fluid at body temperature. *IEEE Transact. Biomed. Eng*. 44, 220–223. doi: 10.1109/10.554770

Brette, R., and Destexhe, A. (2012). *Handbook of Neural Activity Measurement*. Cambridge: Cambridge University Press.

Brodbeck, V., Lascano, A. M., Spinelli, L., Seeck, M., and Michel, C. M. (2009). Accuracy of EEG source imaging of epileptic spikes in patients with large brain lesions. *Clin Neurophysiol*. 120, 679–685. doi: 10.1016/j.clinph.2009.01.011

Buchner, H., Knoll, G., Fuchs, M., Rienäcker, A., Beckmann, R., Wagner, M., et al. (1997). Inverse localization of electric dipole current sources in finite element models of the human head. *Electroencephalogr. Clin. Neurophysiol*. 102, 267–278. doi: 10.1016/S0013-4694(96)95698-9

Buzzell, G. A., Richards, J. E., White, L. K., Barker, T. V., Pine, D. S., and Fox, N. A. (2017). Development of the error-monitoring system from ages 9-35: unique insight provided by MRI-constrained source localization of EEG. *Neuroimage* 157, 13–26. doi: 10.1016/j.neuroimage.2017.05.045

Chen, F., Hallez, H., and Staelens, S. (2010). Influence of skull conductivity perturbations on EEG dipole source analysis. *Med. Phys.* 37, 4475–4484. doi: 10.1118/1.3466831

Cho, J.-H., Vorwerk, J., Wolters, C. H., and Knösche, T. R. (2015). Influence of the head model on EEG and MEG source connectivity analyses. *Neuroimage* 110, 60–77. doi: 10.1016/j.neuroimage.2015.01.043

Costa, F., Batatia, H., Oberlin, T., d'Giano, C., and Tourneret, J.-Y. (2017). Bayesian EEG source localization using a structured sparsity prior. *Neuroimage* 144, 142–152. doi: 10.1016/j.neuroimage.2016.08.064

Dannhauer, M., Lanfer, B., Wolters, C. H., and Knösche, T. R. (2011). Modeling of the human skull in EEG source analysis. *Hum. Brain Mapp.* 32, 1383–1399. doi: 10.1002/hbm.21114

Fernández-Corazza, M., Turovets, S., Luu, P., Price, N., Muravchik, C. H., and Tucker, D. (2017). Skull modeling effects in conductivity estimates using parametric electrical impedance tomography. *IEEE Transact. Biomed. Eng.* 65, 1785–1797. doi: 10.1109/TBME.2017.2777143

Fuchs, M., Wagner, M., Köhler, T., and Wischmann, H.-A. (1999). Linear and nonlinear current density reconstructions. *J. Clin. Neurophysiol.* 16, 267–295. doi: 10.1097/00004691-199905000-00006

Fuchs, M., Wagner, M., Wischmann, H.-A., Köhler, T., Theißen, A., Drenckhahn, R., et al. (1998). Improving source reconstructions by combining bioelectric and biomagnetic data. *Electroencephalogr. Clin. Neurophysiol.* 107, 93–111. doi: 10.1016/S0013-4694(98)00046-7

Gao, C., Conte, S., Richards, J. E., Xie, W., and Hanayik, T. (2019). The neural sources of N170: understanding timing of activation in face-selective areas. *Psychophysiology* 56:e13336. doi: 10.1111/psyp.13336

Gençer, N. G., and Acar, C. E. (2004). Sensitivity of EEG and MEG measurements to tissue conductivity. *Phys. Med. Biol.* 49:701. doi: 10.1088/0031-9155/49/5/004

Gutiéerrez, D., Nehorai, A., and Muravchik, C. H. (2004). Estimating brain conductivities and dipole source signals with EEG arrays. *IEEE Transact. Biomed. Eng.* 51, 2113–2122. doi: 10.1109/TBME.2004.836507

Haueisen, J., Ramon, C., Eiselt, M., Brauer, H., and Nowak, H. (1997). Influence of tissue resistivities on neuromagnetic fields and electric potentials studied with a finite element model of the head. *IEEE Transact. Biomed. Eng.* 44, 727–735. doi: 10.1109/10.605429

Hoekema, R., Wieneke, G., Leijten, F., Van Veelen, C., Van Rijen, P., Huiskamp, G., et al. (2003). Measurement of the conductivity of skull, temporarily removed during epilepsy surgery. *Brain Topogr.* 16, 29–38. doi: 10.1023/A:1025606415858

Huang, M.-X., Song, T., Hagler Jr, D. J., Podgorny, I., Jousmaki, V., Cui, L., et al. (2007). A novel integrated MEG and EEG analysis method for dipolar sources. *Neuroimage* 37, 731–748. doi: 10.1016/j.neuroimage.2007.06.002

Huang, Y., Parra, L. C., and Haufe, S. (2016). The New York Head—a precise standardized volume conductor model for EEG source localization and tES targeting. *Neuroimage* 140, 150–162. doi: 10.1016/j.neuroimage.2015.12.019

Janon, A., Klein, T., Lagnoux, A., Nodet, M., and Prieur, C. (2014). Asymptotic normality and efficiency of two Sobol index estimators. *ESAIM Prob. Stat.* 18, 342–364. doi: 10.1051/ps/2013040

Knösche, T. R. (1997). *Solutions of the neuroelectromagnetic inverse problem: an evaluation study (PhD thesis)*. University of Twente, Enschede, Netherlands.

Knösche, T. R., and Haueisen, J. (2022). *EEG/MEG Source Reconstruction: Textbook for Electro-and Magnetoencephalography*. Cham: Springer.

Kybic, J., Clerc, M., Abboud, T., Faugeras, O., Keriven, R., and Papadopoulo, T. (2005). A common formalism for the integral formulations of the forward EEG problem. *IEEE Trans. Med. Imaging* 24, 12–18. doi: 10.1109/TMI.2004.837363

Lanfer, B., Scherg, M., Dannhauer, M., Knösche, T. R., Burger, M., and Wolters, C. H. (2012). Influences of skull segmentation inaccuracies on EEG source analysis. *Neuroimage* 62, 418–431. doi: 10.1016/j.neuroimage.2012.05.006

Lucka, F., Pursiainen, S., Burger, M., and Wolters, C. H. (2012). Hierarchical bayesian inference for the EEG inverse problem using realistic FE head models: depth localization and source separation for focal primary currents. *Neuroimage* 61, 1364–1382. doi: 10.1016/j.neuroimage.2012.04.017

Marelli, S., and Sudret, B. (2014). "UQLab: a framework for uncertainty quantification in MATLAB, stefano marelli and bruno sudret," in *The 2nd International Conference on Vulnerability and Risk Analysis and Management (ICVRAM 2014)* (University of Liverpool), 2554–2563. doi: 10.1061/9780784413609.257

McCann, H., and Beltrachini, L. (2022). Impact of skull sutures, spongiform bone distribution, and aging skull conductivities on the EEG forward and inverse problems. *J. Neural Eng.* 19:016014. doi: 10.1088/1741-2552/ac43f7

McCann, H., Pisano, G., and Beltrachini, L. (2019). Variation in reported human head tissue electrical conductivity values. *Brain Topogr.* 32, 825–858. doi: 10.1007/s10548-019-00710-2

Meijs, J. W., Weier, O. W., Peters, M. J., and Van Oosterom, A. (1989). On the numerical accuracy of the boundary element method (EEG application). *IEEE Transact. Biomed. Eng.* 36, 1038–1049. doi: 10.1109/10.40805

Montes-Restrepo, V., van Mierlo, P., Strobbe, G., Staelens, S., Vandenberghe, S., and Hallez, H. (2014). Influence of skull modeling approaches on EEG source localization. *Brain Topogr.* 27, 95–111. doi: 10.1007/s10548-013-0313-y

Neugebauer, F., Möddel, G., Rampp, S., Burger, M., and Wolters, C. H. (2017). The effect of head model simplification on beamformer source localization. *Front. Neurosci.* 11:625. doi: 10.3389/fnins.2017.00625

Nielsen, J. D., Puonti, O., Xue, R., Thielscher, A., and Madsen, K. H. (2023). Evaluating the influence of anatomical accuracy and electrode positions on EEG forward solutions. *Neuroimage* 277:120259. doi: 10.1016/j.neuroimage.2023.120259

Oostenveld, R., and Oostendorp, T. F. (2002). Validating the boundary element method for forward and inverse EEG computations in the presence of a hole in the skull. *Hum. Brain Mapp.* 17, 179–192. doi: 10.1002/hbm.10061

Pascual-Marqui, R. D. (2002). Standardized low-resolution brain electromagnetic tomography (sLORETA): technical details. *Methods Find. Exp. Clin. Pharmacol.* 24 (Suppl. D): 5–12.

Piai, V., Meyer, L., Dronkers, N. F., and Knight, R. T. (2017). Neuroplasticity of language in left-hemisphere stroke: evidence linking subsecond electrophysiology and structural connections. *Hum. Brain Mapp.* 38, 3151–3162. doi: 10.1002/hbm.23581

Puonti, O., Van Leemput, K., Saturnino, G. B., Siebner, H. R., Madsen, K. H., and Thielscher, A. (2020). Accurate and robust whole-head segmentation from magnetic resonance images for individualized head modeling. *Neuroimage* 219:117044. doi: 10.1016/j.neuroimage.2020.117044

Ramon, C., Schimpf, P., Haueisen, J., Holmes, M., and Ishimaru, A. (2004). Role of soft bone, csf and gray matter in EEG simulations. *Brain Topogr.* 16, 245–248. doi: 10.1023/B:BRAT.0000032859.68959.76

Ramon, C., Schimpf, P. H., and Haueisen, J. (2006). Influence of head models on EEG simulations and inverse source localizations. *Biomed. Eng. Online* 5, 1–13. doi: 10.1186/1475-925X-5-10

Rezaei, A., Koulouri, A., and Pursiainen, S. (2020). Randomized multiresolution scanning in focal and fast E/MEG sensing of brain activity with a variable depth. *Brain Topogr.* 33, 161–175. doi: 10.1007/s10548-020-00755-8

Rullmann, M., Anwander, A., Dannhauer, M., Warfield, S. K., Duffy, F. H., and Wolters, C. H. (2009). EEG source analysis of epileptiform activity using a 1 mm anisotropic hexahedra finite element head model. *Neuroimage* 44, 399–410. doi: 10.1016/j.neuroimage.2008.09.009

Saturnino, G. B., Thielscher, A., Madsen, K. H., Knösche, T. R., and Weise, K. (2019). A principled approach to conductivity uncertainty analysis in electric field calculations. *Neuroimage* 188, 821–834. doi: 10.1016/j.neuroimage.2018.12.053

Sekihara, K., and Nagarajan, S. S. (2008). *Adaptive Spatial Filters for Electromagnetic Brain Imaging*. Berlin: Springer Science & Business Media.

Sobol, I. M. (2001). Global sensitivity indices for nonlinear mathematical models and their Monte Carlo estimates. *Math. Comput. Simul.* 55, 271–280. doi: 10.1016/S0378-4754(00)00270-6

Staljanssens, W., Strobbe, G., Holen, R. V., Birot, G., Gschwind, M., Seeck, M., et al. (2017). Seizure onset zone localization from ictal high-density EEG in refractory focal epilepsy. *Brain Topogr.* 30, 257–271. doi: 10.1007/s10548-016-0537-8

Stenroos, M., and Hauk, O. (2013). Minimum-norm cortical source estimation in layered head models is robust against skull conductivity error. *Neuroimage* 81, 265–272. doi: 10.1016/j.neuroimage.2013.04.086

Vallaghé, S., and Clerc, M. (2008). A global sensitivity analysis of three-and four-layer EEG conductivity models. *IEEE Transact. Biomed. Eng.* 56, 988–995. doi: 10.1109/TBME.2008.2009315

Vanrumste, B., Van Hoey, G., Van de Walle, R., D'havé, M., Lemahieu, I., and Boon, P. (2000). Dipole location errors in electroencephalogram source analysis due to volume conductor model errors. *Med. Biol. Eng. Comp.* 38, 528–534. doi: 10.1007/BF02345748

Vorwerk, J., Aydin, Ü., Wolters, C. H., and Butson, C. R. (2019a). Influence of head tissue conductivity uncertainties on EEG dipole reconstruction. *Front. Neurosci.* 13:531. doi: 10.3389/fnins.2019.00531

Vorwerk, J., Cho, J.-H., Rampp, S., Hamer, H., Knösche, T. R., and Wolters, C. H. (2014). A guideline for head volume conductor modeling in EEG and MEG. *Neuroimage* 100, 590–607. doi: 10.1016/j.neuroimage.2014.06.040

Vorwerk, J., Hanrath, A., Wolters, C. H., and Grasedyck, L. (2019b). The multipole approach for EEG forward modeling using the finite element method. *Neuroimage* 201:116039. doi: 10.1016/j.neuroimage.2019.116039

Vorwerk, J., Oostenveld, R., Piastra, M. C., Magyari, L., and Wolters, C. H. (2018). The FieldTrip-SimBio pipeline for EEG forward solutions. *Biomed. Eng. Online* 17, 1–17.

Westner, B. U., Dalal, S. S., Gramfort, A., Litvak, V., Mosher, J. C., Oostenveld, R., et al. (2022). A unified view on beamformers for M/EEG source reconstruction. *Neuroimage* 246:118789. doi: 10.1016/j.neuroimage.2021.118789

Yan, Y., Nunez, P., and Hart, R. (1991). Finite-element model of the human head: scalp potentials due to dipole sources. *Med. Biol. Eng. Comp.* 29, 475–481. doi: 10.1007/BF02442317

Zaky, M. H., Shoorangiz, R., Poudel, G. R., Yang, L., Innes, C. R., and Jones, R. D. (2023). Increased cerebral activity during microsleeps reflects an unconscious drive to re-establish consciousness. *Int. J. Psychophysiol.* 189, 57–65. doi: 10.1016/j.ijpsycho.2023.05.349

frontiers | Frontiers in Human Neuroscience

TYPE Technology and Code
PUBLISHED 13 March 2024
DOI 10.3389/fnhum.2024.1359753

OPEN ACCESS

EDITED BY
Sampsa Pursiainen,
Tampere University, Finland

REVIEWED BY
Errikos-Chaim Michael Ventouras,
University of West Attica, Greece
Johannes Vorwerk,
UMIT TIROL - Private University for Health Sciences and Health Technology, Austria

*CORRESPONDENCE
Alberto Sorrentino
✉ sorrentino@dima.unige.it

RECEIVED 21 December 2023
ACCEPTED 19 February 2024
PUBLISHED 13 March 2024

CITATION
Luria G, Viani A, Pascarella A, Bornfleth H, Sommariva S and Sorrentino A (2024) The SESAMEEG package: a probabilistic tool for source localization and uncertainty quantification in M/EEG.
Front. Hum. Neurosci. 18:1359753.
doi: 10.3389/fnhum.2024.1359753

The SESAMEEG package: a probabilistic tool for source localization and uncertainty quantification in M/EEG

Gianvittorio Luria[1], Alessandro Viani[2], Annalisa Pascarella[3], Harald Bornfleth[4], Sara Sommariva[2] and Alberto Sorrentino[2]*

[1]Bayesian Estimation for Engineering Solutions srl, Genoa, Italy, [2]Department of Mathematics, University of Genoa, Genoa, Italy, [3]CNR, Institute for Applied Mathematics "Mauro Picone", Rome, Italy, [4]BESA GmbH, Gräfelfing, Germany

Source localization from M/EEG data is a fundamental step in many analysis pipelines, including those aiming at clinical applications such as the pre-surgical evaluation in epilepsy. Among the many available source localization algorithms, SESAME (SEquential SemiAnalytic Montecarlo Estimator) is a Bayesian method that distinguishes itself for several good reasons: it is highly accurate in localizing focal sources with comparably little sensitivity to input parameters; it allows the quantification of the uncertainty of the reconstructed source(s); it accepts user-defined *a priori* high- and low-probability search regions in input; it can localize the generators of neural oscillations in the frequency domain. Both a Python and a MATLAB implementation of SESAME are available as open-source packages under the name of SESAMEEG and are well integrated with the main software packages used by the M/EEG community; moreover, the algorithm is part of the commercial software BESA Research (from version 7.0 onwards). While SESAMEEG is arguably simpler to use than other source modeling methods, it has a much richer output that deserves to be described thoroughly. In this article, after a gentle mathematical introduction to the algorithm, we provide a complete description of the available output and show several use cases on experimental M/EEG data.

KEYWORDS

Bayesian inference, inverse problems, MEG, EEG, open-source software, MATLAB, Python

1 Introduction

The electromagnetic signals at the scalp produced by neural currents in the brain are the most direct consequences of brain electrical activity and can be non–invasively measured by means of MagnetoEncephaloGraphy (Hämäläinen et al., 1993) (MEG) and ElectroEncephaloGraphy (Baillet et al., 2001) (EEG). Remarkably, M/EEG recordings can be acquired at the outstanding sampling rate of the order of the millisecond (Gratta et al., 2001), thus opening the door to the study of the dynamics of neural processes in a wide variety of conditions, both normal (Sorrentino et al., 2006; Brookes et al., 2011) and pathological (Stoffers et al., 2007; Stam et al., 2009; Uda et al., 2012; Luria et al., 2020), with very high precision in time.

Mapping the activity of known sources in the brain to the corresponding M/EEG signals is called the *forward* problem (Pursiainen et al., 2011; Vorwerk et al., 2016). This is a well-posed problem which is solved by giving a parametric representation of the sources and by modeling how the electromagnetic field propagates through the brain compartments. Two main source models have been proposed in the literature so far: the Distributed Source (DS) model and the Equivalent Current Dipole (ECD) model. While in the former the neural current is assumed to be a continuous vector field inside the brain volume, the latter model assumes instead the whole brain activity underlying the M/EEG measurements to occur only in a small number of clusters of thousands of synchronously activated pyramidal cortical neurons. In this setting, each cluster is represented by a point source, called ECD, and the whole primary current distribution is approximated by the superposition of a given number of ECDs. Notably, the ECD model is currently the standard approach in clinical applications of MEG, such as the pre-surgical localization of epileptic spikes, and the only one recommended by the American Clinical Magnetoencephalography Society (Bagic et al., 2011; Carrette and Stefan, 2019). In order to model the propagation of the electromagnetic field through the head, it is crucial to exploit the information about the physical and geometrical properties of the head, which can be gathered from high resolution anatomical Magnetic Resonance Imaging (MRI). Then, discretization of the differential equations governing the electromagnetic fields can be done using Boundary Element Methods (BEM) or Finite Element Methods (FEM); however, BEM can only be used to model homogeneous and isotropic conductivity, which is clearly a too simplistic model; FEM, on the other hand, allow to model inhomogeneous and anisotropic conductivity, but accurate estimates of the spatially-varying conductivity tensor are typically difficult to obtain. As a consequence, despite being a well-posed problem, the forward solution is typically affected by modeling errors as well as numerical inaccuracies.

The capability of solving the forward problem leads to the possibility of inferring the location of the generators of brain activity from M/EEG data, which in turn is called the *inverse* problem. This last is ill-posed, since it suffers from the non-uniqueness of the solution, and exhibits a high sensitivity to noise. As a consequence, data need to be complemented with anatomical and physiological prior knowledge, thus sacrificing the exact match between the recorded and the reconstructed electromagnetic field.

The vast majority of available methods for source localization provide a single, unique "best" reconstruction of neural activity from a given dataset, with no quantification of the degree of reliability of the reconstruction itself, nor any clue about the existence of alternative solutions. However, ill-posedness implies that it is impossible to restore the neural generators exactly; hence, when solving the inverse problem we should not content ourselves with a single best estimate, and should instead answer the following questions too: are there *other* potential solutions? how certain are we of the single estimate provided? Answering these questions is difficult: in order to do it, it is necessary to characterize the probability distribution of the neural current conditioned on the measured data, i.e. the posterior distribution of the Bayesian approach.

In a set of publications (Sorrentino et al., 2013, 2014; Luria et al., 2019; Viani et al., 2021, 2022) we proposed a fully Bayesian algorithm, based on the ECD source model and belonging to the class of Sequential Monte Carlo (SMC) samplers (Del Moral et al., 2006), to solve the M/EEG localization problem. This inverse solver, called SEquential Semi-Analytic Montecarlo Estimator (SESAME), is able to sample the whole posterior distribution for the multi-dipole configuration, thereby providing multiple alternative solutions, each with an associated quantification of its reliability. In a couple of recent studies SESAME has been shown to score very well in terms of localization accuracy when compared to wMNE and MUSIC in Luria et al. (2020) and to a larger set of inverse solvers in Pascarella et al. (2023), while also being particularly stable with respect to input parameters.

In the present paper we present both a Python and a MATLAB open-source implementation of SESAME, under the name of the SESAMEEG package. The main idea behind SESAMEEG is to provide a user-friendly tool that can be used out-of-the-box by the general audience, but also lets the experienced user the possibility of providing different kinds of prior knowledge about the problem. Moreover, to facilitate the entire analysis pipeline, SESAMEEG is well integrated with the most popular open source M/EEG software and SESAME is also implemented in the commercial CE-marked software package BESA Research.

The paper is organized as follows. In Sections 2.1.1–2.1.2 we provide a gentle mathematical introduction to the ECD model and to the Bayesian approach to source modeling. In Section 2.1.3 we discuss the impact of input (hyper)parameters on the output of SESAME, described in Section 2.1.5 A very brief summary of the computations behind SESAME is provided in Section 2.1.4 and the factors affecting the computational cost of the algorithm are discussed in 2.1.6. The SESAMEEG package is described in Section 2.2 and we then proceed with exemplar analysis of experimental datasets: an MEG dataset in Section 3.1 and an EEG dataset in Section 3.2. Finally, in Section 4 we discuss the current and future work.

2 Method

2.1 SESAME: a Bayesian algorithm for M/EEG source modeling

2.1.1 The source model

Source localization of M/EEG data is typically based on the following model:

$$y(t) = \sum_{i=1}^{N} G(r_i)\, q_i(t) + \epsilon(t) \tag{1}$$

where:

- $y(t)$ is the measured data at time t, modeled as the superposition of contributions of different sources;
- $G(r_i)$ is the lead field corresponding to a point source located at r_i;
- $q_i(t)$ represents the neural current at location r_i at time t;
- $\epsilon(t)$ is (Gaussian) noise, accounting for measurements noise as well as forward modeling errors.

In (1) the sum over i represents the additive contributions of sources located at different points r_i in a given discretized source space. For the sake of simplicity, we henceforth omit the time dependence of all variables.

We underline that it is perhaps not common to include forward modeling errors in the additive noise term ϵ; however, we reckon it is important to do so because even exact measurements cannot be explained exactly in a real environment, due to the unavoidable approximations in the forward model. The use of a Gaussian distribution to model this contribution might be questionable: so far this choice is mainly based on practical reasons and lack of better knowledge; the same model was used in other studies, e.g., Rimpiläinen et al. (2019).

In distributed models, source locations $\{r_i\}_{i=1,\ldots,N}$ are assumed to be known *a priori* and the number N of distinct source locations is typically large ($\sim$ 10,000). The only unknowns would be the values $\{q_i\}_{i=1,\ldots,N}$: once these have been estimated, one can localize brain activity as the points corresponding to maximum values of q_i. The number of unknowns is large ($\sim 3 \times 10,000$) but data depend linearly on the unknowns.

In the multi-dipole model, the same Equation (1) is used with the following differences: the number N is now unknown but small (lower than 10); source locations are also unknown. Therefore the total number of unknown parameters to be estimated is much fewer than the corresponding number in the distributed model, but data depend non-linearly on N and $\{r_i\}_{i=1,\ldots,N}$, which makes the problem harder.

In our formulation, we adopt a multi-dipole model for brain activity. We assume that, within the considered time interval, both the number and location of the active sources remain fixed; the only parameter that has a time dependence is the intensity of each active source.

2.1.2 The Bayesian model

The starting point of Bayesian methods is a set of conceptual tenets (Kaipio and Somersalo, 2007; Pascarella and Sorrentino, 2011):

- probability is used to quantify uncertainty about any variable involved in the problem;
- because of the previous item, all variables are considered random variables; this does not imply that such variables are *random* in an ontological sense, but just that our knowledge of their values is imperfect, and such imperfection can be represented with a probability distribution;
- the mathematical rule to combine *a priori* information with information coming from the data is Bayes rule.

SESAME is a Bayesian inference tool applied to a multi-dipole model: it aims at approximating the posterior distribution of the number of sources N, the source locations $R = \{r_i\}_{i=1,\ldots,N}$ and the source strengths $Q = \{q_i\}_{i=1,\ldots,N}$, given the data

$$p(N, R, Q \mid y) = \frac{p(y \mid N, R, Q)\, p(N, R, Q)}{p(y)}$$

where

- $p(N, R, Q \mid y)$ at the left hand side is the posterior distribution;
- the likelihood function $p(y \mid N, R, Q)$ is set to be Gaussian of standard deviation σ_ϵ, accounting for the presence of noise in the data as well as errors in the forward model;
- the second term at the right hand side is the prior $p(N, R, Q)$;
- the denominator is a normalizing constant.

In SESAME we make the further assumption that the unknowns are *a priori* independent $p(N, R, Q) = p(N)\, p(R)\, p(Q)$ and set a Gaussian prior on the source strengths $p(Q) = \mathcal{N}(0, \sigma_q)$; combined with the Gaussian likelihood, this leads to a conditionally linear Gaussian model for source strengths. As a consequence, in the following standard splitting of the posterior

$$p(N, R, Q \mid y) = p(Q \mid N, R, y)\, p(N, R \mid y)$$

the first bit at the right hand side can be computed analytically, while the second bit is approximated with a SMC sampler algorithm (Del Moral et al., 2006), briefly described in Section 2.1.4.

2.1.3 Hyper-parameters

It is important to remark that the posterior distribution depends on the two hyper-parameters mentioned above, namely the standard deviation σ_ϵ of the Gaussian likelihood and the standard deviation σ_q of the Gaussian prior on the dipole strength. Here we briefly explain how to deal with them.

We start by considering the Gaussian prior on the dipole strength, with its corresponding standard deviation σ_q. It is important to remark that a Gaussian prior is a fairly strong prior, that forces the unknown to be of the same order of magnitude as the standard deviation. In principle, this fact can be even used to our own advantage: in Luria et al. (2019) we showed that SESAME can be used to mimick distributed sources by setting a small σ_q, that forces small dipoles and produces more widespread reconstructions. On the other hand, for a standard analysis with a purely dipolar model the dependence of the solution on the value of σ_q is actually annoying, but can be strongly reduced by introducing a *hyper-prior*, i.e. a prior on the hyper-parameter σ_q. This was done originally in Viani et al. (2021), where we presented an updated model in which the hyper-parameter σ_q is considered unknown, and treated as an additional parameter, i.e. sampled from the hyper-prior and then updated in the SMC steps. In order to provide as little information as possible on the order of magnitude of the sources, we chose to use a log-uniform hyper-prior in the interval $[\sigma_q^{min}, 10^3\sigma_q^{min}]$, where σ_q^{min} is chosen based on the order of magnitude of the data and of the lead field. We have shown that the introduction of the hyper-prior makes the estimated configuration stable across over three orders of magnitude of the (hyper-)hyper-parameter. In the SESAMEEG package, the user can choose whether to use the hyper-prior and basically ignore the problem of setting σ_q, or else to use the value estimated from the lead field and the data, or else to set a value manually.

The standard deviation of the Gaussian likelihood σ_ϵ currently represents the main hyper-parameter of SESAME. Understanding its role is key for an effective use of the algorithm. Roughly speaking, the value σ_ϵ represents a threshold below which the discrepancy between the measured data and the data produced by the solution can be ignored: if this threshold is set low, then the algorithm will do its best to reproduce the data accurately; to this aim, it will likely produce solutions with larger number of dipoles (which also takes a lot of time). If the threshold is set high, then the algorithm will produce simple solutions that fit the data only approximately. As already pointed out in Section 2.1.2, the role of this hyper-parameter in the Bayesian model is to take into account both noise in the data and uncertainties/errors in the forward model. Therefore finding a good value is not always straightforward, and we are working on removing the dependence on this hyper-parameter too (Viani et al., 2023). In the open-source SESAMEEG packages, σ_ϵ is by default estimated as the 20% of the peak of the signal, as a rule-of-thumb assessment of the two contributions of measurement noise and forward modeling error; the experienced user is allowed to change the value of this hyper-parameter to their liking.

2.1.4 The SMC sampler algorithm

At the core of SESAME is a Sequential Monte Carlo sampler that approximates $p(N, R \mid y)$ with a weighted set of candidate solutions, termed *particles*, $\{(N_i, R_i), w_i\}_{i=1,\ldots,I}$, where w_i represents the weight of the i-th candidate solution (N_i, R_i).

In this subsection we provide a very brief summary of the computations behind SESAME: for more details we invite the reader to consult (Sommariva and Sorrentino, 2014; Sorrentino et al., 2014; Viani et al., 2021), where the mathematical model and the algorithm have been thoroughly described.

The recipe is as follows. An initial set of particles is drawn from the prior distribution, then the following steps are repeated until convergence:

1 [MCMC step] each particle is randomly perturbed within a neighborhood; also, dipoles can be added or removed from the particle; the perturbation can be accepted or rejected, based on whether the perturbed version fits the data better than the original one;
2 [Reweighting] particle weights are updated based on an importance sampling rule,
3 [Resampling] the particle set may undergo a *resampling* procedure, i.e.: particles with low weights are discarded and particles with large weights are duplicated.

The final set of particles is then used to produce estimates from the posterior distribution.

2.1.5 SESAME output

Once the posterior has been approximated, SESAME can provide answers to the following questions: how many sources are there? What are most probable source locations? How certain are we about the source locations?

In particular, standard SESAME output encompasses:

- the posterior probability of different number of sources $p(N = i \mid y)$ for $i = 0, 1, \ldots$; this can be visualized e.g. as a pie chart, as is done below;
- the posterior probability of source locations $p(R \mid y)$, typically visualized as a probability map on the brain surface or in the brain volume; here, a highly focused map indicates low uncertainty on the estimated source locations; on the contrary, a widespread map indicates high uncertainty;
- the most probable source locations, identified by first estimating the number of sources as the number $\hat{N}$ by maximizing $P(N \mid y)$, and then identifying $\hat{N}$ peaks in the posterior probability $p(R \mid y, \hat{N})$;
- the source time courses of the most probable sources.

At times, the posterior probability of the number of sources will assign comparable probabilities to distinct models: for example, it can happen that 60% probability is assigned to a one-dipole model and 40% probability is assigned to a two-dipole model. In these cases, SESAME provides both alternative solutions, so that the user can evaluate which one is more likely to be correct, based on additional information they might have.

2.1.6 SESAME computational cost

While the specific implementation, outlined in the next Section, has an impact on the computational cost of the algorithm, few basic facts are common to all implementations:

- the vast majority of the computational cost is due to the Monte Carlo sampling of $p(N, R \mid y)$, while the subsequent calculation of the source time courses according to $p(Q \mid N, R, y)$ has a comparably negligible cost;
- the computational cost of the SMC sampler depends on the complexity of the posterior distribution, and in particular grows non-linearly with the estimated number of sources;
- such computational cost is linear in the number of particles.

2.2 The SESAMEEG packages

The SESAME algorithm has been implemented into two distinct open–source packages, one coded in Python and one coded in MATLAB, under the collective name of SESAMEEG; a commercial version is also available as a part of the BESA Research 7.0+ software. The software is platform independent and has been tested on Windows, macOS and Linux. Apart from being able to be used as a standalone software, SESAMEEG is well integrated within the most popular open–source packages for analyzing human neurophysiological data: Brainstorm (Tadel et al., 2011), MNE–Python (Gramfort et al., 2013a), FieldTrip (Oostenveld et al., 2011) and Zeffiro Interface (He et al., 2020). Such integration has the virtue of letting the user perform all the analysis pipeline steps—such as data pre-processing and visualization—within the same toolbox.

Figure 1 summarizes the main inputs of the algorithm; for more advanced settings the reader is referred to the API documentation, as detailed below.

The mandatory inputs are the forward solution (namely the source space and the lead field matrix) and the M/EEG data. SESAMEEG can run in different analysis scenarios: the source space can be both cortically constrained and volumetric, and the

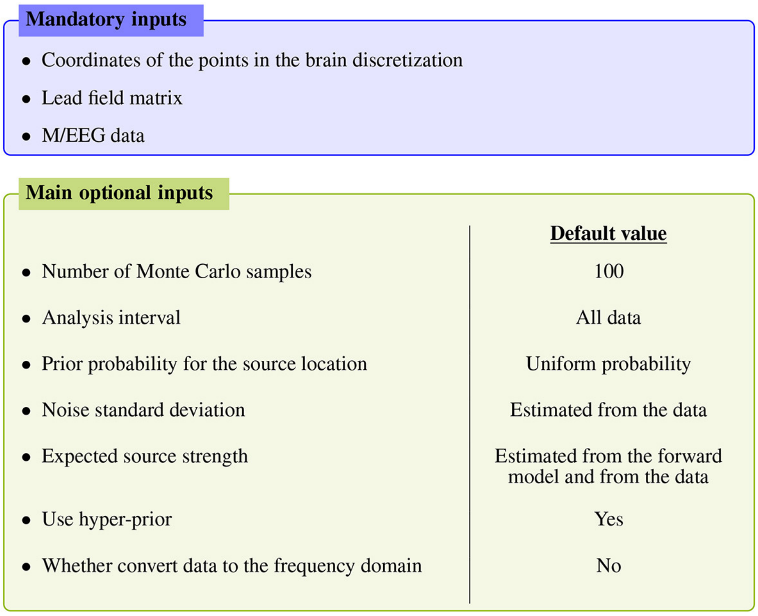

Mandatory inputs

- Coordinates of the points in the brain discretization
- Lead field matrix
- M/EEG data

Main optional inputs

	Default value
Number of Monte Carlo samples	100
Analysis interval	All data
Prior probability for the source location	Uniform probability
Noise standard deviation	Estimated from the data
Expected source strength	Estimated from the forward model and from the data
Use hyper-prior	Yes
Whether convert data to the frequency domain	No

FIGURE 1
Main inputs of the SESAME algorithm. Apart from the mandatory inputs listed in the top blue box, all other inputs have an automatically estimated default value.

source orientations in the forward solution can be both free and orthogonal to the surface of the cortex.

Each of the remaining inputs has its own default value, which has been engineered to let SESAMEEG perform well out–of–the–box in most common scenarios. However, a high degree of customization is available to experienced users.

As described in Section 2.1.5, the output of SESAME is an empirical posterior distribution for a variable number of sources and for their parameters.

From this distribution, maximum a posteriori estimates are computed and—conditioned on the estimated number of sources—a cortical probability map is worked out, which quantifies for each voxel the posterior probability of containing a dipolar source.

SESAMEEG can visualize SESAME outputs in several different ways, which vary according to the software environment and which may also depend on the inputs: as an example, whenever a volumetric source space is used and a MRI image such as T1 is available, it becomes feasible to visualize source estimates overlaid on MRI and to morph estimates to a template brain for group analysis.

2.2.1 SESAMEEG Python

The Python package SESAMEEG is available at the Python Package Index (PyPI) repository (https://pypi.org/project/sesameeg/) and distributed under a Berkeley Software Distribution (BSD) 3-Clause "New" or "Revised" License. The source code is available at the GitHub repository (https://github.com/pybees/sesameeg) while the documentation can be found at https://pybees.github.io/sesameeg/ and comes with an example gallery in which all most common use cases are illustrated.

The code is object oriented and its core functionalities are implemented in the class `Sesame`. When working in the MNE–Python framework the latter class has to be instantiated by means of the function `mne.prepare_sesame`; otherwise, if SESAMEEG is used as a standalone software, it has to be instantiated directly.

Calling the method `apply_sesame` on the `Sesame` instance then applies SESAME on the given M/EEG data and computes point estimates from the posterior distribution.

SESAME output can be visualized in multiple ways by means of the following built-in methods:

- `plot_source_number` plots the posterior probability of the number of sources $p(N = i \mid y)$ as either a pie chart or a bar plot;
- `plot_source_amplitudes` plots the amplitude of the estimated sources as function of time;
- `plot_sources` plots the posterior probability of source locations $p(R \mid y)$ and the estimated sources. By default, these quantities are visualized on the cortical surface or superimposed on the MRI image when working within the MNE–Python framework, and as a PyVista (Sullivan and Kaszynski, 2019) `PolyData` object otherwise.

The entire source model analysis can be saved into and loaded from Hierarchical Data Format (HDF) files by means of the built-in methods `save_h5` and `io.read_h5`.

Regarding the software architecture, SESAMEEG consists of the modules `sesame.py`, `emp_pdf.py`, `particles.py` and `dipoles.py`, and also comprises several subpackages:

- `sesameeg.io` implements functionality to save and load SESAMEEG output;

- `sesameeg.viz` implements several functions to visualize SESAMEEG output;
- `sesameeg.mne` implements functionality to interface with MNE–Python objects;
- `sesameeg.metrics` implements the metrics Goodness of Fit (GOF), Optimal subpattern assignment (OSPA) (Schuhmacher et al., 2008), Map Localization Discrepancy (MLD) and Spatial Dispersion (SD) (Luria et al., 2020). GOF provides information on how well the reconstructed electromagnetic field fits the measured data, while SD quantifies the spatial dispersion of each cortical map and thus the uncertainty of the reconstruction. By default, GOF and SD are evaluated and printed at the end of each run of SESAME. All the four metrics help in quantifying the performance of SESAME whenever the ground truth is known.
- `sesameeg.utils` implements a number of utility functions. These include `estimate_noise_std`, which estimates the standard deviation σ_ϵ as the 20% of the analyzed signal peak and `estimate_dip_mom_std`, which estimates the hyper-parameter σ_q from both the lead field and the data.

2.2.2 SESAMEEG MATLAB

The Matlab version of SESAMEEG is available at https://github.com/pybees/sesameeg_MATLAB. The documentation, which comes with an example script, can be found at https://pybees.github.io/sesameeg_MATLAB/.

The code is function oriented: SESAME is run by calling the `inverse_SESAME` function, taking as input the lead field matrix, the data matrix and the source space matrix as well as a configuration structure containing optional configuration parameters; the output of `inverse_SESAME` is a structure containing analysis parameters and representations of the posterior probability distribution; the essential information can be visualized by the `inverse_SESAME_viewer` function which shows both the posterior probability distribution for the number of sources and the cortical probability map.

A Brainstorm plugin is also available at https://github.com/pybees/sesameeg_MATLAB/tree/main/Brainstorm in the form of the two scripts `process_sesame` and `process_posterior`: the former runs SESAME with the inputs that have been set in the Pipeline editor GUI (Figure 2); the latter takes the posterior distribution (which is the output of `process_sesame`) in input and computes point estimates.

As detailed in the Brainstorm tutorial on creating new processes (https://neuroimage.usc.edu/brainstorm/Tutorials/TutUserProcess), the provided scripts must be copied into the Brainstorm user folder in order to make SESAMEEG available in the pipeline editor menus.

2.2.3 Commercial version: BESA

SESAME is also implemented in the commercial CE-marked software package BESA Research version 7.0 and higher. While not being substantially different from its open-source counterparts, SESAME in BESA has the added value of being part of a complete, user friendly software for EEG and MEG data analysis. The user can analyze any data segment of EEG, MEG, or combined M/EEG data. Unlike in the open-source packages, the baseline interval is used to estimate the noise variance. Like in the open-source packages, parameters for noise and signal estimation, as well as hyper-prior usage can be adjusted by the user; spatially non-uniform priors can be set additionally, e.g., by reading in other modality data like fMRI or by running a different distributed source reconstruction method prior to invoking the SESAME algorithm. The posterior probability map is displayed in a 3D viewer. The user can browse through detected maxima in the map, and seed discrete sources from those, e.g. to determine the precise temporal activation pattern. The computation time depends on the complexity of the probability distribution. Figure 3 shows the application to an averaged EEG segment of inter-ictal epileptic discharges that had several activation foci. For this data set, computation with default parameters (using hyper-priors, perform 50 iterations) took 15 seconds on a Windows laptop with Intel Core i9 processor (2.4 GHz) and 8 cores.

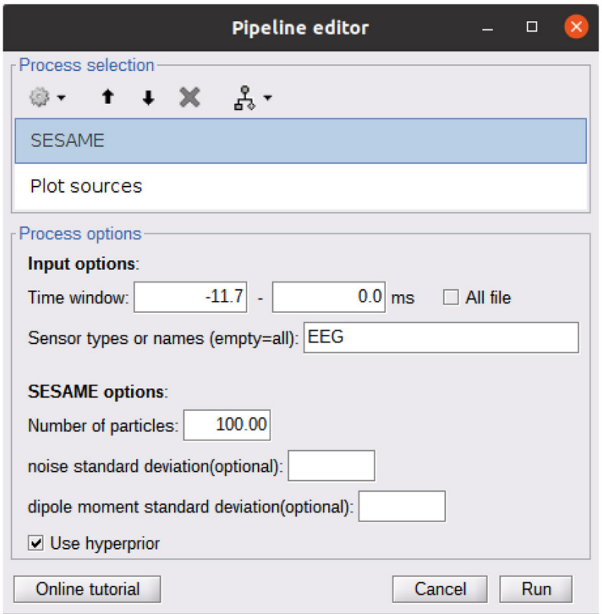

Input options:

Time window: -11.7 - 0.0 ms ☐ All file

Sensor types or names (empty=all): EEG

SESAME options:

Number of particles: 100.00

noise standard deviation(optional):

dipole moment standard deviation(optional):

☑ Use hyperprior

FIGURE 2
Pipeline editor GUI of Brainstorm calling the SESAME algorithm. The first process (SESAME) runs the algorithm in the selected time window, with the optional input parameters. The output of SESAME may be the input of the `Plot Sources` process which computes dipole estimates from the posterior distribution.

3 Results

The present Section showcases the application of SESAMEEG in source modeling analyses from M/EEG experimental datasets. The main focus of this Section is on the presentation and interpretation of SESAME output, particularly how this is affected by the choice of the noise standard deviation parameter. For examples concerning the benefits of using of non-uniform

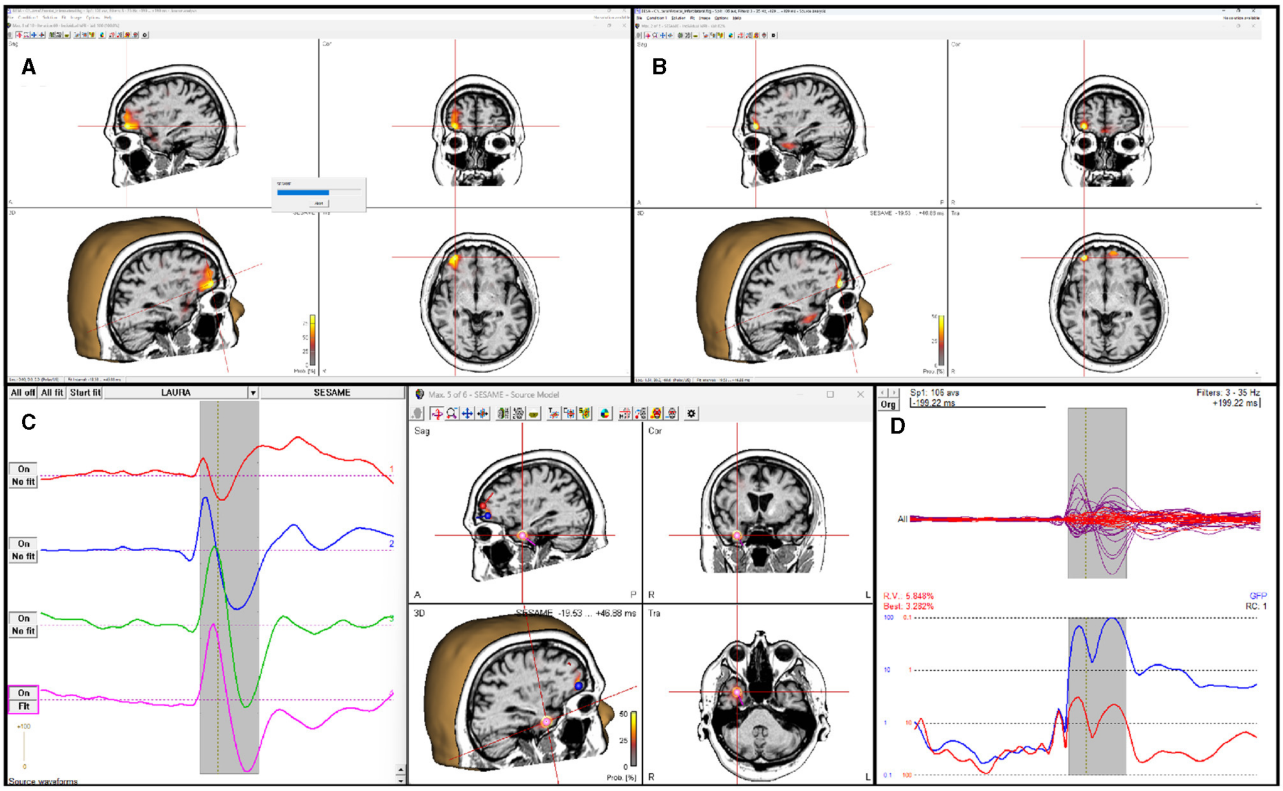

FIGURE 3
SESAME implementation in the BESA software applied to an averaged EEG segment of inter-ictal epileptic discharges. **(A)** SESAME runs through several iterations, converging to the most likely posterior map. **(B)** After completion, the user can browse through the maxima. **(C)** Sources can be seeded from maxima to examine the temporal activation pattern. **(D)** display of model, residual, and global field power after the SESAME-informed dipole solution was created.

spatial priors we refer to Viani et al. (2022), while for an example of application in the frequency domain we refer to Luria et al. (2019).

3.1 MEG experimental data

Figures 4A, B portray experimental MEG data consisting in the average evoked response to auditory stimuli presented to the left ear. The description of the entire experiment can be found in Gramfort et al. (2013a,b) and will not be repeated here. Data and the forward solution are freely available in the `sample` open dataset which comes with the MNE-Python package.

In this Section, we exploit these data to conduct a threefold analysis with SESAMEEG Python: we first show how SESAME reconstructs the brain activity when default values are used as input parameters; then we explore how the choice of the noise standard deviation influences the obtained solution in terms of both the number and the location of the estimated dipoles; finally we present an example in which SESAME finds two alternative scenarios with non-negligible probabilities.

We extract the topographies from 45 ms to 135 ms around the M100 peak and we perform the source localization running SESAMEEG with its default values (see Figure 1).

As shown in Figures 4C, D, SESAME identifies, with full probability, two active dipoles as the generators of the measured field. Figure 4C depicts the cortical probability map on an inflated brain, with colored dots representing the estimated dipole locations, one in the right auditory cortex and the other contralateral very near to the auditory cortex. The posterior distribution looks sharply peaked around the estimated loci, which holds the information of a very small uncertainty in the reconstruction. We stress the fact that this map is distinct from an intensity map, as it is solely associated with the probability of the source locations. Figure 4D shows the estimated source amplitude time courses, with the same color code as in Figure 4C: the source located in the right hemisphere activates before the other, with a peak to peak latency difference between the cortices for the M100 activity that is quantified in 17 ms. The estimated source configuration is therefore fairly in line with the literature (Kaiser et al., 2000; Gramfort et al., 2013b).

The whole script can be found in the documentation example gallery. For this data set, computation with the default parameters took 79 seconds on a Linux laptop with Intel Core i7 processor (3.3 GHz) and 8 cores.

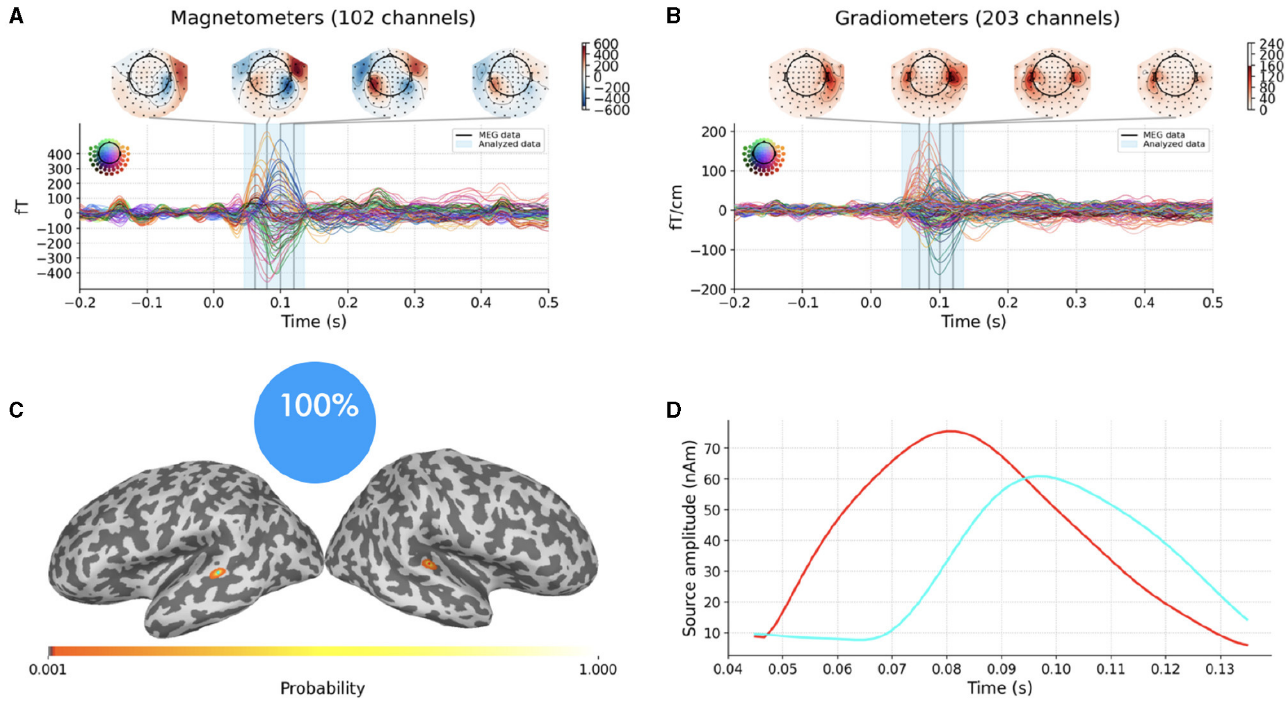

FIGURE 4
Top row: average evoked response to auditory stimuli presented to the left ear as recorded by MEG magnetometers **(A)** and gradiometers **(B)**; the vertical blue translucent rectangle denotes the time window from 45 ms to 135 ms analyzed by SESAME. Bottom row: Reconstructed source configuration. **(C)** shows a pie chart indicating 100% probability of the 2-dipole configuration, and the cortical probability map on an inflated brain, with colored dots representing the estimated dipole locations; preserving the same color code, the estimated source amplitude time courses are plotted in **(D)**.

We now want to show the impact of the noise standard deviation parameter on the solution, as discussed in Section 2.1.3. To do so, we modify the analysis setting by explicitly underestimating and overestimating the parameter value with respect to SESAMEEG's default. We present the results in Figure 5.

In the top row the parameter value has been underestimated as the 6.5% of the maximum measured magnetic field. The estimated number of sources is six, with negligible probability assigned to other configurations. This result is in line with Section 2.1.3: when underestimating the noise standard deviation, SESAME has to introduce additional sources in order to explain finer details of the data. In this case, each of the two sources of Figure 4 is practically split into three components.

In the bottom row the parameter value has been overestimated as the 65% of the data peak. The estimated number of sources is one, again with negligible probability assigned to other configurations. This result is in line with Section 2.1.3 too: as lesser fit is required with the data, the estimated solution is simpler, the location is more uncertain and the estimated source time course weaker. Of the two sources of Figure 4 only the stronger one has survived.

In Figure 6 we finally present a case where SESAME provides two alternative solutions with non-negligible probabilities. This output was obtained by setting the noise standard deviation as the 64% of the data peak, i.e., slightly smaller than the value used in Figures 5C, D. We happen to fall in a borderland in which both the one dipole configuration and the two dipoles configuration can possibly explain the measured field: the most probable solution clearly resembles that of Figure 5; however, with a 20% of probability, SESAME consider an alternative scenario more similar to that of Figure 4, even if the spatial localization is more uncertain in this case.

We stress the fact that being able to automatically provide information about the existence of alternative solutions and characterize their relative probabilities is an asset of SESAME which, to the best of our knowledge, is not provided by other inverse solvers that typically limit their output only to the most probable source configuration.

3.2 EEG experimental data

Figure 7A shows the average of multiple Interictal Epileptiform Discharges (IED) as recorded by a 128 channels EEG and acquired in a patient who suffered from focal epilepsy. Data are part of a Brainstorm tutorial dataset (https://neuroimage.usc.edu/brainstorm/Tutorials/Epilepsy) and we refer the reader therein for a thorough clinical description. For application of SESAME we built a BEM forward model using OpenMEEG (Gramfort et al., 2011) with three compartments and standard conductivities (scalp 1, skull 0.0125, brain 1).

We perform a source modeling analysis by means of the Brainstorm plugin of SESAMEEG. Referring to the Pipeline editor

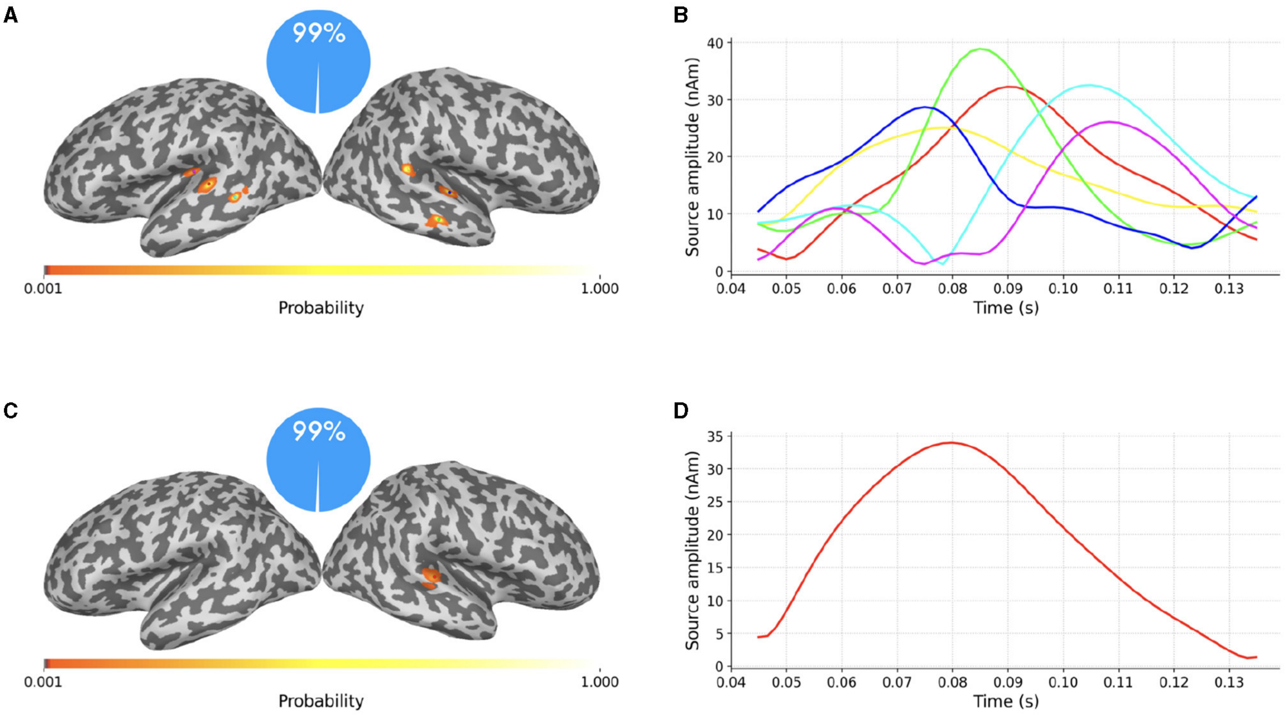

FIGURE 5
(A–D) SESAME source modeling results from the same data portrayed in Figure 4, with different values of σ_ϵ. Top row: Parameter value underestimated as the 6.5% of the maximum measured magnetic field. Bottom row: Parameter value overestimated as the 65% of the data peak. Left column: cortical probability maps, with colored dots representing the estimated dipole locations. Right column: the estimated source amplitudes.

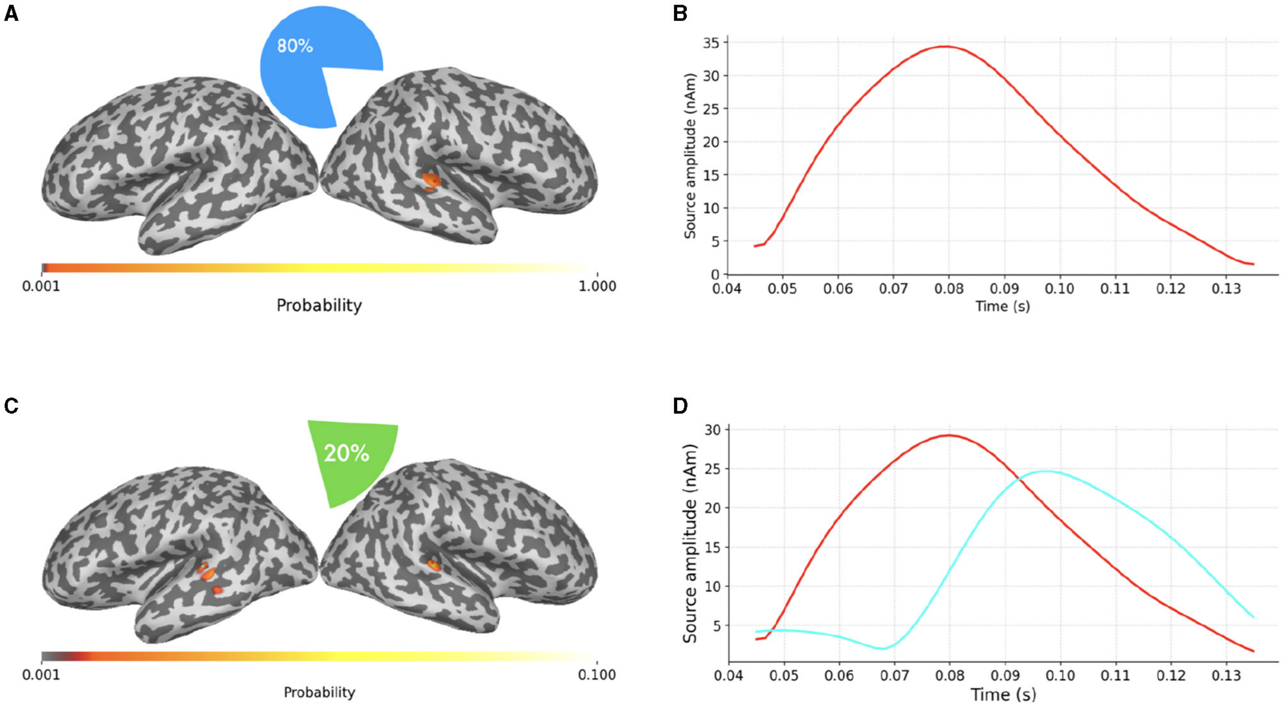

FIGURE 6
(A–D) Alternative SESAME solutions from the same data portrayed in Figure 4, with σ_ϵ set to the 64% of the data peak.

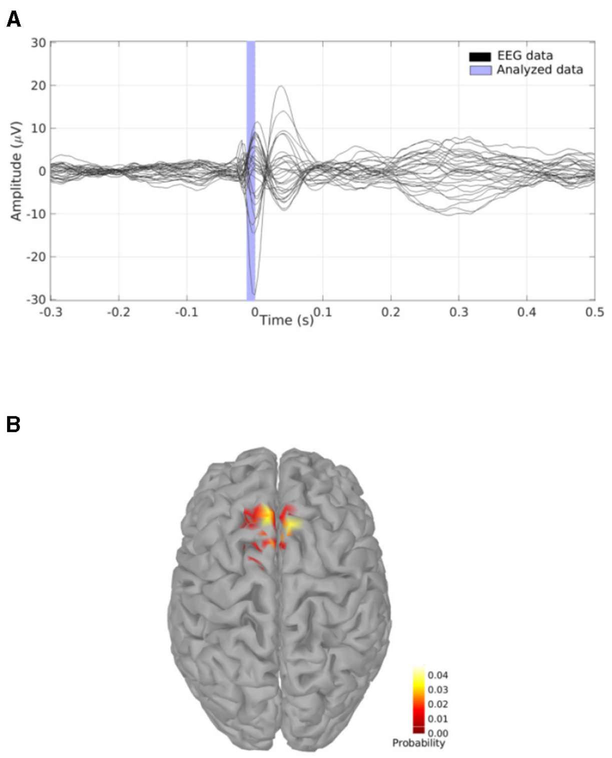

FIGURE 7
(A) EEG experimental data consisting in the average of multiple IEDs acquired in a patient who suffered from focal epilepsy; the vertical blue translucent rectangle denotes the time window from -11 ms to 0 ms analyzed by SESAME. **(B)** Cortical probability map which indicates that the irritative zone is probably contained within the superior frontal gyrus.

GUI depicted in Figure 2, we select the time window from -11 ms to 0 ms, we leave the `noise standard deviation` field empty so that SESAMEEG automatically estimates the parameter value as the 20% of the analyzed signal peak and we run the SESAME process using 100 Monte Carlo samples.

The resulting cortical probability map shown in Figure 7B indicates that SESAME localizes the irritative zone in the superior frontal gyrus with the estimated epileptic focus in the left hemisphere. This agrees with the clinical history of the patient who, after invasive monitoring of the supposed epileptogenic zone (Dümpelmann et al., 2012), underwent a left frontal resection which led to an Engel 1A postsurgical outcome with a follow-up of 5 years.

For this data set, computation with the default parameters took 27 seconds on a Linux laptop with Intel Core i7 processor (3.0 GHz) and 8 cores.

4 Discussion

Amongst available methods for source localization from M/EEG data, SESAME represents an *unicum*: on the one hand, it outperforms the majority of other localization methods in terms of reconstruction accuracy with focal sources, as shown recently (Pascarella et al., 2023); on the other hand, to the best of our knowledge, it features the unique capability of quantifying the degree of confidence of the estimated source configuration, and to provide multiple alternative scenarios whenever the data are ambiguous.

In this paper we presented SESAMEEG, a set of software packages written in different languages and easily integrated in most commonly used software analysis pipelines. In Section 3 we showed that SESAMEEG provides good reconstructions of neural activity from both MEG and EEG data when used with the default parameters. The aim of SESAMEEG is therefore to make the benefits of Bayesian source modeling of M/EEG data available to the largest possible audience.

A long way has been gone but there is still just as much to go.

To begin with, the dipolar model SESAME is based on clearly limits the applicability of the method to experimental conditions in which the involved sources are highly focused. We are currently working at a generalization of the method that encompasses the source extent among the unknown parameters to be estimated. Successful work in this direction would have the additional benefit of enabling a quantification of the extent of the source, with its associated uncertainty.

A second key point in the future development of SESAME concerns a more detailed modeling of the forward model errors. While these are currently accounted for as an zero-mean additive component, more can be done along the lines suggested e.g., in Rimpiläinen et al. (2019). Better modeling of this component would lead to more accurate source reconstruction as well as better uncertainty quantification.

Finally, as the whole Monte Carlo procedure underlying SESAME can be a bit heavy particularly when the number of sources is large, implementation of the code in a parallel environment exploiting GPUs should be pursued.

Data availability statement

Publicly available datasets were analyzed in this study. This data can be found here: https://mne.tools/stable/generated/mne.datasets.sample.data_path.html; https://neuroimage.usc.edu/brainstorm/Tutorials/Epilepsy.

Ethics statement

The studies involving humans were approved by the Corresponding Ethics Committee. The studies were conducted in accordance with the local legislation and institutional requirements. Written informed consent for participation was not required from the participants or the participants' legal guardians/next of kin in accordance with the national legislation and institutional requirements.

Author contributions

GL: Conceptualization, Methodology, Software, Writing – original draft, Data curation, Investigation, Writing – review & editing. AV: Conceptualization, Investigation, Methodology, Software, Writing – original draft, Writing – review & editing. AP: Conceptualization, Investigation, Software, Writing – original draft, Methodology, Writing – review & editing. HB: Software, Writing – review & editing. SS: Software, Writing – review & editing, Conceptualization. AS: Software, Conceptualization, Methodology, Writing – original draft, Writing – review & editing.

Funding

The author(s) declare that financial support was received for the research, authorship, and/or publication of this article. The research by AS, SS, and AV was supported in part by the MIUR Excellence Department Project awarded to Dipartimento di Matematica, Università di Genova, CUP D33C23001110001.

Acknowledgments

AS, AP, and AV kindly acknowledge the Gruppo Nazionale per il Calcolo Scientifico for financial support.

Conflict of interest

GL was employed by Bayesian Estimation for Engineering Solutions srl. HB was employed by BESA GmbH.

The remaining authors declare that the research was conducted in the absence of any commercial or financial relationships that could be construed as a potential conflict of interest.

Publisher's note

References

Bagic, A. I., Knowlton, R. C., Rose, D. F., Ebersole, J. S., and ACMEGS Clinical Practice Guideline (CPG) Committee (2011). American clinical magnetoencephalography society clinical practice guideline 1: recording and analysis of spontaneous cerebral activity. *J. Clini. Neurophysiol.* 28, 348–354. doi: 10.1097/WNP.0b013e3182272fed

Baillet, S., Mosher, J. C., and Leahy, R. M. (2001). Electromagnetic brain mapping. *Signal Proc. Magaz. IEEE* 18, 14–30. doi: 10.1109/79.962275

Brookes, M., Woolrich, M., Luckhoo, H., Price, D., Hale, J., Stephenson, M., et al. (2011). Investigating the electrophysiological basis of resting state networks using magnetoencephalography. *PNAS* 108, 16783–16788. doi: 10.1073/pnas.1112685108

Carrette, E., and Stefan, H. (2019). Evidence for the role of magnetic source imaging in the presurgical evaluation of refractory epilepsy patients. *Front. Neurol.* 10, 933. doi: 10.3389/fneur.2019.00933

Del Moral, P., Doucet, A., and Jasra, A. (2006). Sequential Monte Carlo samplers. *J. Royal Statist. Soc. B* 68, 411–436. doi: 10.1111/j.1467-9868.2006.00553.x

Dümpelmann, M., Ball, T., and Schulze-Bonhage, A. (2012). sloreta allows reliable distributed source reconstruction based on subdural strip and grid recordings. *Hum. Brain Mapp.* 33, 1172–1188. doi: 10.1002/hbm.21276

Gramfort, A., Luessi, M., Larson, E., Engemann, D. A., Strohmeier, D., Brodbeck, C., et al. (2013a). MEG and EEG data analysis with MNE-Python. *Front. Neurosci.* 26, 267. doi: 10.3389/fnins.2013.00267

Gramfort, A., Papadopoulo, T., Olivi, E., and Clerc, M. (2011). Forward field computation with openmeeg. *Comput. Intell. Neurosci.* 2011, 923703. doi: 10.1155/2011/923703

Gramfort, A., Strohmeier, D., Haueisen, J., Hämäläinen, M. S., and Kowalski, M. (2013b). Time-frequency mixed-norm estimates: Sparse M/EEG imaging with non-stationary source activations. *Neuroimage* 70, 410–422. doi: 10.1016/j.neuroimage.2012.12.051

Gratta, C. D., Pizzella, V., Tecchio, F., and Romani, G. (2001). Magnetoencephalography - a noninvasive brain imaging method with 1 ms time resolution. *Rep. Prog. Phys.* 64, 1759–1814. doi: 10.1088/0034-4885/64/12/204

Hämäläinen, M., Hari, R., Knuutila, J., and Lounasmaa, O. (1993). Magnetoencephalography: theory, instrumentation and applications to non-invasive studies of the working human brain. *Rev. Mod. Phys.* 65, 413–498. doi: 10.1103/RevModPhys.65.413

He, Q., Rezaei, A., and Pursiainen, S. (2020). Zeffiro user interface for electromagnetic brain imaging: a GPU accelerated FEM tool for forward and inverse computations in Matlab. *Neuroinformatics* 18, 237–250. doi: 10.1007/s12021-019-09436-9

Kaipio, J., and Somersalo, E. (2007). Statistical inverse problems: discretization, model reduction and inverse crimes. *J. Comput. Appl. Math.* 198, 493–504. doi: 10.1016/j.cam.2005.09.027

Kaiser, J., Lutzenberger, W., Preissl, H., Ackermann, H., and Birbaumer, N. (2000). Right-hemisphere dominance for the processing of sound-source lateralization. *J. Neurosci.* 20, 6631. doi: 10.1523/JNEUROSCI.20-17-06631.2000

Luria, G., Duran, D., Visani, E., Rossi Sebastiano, D., Sorrentino, A., Tassi, L., et al. (2020). Towards the automatic localization of the irritative zone through magnetic source imaging. *Brain Topogr.* 33, 651–663. doi: 10.1007/s10548-020-00789-y

Luria, G., Duran, D., Visani, E., Sommariva, S., Rotondi, F., Sebastiano, D. R., et al. (2019). Bayesian multi-dipole modelling in the frequency domain. *J. Neurosci. Methods* 312, 27–36. doi: 10.1016/j.jneumeth.2018.11.007

Oostenveld, R., Fries, P., Maris, E., and Schoffelen, J.-M. (2011). Fieldtrip: open source software for advanced analysis of MEG, EEG, and invasive electrophysiological data. *Comput. Intell. Neurosci.* 2011, 1–9. doi: 10.1155/2011/156869

Pascarella, A., Mikulan, E., Sciacchitano, F., Sarasso, S., Rubino, A., Sartori, I., et al. (2023). An in-vivo validation of esi methods with focal sources. *NeuroImage* 277, 120219. doi: 10.1016/j.neuroimage.2023.120219

Pascarella, A., and Sorrentino, A. (2011). "Statistical approaches to the inverse problem," in *Magnetoencephalography*. Atyrau: InTech.

Pursiainen, S., Sorrentino, A., Campi, C., and Piana, M. (2011). Forward simulation and inverse dipole localization with the lowest order Raviart - Thomas elements for electroencephalography. *Inverse Probl.* 27, 045003. doi: 10.1088/0266-5611/27/4/045003

Rimpiläinen, V., Koulouri, A., Lucka, F., Kaipio, J. P., and Wolters, C. H. (2019). Improved eeg source localization with bayesian uncertainty modelling of unknown skull conductivity. *Neuroimage* 188, 252–260. doi: 10.1016/j.neuroimage.2018.11.058

Schuhmacher, D., Vo, B.-T., and Vo, B.-N. (2008). A consistent metric for performance evaluation of multi-object filters. *IEEE Trans. Signal Proc.* 56, 3447–3457. doi: 10.1109/TSP.2008.920469

Sommariva, S., and Sorrentino, A. (2014). Sequential Monte Carlo samplers for semi-linear inverse problems and application to magnetoencephalography. *Inverse Probl.* 30, 114020. doi: 10.1088/0266-5611/30/11/114020

Sorrentino, A., Johansen, A., Aston, J., Nichols, T., and Kendall, W. (2013). Dynamic filtering of static dipoles in Magnetoencephalography. *Ann. Appl. Stat.* 7, 955–988. doi: 10.1214/12-AOAS611

Sorrentino, A., Luria, G., and Aramini, R. (2014). Bayesian multi-dipole modeling of a single topography in MEG by Adaptive Sequential Monte-Carlo Samplers. *Inverse Probl.* 30, 045010. doi: 10.1088/0266-5611/30/4/045010

Sorrentino, A., Parkkonen, L., Piana, M., Massone, A. M., Narici, L., Carozzo, S., et al. (2006). Modulation of brain and behavioural responses to cognitive visual stimuli with varying signal-to-noise ratios. *Clini. Neurophysiol.* 117, 1098–1105. doi: 10.1016/j.clinph.2006.01.011

Stam, C. J., de Haan, W., Daffertshofer, A., Jones, B. F., Manshanden, I., van Cappellen van Walsum, A. M., et al. (2009). Graph theoretical analysis of magnetoencephalographic functional connectivity in Alzheimer's disease. *Brain* 132, 213–224. doi: 10.1093/brain/awn262

Stoffers, D., Bosboom, J., Deijen, J., C., Wolters, E., Berendse,1, H., et al. (2007). Slowing of oscillatory brain activity is a stable characteristic of Parkinson's disease without dementia. *Brain* 130, 1847–1860. doi: 10.1093/brain/awm034

Sullivan, B., and Kaszynski, A. (2019). PyVista: 3D plotting and mesh analysis through a streamlined interface for the Visualization Toolkit (VTK). *J. Open Source Softw*. 4, 1450. doi: 10.21105/joss.01450

Tadel, F., Baillet, S., Mosher, J. C., Pantazis, D., and Leahy, R. M. (2011). Brainstorm: a user-friendly application for MEG/EEG analysis. *Comput. Intell. Neurosci.* 2011, 1–13. doi: 10.1155/2011/879716

Uda, T., Tsuyuguchi, N., Okumura, E., Sakamoto, S., Morino, M., Nagata, T., et al. (2012). sLORETA-qm for interictal MEG epileptic spike analysis: comparison of location and quantity with equivalent dipole estimation. *Clini. Neurphysiol*. 123, 1496–1501. doi: 10.1016/j.clinph.2011.12.008

Viani, A., Johansen, A. M., and Sorrentino, A. (2023). Cost free hyper-parameter selection/averaging for Bayesian inverse problems with vanilla and Rao-Blackwellized SMC samplers. *Stat. Comput*. 33, 126. doi: 10.1007/s11222-023-10294-4

Viani, A., Luria, G., and Sorrentino, A. (2022). "Non-uniform spatial priors for multi-dipole localization from MEG/EEG data," in *2022 IEEE International Conference on E-health Networking, Application & Services (HealthCom)* (Genoa: IEEE), 149–154.

Viani, A., Luria, G., Sorrentino, A., and Bornfleth, H. (2021). Where Bayes tweaks Gauss: conditionally Gaussian priors for stable multi-dipole estimation. *Inverse Prob. Imag*. 15, 1099–1119. doi: 10.3934/ipi.2021030

Vorwerk, J., Engwer, C., Pursiainen, S., and Wolters, C. H. (2016). A mixed finite element method to solve the EEG forward problem. *IEEE Trans. Med. Imaging* 36, 930–941. doi: 10.1109/TMI.2016.2624634

Frontiers in Human Neuroscience

TYPE Original Research
PUBLISHED 07 April 2025
DOI 10.3389/fnhum.2025.1386275

EDITED BY
Takfarinas Medani,
University of Southern California,
United States

REVIEWED BY
Johannes Vorwerk,
UMIT TIROL - Private University for Health Sciences and Health Technology, Austria
Deirel Paz-Linares,
Precision Medicine & Clinical Research Solutions, Mexico

*CORRESPONDENCE
Chang Cai
✉ cchangenergy@gmail.com
Srikantan S. Nagarajan
✉ sri@ucsf.edu

RECEIVED 14 February 2024
ACCEPTED 11 March 2025
PUBLISHED 07 April 2025

CITATION
Ghosh S, Cai C, Hashemi A, Gao Y, Haufe S, Sekihara K, Raj A and Nagarajan SS (2025) Structured noise champagne: an empirical Bayesian algorithm for electromagnetic brain imaging with structured noise. *Front. Hum. Neurosci.* 19:1386275.
doi: 10.3389/fnhum.2025.1386275

Structured noise champagne: an empirical Bayesian algorithm for electromagnetic brain imaging with structured noise

Sanjay Ghosh[1,2], Chang Cai[3]*, Ali Hashemi[4], Yijing Gao[1], Stefan Haufe[4], Kensuke Sekihara[5], Ashish Raj[1] and Srikantan S. Nagarajan[1]*

[1]Biomagetic Imaging Laboratory, University of California San Francisco, Department of Radiology and Biomedical Imaging, San Francisco, CA, United States, [2]Department of Electrical Engineering, Indian Institute of Technology Kharagpur, Kharagpur, India, [3]National Engineering Research Center for E-Learning, Central China Normal University, Wuhan, China, [4]Technical University Berlin, Berlin, Germany, [5]Signal Analysis Inc., Tokyo, Japan

Introduction: Electromagnetic brain imaging is the reconstruction of brain activity from non-invasive recordings of electroencephalography (EEG), magnetoencephalography (MEG), and also from invasive ones such as the intracranial recording of electrocorticography (ECoG), intracranial electroencephalography (iEEG), and stereo electroencephalography EEG (sEEG). These modalities are widely used techniques to study the function of the human brain. Efficient reconstruction of electrophysiological activity of neurons in the brain from EEG/MEG measurements is important for neuroscience research and clinical applications. An enduring challenge in this field is the accurate inference of brain signals of interest while accounting for all sources of noise that contribute to the sensor measurements. The statistical characteristic of the noise plays a crucial role in the success of the brain source recovery process, which can be formulated as a sparse regression problem.

Method: In this study, we assume that the dominant environment and biological sources of noise that have high spatial correlations in the sensors can be expressed as a structured noise model based on the variational Bayesian factor analysis. To the best of our knowledge, no existing algorithm has addressed the brain source estimation problem with such structured noise. We propose to apply a robust empirical Bayesian framework for iteratively estimating the brain source activity and the statistics of the structured noise. In particular, we perform inference of the variational Bayesian factor analysis (VBFA) noise model iteratively in conjunction with source reconstruction.

Results: To demonstrate the effectiveness of the proposed algorithm, we perform experiments on both simulated and real datasets. Our algorithm achieves superior performance as compared to several existing benchmark algorithms.

Discussion: A key aspect of our algorithm is that we do not require any additional baseline measurements to estimate the noise covariance from the sensor data under scenarios such as resting state analysis, and other use cases wherein a noise or artifactual source occurs only in the active period but not in the baseline period (e.g., neuro-modulatory stimulation artifacts and speech movements).

KEYWORDS

electromagnetic brain imaging, magnetoencephalography (MEG), brain source reconstruction, Bayesian inference, structured noise learning, factor analysis

1 Introduction

Electromagnetic brain imaging is an effective technique being used intensively to understand the neural mechanisms of the complex human brain and behavior important for both neuroscience research and clinical applications (Phillips et al., 1997; He et al., 2018). In particular, electroencephalography (EEG) and magnetoencephalography (MEG) are two widely used techniques that provide non-invasive recordings of the electrical activity of the brain by sensing its remote magnetic and electric fields, respectively (Baillet et al., 2001). Electromagnetic brain imaging requires solving an ill-posed inverse problem for reconstruction of brain activity (at cortical brain sources) from non-invasive EEG/MEG recordings. In particular, it is crucial to determine both the spatial location and the temporal dynamics of neurophysiological activity. In tomographic EEG/MEG source localization pipelines, current dipole sources are considered to be located on each voxel inside the brain. As a result, the number of locations of potential brain sources (thousands of voxels) is typically much larger than the number of sensors (just a few hundred). In addition, several types of noise (such as environmental interference and sensor noise) inevitably affect EEG/MEG signals (Michel and He, 2019; Edelman et al., 2015). Therefore, reconstructing brain source activities accurately from scalp EEG/MEG measurements becomes a challenging task. It opens up the possibility of using sophisticated mathematical or neurophysiological priors of both brain signals and noise statistics to achieve improved recovery of brain activities.

Integral to inverse modeling algorithm in electromagnetic brain imaging (Riaz et al., 2023) are forward models. The primary current density is mathematically defined as a *vector field* in a continuum (volume space or surface space, depending on the assumptions for the source space). Then an electric scalar field or magnetic vector field that is produced by the primary current density is described by quasi-static equations of electromagnetism. A discretization of the space of the brain and surrounding tissues is employed to provide these equations with a numerical solution. Note that the forward problem aims to achieve a solution for the electric or magnetic fields given the location and timing of brain source activity. The recovery of the primary current source location and timing is basically the Cauchy inverse problem of electromagnetism (Riaz et al., 2023).

Several methods have been introduced over the past decades to solve the inverse problem of brain source imaging. Common inverse solvers for EEG/MEG source imaging can be broadly classified into three categories—model-based dipole fitting, dipole scanning methods, and distributed whole brain source imaging methods (Baillet et al., 2001; Cai et al., 2018; Hosseini et al., 2018; Cai et al., 2023). The working principle of dipole fitting methods is to approximate brain activity with a small number of equivalent current dipoles (Scherg, 1990). These classical methods achieve good solutions when the source activity is relatively simple consisting only one to two dipoles (Delorme et al., 2012; Matsuura and Okabe, 1995). However, the quality of their solutions degrades for even slightly more complicated source configurations (Mosher et al., 1992). In addition, it is practically challenging for dipole fitting-based methods to determine the true number of current dipoles to be estimated. Dipole scanning methods are also referred to as methods of spatial filtering or beamforming which estimate the time course at every candidate location while suppressing the interference from activity at the other candidate source locations (Van Veen et al., 1997; Zumer et al., 2006; Cai et al., 2023). Examples of scanning techniques are minimum-variance adaptive beamforming (Robinson and Rose, 1992; Sekihara and Scholz, 1996) as well as several variants of adaptive beamformers (Sekihara and Nagarajan, 2008). The fidelity of such brain signal estimates is affected by many factors such as signal-to-noise ratio (SNR), source correlations, and the number of time samples. However, the reconstruction performance of beamforming methods can be significantly compromised if the brain sources are highly correlated, although recent Bayesian extensions overcome this limitation (Cai et al., 2023).

Distributed whole-brain source imaging methods do not require prior knowledge of the number of sources (Wipf and Nagarajan, 2009). These methods approximate the primary electrical current density by discretizing the whole brain volume, assuming a dipolar current source at each voxel. The task is then to estimate the amplitudes (and orientations) of the sources by minimizing a cost function (He et al., 2011). Some form of prior constraints or regularizers are used to obtain a unique and neurophysiological meaningful solution (Ioannides et al., 1990). The minimum-norm estimation algorithm (MNE) (Hämäläinen and Ilmoniemi, 1994) minimizes the L_2 norm of the solution favoring smaller overall power of the brain activity. Other variants of MNE include the weighted MNE (wMNE) (Dale and Sereno, 1993), low-resolution brain electromagnetic tomography (LORETA) (Pascual-Marqui et al., 1994), and standardized LORETA (sLORETA) (Pascual-Marqui et al., 2002). However, L_2 norm minimization methods produce diffuse estimates that lack sufficient resolution to localize and distinguish multiple sources. To overcome this limitation, algorithms based on L_1 norm minimization (Ding and He, 2008; Liu et al., 2022) and sparsity-inducing norms induced by empirical Bayesian inference (referred to as sparse Bayesian learning, SBL) (Wipf et al., 2010) are developed. Friston et al. (2008) introduced a sparse solution for distributed sources, of the sort enforced by equivalent current dipole (ECD) models. These sparsity-based source reconstruction algorithms can be derived within a Bayesian framework (Wipf et al., 2010; Liu et al., 2019; Oikonomou and Kompatsiaris, 2020; Liu et al., 2020; Cai et al., 2021; Hashemi et al., 2021b, 2022; Ghosh et al., 2023; Cai et al., 2023). We argue that these Bayesian techniques are found to be most efficient in estimating the model hyper-parameters directly from the data using hierarchical algorithms. Importantly, the Champagne algorithm (Wipf et al., 2010) is derived in an empirical Bayesian fashion, incorporating deep theoretical ideas about sparse-source recovery from noisy constrained measurements. Inspired by its promising performance, attempts have further been made by several researchers to improve upon Champagne algorithm (Wipf et al., 2010). One potential direction of improvement is to accurately model noise that exhibits structured precision parameter (Liu et al., 2020).

Accurate inference of brain signals of interest while accounting for all sources of noise that contribute to sensor measurements is the key challenge in electromagnetic brain imaging. Noise statistics in the model play a crucial role in the success of sparse source recovery. In particular, the statistical characteristics of the noise in sensor data plays an important role in the working of Bayesian algorithms for electromagnetic brain imaging. Existing studies have considered noise covariance matrices with either diagonal (Wipf et al., 2010; Cai et al., 2019) or full structure (Hashemi et al., 2022). In this study, we consider another type of realistic noise whose covariance can be characterized by a structured matrix. This type of noise is present when there are just a few active sources of environmental noise, each of which may be picked up by multiple MEG/EEG sensors with high spatial correlations. A key aspect of our noise estimation algorithm is that we do not require any additional baseline measurements to estimate the noise covariance from the sensor data under scenarios such as resting-state analysis, and other use cases wherein a noise or artifactual source occurs only in the active period but not in the baseline period (e.g., neuromodulatory stimulation artifacts and speech movements). To the best of our knowledge, no existing algorithm has addressed the brain source estimation problem with a structure-noise covariance.

The main contributions of this paper are as follows:

1. We introduce a novel robust empirical Bayesian framework for electromagnetic brain imaging under the structured noise covariance assumption. In particular, we perform inference of the variational Bayesian factor analysis (VBFA) noise model iteratively in conjunction with source reconstruction. It provides us a tractable algorithm for iteratively estimating the noise covariance and the brain source activity. The proposed algorithm is found to be quite robust to initialization and computationally efficient.
2. The proposed algorithm does not require any additional baseline measurements to estimate noise covariance from sensor data. We note that this is not the case for many of the existing algorithms for electromagnetic brain imaging.
3. We perform exhaustive experiments to demonstrate the effectiveness of the proposed electromagnetic brain imaging algorithm on both simulated and real datasets. In particular, we quantify the correctness of the localization of the sources and the estimation of source time courses for simulated brain noise with structured covariance matrix. We show that the new algorithm achieves competitive performance with respect to benchmark methods on both synthetic and real MEG data and is able to resolve distinct and functionally relevant brain areas.

This paper is summarized as follows. In Section 2.1, we introduce generative model of the inverse problem. Table 1 list a summary of the variables and definitions used in Section 2. The proposed Bayesian formulation along with a brief account of existing Bayesian frameworks are presented in Section 2.2 and Section 2.3. Then, we present experiments applying our approach on synthetic (Section 3) and real MEG data (Section 4), where we also compare the proposed algorithm with baseline and state-of-the-art methods for electromagnetic brain imaging. Finally, we discuss implications and future directions in Section 5.

2 Method

2.1 Generative model

In the typical electromagnetic brain imaging problem setup, brain activity is modeled by a number of electric current dipoles, where the location, orientation, and magnitude of each dipole collectively determine the signal observed at the EEG/MEG electrodes. The position of the dipoles within the brain contains valuable information on brain function, which is used in clinical applications and cognitive neuroscience studies (Leahy et al., 1998; Gross, 2019). The inverse problem of estimating the locations and the moments of the current dipoles from the recorded EEG signal is ill-posed in nature.

The forward model, describing the EEG/MEG measurements as a function of the brain sources, is given by

$$\boldsymbol{y}_k = \boldsymbol{L}\boldsymbol{x}_k + \boldsymbol{z_k}, \tag{1}$$

where $\boldsymbol{y}_k = [y_k(1), \cdots, y_k(m)]^\top, \boldsymbol{y}_k \in \mathbb{R}^{m\times 1}$ is the sensor measurements at time point k, m is the number of sensor measurements. Moreover, $\boldsymbol{x}_k = [x_k(1), \cdots, x_k(n)]^\top$, $\boldsymbol{x}_k \in \mathbb{R}^{n\times 1}$ is the activity of the brain sources at time point k, n is the number of voxels. In addition, the whole time series data $\{\boldsymbol{y}_1, \boldsymbol{y}_2, \ldots, \boldsymbol{y}_K\}$ are collectively denoted $\boldsymbol{y}$, and the whole time series data $\{\boldsymbol{x}_1, \boldsymbol{x}_2, \ldots, \boldsymbol{x}_K\}$ are collectively denoted $\boldsymbol{x}$. The lead-field matrix is given by $\boldsymbol{L} = [\boldsymbol{l}_1, \boldsymbol{l}_2, \cdots, \boldsymbol{l}_n] \in \mathbb{R}^{m\times n}$ whose columns reflect the sensors response induced by the unit current sources. Note that, in simulations here, we assume a pre-defined orientation (e.g., normal constraint) for the local lead-field at each voxel. Therefore, it can be reduced to a $m \times 1$ vector (Sekihara and Nagarajan, 2015). However for real data, we use a three-column lead-field for each voxel and estimate the source time-series at the orientation corresponding to maximum power at each vowel. Furthermore, $\boldsymbol{z}_k \in \mathbb{R}^{m\times 1}$ refers to additive noise in the measurements not arising from brain sources. We consider that $\boldsymbol{z}_k$ is drawn from a multivariate Gaussian probability distribution parameterized by the precision matrix $\boldsymbol{\Lambda}^{-1}$. In particular, we assume that noise refers to any background interference including biological and environmental sources outside the span of the lead-field as well as sensor noise. It is assumed that EEG/MEG measurements are collected for spontaneous brain activity (i.e., resting-state), such that separate recording time-windows capturing noise only activity might not be available. Another scenario where noise-only recordings may not be available are task-induced contrastive experimental designs where noise or artifact signals are only present in the active condition but not in the baseline. One such example is active post-movement related paradigms such as speaking or other movement tasks wherein any artifacts observed in the sensors due to the movement will be present in the post-movement period; that is, the baseline pre-movement periods cannot be used to estimate the noise statistics. Therefore, here, we jointly infer both source estimate and noise statistics from the same data segment as described below.

TABLE 1 Summary of the variables and definitions used in Section 2 Method.

Symbol	Description
n	Number of voxels in the brain.
m	Number of MEG/EEG sensors.
K	Number of time-points in the MEG/EEG signal.
$\boldsymbol{x}$	Brain source signal. (size $n \times K$)
$\boldsymbol{y}$	Observed MEG/EEG sensor data. (size $m \times K$)
$\boldsymbol{L}$	Lead-field matrix of size $m \times n$.
$\boldsymbol{\Lambda}$	Precision of normal distribution of noise. (size $m \times m$)
$\boldsymbol{\Phi}$	Precision of normal distribution of source signal. (size $n \times n$)
$\boldsymbol{\Gamma}$	Precision of normal posterior distribution of source signal x given observed data y. (size $n \times n$)
$p(\boldsymbol{x}_k)$	Prior distribution of $\boldsymbol{x}_k$.
$p(\boldsymbol{y}_k \vert \boldsymbol{x}_k)$	Conditional probability density of $\boldsymbol{y}_k$ given $\boldsymbol{x}_k$.
$p(\boldsymbol{x}_k \vert \boldsymbol{y}_k)$	Posterior probability density of $\boldsymbol{x}_k$ observed $\boldsymbol{y}_k$.
$\bar{\boldsymbol{x}}_k$	Posterior mean of $p(\boldsymbol{x}_k \vert \boldsymbol{y}_k)$.
$p(\boldsymbol{y} \vert \boldsymbol{\Phi})$	Marginal likelihood.
$\mathcal{F}(\boldsymbol{\Phi})$	Logarithm of marginal likelihood $\log p(\boldsymbol{y} \vert \boldsymbol{\Phi})$.
$\tilde{\mathcal{F}}(\boldsymbol{\Phi})$	Cost function with the convex bounding.
$\boldsymbol{z}_k^{(l)}$	Residual noise at k-th time-point during l-th iteration. (size $m \times 1$)
$\boldsymbol{A}$	Mixing matrix for the factor analysis. (size $m \times q$)
$\boldsymbol{u}_k$	k-th component of factor analysis. (size $q \times 1$)
ε	Modeling noise of factor analysis. (size $m \times 1$)
$\boldsymbol{\Omega}$	Diagonal precision matrix of the modeling noise at factor analysis step.
$\boldsymbol{\Psi}$	Precision matrix of the posterior distribution of column of mixing matrix $\boldsymbol{A}$.
$\boldsymbol{R}_{zz}$	Covariance of residual noise $\boldsymbol{z}$.
$\boldsymbol{R}_{uu}$	Covariance of factor analysis coefficient vector $\boldsymbol{u}$.

2.2 Source estimation

Given prior distributions of sources and noise, the generative model in Equation 1 becomes a probabilistic model. We assume a zero-mean Gaussian prior with diagonal covariance $\boldsymbol{\Phi} = \text{diag}(\boldsymbol{\phi})$ for the underlying source distribution. In other words, $\boldsymbol{x}_k \sim \mathcal{N}(\boldsymbol{0}, \boldsymbol{\Phi}^{-1})$, $k = 1, \ldots, K$, where the diagonal $\boldsymbol{\phi} = [\phi_1, \ldots, \phi_n]^\top$ contains n distinct unknown variances associated with n brain sources.

We propose to solve the inverse problem within the Bayesian learning framework. Modeling independent sources through a Gaussian zero-mean prior with diagonal covariance matrix leads to sparsity of the resulting source distributions, that is, at the optimum many of the estimated source variances are zero. The goal is to find the maximum a posteriori probability (MAP) solution for x_k. The posterior probability $p(\boldsymbol{x}_k|\boldsymbol{y}_k)$ can be derived by using Bayes' theorem (Sekihara and Nagarajan, 2015):

$$p(\boldsymbol{x}_k|\boldsymbol{y}_k) \propto p(\boldsymbol{y}_k|\boldsymbol{x}_k)p(\boldsymbol{x}_k), \tag{2}$$

where $p(\boldsymbol{y}_k|\boldsymbol{x}_k) = \mathcal{N}(\boldsymbol{L}\boldsymbol{x}_k, \boldsymbol{\Lambda}^{-1})$ and $p(\boldsymbol{x}_k) = \mathcal{N}(\boldsymbol{0}, \boldsymbol{\Phi}^{-1})$. In this case, it is straightforward to show that the posterior probability density $p(\boldsymbol{x}_k|\boldsymbol{y}_k)$ is also Gaussian. Suppose, the posterior probability takes the following form:

$$p(\boldsymbol{x}_k|\boldsymbol{y}_k) = \mathcal{N}(\bar{\boldsymbol{x}}_k, \boldsymbol{\Gamma}^{-1}),$$

where $\bar{\boldsymbol{x}}_k$ is the posterior mean, and $\boldsymbol{\Gamma}$ is the posterior precision matrix. Furthermore, we adapt the derivation in Sekihara and Nagarajan (2015)[See pages 233–235 in Section B.3] to obtain:

$$\begin{aligned} \boldsymbol{\Gamma} &= \boldsymbol{\Phi} + \boldsymbol{L}^T\boldsymbol{\Lambda}\boldsymbol{L}, \\ \bar{\boldsymbol{x}}_k &= \boldsymbol{\Phi}^{-1}\boldsymbol{L}^\top(\boldsymbol{\Lambda}^{-1} + \boldsymbol{L}\boldsymbol{\Phi}^{-1}\boldsymbol{L}^\top)^{-1}\boldsymbol{y}_k. \end{aligned} \tag{3}$$

Note that we need both $\boldsymbol{\Phi}$ and $\boldsymbol{\Lambda}$ to compute $\bar{\boldsymbol{x}}_k$. Assuming $\boldsymbol{\Lambda}$ and $\boldsymbol{\Phi}$ as follows are known, we repeat the following three iterative steps until convergence. At the $(l+1)$-th iteration:

1. Estimate $\bar{\boldsymbol{x}}_k^{(l+1)}$, assuming known $\boldsymbol{\Lambda}^{(l)}$ and $\boldsymbol{\Phi}^{(l)}$.
2. Estimate $\boldsymbol{\Phi}^{(l+1)}$, assuming known $\bar{\boldsymbol{x}}_k^{(l+1)}$ and $\boldsymbol{\Lambda}^{(l)}$.
3. Estimate $\boldsymbol{\Lambda}^{(l+1)}$, assuming known $\bar{\boldsymbol{x}}_k^{(l+1)}$ and $\boldsymbol{\Phi}^{(l+1)}$.

We estimate $\boldsymbol{\Phi}$ in the $(l+1)$-th iteration by maximizing the following cost function, which is defined as the logarithm of marginal likelihood $p(\boldsymbol{y}|\boldsymbol{\Phi})$ given $\boldsymbol{\Phi}$:

$$\mathcal{F}(\boldsymbol{\Phi}) = \log|\boldsymbol{\Sigma}_y| + \frac{1}{k}\sum_{k=1}^{K} \boldsymbol{y}_k^\top \boldsymbol{\Sigma}_y^{-1} \boldsymbol{y}_k, \tag{4}$$

where the model data covariance

$$\boldsymbol{\Sigma}_y = \boldsymbol{\Lambda}^{-1} + \boldsymbol{L}\boldsymbol{\Phi}^{-1}\boldsymbol{L}^\top. \tag{5}$$

Then, similar to Champagne (Wipf et al., 2010; Cai et al., 2019), we utilize a convex bounding on the cost logarithm (Equation 4),

$$\begin{aligned} \tilde{\mathcal{F}}(\boldsymbol{\Phi}) = &\frac{1}{K}\sum_{k=1}^{K}\left[(\boldsymbol{y}_k - \boldsymbol{L}\bar{\boldsymbol{x}}_k)^\top \boldsymbol{\Lambda}^{-1}(\boldsymbol{y}_k - \boldsymbol{L}\bar{\boldsymbol{x}}_k)\right] \\ &+ \frac{1}{K}\sum_{k=1}^{K} \bar{\boldsymbol{x}}_k^\top \boldsymbol{\Phi}^{-1}\bar{\boldsymbol{x}}_k + \text{tr}(\boldsymbol{g}^\top\boldsymbol{\Phi}) + g_0, \end{aligned} \tag{6}$$

where $\boldsymbol{g} = \text{diag}(g_1, g_2, \cdots, g_n)$ and g_0 are auxiliary variables. Setting the derivative of $\tilde{\mathcal{F}}(\boldsymbol{\Phi})$ with respect to ϕ_i and g_i generates the update rules below,

$$\begin{aligned} \hat{\phi}_i &= \sqrt{\frac{\frac{1}{K}\sum_{k=1}^{K}\bar{x}_k^2(i)}{\hat{g}_i}}, \\ \hat{g}_i &= \boldsymbol{l}_i^\top\boldsymbol{\Sigma}_y^{-1}\boldsymbol{l}_i. \end{aligned} \tag{7}$$

The update rule of $\boldsymbol{\Phi}$ is defined as $\hat{\boldsymbol{\Phi}} = diag(\hat{\phi}_1, \hat{\phi}_2, \cdots, \hat{\phi}_n)$.

2.3 Structured noise estimation using variational Bayesian factor analysis

To estimate $\mathbf{\Lambda}$, we perform inference on a variational Bayesian factor analysis model of the following residual noise at the l-th iteration (Nagarajan et al., 2007):

$$\boldsymbol{z}_k = \boldsymbol{y}_k - \boldsymbol{L}\bar{\boldsymbol{x}}_k, \tag{8}$$

where the residual noise at the k-th time-point is $\boldsymbol{z}_k \in \mathbb{R}^{m\times 1}$. We note that our estimation problem involving a multivariate Gaussian noise process becomes intractable if both the source covariance is non-diagonal and non-sparse and the noise covariance is full rank. The assumption of structured noise helps with accurate estimation with the use of the variational Bayesian factor analysis methods which are robust to smaller data sizes and to the underlying factor dimension specification. The joint estimation of both diagonal sparse source covariance and structured noise covariance is what we are aiming for. Currently, we perform factor analysis-based decomposition of $\boldsymbol{x}_k$ as follows:

$$\boldsymbol{z}_k = \boldsymbol{A}\boldsymbol{u}_k + \boldsymbol{\varepsilon},$$

where $\boldsymbol{A} \in \mathbb{R}^{m\times q}$ is a mixing matrix, $\boldsymbol{u}_k$ is a q-dimensional column vector, and $\boldsymbol{\varepsilon}$ is modeling noise. Notice that we drop the iteration symbol l for simplification of notations.

We further assume the prior probability distribution of the factor u_k to be the zero-mean Gaussian with its precision matrix equal to the identity matrix as follows:

$$p(\boldsymbol{u}_k) = \mathcal{N}(\mathbf{0}, \mathbf{I}).$$

We define the j-th row of mixing matrix A as a column vector $\boldsymbol{a}_j$ such that

$$\boldsymbol{A} = \begin{bmatrix} \boldsymbol{a}_1^T \\ \boldsymbol{a}_2^T \\ \vdots \\ \boldsymbol{a}_M^T \end{bmatrix}.$$

Currently we assume the prior distribution of $\boldsymbol{a}_j$ to be:

$$p(\boldsymbol{a}_j) = \mathcal{N}\big(\mathbf{0}, (\sigma_j\boldsymbol{\alpha})^{-1}\big), \tag{9}$$

where the j-th diagonal element of the modeling noise precision matrix Σ is denoted σ_j, and $\boldsymbol{\alpha} = \mathrm{diag}(\alpha_1, \alpha_2, \ldots, \alpha_q)$ is a diagonal matrix. It can be further shown that the posterior probability distribution has the form of the Gaussian distribution:

$$p(\boldsymbol{a}_j|\boldsymbol{z}) = \mathcal{N}\big(\bar{\boldsymbol{a}}_j, (\sigma_j\boldsymbol{\Psi})^{-1}\big),$$

where $\boldsymbol{z} = [\boldsymbol{z}_1, \cdots, \boldsymbol{z}_K]$ is the residual signal of K time points, and $\bar{\boldsymbol{a}}_j$ and $\sigma_j\boldsymbol{\Psi}$ are the mean and precision matrix of the posterior distribution.

For simplicity, the prior probability distribution of the factor $\boldsymbol{u}_k$ is assumed to be the zero-mean Gaussian with its precision matrix equal to the identity matrix,

$$p(\boldsymbol{u}_k) = \mathcal{N}(\mathbf{0}, \mathbf{I}).$$

The factor activity $\boldsymbol{u} = [\boldsymbol{u}_1, \cdots, \boldsymbol{u}_K]$ is assumed to be independent across time. Thus, the joint prior distribution has the form

$$p(\boldsymbol{u}) = \prod_{k=1}^{K} p(\boldsymbol{u}_k) = \prod_{k=1}^{K} \mathcal{N}(\mathbf{0}, \mathbf{I}),$$

where $\mathbf{I}$ is an identity matrix of size $P \times P$. The modeling noise ε is assumed to be Gaussian with the mean of zero:

$$p(\boldsymbol{\varepsilon}) = \mathcal{N}(\mathbf{0}, \mathbf{\Omega}^{-1}),$$

where $\mathbf{\Omega}$ is a diagonal precision matrix. Currently, one can show that the posterior distribution $p(\boldsymbol{u}_k|z_k)$ is also Gaussian, which we assume to be:

$$p(\boldsymbol{u}_k|\boldsymbol{z}_k) = \mathcal{N}(\bar{\boldsymbol{u}}_k, \mathbf{\Sigma}_u^{-1}),$$

where $\bar{\boldsymbol{u}}_k$ and $\mathbf{\Sigma}_u$ are mean and precision, respectively.

By using the variational Bayesian expectation maximization (EM) algorithm, it can be derived that

$$\begin{aligned} \mathbf{\Sigma}_u &= \boldsymbol{A}^\top\mathbf{\Omega}\boldsymbol{A} + m\boldsymbol{\Psi}^{-1} + \mathbf{I} && (10)\\ \bar{\boldsymbol{u}}_k &= \mathbf{\Sigma}_u^{-1}\boldsymbol{A}^\top\mathbf{\Omega}\boldsymbol{z}_k && (11)\\ \boldsymbol{A} &= \boldsymbol{R}_{zu}(\boldsymbol{R}_{uu} + \boldsymbol{\alpha})^{-1} && (12)\\ \boldsymbol{\Psi} &= \boldsymbol{R}_{uu} + \boldsymbol{\alpha}, && (13) \end{aligned}$$

where $\boldsymbol{R}_{uu} = E_u\big[\sum_{k=1}^{K} \boldsymbol{u}_k\boldsymbol{u}_k^\top\big]$, $\boldsymbol{R}_{zu} = E_u\big[\sum_{k=1}^{K} \boldsymbol{z}_k\boldsymbol{u}_k^T\big]$. Note that the hyper-parameters $\boldsymbol{\alpha}$ and $\mathbf{\Omega}$ can be updated as follows:

$$\begin{aligned} \boldsymbol{\alpha}^{-1} &= \mathrm{diag}\Big[\frac{1}{m}\boldsymbol{A}^\top\mathbf{\Omega}\boldsymbol{A} + \boldsymbol{\Psi}^{-1}\Big] \\ \mathbf{\Omega}^{-1} &= \frac{1}{K}\big[\boldsymbol{R}_{zz} - \boldsymbol{A}\boldsymbol{R}_{uz}\big], \end{aligned} \tag{14}$$

where $\boldsymbol{R}_{zz} = E_u\big[\sum_{k=1}^{K} \boldsymbol{z}_k\boldsymbol{z}_k^\top\big]$ and $\boldsymbol{R}_{uz} = \boldsymbol{R}_{zu}^T$. Finally, we iteratively update the above equations until the free energy function converged and the covariance matrix of the structured noise computed only using the signal of interest is given by

$$\mathbf{\Lambda} = E[\boldsymbol{z}\boldsymbol{z}] = \frac{1}{K}\boldsymbol{A}\boldsymbol{R}_{uu}\boldsymbol{A}^\top + \frac{1}{K}\mathbf{\Omega}^{-1}\mathrm{tr}(\boldsymbol{R}_{uu}\boldsymbol{\Psi}^{-\mathbf{1}}). \tag{15}$$

We refer to the proposed brain source imaging method as *structured noise Champagne (SNC)*. The key aspect is the novel way of estimating the covariance of the residual noise within each iteration.

3 Simulation experiments

In this section, we focus on experiments with simulated data. In particular, we follow a standard protocol from the literature for simulating MEG source signals. We combine this with simulated structured noise of which the precision matrix has low rank. More details are provided in Section 3.3.

3.1 Quantifying performance

The performance of brain source reconstructions is evaluated using response receiver operating characteristics (FROC) (Cai et al., 2021). It basically measures the probability of detecting a true source in an image vs. the expected value of the number of false-positive detection per image. We further compute the A' metric which is the area under the FROC curve (Owen et al., 2012; Snodgrass and Corwin, 1988). Note that the A' metric determines the hit rate (h_r) of correctly detecting the active sources. We define the hit rate (h_r) as the number of hits for dipolar sources divided by the true number of dipolar sources in the brain. A dipolar source is considered as hit when recovered signal power is beyond a certain threshold value. First, the voxels localized by each algorithm that are included in the calculation of hit rates are defined as voxels that are (i) at least 1% of the maximum activation of the localization result and (ii) within the largest 10% of all of the voxels in the brain. Within these subsets of voxels, we test whether each voxel is within the ten nearest voxels to a true source. If estimated activity of a particular voxel lies within a true source, that source gets labeled as a "hit." We also define another metric false positive rate (f_r) as the number of potential false-positive dipolar sources divided by the total number of false dipolar sources. Note that a larger AOC value indicates a higher hit rate (h_r) than a false-positive rate (f_r). The expression for the A' metric (Owen et al., 2012) is given by:

$$A' = \frac{1}{2}(h_r + f_r) + \frac{1}{2}. \tag{16}$$

In our experiments, we also study the accuracy of the time course reconstructions. This accuracy metric $\overline{R}$ is defined as the correlation coefficient between the seed and estimated source time courses for each hit. The overall performance of both the accuracy of the localization and reconstruction of time courses is computed by combining A' and $\overline{R}$. The aggregated performance (AP) is given by Cai et al. (2019):

$$AP = \frac{1}{2}(A' + h_r\overline{R}). \tag{17}$$

We see that AP values range in $[0, 1]$. A higher value of AP indicates a better overall performance of source localization and time course reconstruction.

3.2 Benchmarking methods

We compare our method *structured noise Champagne (SNC)* with the following existing source localization methods:

1. Minimum current estimate (MCE) (Matsuura and Okabe, 1995),
2. Standardized low-resolution brain electromagnetic tomography (sLORETA) (Pascual-Marqui et al., 2002),
3. Linearly constrained minimum variance (LCMV) (Van Veen et al., 1997),
4. Noise learning Champagne (NLC) (Cai et al., 2021).

We apply these existing methods within the targeted structured noise model. For experiments with real data, we first estimate the noise variance using the variational Bayesian factor analysis (VBFA) algorithm (Nagarajan et al., 2007) and use the original Champagne (Nagarajan et al., 2007) to estimate the location of active brain sources. This result would set an upper bound on the performance of Champagne with noise learning when baseline data are not available for real data.

3.3 MEG simulations

We generate source signal data by simulating dipole sources with a fixed orientation. Damped sinusoidal oscillations with frequencies sampled randomly between 1 and 75 Hz are created as voxel source time courses. The time-courses are then projected to the sensors using the lead-field matrix generated by the forward model. We consider 271 MEG sensors and a single-shell spherical model (Hallez et al., 2007) implemented in SPM12 (http://www.fil.ion.ucl.ac.uk/spm) at the default spatial resolution of 8,196 voxels corresponding approximately to a 5-mm inter-voxel spacing. We simulated 480 samples for which sampling frequency is 1200 Hz and signal duration is 0.8 s.

To evaluate the robustness of the proposed method, we randomly choose noise activity with real brain noise consisting of actual resting-state sensor recordings collected from ten human subjects presumed to have only spontaneous brain activity and sensor noise. Signal-to-noise ratio (SNR) and correlations between voxel time courses are varied to examine algorithm performance. The SNR and time course correlation are defined in Owen et al. (2012). We show an example of time-course reconstruction using our proposed method in Figures 1, 2. The top plot in Figure 1 is the simulated ground-truth MEG signal with five active sources. This is followed by the time-course at the MEG sensor (before adding the noise). Moreover, finally, the time-course at the bottom in Figure 1 is the measured signal at the MEG sensor with additive noise of 5 dB. The reconstructed time-series using our method SNC is shown in Figure 2. We also display the time-series reconstructions obtained using NLC (Cai et al., 2021), sLORETA (Pascual-Marqui et al., 2002), LCMV (Van Veen et al., 1997), and MCE (Matsuura and Okabe, 1995). It is noteworthy that the new method SNC is able to reconstruct the time-series best. For all simulations, the inter-source correlation coefficient was fixed at 0.99 and the SNR was fixed at 3 dB. To highlight the source localization by all five methods, we show the power at each voxel of the reconstructed time-series and compare it with the ground-truth in Figure 3. Notice that our method SNL achieves the best results to rightly localize the brain sources. In other words, it shows the localization performance of the methods in the simulation experiment.

We also evaluate algorithm performance as a function of SNR, as shown in Figure 4. The reconstruction performance is evaluated for five randomly seeded dipolar sources with an inter-source correlation coefficient of 0.99. The simulations were performed at SNRs from −8 dB to 10 dB at a step of 1 dB. Both metrics suggest that our method structured noise Champagne (SNC) is able to localize the active brain sources more accurately than the existing methods.

Our method structured noise Champagne (SNC) deviates from the original Champagne algorithm by the way of noise precision update step. In the original Champagne algorithm, Λ is learnt

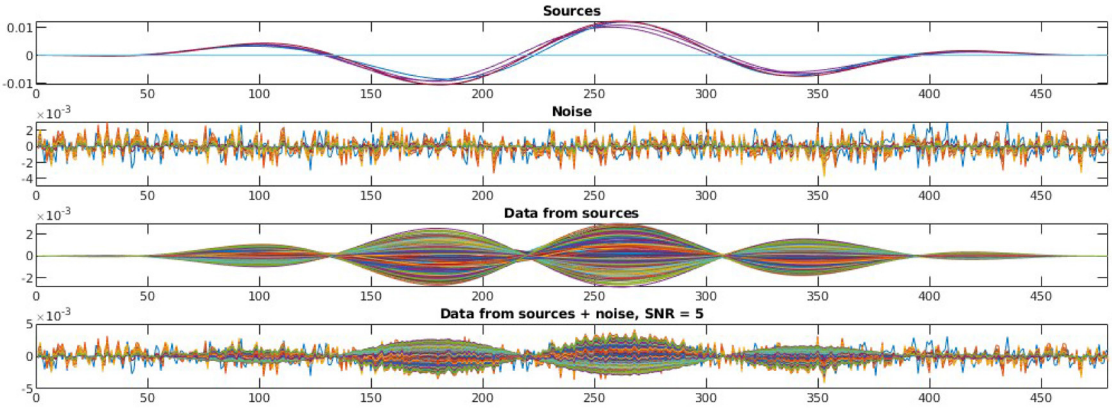

FIGURE 1
Simulated MEG signal, structured noise, and measurement from MEG sensors. In this experiment, we have five brain sources as we see on the top plot. The second plot shows the noise generated as per our model of structured noise. The third plot presents the measured signal at the MEG sensor resulting only from the active brain source time-series—Lx in Equation 1. Finally, the time-series at the bottom is the one captured at MEG sensors resulting from both active sources and noise—y in Equation 1. For all these, we show 480 time-points.

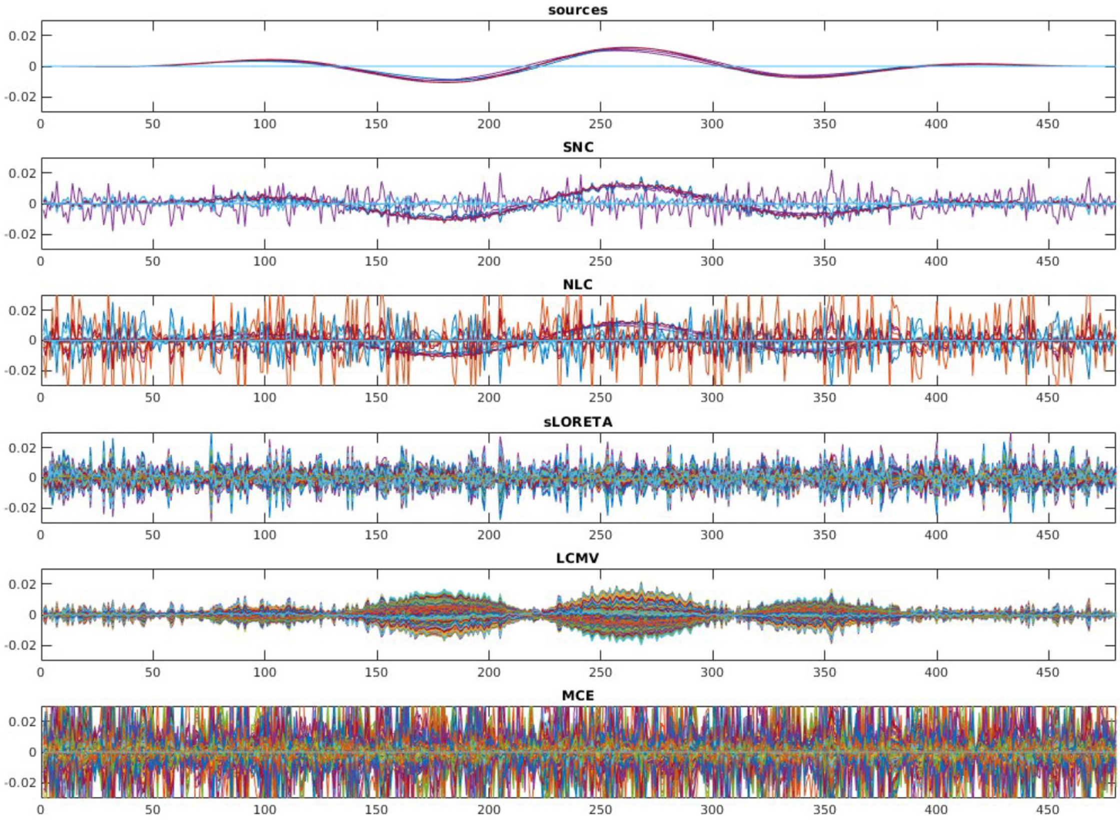

FIGURE 2
Reconstruction results on the simulated MEG measurement shown in Figure 1. Recall, we have five brain sources in this experiment. It is desirable for a good brain source imaging method to recover the brain source signal successfully while also suppressing the noise. Notice that in this experiment for the considered structured noise model, noise learning Champagne (NLC), and our method structured noise Champagne (SNC) are able to mitigate the noise more successfully. Between them, SNC is able to produce cleaner brain source time-series. In this experiment, standardized low-resolution brain electromagnetic tomograph (sLORETA), linearly constrained minimum variance (LCMV), and minimum current estimate (MCE) failed to achieve satisfactory reconstruction.

from available baseline or control measurements (Wipf et al., 2010). In contrast, here in structured noise Champagne (SNC), we update rules for estimation of a diagonal noise covariance, without baseline measurements. In Figure 5, we demonstrate how well the structured noise is reconstructed. In particular, we compute the geodesic distance (Venkatesh et al., 2020) between true structured

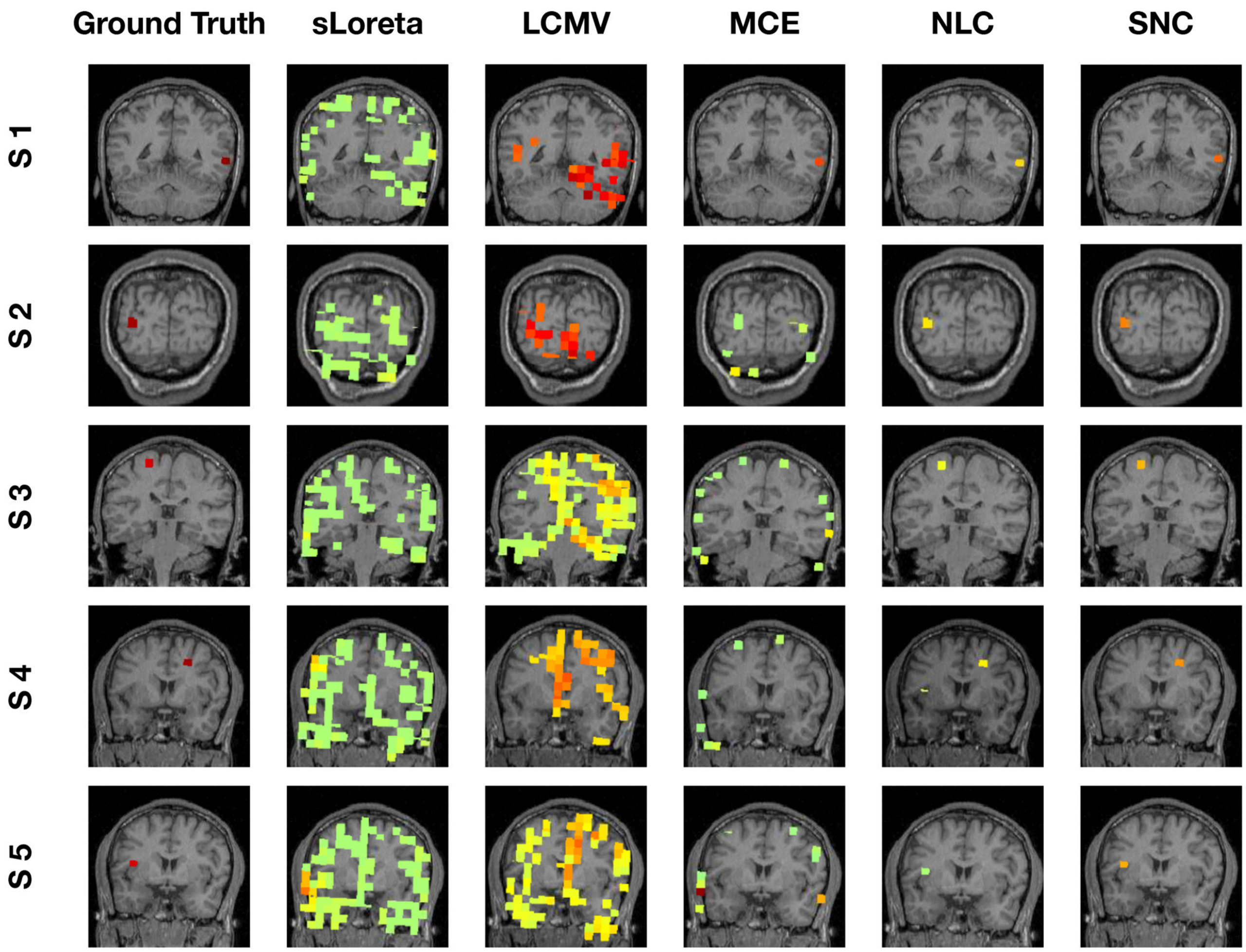

FIGURE 3
Localization results of simulation experiment (visualization of brain sources power). In this experiment, we simulated five brain sources: S1, S2, S3, S4, and S5. For each brain source, we display the localization by all five methods. Notice that our method SNC is able to localize the sources most accurately.

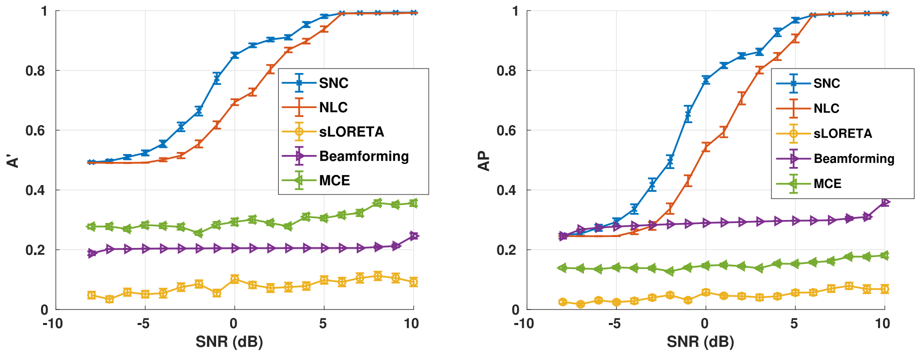

FIGURE 4
Aggregate performance in simulations for varying noise levels for the number of noise factors $m = 40$. In this experiment, we use five active brain sources in our simulation. On the other hand, we first simulated a structured noise drawn from $\mathcal{N}(0, \Lambda^{-1})$. Furthermore, we use the knowledge of the structured noise model at the heart of our method to reconstruct the voxel-level time-series. Notice that our method structured noise Champagne (SNC) performs better than every existing method in terms of correctly localizing the active brain sources.

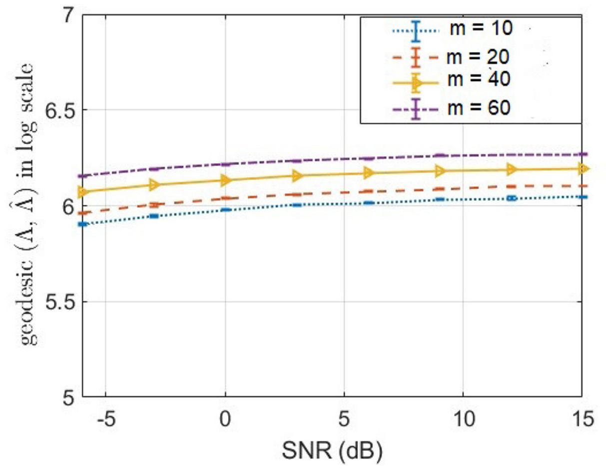

FIGURE 5
Geodesic distance (Venkatesh et al., 2020) between true and estimated precision matrices of structured noise for a different number of noise factors *m*.

noise and the reconstructed one using SNC. Then, we plot the geodesic distance across a range of signal-to-noise ratio (SNR) for different values of rank. We found that our method SNC is able to predict the structured noise fairly consistently across SNR values. However, we empirically also found that there is still scope for improvement in the estimated noise precision. We will focus on new technical innovations to address this limitation in our future research.

4 Analysis on real MEG data

Real MEG data were acquired in the Biomagnetic Imaging Laboratory at the University of California, San Francisco (UCSF) with a CTF Omega 2000 whole-head MEG system from VSM MedTech (Coquitlam, BC, Canada) at a 1,200 Hz sampling rate. Formal consent was collected from each participant in our study for using his/her data for research studies. All study protocols were approved by the Committee for Human Research at UCSF. The lead-field for each subject was calculated in NUTMEG (Hinkley et al., 2020) using a single-sphere head model and an 8-mm voxel grid corresponding to 5,300 voxels. Each lead-field column was normalized to have a norm of unity. The MEG data were digitally filtered from 1 to 45 Hz to remove artifacts and DC offset. In addition, trials with clear artifacts or visible noise in the MEG sensors that exceeded 10 pT fluctuations were excluded prior to source localization analysis. We experimented on one real MEG auditory evoked fields (AEF) dataset (Cai et al., 2021) to evaluate the performance of our newly introduced brain source imaging method SNC.

4.1 Auditory evoked fields data

In this section, we discuss the neural source localization performance of our method structured noise Champagne (SNC) on auditory evoked fields (AEF) in the MEG signal. AEF are often characterized as a function of latency, scalp topography, and the perceptual/cognitive process (Godey et al., 2001). Source localization from auditory evoked fields (AEF) data using MEG measurement is a potential alternative for studying human brain function (Teale et al., 1996). In all experiments with AEF data, the neural response time-series was elicited during passive listening to binaural tones (600 ms duration, carrier frequency of 1 kHz, 40 dB SL). The post-stimulus window in which AEF were analyzed was set to be +50 ms to +150 ms.

Figure 6 shows auditory evoked field (AEF) localization results vs. the number of trials from a single representative subject. We compare our result with other methods—sLORETA, LCMV, MCE, and NLC. The power at each voxel around the M100 peak is plotted for each algorithm. SNC is able to localize the expected bilateral brain activation with focal reconstructions under all trial settings. Specifically, the activities localize to Heschl's gyrus in the temporal lobe, which is the characteristic location of the primary auditory cortex. NLC is able to localize the bilateral auditory activity but with shrinkage on one side of the brain activity. The other algorithms do not show robustness compared to SNC. Notice that localization of MCE is biased toward the edge of the head. On the other hand, sLORETA and LCMV produce several areas of pseudo-brain activity. We further note that the LCMV beamformer has a disadvantage in this structured noise scenario due to its well-described weakness for temporally correlated sources as they occur in the auditory cortices for AEFs.

In Figure 7, we present the performance results of sLORETA, LCMV, MCE, NLC, and SNC for AEF localization vs. number of trials for one subject. The error bars in each plot show standard error. Trials are randomly chosen from around 120 trials from each subject, and the number of trials is set in a range from 5 to 60. Each condition is repeated over 30 times for each subject. In this case, we consider the ground truth as the brain activity estimated from approximately 120 trials. In general, increasing the number of trials increases the performance of all algorithms. Notice that all algorithms perform similar when the number of trials is under 10. However, both NLC and SNC work better when the number of trials is above 20. Importantly, when the number of trials increases higher than 40, SNC outperforms all other methods in terms of efficiently localizing the active brain sources.

5 Discussion

This study offers an efficient way to estimate contributions to sensors from noise without the need for additional "baseline" or "control" data, while preserving robust reconstruction of complex brain source activity. The underlying data estimation part of our algorithm is based on a principled idea of estimating noise statistics from the model residuals at each iteration of the alternating minimization step of the Champagne algorithm. The key step of the noise learning operation is accomplished by the fact that the residual noise at each iteration exhibits structured precision statistics. The proposed algorithm is readily available to handle a variety of configurations of brain sources under high noise and interference conditions without the need for additional baseline measurements—a requirement that commonly arises in datasets

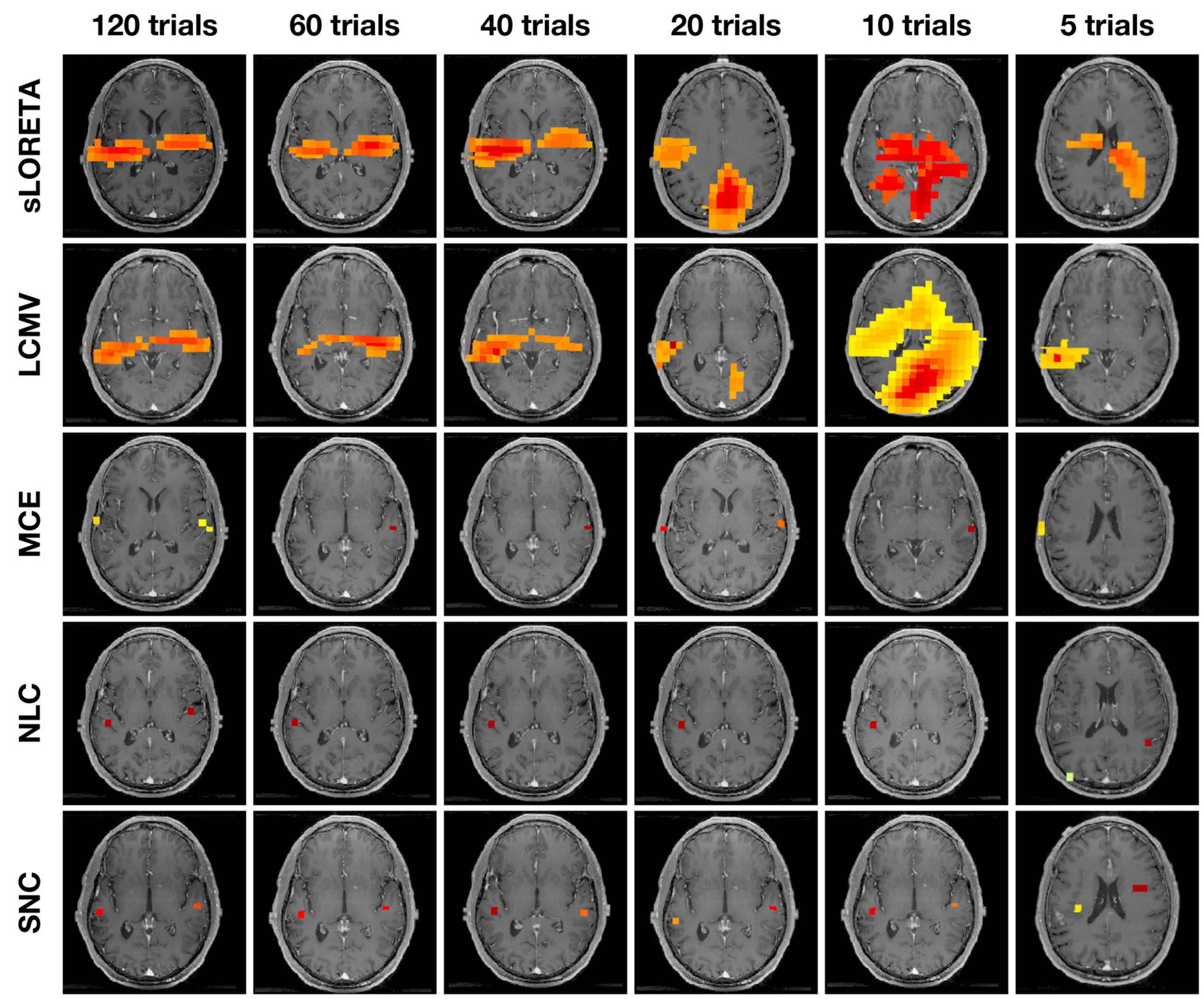

FIGURE 6
Auditory evoked field (AEF) localization results vs. number of trials from one representative subject using standardized low-resolution brain electromagnetic tomograph (sLORETA), linearly constrained minimum variance (LCMV), minimum current estimate (MCE), noise learning Champagne (NLC), and our method structured noise Champagne (SNC). Note that NLC is able to localize the bilateral auditory activity. In contrast, MCE localization is biased toward the edge of the head. Both sLORETA and LCMV produce some areas of pseudo brain activity.

like resting state data analyses. In this context, we note some of the noise/interference reduction strategies—signal space separation (SSS) (Taulu et al., 2005), signal-space projection (SSP) (Uusitalo and Ilmoniemi, 1997), and dual signal subspace projection (DSSP) (Sekihara et al., 2016) for EEG/MEG signals. These methods are primary preprocessing techniques for the EEG/MEG analysis pipeline. In fact, these methods are precisely used to mitigate the noise/interference from the MEG/EEG sensor and external sources. However, none of these are designed to reconstruct the voxel-level time-series. On contrary, our method SNC estimates the MEG/EEG time-series at each voxel of the sensor data.

Exhaustive experimental results demonstrate that the proposed source imaging method offers significant theoretical and empirical advantages over the existing benchmark algorithms when the noise covariance cannot be accurately determined in advance. In simulations, we particularly explored noise learning algorithmic performance for complex source configurations with highly correlated time-courses, and high levels of noise and interference. These simulation results establish the fact that our method outperforms the classical Champagne algorithm (Nagarajan et al., 2007) with an incorrect noise covariance as it achieves higher score of aggregated performance as compared to this and other existing benchmarking methods (Matsuura and Okabe, 1995; Pascual-Marqui et al., 2002; Van Veen et al., 1997; Cai et al., 2021). It is relevant to mention that data-driven approaches, that is, artificial neural networks (ANN)-based inverse solutions, are receiving increasing interest in the literature (Razorenova et al., 2020; Sun et al., 2020; Hecker et al., 2021; Liang et al., 2023). It would be an interesting future extension to explore the scope of our proposed noise learning scheme within these recent artificial intelligence techniques.

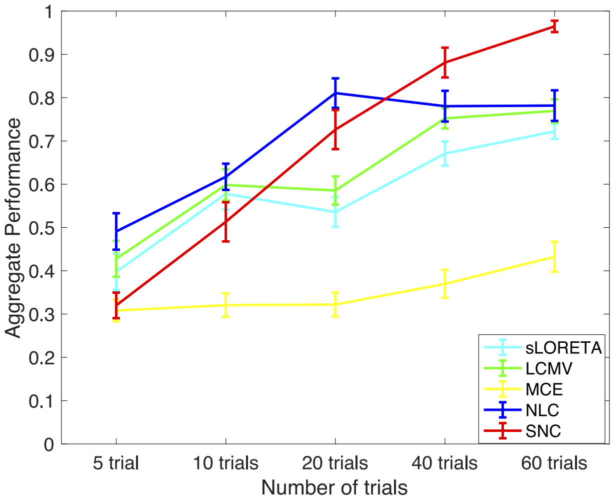

FIGURE 7
Aggregate performance results vs. number of trials for auditory evoked field (AEF) data using standardized low-resolution brain electromagnetic tomograph (sLORETA), linearly constrained minimum variance (LCMV), minimum current estimate (MCE), noise learning Champagne (NLC), and our method structured noise Champagne (SNC). It is interesting to note that SNC achieves the best aggregated performance after 40 trials. As expected, the performance also improves with the number of trials.

To the best of our understanding, the improved performance of this algorithm arises from the efficient the method of estimating the noise statistics via factor analysis of the residual component. Moreover, the proposed structured noise Champagne (SNC) algorithm is found to be robust even when the algorithms are initialized to incorrect noise values. Most importantly, the proposed method is able to robustly localize brain activity with a few trials or even with a single trial in the AEF dataset. This is indeed a significant advancement in electromagnetic brain imaging. We argue that this phenomenon may dramatically cut down the duration of data collection up to 10-fold. This scan-time reduction is particularly important in studies involving children with autism, patients with dementia, or any other subjects who have difficulty tolerating long periods of data collection. In summary, our proposed method offers significant advantages over many existing benchmark algorithms for electromagnetic brain source imaging.

Finally, we would like to discuss some tradeoffs in the current algorithm. Here, we restrict to a diagonal source covariance matrix estimate, which ensures the sparsity of brain sources (Hashemi et al., 2021a), and our convex bounding cost function ensures guaranteed convergence (Wipf et al., 2011; Wipf and Nagarajan, 2009). The structured low-dimensional manifold assumption of the noise covariance helps with accurate estimation with the use of the variational Bayesian factor analysis methods which are robust to smaller data sizes and to the underlying factor dimension specification (Nagarajan et al., 2006, 2007). However, if we want to solve a joint signal and noise estimation problem where both the source and noise covariances are non-diagonal and non-sparse, this problem can become intractable (Hashemi et al., 2020, 2021a). We hope to examine this problem in our future study.

Data availability statement

The raw data supporting the conclusions of this article will be made available by the authors, without undue reservation.

Ethics statement

The studies involving humans were approved by the UCSF Human Research Protection Program Institutional Review Board. The studies were conducted in accordance with the local legislation and institutional requirements. The participants provided their written informed consent to participate in this study.

Author contributions

SG: Formal analysis, Methodology, Software, Validation, Writing – original draft, Writing – review & editing, Conceptualization, Data curation, Visualization. CC: Formal analysis, Methodology, Software, Validation, Writing – original draft, Writing – review & editing, Conceptualization, Data curation, Visualization. AH: Formal analysis, Methodology, Software, Validation, Writing – original draft, Writing – review & editing, Conceptualization, Data curation, Visualization. YG: Formal analysis, Methodology, Software, Validation, Writing – original draft, Writing – review & editing, Conceptualization, Data curation, Visualization. SH: Conceptualization, Funding acquisition, Investigation, Supervision, Writing – original draft, Writing – review & editing, Methodology, Project administration, Resources. KS: Conceptualization, Funding acquisition, Investigation, Supervision, Writing – original draft, Writing – review & editing, Methodology, Project administration, Resources. AR: Conceptualization, Funding acquisition, Investigation, Supervision, Writing – original draft, Writing – review & editing, Methodology, Project administration, Resources. SN: Conceptualization, Funding acquisition, Investigation, Supervision, Writing – original draft, Writing – review & editing, Methodology, Project administration, Resources.

Funding

The author(s) declare that financial support was received for the research and/or publication of this article. This study was supported by the National Institutes of Health grants: R01DC013979 (SN), R01NS066654 (SN), R01NS64060 (SN), P50DC019900 (SN), National Science Foundation Grant BCS-1262297 (SN), and the Knowledge Innovation Program of Wuhan-Shuguang Project 2023010201010124, National Natural Science Foundation of China under Grant 62277023 and financially supported by self-determined research funds of CCNU from the colleges' basic research and operation of MOE under Grant CCNU24JCPT037; and an industry contract from Ricoh MEG USA Inc. Ricoh MEG USA Inc. was not involved in the study design,

collection, analysis, interpretation of data, the writing of this article, or the decision to submit it for publication.

Acknowledgments

We would like to thank all the members of the Biomagnetic Imaging Laboratory for their invaluable contributions to the MEG data acquisition and data curation.

Conflict of interest

SN is a founding advisory board member of HippoClinic Inc. and is a consultant to MEGIN Inc. He has previously served on the advisory board of Rune Labs, and is also the recipient of a industry contract from Ricoh MEG USA Inc. KS was employed by Signal Analysis Inc.

The remaining authors declare that the research was conducted in the absence of any commercial or financial relationships that could be construed as a potential conflict of interest.

The author(s) declared that they were an editorial board member of Frontiers, at the time of submission. This had no impact on the peer review process and the final decision.

Publisher's note

References

Baillet, S., Mosher, J. C., and Leahy, R. M. (2001). Electromagnetic brain mapping. *IEEE Signal Process. Mag.* 18, 14–30. doi: 10.1109/79.962275

Cai, C., Diwakar, M., Chen, D., Sekihara, K., and Nagarajan, S. S. (2019). Robust empirical bayesian reconstruction of distributed sources for electromagnetic brain imaging. *IEEE Trans. Med. Imaging* 39, 567–577. doi: 10.1109/TMI.2019.2932290

Cai, C., Hashemi, A., Diwakar, M., Haufe, S., Sekihara, K., and Nagarajan, S. S. (2021). Robust estimation of noise for electromagnetic brain imaging with the Champagne algorithm. *Neuroimage* 225:117411. doi: 10.1016/j.neuroimage.2020.117411

Cai, C., Long, Y., Ghosh, S., Hashemi, A., Gao, Y., Diwakar, M., et al. (2023). Bayesian adaptive beamformer for robust electromagnetic brain imaging of correlated sources in high spatial resolution. *IEEE Trans. Med. Imag.* 42, 2502–2512. doi: 10.1109/TMI.2023.3256963

Cai, C., Sekihara, K., and Nagarajan, S. S. (2018). Hierarchical multiscale Bayesian algorithm for robust MEG/EEG source reconstruction. *Neuroimage* 183, 698–715. doi: 10.1016/j.neuroimage.2018.07.056

Dale, A. M., and Sereno, M. I. (1993). Improved localization of cortical activity by combining EEG and MEG with MRI cortical surface reconstruction: a linear approach. *J. Cogn. Neurosci.* 5, 162–176. doi: 10.1162/jocn.1993.5.2.162

Delorme, A., Palmer, J., Onton, J., Oostenveld, R., and Makeig, S. (2012). Independent EEG sources are dipolar. *PLoS ONE* 7:e30135. doi: 10.1371/journal.pone.0030135

Ding, L., and He, B. (2008). Sparse source imaging in electroencephalography with accurate field modeling. *Hum. Brain Mapp.* 29, 1053–1067. doi: 10.1002/hbm.20448

Edelman, B. J., Johnson, N., Sohrabpour, A., Tong, S., Thakor, N., and He, B. (2015). Systems neuroengineering: understanding and interacting with the brain. *Engineering* 1, 292–308. doi: 10.15302/J-ENG-2015078

Friston, K., Harrison, L., Daunizeau, J., Kiebel, S., Phillips, C., Trujillo-Barreto, N., et al. (2008). Multiple sparse priors for the m/EEG inverse problem. *Neuroimage* 39, 1104–1120. doi: 10.1016/j.neuroimage.2007.09.048

Ghosh, S., Cai, C., Gao, Y., Hashemi, A., Haufe, S., Sekihara, K., et al. (2023). "Bayesian inference for brain source imaging with joint estimation of structured low-rank noise," in *IEEE International Symposium on Biomedical Imaging (ISBI)*, 1–5. doi: 10.1109/ISBI53787.2023.10230330

Godey, B., Schwartz, D., De Graaf, J., Chauvel, P., and Liegeois-Chauvel, C. (2001). Neuromagnetic source localization of auditory evoked fields and intracerebral evoked potentials: a comparison of data in the same patients. *Clin. Neurophysiol.* 112, 1850–1859. doi: 10.1016/S1388-2457(01)00636-8

Gross, J. (2019). Magnetoencephalography in cognitive neuroscience: a primer. *Neuron* 104, 189–204. doi: 10.1016/j.neuron.2019.07.001

Hallez, H., Vanrumste, B., Grech, R., Muscat, J., De Clercq, W., Vergult, A., et al. (2007). Review on solving the forward problem in EEG source analysis. *J. Neuroeng. Rehabil.* 4:46. doi: 10.1186/1743-0003-4-46

Hämäläinen, M. S., and Ilmoniemi, R. J. (1994). Interpreting magnetic fields of the brain: minimum norm estimates. *Med. Biol. Eng. Comput.* 32, 35–42. doi: 10.1007/BF02512476

Hashemi, A., Cai, C., Gao, Y., Ghosh, S., Müller, K.-R., Nagarajan, S. S., et al. (2022). Joint learning of full-structure noise in hierarchical Bayesian regression models. *IEEE Trans. Med. Imag.* 43, 610–624. doi: 10.1109/TMI.2022.3224085

Hashemi, A., Cai, C., Kutyniok, G., Müller, K.-R., Nagarajan, S., and Haufe, S. (2020). Unification of sparse Bayesian learning algorithms for electromagnetic brain imaging with the majorization minimization framework. *bioRxiv*. doi: 10.1101/2020.08.10.243774

Hashemi, A., Cai, C., Muller, K. R., Nagarajan, S., and Haufe, S. (2021a). Joint learning of full-structure noise in hierarchical Bayesian Regression models. *bioRxiv*. doi: 10.1101/2021.11.28.470264

Hashemi, A., Gao, Y., Cai, C., Ghosh, S., Müller, K.-R., Nagarajan, S., et al. (2021b). "Efficient hierarchical bayesian inference for spatio-temporal regression models in neuroimaging," in *Advances in Neural Information Processing Systems*, 24855–24870.

He, B., Sohrabpour, A., Brown, E., and Liu, Z. (2018). Electrophysiological source imaging: a noninvasive window to brain dynamics. *Annu. Rev. Biomed. Eng.* 20, 171–196. doi: 10.1146/annurev-bioeng-062117-120853

He, B., Yang, L., Wilke, C., and Yuan, H. (2011). Electrophysiological imaging of brain activity and connectivity-challenges and opportunities. *IEEE Trans. Biomed. Eng.* 58, 1918–1931. doi: 10.1109/TBME.2011.2139210

Hecker, L., Rupprecht, R., Tebartz Van Elst, L., and Kornmeier, J. (2021). Convdip: A convolutional neural network for better EEG source imaging. *Front. Neurosci.* 15:569918. doi: 10.3389/fnins.2021.569918

Hinkley, L. B., Dale, C. L., Cai, C., Zumer, J., Dalal, S., Findlay, A., et al. (2020). NUTMEG: open source software for M/EEG source reconstruction. *Front. Neurosci.* 14:710. doi: 10.3389/fnins.2020.00710

Hosseini, S. A. H., Sohrabpour, A., Akçakaya, M., and He, B. (2018). Electromagnetic brain source imaging by means of a robust minimum variance beamformer. *IEEE Trans. Biomed. Eng.* 65, 2365–2374. doi: 10.1109/TBME.2018.2859204

Ioannides, A. A., Bolton, J. P., and Clarke, C. (1990). Continuous probabilistic solutions to the biomagnetic inverse problem. *Inverse Probl.* 6:523. doi: 10.1088/0266-5611/6/4/005

Leahy, R., Mosher, J., Spencer, M., Huang, M., and Lewine, J. (1998). A study of dipole localization accuracy for MEG and EEG using a human skull phantom. *Electroencephalogr. Clin. Neurophysiol.* 107, 159–173. doi: 10.1016/S0013-4694(98)00057-1

Liang, J., Yu, Z. L., Gu, Z., and Li, Y. (2023). Electromagnetic source imaging with a combination of sparse bayesian learning and deep neural network. *IEEE Trans. Neural Syst. Rehabilit. Eng.* 31, 2338–2348. doi: 10.1109/TNSRE.2023.3251420

Liu, F., Wan, G., Semenov, Y. R., and Purdon, P. L. (2022). "Extended electrophysiological source imaging with spatial graph filters," in *International Conference on Medical Image Computing and Computer-Assisted Intervention* (Springer), 99–109. doi: 10.1007/978-3-031-16431-6_10

Liu, F., Wang, L., Lou, Y., Li, R.-C., and Purdon, P. L. (2020). Probabilistic structure learning for EEG/MEG source imaging with hierarchical graph priors. *IEEE Trans. Med. Imaging* 40, 321–334. doi: 10.1109/TMI.2020.3025608

Liu, K., Yu, Z. L., Wu, W., Gu, Z., Zhang, J., Cen, L., et al. (2019). Bayesian electromagnetic spatio-temporal imaging of extended sources based on matrix factorization. *IEEE Trans. Biomed. Eng.* 66, 2457–2469. doi: 10.1109/TBME.2018.2890291

Matsuura, K., and Okabe, Y. (1995). Selective minimum-norm solution of the biomagnetic inverse problem. *IEEE Trans. Biomed. Eng.* 42, 608–615. doi: 10.1109/10.387200

Michel, C. M., and He, B. (2019). EEG source localization. *Handb. Clin. Neurol.* 160, 85–101. doi: 10.1016/B978-0-444-64032-1.00006-0

Mosher, J. C., Lewis, P. S., and Leahy, R. M. (1992). Multiple dipole modeling and localization from spatio-temporal MEG data. *IEEE Trans. Biomed. Eng.* 39, 541–557. doi: 10.1109/10.141192

Nagarajan, S. S., Attias, H. T., Hild, I. I., K. E., and Sekihara, K. (2006). A graphical model for estimating stimulus-evoked brain responses from magnetoencephalography data with large background brain activity. *Neuroimage* 30, 400–416. doi: 10.1016/j.neuroimage.2005.09.055

Nagarajan, S. S., Attias, H. T., Hild, K. E., and Sekihara, K. (2007). A probabilistic algorithm for robust interference suppression in bioelectromagnetic sensor data. *Stat. Med.* 26, 3886–3910. doi: 10.1002/sim.2941

Oikonomou, V. P., and Kompatsiaris, I. (2020). A novel Bayesian approach for EEG source localization. *Comput. Intell. Neurosci.* 2020:8837954. doi: 10.1155/2020/8837954

Owen, J. P., Wipf, D. P., Attias, H. T., Sekihara, K., and Nagarajan, S. S. (2012). Performance evaluation of the Champagne source reconstruction algorithm on simulated and real M/EEG data. *Neuroimage* 60, 305–323. doi: 10.1016/j.neuroimage.2011.12.027

Pascual-Marqui, R. D. (2002). Standardized low-resolution brain electromagnetic tomography (sloreta): technical details. *Methods Find. Exp. Clin. Pharmacol.* 24, 5–12. Available online at: https://www.institutpsychoneuro.com/wp-content/uploads/2015/10/sLORETA2002.pdf

Pascual-Marqui, R. D., Michel, C. M., and Lehmann, D. (1994). Low resolution electromagnetic tomography: a new method for localizing electrical activity in the brain. *Int. J. Psychophysiol.* 18, 49–65. doi: 10.1016/0167-8760(84)90014-X

Phillips, J. W., Leahy, R. M., Mosher, J. C., and Timsari, B. (1997). Imaging neural activity using MEG and EEG. *IEEE Eng. Med. Biol. Magaz.* 16, 34–42. doi: 10.1109/51.585515

Razorenova, A., Yavich, N., Malovichko, M., Fedorov, M., Koshev, N., and Dylov, D. V. (2020). "Deep learning for non-invasive cortical potential imaging," in *International Workshop on Machine Learning in Clinical Neuroimaging* (Springer), 45–55. doi: 10.1007/978-3-030-66843-3_5

Riaz, U., Razzaq, F. A., Areces-Gonzalez, A., Piastra, M. C., Vega, M. L. B., Paz-Linares, D., et al. (2023). Automatic quality control of the numerical accuracy of EEG lead fields. *Neuroimage* 273:120091. doi: 10.1016/j.neuroimage.2023.120091

Robinson, S. E., and Rose, D. F. (1992). "Current source image estimation by spatially filtered MEG," in *Biomagnetism Clinical Aspects*, eds. M. Hoke, et al. (New York: Elsevier Science Publishers), 761–765.

Scherg, M. (1990). Fundamentals of dipole source potential analysis. Auditory evoked magnetic fields and electric potentials. *Adv. Audiol.* 6:25.

Sekihara, K., Kawabata, Y., Ushio, S., Sumiya, S., Kawabata, S., Adachi, Y., et al. (2016). Dual signal subspace projection (DSSP): a novel algorithm for removing large interference in biomagnetic measurements. *J. Neural Eng.* 13:036007. doi: 10.1088/1741-2560/13/3/036007

Sekihara, K., and Nagarajan, S. S. (2008). *Adaptive Spatial Filters for Electromagnetic Brain Imaging*. Berlin, Heidelber: Springer-Verlag.

Sekihara, K., and Nagarajan, S. S. (2015). *Electromagnetic Brain Imaging: a Bayesian Perspective*. Cham: Springer. doi: 10.1007/978-3-319-14947-9

Sekihara, K., and Scholz, B. (1996). "Generalized Wiener estimation of three-dimensional current distribution from biomagnetic measurements," in *Biomag 96: Proceedings of the Tenth International Conference on Biomagnetism*, eds. C. J. Aine, et al. (New York: Springer-Verlag), 338–341. doi: 10.1007/978-1-4612-1260-7_82

Snodgrass, J. G., and Corwin, J. (1988). Pragmatics of measuring recognition memory: applications to dementia and amnesia. *J. Exper. Psychol.* 117:34. doi: 10.1037//0096-3445.117.1.34

Sun, R., Sohrabpour, A., Ye, S., and He, B. (2020). SIFNet: electromagnetic source imaging framework using deep neural networks. *bioRxiv, 2020–05*. doi: 10.1101/2020.05.11.089185

Taulu, S., Simola, J., and Kajola, M. (2005). Applications of the signal space separation method. *IEEE Trans. Signal Proc.* 53, 3359–3372. doi: 10.1109/TSP.2005.853302

Teale, P., Goldstein, L., Reite, M., Sheeder, J., Richardson, D., Edrich, J., et al. (1996). Reproducibility of MEG auditory evoked field source localizations in normal human subjects using a seven-channel gradiometer. *IEEE Trans. Biomed. Eng.* 43, 967–969. doi: 10.1109/10.532131

Uusitalo, M., and Ilmoniemi, R. (1997). Signal-space projection method for separating MEG or EEG into components. *Med. Biol. Eng. Comput.* 35, 135–140. doi: 10.1007/BF02534144

Van Veen, B. D., Van Drongelen, W., Yuchtman, M., and Suzuki, A. (1997). Localization of brain electrical activity via linearly constrained minimum variance spatial filtering. *IEEE Trans. Biomed. Eng.* 44, 867–880. doi: 10.1109/10.623056

Venkatesh, M., Jaja, J., and Pessoa, L. (2020). Comparing functional connectivity matrices: a geometry-aware approach applied to participant identification. *Neuroimage* 207:116398. doi: 10.1016/j.neuroimage.2019.116398

Wipf, D., and Nagarajan, S. (2009). A unified Bayesian framework for MEG/EEG source imaging. *Neuroimage* 44, 947–966. doi: 10.1016/j.neuroimage.2008.02.059

Wipf, D. P., Owen, J. P., Attias, H. T., Sekihara, K., and Nagarajan, S. S. (2010). Robust Bayesian estimation of the location, orientation, and time course of multiple correlated neural sources using MEG. *Neuroimage* 49, 641–655. doi: 10.1016/j.neuroimage.2009.06.083

Wipf, D. P., Rao, B. D., and Nagarajan, S. (2011). Latent variable Bayesian models for promoting sparsity. *IEEE Trans. Inf. Theory* 57, 6236–6255. doi: 10.1109/TIT.2011.2162174

Zumer, J., Attias, H., Sekihara, K., and Nagarajan, S. (2006). "A probabilistic algorithm integrating source localization and noise suppression of MEG and EEG data," in *Advances in Neural Information Processing Systems*, 19. doi: 10.7551/mitpress/7503.003.0208

Appendix

A1. Proof of Equation 3

Recall that the posterior probability distribution function $p(x_k|y_k)$ is Gaussian which we assumed to be $\mathcal{N}(\bar{x}_k, \mathbf{\Gamma}^{-1})$. Furthermore, the exponential part of this Gaussian distribution is given by:

$$\begin{aligned}&-\tfrac{1}{2}(x_k-\bar{x}_k)^T\mathbf{\Gamma}(x_k-\bar{x}_k)\\&=-\tfrac{1}{2}x_k^T\mathbf{\Gamma}x_k+x_k^T\mathbf{\Gamma}\bar{x}_k+\mathcal{C},\end{aligned} \tag{18}$$

where $\mathcal{C}$ stands for the terms that do not contain x_k.

We also know that $p(y_k|x_k) = \mathcal{N}(\boldsymbol{L}x_k, \mathbf{\Lambda}^{-1})$ and $p(x_k) = \mathcal{N}(0, \mathbf{\Phi}^{-1})$. Hence, the posterior probability $p(x_k|y_k)$ can be derived by using Bayes' rule in Equation 2. We see that the exponential part of the posterior probability $p(x_k|y_k)$ takes the form:

$$\begin{aligned}&-\tfrac{1}{2}\left[x_k^T\mathbf{\Phi}x_k+(y_k-\boldsymbol{L}x_k)^T\mathbf{\Lambda}(y_k-\boldsymbol{L}x_k)\right]\\&=-\tfrac{1}{2}x_k^T(\mathbf{\Phi}+\boldsymbol{L}^T\mathbf{\Lambda}\boldsymbol{L})x_k+x_k^T\boldsymbol{L}^T\mathbf{\Lambda}y_k+\mathcal{C}\simeq,\end{aligned} \tag{19}$$

where $\mathcal{C}\simeq$ again stands for the terms that do not contain x_k.

Comparing the quadratic terms of x_k on the right sides of Equations 18, 19:

$$\mathbf{\Gamma}=\mathbf{\Phi}+\boldsymbol{L}^T\mathbf{\Lambda}\boldsymbol{L}. \tag{20}$$

Similarly, comparing the linear terms of x_k on the right sides of Equations 18, 19:

$$\bar{x}_k=\mathbf{\Gamma}^{-1}\boldsymbol{L}^T\mathbf{\Lambda}y_k. \tag{21}$$

Furthermore, using the matrix inversion formula of Equation (C.92) in Sekihara and Nagarajan (2015), Equation 21 can be rewritten as:

$$\bar{\boldsymbol{x}}_k=\mathbf{\Phi}^{-1}\boldsymbol{L}^\top(\mathbf{\Lambda}^{-1}+\boldsymbol{L}\mathbf{\Phi}^{-1}\boldsymbol{L}^\top)^{-1}\boldsymbol{y}_k. \tag{22}$$

Frontiers in
Human Neuroscience

Bridges neuroscience and psychology to understand the human brain

The second most-cited journal in the field of psychology, that bridges research in psychology and neuroscience to advance our understanding of the human brain in both healthy and diseased states.

Discover the latest Research Topics

See more →

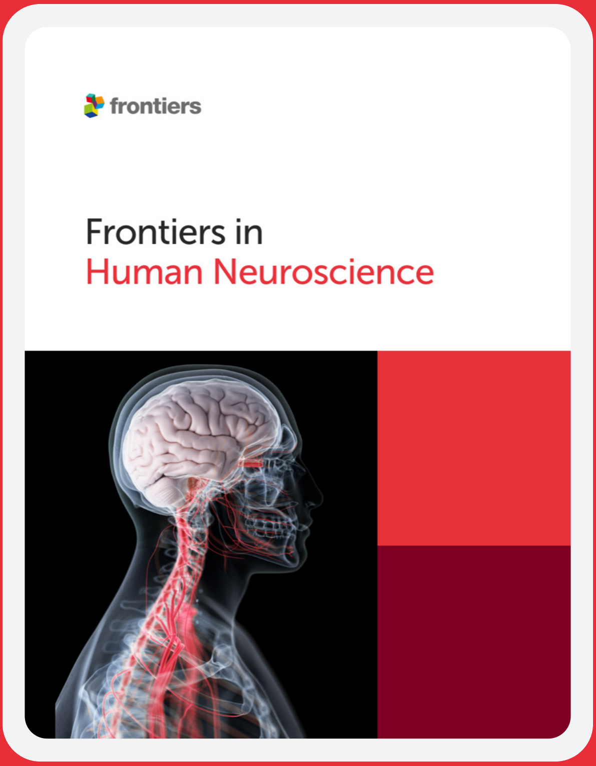

frontiers

Frontiers in
Human Neuroscience

Frontiers

Avenue du Tribunal-Fédéral 34
1005 Lausanne, Switzerland
frontiersin.org

Contact us

+41 (0)21 510 17 00
frontiersin.org/about/contact